# FLEXURAL ANCHORAGE PERFORMANCE AND STRENGTHENING ON NEGATIVE MOMENT REGIONS USING NEAR-SURFACE MOUNTED RETROFITTING IN REINFORCED CONCRETE BRIDGE GIRDERS

LAURA BARKER

M.S.

OREGON STATE UNIVERSITY

AN ABSTRACT OF THE THESIS OF

Laura Barker for the degree of Master of Science in Civil Engineering presented on August 15, 2014.

Title: Flexural Anchorage Performance and Strengthening on Negative Moment Regions Using Near-Surface Mounted Retrofitting in Reinforced Concrete Bridge Girders

Abstract approved: _____

Christopher C. Higgins

Large numbers of reinforced concrete deck girder (RCDG) bridges were built during the highway infrastructure boom of the 1950's. The advent of standardized deformed steel reinforcing bars during this time allowed for straight bar terminations in flexural tension regions. Designers of the time terminated reinforcing bars where they were no longer required by calculation and did not account for additional demands from the combination of shear and flexure. The design provisions of the time allowed higher shear stresses in the concrete than allowed in standards today which reduced the required quantity of transverse reinforcing steel. In addition, heavier trucks and higher traffic volumes on roadways today have greatly increased the service loading on these bridges.

Engineers evaluating these older RCDG bridges often determine unsatisfactory load ratings due to flexural anchorage deficiencies in the girders, especially when the influence of shear is considered. These deficiencies result from inadequate capacity compared to current design standards due to poor cutoff details used in the initial design. Strengthening methods are necessary because comprehensive replacements of the large number of bridges are not economically feasible.

Experimental research was conducted to evaluate the behavior of poorly detailed flexural anchorages and to develop methods to strengthen them. Realistic vintage girder specimens were constructed, retrofitted, instrumented, and tested to failure. The specimens reported in this thesis were full-scale inverted-T (IT) beams. Some of the specimens contained straight bar terminations crossing a preformed diagonal crack in the flexural tension region to investigate the influence of shear on the retrofit schemes. Instrumentation focused on measurement of the reinforcing steel stresses surrounding the diagonal crack and along the development length of the cutoff bars. Using results of past research to quantify the behavior of girders with straight-bar flexural anchorages in flexural tension regions, an innovative strengthening technique was developed using either near-surface mounted (NSM) stainless steel or titanium. Results from the NSM strengthening technique demonstrated the ability to delay or prevent flexural anchorage failures, with increased deformation capacities and increased strengths from 17% to 39% over baseline specimens.

To show the success of this research and the immediate need for strengthened flexural anchorages, this research has already been implemented on a bridge in Mosier, Oregon. This groundbreaking research is described in detail in Appendix F.

# Flexural Anchorage Performance and Strengthening on Negative Moment Regions Using Near-Surface Mounted Retrofitting in Reinforced Concrete Bridge Girders

by

Laura Barker

A THESIS

submitted to

Oregon State University

in partial fulfillment of

the requirements for the

degree of

Master of Science

Presented August 15, 2014

Commencement June 2015

Master of Science thesis of Laura Barker presented on August 15, 2014.

APPROVED:

_____

Major Professor, representing Civil Engineering

_____

Head of the School of Civil and Construction Engineering

_____

Dean of the Graduate School

I understand that my thesis will become part of the permanent collection of Oregon State University libraries. My signature below authorizes release of my thesis to any reader upon request.

_____

Laura Barker, Author

# ACKNOWLEDGEMENTS

I would like to extend my sincerest gratitude to Dr. Christopher Higgins for his guidance and the opportunity to work on this project. His patience and support are what led to the success of this project.

I would like to thank the Oregon Department of Transportation for their technical and financial support of this project.

The input and feedback provided on this thesis by my graduate committee members Dr. Jason Ideker, Dr. Burkan Isgor, and Dr. Christoph Thomas are greatly appreciated.

Construction, instrumentation, and testing of full-scale specimens are huge undertakings. I would like to sincerely thank Deanna Amneus for working alongside me every day. I appreciate the assistance given by Drew Strahler and Mike Dyson. This project could not have been completed in such a timely manner without the help of undergraduate helpers Kyle England, Brandon Zaikoski, and Caleb Lennon.

Lastly, I would like to acknowledge and thank my family for their tireless support throughout my schooling process. Their commitment, love, and encouragement are what carried me through this process.

TABLE OF CONTENTS

TABLE OF CONTENTS (Continued)

Page

TABLE OF CONTENTS (Continued)

Page

TABLE OF CONTENTS (Continued)

Page

LIST OF FIGURES

Figure Page

LIST OF FIGURES (Continued)

Figure Page

LIST OF FIGURES (Continued)

Figure Page

LIST OF FIGURES (Continued)

Figure Page

LIST OF FIGURES (Continued)

Figure Page

LIST OF FIGURES (Continued)

Figure Page

LIST OF TABLES

LIST OF TABLES (Continued)

Table Page

LIST OF APPENDICES

# FLEXURAL ANCHORAGE PERFORMANCE AND STRENGTHENING ON NEGATIVE MOMENT REGIONS USING NEAR-SURFACE MOUNTED RETROFITTING IN REINFORCED CONCRETE BRIDGE GIRDERS

## 1. INTRODUCTION

Large numbers of short and medium span bridges with reinforced concrete deck girders (RCDG) were built during the infrastructure boom in the 1950's. The advent of standardized deformed steel reinforcing bars during this time allowed for straight bar terminations in flexural tension regions. Standardized bars were thought to provide sufficient anchorage without the need for bends or hooks as was required prior for proprietary reinforcing bars. Terminations were permitted where bars were no longer required by calculation and the additional demands from the combination of shear and flexure were not accounted for in the design. Older design provisions also allowed higher shear stresses in the concrete than are permissible in modern standards, which reduced the quantity of transverse reinforcing steel below what would be allowed today.

Heavier trucks and higher traffic volume on roadways today have greatly increased the service loading on these bridges. Many of these bridges exhibit diagonal cracking due to shrinkage and thermal strains, live loading, and previous poor detailing practices. Diagonal cracks are commonly found at locations along the span where flexural reinforcing steel terminates and are a cause of concern for owners and bridge engineers. Diagonal cracking around the termination of a flexural bar increase the bond stresses in the developing bar. If the anchorage of a cutoff bar fails, the remaining reinforcing steel bars may not be adequate to carry the applied loads.

Current load ratings of these older bridges can exhibit controlling unsatisfactory bridge ratings due to flexural anchorage deficiencies along the girders. These deficiencies result from inadequate capacity compared to current design standards due to poorly detailed cutoffs in the original design. Some RCDG bridges have posted load limits due to the poorly detailed flexural anchorages. The ratings are significantly reduced when the influence of shear is considered. Strengthening methods are necessary because wholesale replacements of these bridges are not economically feasible.

Over the last ten years, Oregon State University has conducted a large number of experimental tests on full-scale vintage RCDG bridge girder details (Higgins, *et al*. 2004). These realistic girder specimens were constructed, instrumented, and tested to failure. The specimens were 26 ft (7.9 m) long inverted-T (IT) beams with a 14 in. by 42 in. (356 mm x 1069 mm) stem and a 36 in. by 6 in. (914 mm x 152 mm) integral deck. Both T and IT specimens were tested, focusing on the positive and negative moment regions, respectively. The design concrete strength, concrete mixture, and transverse steel used were representative of that used in the 1950's. Some of the specimens contained straight bar terminations crossing a preformed diagonal crack in the flexural tension region combined with shear. Instrumentation focused on stresses along the reinforcement surrounding the crack and along the development length of the cutoff bars. This past research has helped to quantify the behavior of poorly detailed flexural anchorages.

The present experimental research was conducted to develop methods to strengthen RCDGs with deficient flexural anchorages. An innovative strengthening technique was developed

using near-surface mounted (NSM) metallic alloys. Stainless steel and titanium were chosen as the two metallic alloys due to their environmental durability, ductility, high strength, and ability to fabricate mechanical anchorages at the ends of the bars. The NSM strengthening technique increased the baseline specimen capacity over 60 kips (267 kN) with failure loads over 420 kips (1868 kN) and demonstrated the ability to prevent flexural anchorage failures. Supplemental tests of hook ductility and bond beams were also conducted.

In addition to the full-scale IT specimens, a case study was conducted on an existing in-service bridge and the results contributed to the NSM technique being implemented to retrofit the bridge. The case study is described in Appendix F. The research and case study determined that stainless steel and titanium are viable material options for strengthening flexurally deficient RCDGs. Based on this research, bridge designers should be able to economically and effectively improve vintage RCDG bridge load ratings that are controlled by deficient flexural anchorages by deploying these retrofitting techniques. This NSM retrofitting technique could ultimately help to maintain and improve the operational safety and mobility of the transportation system.

## 2. BACKGROUND

Starting in the late 1940's, a large number of experimental test programs investigated the factors that affect bond stress for embedded reinforcing steel. While a limited number of tests were performed using larger bars, most were performed on small-scale beam and cylinder specimens and used smaller sizes of reinforcing bars. A deeper understanding of the behavior of bond stresses over the development length of reinforcement and around cracked locations can help characterize the capacity of cutoff reinforcing bars located in flexural tension regions in vintage RCDG bridges. This chapter 1) summarizes the anchorage concerns surrounding vintage RCDG bridges, 2) reviews past and current literature pertaining to anchorage and bond in both steel and NSM reinforcement, 3) reviews relevant changes in applicable design specifications, 4) summarizes the literature and specifications, and 5) describes the objectives that were incorporated into the research program.

### 2.1. Anchorage Concerns

Before the advent of standardized deformation patterns on reinforcing steel bars, several companies produced proprietary deformation patterns. Smooth bars and the variety of deformed bars were allowed to be used as reinforcement, which relied upon chemical adhesion and friction between the concrete and the bar. Due to the uncertain bond characteristics, designers were required to use hooks and bends to ensure bars were adequately anchored past calculated cutoff points. Flexural tension steel was commonly bent and transitioned into compression steel. Likewise, positive moment reinforcing could be brought up and used as negative moment reinforcing over immediate supports. Fully

anchoring the longitudinal bars provided a factor of safety when using a large number of different deformation patterns on the reinforcement.

In the 1950's, a standard deformation pattern (ASTM 305-47T) was developed that optimized the mechanical interlock between the concrete and reinforcing lugs. After this standardization, designers were permitted to terminate flexural steel where not required by calculation. Materials were comparatively expensive during this time, relative to labor. To minimize costs, reinforcing steel bars were cut off at the earliest possible location. It is now known that these straight-bar terminations in lieu of hooks or bends have left anchorage issues that can lead to pullout or splitting failures.

Anchorage is achieved through bond stresses between the reinforcing bar and the concrete. This transfer of stress produces composite action in the reinforced concrete member. Anchorage can be described as the length of the reinforcing bar required to achieve the full yield stress of the bar from the bond stresses at the concrete-bar interface. Bond stress is influenced by multiple factors including local cracking, concrete strength, bar size, concrete cover, and confinement from supports or transverse reinforcement. Design specifications from the 1950's were based on allowable bond stresses in the reinforcement rather than a required length to develop the full yield stress. Because of this, the actual embedded length of the reinforcing bars may not be sufficient to fully develop the bars. If a reinforcing bar is not adequately anchored, the bar can experience bond stresses that exceed the capacity and may slip through the concrete. Diagonal cracking near cutoff locations can also lead to higher reinforcing steel demands. When a reinforcing bar begins to slip, it can no longer sustain the

force, placing higher demands on the adjacent reinforcing bars. This may lead to failure of the girder if the adjacent reinforcing bars do not have enough reserve capacity.

More recent design specifications such as AASHTO-LFRD and ACI 318 require a minimum development length to ensure reinforcing bar anchorage. There are also regulations as to how and where a reinforcing bar can be terminated which prevent local stress concentrations and provide additional transverse reinforcing to prevent splitting. These specifications are used for new designs, but are also applied to evaluate existing bridges to establish the load ratings. Load rating engineers must check the anchorage of the tension reinforcement along the span, and the check is often found to be inadequate in vintage RCDG bridges with poorly detailed flexural anchorages.

## 2.2. Literature Review

A review of past and current literature was performed to identify the changes in understanding for bond and anchorage behavior of reinforcing steel as well as retrofitting techniques such as near-surface mounting (NSM) and the associated bond and performance characteristics.

### 2.2.1. Steel Reinforcement Anchorage and Bond

Mylrea (1948) conducted experimental tests on plain bars and deformed bars with varying deformation types. Testing compared the pullout resistance of embedded bars to the bond strength of bars in simple beams. Results from earlier work recognized that bond stress was not uniformly distributed over the length of the bar in both types of specimens. Additionally,

the bond resistance was less in beam specimens than in pullout specimens. Before cracking initiated, the bond is assumed perfect and the total stress in the steel directly varies with the moment. After slipping begins, the bond stress at any location was determined to increase with the respective movement of the bar, beginning rapidly, then slowing down as it reached the maximum bond stress, until it gradually dropped off as slipping continued. Cracking greatly modified the overall bond distribution. Mylrea presented an equation for the stress in the reinforcing at any given point as:

$$f_s = 4u\frac{l}{d} \qquad [2.1]$$

where $u$ is the average bond unit stress, $l$ is the embedment length, and $d$ is the diameter of the bar. From this, one can determine the tensile stress that is able to be developed is directly proportional to $l/d$. Based on this research, the conclusion was drawn that the average bond resistance on the deformed bars increased as slip progressed, until the concrete began to be crushed by the deformations, but that how far or how fast the rate will increase was chiefly dependent on the deformation pattern.

Further tests were performed by Clark (1949) on deformed bars' resistance to slip in concrete. Effects on slip resistance, also known as bond, were determined to better understand impacts of the bar size, deformation pattern, and concrete strength. Variations in the specimens included concrete strength, depth of concrete under the bar, bar size, and embedment length. Bar sizes included 1/2 in. (12.7 mm) round, 7/8 in. (22.2 mm) round, and 1-1/8 in. (28.6 mm) square bars. Bond strengths were higher in specimens with bars closer to the bottom. Clark recommended two revisions to ASTM A305-47T. One changed the maximum deformation spacing, while the other changed the minimum deformation height.

The comparison of beam and pullout tests showed that pullout tests can give reliable estimates of deformed bar bond efficiency. Average bond stresses for the 7/8 in. (22 mm) bars were in the 300-400 psi (2.07-2.76 MPa) range. Peak bond stresses measured at the failure crack location ranged from 700-900 psi (4.83-6.20 MPa).

A new technique of placing strain gages inside the reinforcing bar was used to determine bond stresses in beam and pullout specimens (Mains 1951). Based on ASTM A305-47T, bar comparisons were made using plain and deformed bars with both straight and hooked anchorages. Cracks in the beams were shown to have a large effect on the magnitude and distribution of the bond stresses due to increases in the bar forces. In the beam tests, local maximum bond stresses on deformed straight bars were measured at values up to 1800 psi (12.4 MPa) versus only 1200 psi (8.27 MPa) for plain straight bars. This effectively showed bond along a deformed bar was greater than along a plain bar. The contemporary building code procedures often under-predicted the local maximum bond stresses by a factor of 2 or more.

The effect of longer development lengths for #11 (M36) bars was investigated by Ferguson and Thompson (1962). Development lengths ranged from 24*d* to 48*d* that is from 33.8 in. to 67.5 in. (859 mm to 1715 mm). Bond strengths increased with greater cover. While stirrups did help to delay longitudinal splitting, they could not prevent it overall and did little to increase ultimate bond stress. Bond stresses calculated using ACI 318-63 were based on:

$$u = \frac{9.5\sqrt{f_c'}}{D} \qquad [2.2]$$

where $f_c'$ is the concrete strength and D is the bar diameter. The development lengths required by the code stresses were a few inches shorter than those required by the test results.

Lutz and Gergely (1967) discussed the three components of bond: chemical adhesion, friction, and the mechanical interaction between concrete and the reinforcing steel. The bond of deformed bars relies primarily on mechanical interlock between the aggregates and the reinforcing lugs. After chemical adhesion was lost, which initially prevented bar slip, the bar slipped through the concrete through wedging action or concrete crushing. Due to loss of contact between the cylindrical surface of the bar and the concrete, the bond close to a transverse crack was transferred exclusively by bearing on the ribs. As flexural cracking entirely changed the bond stress distribution in a beam, a corresponding large change in the shear stress occurred. Shear combined with diagonal tension cracking influenced the bond to the point that bond failure could result if shear failure occurred. Peak bond stresses were limited to 800 psi (5.52 MPa) based on ACI 318-63.

Based on test results, Orangun, *et al.* (1977) developed an empirical equation to calculate the development length for deformed bars. Using a substitution for the bar strength based on test results, the basic development length for Grade 60 (Grade 420) was determined as:

$$l_d = \frac{10,200 d_b}{\sqrt{f_c'}\left(1 + 2.5\frac{C}{d_b} + K_{tr}\right)\phi} \qquad [2.3]$$

where $d_b$ is the bar diameter, $f_c'$ is the concrete strength, $C$ is the concrete cover, $\phi$ is a capacity reduction factor to be used in lieu of increasing $f_s$, and $K_{tr}$ is defined as:

$$K_{tr} = \frac{A_{tr} f_{yt}}{600 s d_b} \leq 2.5 \qquad [2.4]$$

where $A_{tr}$ is the area of transverse steel, $f_{yt}$ is the transverse steel yield, and $s$ is the stirrup spacing. Modification factors were also provided to adjust the development length. Tests further supported that transverse steel improved the ductility of the anchorage.

Doerr (1978) investigated the bond stress-slip relationship in the cracked state using cylindrical test specimens. Tension testing was performed using #5 (M16) reinforcing bars embedded in 5.91 in. by 23.6 in. (150 mm by 600 mm) concrete cylinders constrained with lateral compressive forces. The lateral forces were varied from 0 to 2175 psi (0 to 15 MPa). The cylinders had a circumferential notch in the center to force crack formation to that location. Based on test results, Doerr concluded the bond stress, $\tau(x)$, along the length of the bar could be calculated as:

$$\tau(x) = -\frac{1}{u}\frac{dP(x)}{dx} \qquad [2.5]$$

where $u$ is the circumference of the reinforcing bar and $P(x)$ is the force at a point $x$ along the bar. He also attributed the large variation in bond stress results previously obtained due to the various dimensions of the test specimens used.

Losberg and Olson (1979) performed three kinds of bond tests on reinforcing bars to determine the best deformation shape to minimize splitting failures while maximizing bond. Variations in the bars included the diameter of the bar, height and inclination of the lug, and the distance between the lugs. Pullout tests were used to determine a uniform bond distribution using short anchorage lengths without splitting failures. Ring pullout tests were

performed to directly measure the splitting component of the bond forces. Beam end tests were conducted to mimic realistic splitting bond tests and produce simple splitting crack pattern failures. Lug spacing was shown to have little influence on the test while inclined lugs resulted in more splitting failures than transverse lugs. The amount of transverse reinforcement crossing the splitting surface had a large impact on the force developed in the reinforcing steel.

Bond stresses were investigated based on the relationship between anchorage and lap lengths as well as the effects of transverse steel on lap splices (Reynolds and Beeby 1982). Tests were conducted using approximately 8 x 4 x 48 in. (200 x 100 x 1220 mm) rectangular beam test specimens and inducing failures in the constant moment zone. They determined that there was no difference between the bond stresses in a single bar anchorage versus those that develop in a lap splice. Tensile forces in the concrete were found to be the same in both lap splices and single anchorages. The same ultimate bond stresses can be generated in a corner bar as can be in the center of the concrete section. Transverse steel was shown to have little effect in the constant moment region. When the lap splice was located in an area of high shear with diagonal cracking, the stirrups were highly stressed by the shear and the presence of the transverse steel lead to a large increase in the bond capacity.

Tests on beam-column connections were performed by Soroushian, *et* al. (1991) to investigate the confinement of the reinforcing bars and develop an empirical model to determine the local bond stress of deformed bars in concrete. Block specimens were constructed with a deformed #8 (M25) bar partially bonded along of its length. The test

program varied the spacing and quantity of the transverse reinforcement and the compressive strength of the concrete. Specimens with plain transverse reinforcement had brittle split cracking failures. Dissimilarly, specimens with more dense transverse reinforcement failed in pullout and were able to restrain the widening of the splitting cracks. The peak bond stress of the confined specimens was almost double that of the unconfined specimens. Much greater bond slip was also achieved in the confined specimens. Increasing the compressive strength of the concrete provided increasingly higher bond stress values. Empirical modeling determined the bond stress, $\tau_1$, in MPa, to be:

$$\tau_1 = \left(20 - \frac{d_b}{4}\right)\sqrt{\frac{f_c'}{30}} \qquad [2.6]$$

where $d_b$ is the bar diameter (mm) and $f_c'$ is the concrete strength (MPa). Using this equation, the typical specimen in their test program has a predicted bond stress of approximately 1.88 ksi (12.9 MPa).

Malvar (1992) recognized the variation in bond stresses from past research was largely due to the various sizes of the test specimens. Under transverse confinement, 12 specimens were tested to investigate the bond-slip characteristics. Single #6 (M19) bars were embedded in 3 in. by 4 in. (76.2 x 102 mm) cylinders and confined using a steel ring split into longitudinal strips. Two types of reinforcing steel were tested with varied lug angle and spacing. The confinement stresses were increased from 500 to 4500 psi (3.45 to 31.0 MPa). These respectively increased the bond stresses from 1650 to 2800 psi (11.4 to 19.3 MPa). From these tests, Mavar achieved consistent bond stress-slip relationships for short embedment lengths for various confining pressures independent of the configuration. During pre-

cracking the influence of confining stress was difficult to establish. In the post-cracking range, the confinement stress was influential to increasing the bond stress.

A new testing technique was developed by Abrishami and Mitchell (1996) to simulate a uniform bond stress distribution by using pullout and push-in tests on #8 and #11 ( M25 and M36) bars. The tests were able to generate a more accurate determination of the bond stress-slip response. Pullout tests resulted in brittle failures due to concrete shearing along the lugs and had a maximum average bond stress of 852 psi (5.87 MPa). Bond-splitting failures had a maximum average bond stress of 420 psi (2.90 MPa) and exhibited a more ductile response. Pullout and push-in tests that failed in splitting exhibited more uniform bond stresses along the reinforcement than standard pullout tests. Pullout specimens had a maximum to average bond stress of about 1.37 whereas the combination of pullout and push-in tests had a ratio of 1.10.

Testing 133 unconfined and 166 transverse confined splice and development length specimens, Darwin, *et al.* (1996) determined that ACI 318-95 typically overestimated splice and development lengths. Past use of $\sqrt{f_c'}$ did not accurately represent the effect of the concrete strength and bond strength over the full range of concrete strengths used at that time. Based on tests with concrete strengths ranging from 2,500 to 16,000 psi (17 to 110 MPa), the proposed design equation modifies the concrete strength term to provide a more accurate representation:

$$\frac{l_d}{d_b} = \frac{\frac{f_y}{\phi f_c'^{1/4}} - 2130\left(0.1\frac{c_M}{c_m} + 0.9\right)}{80.2\left(\frac{c + K_{tr}}{d_b}\right)} \quad [2.7]$$

where $f_y$ is the longitudinal steel yield stress (psi), $\phi$ is a strength reduction factor, $f_c'$ is the concrete strength (psi), $c_m$ and $c_M$ are the minimum and maximum values of the one half the bar clear spacing and side or bottom covers (in.), and $d_b$ is the bar diameter. The concrete cover term, $c$, is defined as:

$$c = \left(c_m + 0.5d_b\right)\left(0.1\frac{c_M}{c_m} + 0.9\right) \quad [2.8]$$

and the transverse reinforcement index, $K_{tr}$, is determined as:

$$K_{tr} = \frac{34.5 t_d A_{tr}}{sn} \quad [2.9]$$

where $t_d = 0.72d_b + 0.28$ and represents the effects of the bar size, $A_{tr}$ is the cross-sectional area of transverse reinforcement crossing the splitting plane ($in^2$), $s$ is the stirrup spacing, and $n$ is the number of bars crossing the splitting plane. This ratio of development length to bar size recognized that the relationship between bond force and development or splice length is linear but not directly proportional.

Six specimens measuring the effect of loss of bond for longitudinal reinforcement were tested by Jeppsson and Thelandersson (2003). Specimens had #5 (M16) longitudinal bars with 0.23 in. (6 mm) stirrups. The length without bond was varied through use of plastic tubes placed around the longitudinal bars, therefore leaving short bond lengths. A control specimen was used for comparison. Results from the experiment showed that decreasing the

bonded length led to an approximate 33% decrease in capacity, even when considering that close to 80% of the bond length was removed. This confirmed that short bond lengths can carry high bond stresses. Also, due to an increase of active stirrups compared to the control beam, the loss of bond did not lead to more brittle failures.

An analytical study was conducted by Harajli (2004) on small beams using normal and high strength concrete. Results showed that compared to correlation using normalizing $f_c'^{1/2}$, the average bond strength using $f_c'^{1/4}$ eliminated the difference between the bond strengths for the normal and high strength concretes within a practical range of development lengths. For shorter development lengths, $f_c'^{1/4}$ largely underestimated the effect of the concrete compressive strength on the bond stresses.

Previous work at Oregon State University by Goodall (2010) researched the influence of diagonal cracks on the flexural anchorage performance in negative moment regions of full-size reinforced concrete deck girder (RCDG) specimens at diagonal crack locations. Similar to previous specimens constructed by Higgins *et al.* (2004), the specimens were 26 ft (7.92 m) long with a 14 x 42 in. (356 x 1067 mm) web, and a 6 x 36 in. (152 x 914 mm) thick deck. Goodall designed, constructed, and tested to failure four RCDG IT-beam specimens containing diagonal cracks that interacted with the cutoffs of flexural steel reinforcing bars. Specimens were designed to replicate vintage RCDG members. To do this, concrete mixtures were used with target strengths of 3300 psi (22.8 MPa) and Grade 40 (Grade 280) stirrups were used. The specimens were constructed with a preformed diagonal crack at an angle of 45º or 60º to prevent aggregate interlock and had either five or six Grade 60 (Grade 420)

flexural reinforcing bars. The specimens were constructed with bars cutoff before they were fully developed. The cutoff bars extended approximately one-half of the minimum development length, determined by ACI 318-08, past where they intersected with the preformed crack. The tests had bond stresses in the developed bars that exceeded the amount predicted by current specifications, therefore a more accurate estimate of bond stress in necessary. Specimen behavior at failure was found to be independent of the initial diagonal preformed crack.

Triska (2010) also researched the flexural steel anchorage performance of full-size reinforced concrete deck girder (RCDG) specimens at diagonal crack locations at Oregon State University. Again, the specimens were 26 ft (7.92 m) long with a 14 x 42 in. (356 x 1067 mm) web, and a 6 x 36 in. (152 x 914 mm) thick deck. Triska tested four RCDG T-beam specimens containing diagonal cracks that interacted with the cutoffs of flexural steel reinforcing bars in positive moment regions. Three of the specimens were constructed with a preformed diagonal crack at an angle of 45º or 60º to prevent aggregate interlock. The forth specimen was used as a control because it did not have a preformed crack, though it did have similar reinforcing details. The specimens were constructed with bars cutoff before they were fully developed. The cutoff bars extended approximately one-third of the minimum development length, determined by ACI 318-08, past where they intersected with the preformed crack. The experiments found that presence of a preformed crack in the T-beam specimens did not ultimately control the failure mode of the specimens, nor did it necessarily weaken the beam structure. Instead, the location of the failure crack as well as the failure

mode were more dependent on other geometric properties such as the bar cutoff location, the number of flexural reinforcing bars, and the stirrup spacing.

### 2.2.2. Near-Surface Mounted Anchorage and Bond

De Lorenzis *et al.* (2000) summarized the state of knowledge of near-surface mounted (NSM) fiber reinforced polymer (FRP) strengthening studies and uses through 2000. The idea of NSM reinforcement using steel was developed in Europe in the late 1940's. NSM installation was a new technique growing in popularity over past external reinforcing techniques and especially useful in the negative moment regions of beams and slabs. Advantages of NSM strengthening over externally bonded reinforcement (EBR) included minimal installation time and resistance against environmental and mechanical damage. An investigation was performed to determine the effectiveness of NSM FRP rods as a strengthening system for reinforced concrete (RC) structures. Tensile and bond characterization of various FRP bar sizes and surface configurations, bonded lengths, and groove sizes was performed to study NSM bars. Good bond was essential to develop composite action as stress was transferred between the reinforced concrete to the NSM reinforcement. Full-size simply supported RC beams with NSM glass and carbon FRP (GFRP and CFRP, respectively) were tested to examine the structural performance of the system. Bonded lengths ranged from 6 to 24 in. (152 to 610 mm). Results showed that with longer bond lengths ultimate load increased while average bond stresses decreased. In specimens that failed by splitting of the epoxy cover, increasing the groove size resulted in respectively higher ultimate loads. Larger grooves had thicker epoxy cover distances which helped to resist splitting effects. The research showed that for #3 (M10) and #4 (M13) bars

the optimal groove sizes were 3/4 in. (19.1 mm) and 1 in. (25.4 mm), respectively. The full-scale NSM GFRP and CFRP retrofitted beams exhibited greatly increased stiffnesses and had up to 25% and 44% increases in capacity, respectively, over the control specimen. Failure in both retrofit types occurred due to debonding.

Rizkalla, *et al*. (2003) proposed design recommendations for FRP systems to strengthen concrete. FRP was a beneficial alternative to conventional steel because of its high strength, light weight, and resistance to corrosion. Factors that influenced the development length of the FRP included the size of the FRP, concrete strength, epoxy or other adhesive properties, internal steel reinforcement ratio and placement, specimen loading, and groove width. NSM FRP bars typically failed in two modes. Splitting of the epoxy cover occurred from high tensile stresses at the FRP-epoxy interface and could typically be mitigated by increasing the epoxy thickness. Concrete cracking around the epoxy occurred when stresses at the concrete-epoxy interface reached the concrete tensile strength. Widening the grooves helped to minimize these tensile stresses and increase the debonding loads. Due to observed cohesive shear failure in the concrete, a formula for the maximum critical shear stress, $\tau_{max}$, at the FRP cutoff point was proposed:

$$\tau_{\max} = \frac{f_c' f_{ct}}{f_c' + f_{ct}} \qquad [2.10]$$

where $f_c'$ is the concrete compressive strength and $f_{ct}$ is the tensile strength of the concrete. The most important general recommendation made was "strengthening limits for concrete members retrofitted with FRP should be specified, such that a loss of FRP reinforcement should leave the concrete member with sufficient capacity to resist at least unfactored dead

and live loads." Research was referred to showing 19% and 36% decreases in CFRP and GFRP strengthened beams, respectively, after exposure to wet-dry cycles. Freeze-thaw cycles were shown to have no detrimental effects on overall structural performance. Thermal exposures to specimens with temperatures ranging from 68 to 482 ˚F (20 to 250˚C) had a large detrimental effect on the bond of FRP reinforcement. The bond strength of the FRP reduced between 80 and 90% compared to only a 38% reduction in conventional steel reinforcement. The thermal results showed important implications for elements subjected to fire.

A similar study was performed by Hassan and Rizkalla (2003). Bond of NSM CRFP strips was investigated in full-scale beam specimens to show the feasibility of using CFRP strips to strengthen concrete structures. At the time, use of NSM FRP rods and strips was thought to prevent delamination type failures compared to conventional externally bonded reinforcement (EBR). Nine test specimens were constructed and tested using simple supports. The T-beam specimens had an 8.2 ft (2.5 m) span and were 11.8 in. (300 mm) deep. The bottom reinforcement consisted of two full length #3 (M10) bars and two discontinuous #5 (M16) bars. The NSM CFRP strips were applied on the bottom of the web as an external splice to the discontinuous internal flexural reinforcement. Shorter retrofit lengths led to debonding failures while longer lengths failed by rupturing the CFRP. The retrofitted stiffnesses were substantially increased and the load capacities were increased up to 53% over the baseline specimen. The development length of the NSM CFRP was determined to decrease with higher concrete compressive strengths or wider groove widths and increase when the internal steel reinforcing ratio increased.

To further investigate bond on NSM FRP, Hassan and Rizkalla (2004) present an analytical model of eight beam specimens similar to their first 2003 study. Based on their model they determined the minimum embedment length needed for the NSM FRP to prevent concrete splitting and epoxy splitting failures respectively as:

$$L_d = G_1 \frac{d}{4} \frac{f_{FRP}}{\mu f_{ct}} \text{ and } L_d = G_2 \text{ or } G_2' \frac{d}{4} \frac{f_{FRP}}{\mu f_a} \quad [2.11]$$

where $G_1$, $G_2$, and $G_2'$ are coefficients taken from a proposed design chart determined from finite element analysis and, $d$ is the bar diameter, $f_{FRP}$ is the allowed stress in the bar, $\mu$ is the coefficient of friction between the bar and the epoxy, and $f_{ct}$ and $f_a$ are the tensile strengths of the concrete and epoxy, respectively. This is compared to the development length given in ACI 440.1R-01:

$$L_d = 0.028 \frac{\pi d^2 f_u}{4\sqrt{f_c'}} \quad [2.12]$$

where $f_u$ is the tensile strength of the bar, and $f_c'$ is the concrete compressive strength. To develop 40% of the ultimate strength of the bars, the test results produced a measured development length of 31.5 in. (800 mm). Eqn. [2.11] provides a required 32.8 in. (834 mm) development length. The ACI 440 development length from Eqn. [2.12] required an 8.7 in. (221 mm) development length which is only 28% of the measured value from the test specimens. Reasons for this large discrepancy were attributed to differences in assumptions. The ACI equation was based on bonding FRP bars to concrete, versus to an epoxy adhesive, and assumes a coefficient of friction of 1.0 when it should be in the 0.3 to 0.6 range. The ACI expression is also based on RC structures with large covers and assumes full confinement of the FRP by other steel and therefore does not incorporate the higher bond

stresses that would result without confinement. The proposal is made to incorporate the cover to bar diameter ratio, *C/d*, and the groove width, *w*, into future design guidelines. Also, based on the experimental testing, the bond strength of NSM FRP bars, $\tau_{max}$, was further refined to:

$$\tau_{\max} = \frac{\mu f_{ct}}{G_1} \qquad [2.13]$$

A series of 45 modified eccentric pullout tests were performed to test the development capacity of steel and FRP NSM bars in grooves (Novidis and Pantazopoulou 2008). The influence of groove dimensions, embedment length, and surface pattern of the bars were studied. The NSM rods were 0.5 in. (12 mm) diameter and embedded from 3 to 10$d_b$. The CFRP bars were sandblasted and had lengthwise helical winding indentations and the steel had either standard deformations or were smooth bars. The typical failure mode was pullout at the epoxy-concrete interface. Increased bond lengths carried higher loads while producing lower average bond strengths. Failures at NSM-epoxy interface produced larger average bond strengths. The maximum average bond strength at the concrete-epoxy interface was from a smooth steel specimen and was measured at 1.02 ksi (7.01 MPa). At the epoxy-bar interface the maximum average bond stress was from a CFRP specimen and measured at 1.64 ksi (11.30 MPa). Test results were used to establish a limit-state bond-slip model for NSM bars for use in design.

Further testing on strengthening RC members with NSM CFRP rods by Al-Mahmoud, *et al*. (2009) looked at the global behavior of retrofitted beams subjected to flexure. Conventional and high strength concretes were used in combination with resin and mortar as the NSM

adhesives. Approximately 0.25 and 0.5 in. (6 and 12 mm) CFRP rods were used as the NSM material. The concrete strength changes did not have an effect on beam capacity when the beams failed due to the NSM system. Both resin and mortar were found to be effective adhesives, but the mortar did experience debonding from the grooves. At the ultimate loading, if the CRFP was longer than the cracked span length the RC beams failed due to pullout of the rods which induced splitting of the cracked concrete surrounding the groove almost simultaneously. But, if the cracking at ultimate extended past the ends of the CFRP rod, the beams failed by delamination of the concrete and retrofit.

Bournas and Triantafillou (2009) looked at flexural strengthening of columns under seismic loading using NSM CFRP, GFRP, or stainless steel. Equal tensile strengths were used for each of the NSM types resulting in an axial stiffness ratio of 1.0:0.7:4.9, respectively. Aside from varying the NSM, some samples had epoxy adhesives while others used a cement-based mortar. A confining jacket was also used on some specimens to protect the NSM reinforcement against premature failure from buckling or debonding. The majority of the strengthened specimens displayed a higher (up to almost 100%) flexural load capacity than the control column. While the epoxy resin was very effective, specimens that used mortar adhesive experienced gradual pullout of the bars during testing. Despite the equal axial strengths, the stainless steel specimens experienced a 64% increase in cyclic bending strength whereas the CRFP only had a 26% increase and the GFRP had a 22% increase. Looking at the deformation capacity, the stainless steel and GFRP bars outperformed the CFRP strips by about 25%. Using jackets to confine the columns resulted in substantial improvements to the responses of the specimens by increasing both the strength and

deformation capacities. Jacketing the CFRP specimens resulted in a strength increase of 36% versus only 4% without, while confining the stainless steel columns increased the strength gain from 64% to 90%.

A study was performed using four composite-based strengthening systems to provide equivalent flexural performance (Rasheed, *et al.* 2010). The four systems were externally bonded CFRP sheets, NSM CFRP strips, externally bonded steel reinforced polymers (SRP), and NSM stainless steel bars. The test program was designed to fully utilize the high strengths of the component systems by effectively using external transverse reinforcement to control premature debonding and delamination failures. Due to the transverse strengthening and confining, more ductile behaviors were observed in the test specimens. Similar ductility levels were observed in both the controls and the retrofitted beams due to the extra transverse anchorage. The two control beams failed at loads close to 50 kips (224 kN) while the four retrofitted beams all failed at similar loads with an average capacity of 75 kips (334 kN). The strengthened beams exhibited much higher ultimate load capacities and failed by rupture or partial delamination of the external reinforcement or confined crushing in the core of the NSM reinforced specimens.

An experiment using pullout test specimens was performed to investigate the NSM-adhesive and adhesive-concrete interfaces (Al-Mahmoud, *et al.* 2011). Sand-coated CFRP rods with 0.5 in. (12 mm) diameters were used as the NSM strengthening material. Conventional and high strength concretes were used with both ready-mixed mortar and epoxy resin adhesives. The grooves widths and depths were varied from 0.8 x 0.8 in. (20 x 20 mm) to 1.2 x 1.2 in.

(30 x 30 mm) and 0.8 x 2.0 in. (20 x 50 mm). Some of the mortar specimens were sandblasted to roughen the surface at the saw-cut groove. Lower ultimate loads were observed for all of the 0.8 x 2.0 in. (20 x 50 mm) groove specimens. The other two groove sizes provided ultimate loads similar to one another. Neglecting the lower values from the large grooves, the epoxy resin produced the highest loads around 7.6 kips (34 kN). As expected, the sandblasted specimens with mortar provided higher loads than the smooth specimens at approximately 4.8 kips (21 kN) and 4.3 (19 kN), respectively. Previous work by the authors placed the CFRP rods directly into the concrete. Independent of the concrete strength and the groove width, the ultimate loads from all of the epoxy specimens were higher than when the CFRP was cast directly in the concrete. The ultimate loads for the mortar were always about half of that for the epoxy resin due to debonding failures at the mortar-concrete interface. Sandblasting the grooves only increased the ultimate strength of the mortar specimens by about 15%. From testing, a groove width to nominal rod diameter ratio between 1.7 and 2.5 was the most optimal for 0.5 in (12 mm) diameter rods.

### 2.2.3. Stainless Steel Investigation

A study was performed by Castro, *et al*. (2003) on the mechanical properties and corrosion behavior of stainless steel bars. Compared to carbon steel, stainless steel had a much greater initial expense. The initial expense was offset by long-term cost savings due to high strengths and corrosion resistance. Hot-rolled and cold-rolled stainless steels were compared. Cold-rolled rib shaping maintained high toughness levels while allowing large increases in the strength properties through strain hardening of the bars. Hot rolled bars showed greater

overall toughness. One cold rolled bar type was much more prone to pitting while the other type maintained exceptional corrosion resistance and had good mechanical properties.

### 2.2.4. Bond Stress Summary

Bond stresses reported in the literature are summarized in Table 1. The literature covers bond stresses in plain and deformed reinforcing steel and CFRP bars.

Table 1 – Reported bond stresses in reinforcement from literature

| Author | Bar Type | Bar Diameter in. (mm) | $\mu_{avg}$ psi (MPa) | $\overline{\mu}_{max}$ psi (MPa) |
|---|---|---|---|---|
| Mylrea | Plain Bar | 1.0 (25.4) | 400 | - |
| Clark | Deformed Rebar | 0.875 (22.2) | 350 (2.41) | 800 (5.52) |
| Mains | Deformed Rebar | 0.875 (22.2) | 460 (3.17) | 900 (6.20) |
| Ferguson | Deformed Rebar | 1.41 (35.8) | - | 560 (3.86) |
| De Lorenzis | CFRP bar | 0.5 (12.7) | - | 620 (4.27) |
| Novidis | CFRP bar | 0.5 (12.7) | - | 1650 (11.4) |
| Goodall | Deformed Rebar | 1.41 (35.8) | 430 (2.96) | 1570 (10.8) |
| Triska | Deformed Rebar | 1.41 (35.8) | 930 (6.41) | 1570 (10.8) |

## 2.3. Design Specification Review

An investigation of historical and current design specifications for determining bond strength was done to compare methods used for vintage RCDG bridge design to current methods. Examined documents include the Standard Specifications for Highway Bridges issued by the American Association of State Highway Officials (AASHO 1953, AASHO 1973), the 2012 AASHTO-LRFD Bridge Design Specifications published by the American Association

of State Highway and Transportation Officials (AASHTO-LRFD), and the 2011 ACI 318 Building Code Requirements for Structural Concrete published by the American Concrete Institute (ACI 318-11). Because NSM strengthening is a relatively new area of research, no specifications exist for design. Recommendations for NSM design are provided by the American Concrete Institute in the Guide for Design and Construction of Externally Bonded FRP Systems for Strengthening Concrete Structures (ACI 440.2R-08).

### 2.3.1. AASHO Working Stress Design

During the 1950's when many RCDG bridges were designed, the Standard Specifications for reinforced concrete were based on working stress design (WSD) which is also known as allowable stress design. The allowable bond stress, $u$, between the concrete and flexural reinforcing bars was computed as:

$$u = \frac{V}{jdZ_o} \qquad \text{AASHO-53 Sec. 3.7.3.(c)} \quad [2.14]$$

where $V$ is the total shear, $jd$ is the moment arm of the resisting couple, and $Z_o$ is the sum of the perimeters of bars in one set. The allowable bond stress of deformed flexural bars was limited to:

$$u = 0.10 f_c^{'} \le 350\, psi \qquad \text{AASHO-53 Sec. 3.4.12.(1)} \quad [2.15]$$

where $f_c$' was the compressive strength of the concrete (psi).

From its beginning until the 1970's, WSD was the sole design philosophy used in the Standard Specifications. Starting in the 1970's, load factor design (LFD) began to take form and become incorporated into the specifications. In AASHO (1973), the transition was made

from simply limiting bond stress to also incorporating a basic development length equation based solely on material properties. For bars other than top bars, the allowable bond stress was determined as:

$$u = \frac{4.8\sqrt{f_c'}}{D} \leq 500\,psi \qquad \text{AASHO-73 Sec. 1.5.1.(D-1)} \qquad [2.16]$$

where $f_c'$ is the concrete compressive strength (psi), and $D$ is the bar diameter (in.).

For #11 (M36) or smaller bars, the basic development length, $L_d$, for bars in tension was defined as:

$$L_d = 0.04\frac{a_s f_y}{\sqrt{f_c'}} \qquad \text{AASHO-73 Sec. 1.5.29.(E-1)} \qquad [2.17]$$

but not less than $0.0004 D f_y$. Where $a_s$ is the area of the steel ($in^2$) and $f_y$ is the yield strength of the reinforcement (psi). Modification factors that may increase or decrease the development length were also listed.

### 2.3.2. AASHTO-LRFD Bridge Design Specifications

After the introduction of LFD, load and resistance factor design (LRFD) was developed. This conceptual change in the design philosophy is expressed in the current design provisions. LRFD requires a minimum development length which replaced the WSD and LFD practices of limiting bond stress. The minimum development length calculation provides the embedded length required to achieve yield in the reinforcing bar.

For straight #11 (M36) and smaller bars, the minimum required development length is:

$$l_d = \frac{1.25 A_b f_y}{\sqrt{f_c'}} \qquad \text{AASHTO-LRFD Sec. 5.11.2.1.1} \qquad [2.18]$$

but not less than $0.4 d_b f_y$ or 12.0 inches (305 mm). $A_b$ is the area of the bar (in$^2$), $f_y$ is the yield strength of the reinforcing bars (ksi), $f_c'$ is the concrete compressive strength in (ksi), and $d_b$ is the bar diameter (in.). Modification factors listed in Sections 5.11.2.1.2 and 5.11.2.1.3 may respectively increase or decrease the development length. Including the decreasing factors is optional and ignoring them produces the most conservative development length.

For hooked reinforcing bars, the development length can be calculated as:

$$l_{hb} = \frac{38.0 d_b}{\sqrt{f_c'}} \qquad \text{AASHTO-LRFD (5.11.2.4.1-1)} \qquad [2.19]$$

but not less than $8.0 d_b$ or 6.0 inches (152 mm). Modification factors for hook development lengths are specified in Section 5.11.2.2.2.

The minimum development length can be related to average bond stress referred to in prior specifications. Using the development length, a comparable average bond stress, $\mu_{avg}$, over an incremental segment of reinforcement can be calculated as:

$$\mu_{avg} = \frac{\Delta f_s d_b}{4 l_d} \qquad [2.20]$$

where $\Delta f_s$ is the change in stress over the length of the reinforcement segment not to exceed the steel yield stress $f_y$, $d_b$ is the diameter of the bar, and $l_d$ is the segment length.

2.3.3. ACI 318 Building Code Requirements for Structural Concrete

ACI design of vintage structures from the 1950's also required the use of allowable stress design (ASD). ACI 318-56 defined the bond stress between the concrete and reinforcement per unit of surface area of bar, *u*, as:

$$u = \frac{V}{\Sigma ojd} \qquad \text{ACI 318-56 Sec. 901 (6)} \qquad [2.21]$$

not to be taken greater than $0.10\sqrt{f_c'}$ or 350 psi. Where *V* is the total shear, *Σo* is the sum of the perimeters of bars in one set, *j* is the ratio of distance between centroid of compression and centroid of tension, and *d* is the depth from the compression face of the beam to the centroid of the longitudinal tensile reinforcement.

Over time, ACI transitioned from ASD to strength design. ACI strength design, like AASHTO-LRFD, requires a minimum bar development length calculation in place of allowable bond stress. The 1971 ACI Code first introduced the development length concept for anchorage of reinforcement to replace the bond requirements from earlier editions. The concept of development length is based on the achievable average bond stress over the embedded length of reinforcement.

Section 12.2 of ACI 318-11 details two methods for calculating straight bar development length. Both methods limit the minimum development length to 12 in. (305 mm) with the maximum allowed $\sqrt{f_c'}$ equal to 100 psi. The simplified method dictates that for #7 (M22) and larger bars, the development length shall be calculated as:

$$l_d = \left( \frac{f_y \, \psi_t \, \psi_e}{20\lambda\sqrt{f_c'}} \right) d_b \qquad \text{ACI 318-11 Sec. 12.2.2} \qquad [2.22]$$

where $f_y$ is the yield strength of the reinforcement, $\psi_t$, $\psi_e$, and $\lambda$ are modification factors based on the reinforcement location, reinforcement coating, and concrete weight, respectively, $f_c'$ is the concrete strength (psi), and $d_b$ is the bar diameter (in.). $\psi_t \psi_e$ may not be taken greater than 1.7.

The complex method includes the effects of concrete cover and stirrup confinement. The complex development length calculation is:

$$l_d = \left( \frac{3}{40} \frac{f_y}{\lambda\sqrt{f_c'}} \frac{\psi_t \, \psi_e \, \psi_s}{\left( \frac{c_b + K_{tr}}{d_b} \right)} \right) d_b \qquad \text{ACI 318-11 (12-1)} \qquad [2.23]$$

where $\psi_s$ is a modification factor based on the reinforcement size and $(c_b + K_{tr}) / d_b$ is the confinement term not to be taken greater than 2.5. Splitting failures are likely to occur when the confinement term is less than 2.5, conversely when the term is above 2.5 a pullout failure is expected and increasing the amount of cover or stirrups will not likely increase the capacity of the anchorage. $c_b$ is taken as the lesser of: half the center to center spacing of the bars and distance from center of the bar to the nearest concrete face on either (in.). Again, $\psi_t \psi_e$ may not be taken greater than 1.7. The transverse reinforcement index, $K_{tr}$, is calculated by:

$$K_{tr} = \frac{40 A_{tr}}{sn} \qquad \text{ACI 318-11 (12-2)} \qquad [2.24]$$

where $A_{tr}$ is area of the transverse steel (in$^2$), $s$ is the stirrup spacing (in.), and $n$ is the number of bars being developed along the splitting plane. $K_{tr}$ taken equal to zero will always provide a conservative design.

For reinforcing bars with 90 degree hooks, Section 12.5 calculates the hooked development length, $l_{dh}$, as:

$$l_{dh} = \left( \frac{0.02\psi_e f_y}{\lambda\sqrt{f_c'}} \right) d_b \qquad \text{ACI 318-11 (12-2)} \quad [2.25]$$

but shall not be taken less than the larger of $8d_b$ and 6 in. (152 mm). Hook reduction factors are described in Section 12.5.3 but should conservatively be ignored.

### 2.3.4. ACI 440 Design Guide for Strengthening Concrete Structures

Recommendations for FRP design in ACI are based on strains in the FRP reinforcement. At the ultimate limit state, the effective strain level, $\varepsilon_{fe}$, can be found using:

$$\varepsilon_{fe} = \varepsilon_{cu}\left( \frac{d_f - c}{c} \right) - \varepsilon_{bi} \le \varepsilon_{fd} \qquad \text{ACI 440-08 (10-3)} \quad [2.26]$$

where $\varepsilon_{cu}$ is the ultimate strain of the of the unconfined concrete, $d_f$ is the effective depth of the flexural FRP reinforcement, $c$ is the distance to the neutral axis from the extreme compression fiber, $\varepsilon_{bi}$ is the initial strain in the substrate, and $\varepsilon_{fd}$ is the effective strain level at which debonding may occur. If the left term of this equation controls, flexural failure will occur by concrete crushing, but if the right term controls, rupture or debonding will control the flexural failure.

The effective strain level should be limited to the strain level at which debonding may occur, $\varepsilon_{fd}$, which can be calculated as:

$$\varepsilon_{fd} = 0.083\sqrt{\frac{f_c'}{nE_f t_f}} \qquad \text{ACI 440-08 (10-2)} \quad [2.27]$$

where $f_c'$ is the specified compression strength of the concrete, $n$ is the number of FRP reinforcing pieces, $E_f$ is the tensile modulus of elasticity of the FRP, and $t_f$ is the nominal thickness of the FRP strip or bar. Assuming perfectly elastic behavior, the stress in the FRP, $f_{fe}$, can be calculated as:

$$f_{fe} = E_f \varepsilon_{fe} \qquad \text{ACI 440-08 (10-4)} \quad [2.28]$$

In NSM systems, the development length, $l_{db}$, for FRP bars can be determined using:

$$l_{db} = \frac{d_b}{4(\tau_b)} f_{fd} \qquad \text{ACI 440-08 (13-3)} \quad [2.29]$$

where $d_b$ is the FRP diameter (in.), $\tau_b$ is the average bond strength for the FRP bars (psi), and $f_{fd}$ is the FRP design stress (psi).

## 2.4. Summary

The majority of the literature for reinforcing steel bond stress and anchorage focused on small-scale concrete specimens using smaller flexural reinforcing bars than those used in bridges. The effects of bond stress on large reinforcing bars in full-scale specimens have not been thoroughly researched. At failure loads, sufficient concrete cover and transverse reinforcement were found to greatly increase attainable bond stresses.

The research covering NSM anchorage and bond concentrated primarily on FRP bars and their ability to add flexural reinforcing capacity to a specimen. While ductility helps give warning before ultimate failure, FRP was shown to have primarily non-ductile failures. Groove dimensions and spacing influenced ultimate failure loads. Limited research on stainless steel has shown it has good potential as a NSM strengthening material, but more extensive testing is needed. Overall, little research has been performed using strengthening materials other than FRP. Other high strength and environmentally insensitive materials that have the ability to be mechanically anchored have not been investigated.

The code specifications illustrated the shift from designing using an allowable bond stress to prescribing anchorage lengths on the development lengths of the reinforcing bars. The allowable bond stresses are based research using smaller reinforcing sizes. Determining the effects of bond stress in larger bars will help to define the accuracy of current specifications. The guidelines for FRP strengthening detailed allowable strains and basic FRP development length. Guidelines need to be developed to incorporate strengthening materials other than FRPs.

### 2.5. Research Objectives

Current load ratings for RCDG bridges from the 1950's are resulting in unsatisfactory bridge ratings due to flexural anchorage deficiencies in the girders. In order to mitigate posting or replacement of these RCDG bridges, a method of externally strengthening the existing girders is necessary. A retrofitting technique using near-surface mounted (NSM) bars has been shown to increase the strength of deficient RC specimens. Past NSM research has

focused on carbon fiber reinforced polymers (CFRP). The CFRP materials show no ductility, rarely achieve their full material strength due to issues in bond and anchorage, and while specimens with NSM-CFRP exhibit higher strength, they have reduced deformations at failure. At the same time, there is limited prior research on metallics in NSM applications. On the basis of these two ideas, environmentally insensitive metallics with high strength, ductility, and the ability to fabricate mechanical anchorages were studied in the present work. A stainless steel and a titanium alloy were selected for the research program.

The objectives of this research were to:

- Develop NSM methods using metallic bars to strengthen poorly detailed flexural anchorages in existing reinforced concrete deck girders in negative moment regions.
- Use experimental findings to develop design guidance for metallic NSM bars.

Proven strengthening methods are necessary because flexural steel anchorages in cracked RCDG bridges have limited reserve capacity. The NSM technique is used to strengthen RC girders by cutting a groove in the concrete surface and installing a strengthening material, typically carbon fiber reinforced polymer (CFRP), into the groove using an epoxy adhesive to bond the strengthening material to the concrete. For this research, metallic alloys were investigated to allow the NSM material to have a hooked anchorage at the end of the NSM bar. The mechanical deformation patterns on metallic alloys may also allow higher bond strength at the epoxy interface than that of CRFP. Application of these methods may allow

locally deficient, yet otherwise serviceable bridges to be efficiently rehabilitated instead of being replaced or posted with lower load limits.

# 3. EXPERIMENTAL PROGRAM

An experimental program was developed to provide data on strength and behavior of full-size RCGD specimens in negative moment regions strengthened with NSM titanium or stainless steel bars. The research program consisted of specimen design and construction, application of the near-surface mounted (NSM) strengthening materials, and loading of specimens to failure. Specimens were designed to characterize the local behaviors and overall structural performance.

## 3.1. Specimen Design

The research focused on the negative moment region of existing RCDGs with poorly detailed flexural reinforcing steel that is cutoff in the flexural tension region. The specimens were specifically designed to have poorly detailed flexural steel and then retrofitted with NSM bars. The specimens used in the test program are based on previous research on full-size girders conducted over a 10 year period. In particular, Goodall (2010) conducted a number of experiments with IT girders having poor flexural anchorages. Goodall's specimen size and proportioning were based on a database of RCDG bridges constructed in the 1950's (Higgins *et al*. 2004). All of the beam specimens were 26 ft (7.92 m) long with 14 x 42 in. (356 x 1067 mm) stems and a 36 x 6 in. (914 x 152 mm) deck. All of the specimens contained three hooked #11 (M36) bars for compression steel, located in the top of the web. Deck steel was provided by #4 (M13) bars placed in two layers at 12 in. (305 mm) on center.

Three of Goodall's specimens were used as baseline comparison specimens in the present work. These specimen designations used by Goodall were renamed as seen in Table 2 to be

consistent with the naming convention in this thesis. The number in the final parentheses i.e. (5) represents the number of flexural bars in the flange of the beam. Specimens SPR IT.45.Ld2(10).(5) and SPR IT.45.Ld2(10).(6) had a 10 in. (254 mm) stirrup spacing on the critical side of the beam (cutoff bar and preformed crack) and were both over-reinforced using 6 in. (152 mm) stirrup spacing on the non-critical side of the beam. The last specimen, SPR IT.0.0(10).(5) was fully reinforced (no cutoff bars) and had symmetrical 10 in. (254 mm) stirrup spacing on both sides of the beam.

Table 2 – SPR naming convention

| **Initial** | **New** |
|---|---|
| IT.45.Ld2(5) | SPR IT.45.Ld2(10).(5) |
| IT.45.Ld2 | SPR IT.45.Ld2(10).(6) |
| 2IT10 | SPR IT.0.0(10).(5) |

Four inverted-T (IT) specimens were designed and used in the present test program. Three of the specimens had similar geometries with variations in the transverse steel spacing and the type of NSM material. These three specimens contained preformed diagonal cracks intersecting the flexural reinforcing steel near the cutoff location, similar to the method used by Goodall. The fourth specimen did not contain a preformed diagonal crack, used less flexural reinforcement, and the cutoff location was located at midspan. Figure 3.1 illustrates the naming convention used for the specimens in the test program.

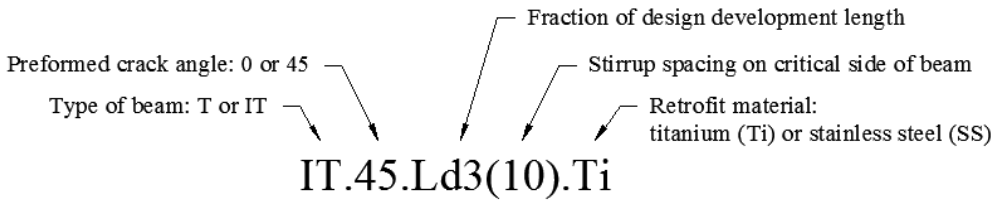


Figure 3.1 – Specimen naming convention

To create an anchorage deficiency in the specimens, some of the flexural tension bars were cutoff before they were fully developed within the flexural-tension region. The cutoff bars extended only a fraction of their development length past where they intersected a preformed diagonal crack. To locate the critical location for the diagonal crack and to proportion the reinforcing steel bars, the development lengths were calculated using both AASHTO-LRFD and ACI 318-11. The minimum development length was determined and used for the specimen design because it provided the least conservative anchorage length. To reflect representative material properties that would likely be used in the specimens (actual properties statistically likely to be higher than nominal), calculations were performed using a flexural yield stress of 68,500 psi (472 MPa) and concrete compressive strength of 3,500 psi (24.1 MPa).

The AASHTO and ACI procedures to calculate development length were described previously. The detailed ACI method (Eqn. 2.22) provided the shortest theoretical development length as seen in Table 3.

Table 3 – Development length summary

| Method | AASHTO in. (mm) | ACI in. (mm) |
|---|---|---|
| Straight Bar Simplified | - | 81.6 (2073) |
| Straight Bar | 71.4 (1814) | 61.2 (1554) |
| Hooked Bar | 28.6 (726) | 37.2 (945) |

Goodall tested IT-beam specimens with a development length closer to one-half that recommended by ACI or 30 in. (76.2 mm) past a preformed diagonal crack. To ensure anchorage failure occurred for the present specimens and to place additional demands into the NSM bars, the embedment length of the cutoff bars past the preformed diagonal crack was decreased to one-third of the theoretical minimum development length. The extension of the cutoff reinforcing bars past the preformed crack was 20.4 in. (518 mm).

## 3.2. Specimen Details

### 3.2.1. Internal Reinforcing Steel Details

Three of the specimens (IT.45.Ld3(10).Ti, IT.45.Ld3(6).Ti, and IT.45.Ld3(6).SS) had one layer consisting of five straight #11 (M36) flexural steel bars located in the flange. These specimens also contained a 1/16 in. (1.6 mm) polycarbonate preformed diagonal crack oriented at a 45° angle. The three interior flexural bars were continuous throughout the entire length of the specimen and hooked at the ends. The two exterior flexural bars were fully anchored on one end and cutoff past the preformed crack at 1/3 of their theoretical development length. In order to ensure failure on the half of the specimen where the cutoff bar, retrofit, and instrumentation were located, the opposite half of the beam was over-

reinforced with #4 (M13) stirrups spaced at 6 in. (152 mm). Beginning at the closest load point, the under-reinforced half of this specimen contained 10 in. (245 mm) stirrup spacing. The other two specimens contained 6 in. (152 mm) stirrup spacing throughout the entire length of the beams. Two of these specimens were retrofitted with NSM-titanium and the third with NSM-stainless steel. Four titanium and eight stainless steel 5/8 in. (16 mm) round bars were used as NSM reinforcement for their respective specimens. The NSM materials had a 12.5 ft (3.81 m) out-to-out length.

The fourth specimen consisted of three hooked #11 (M36) flexural bars located in the flange. These bars were cut, leaving a 2 in. (51 mm) gap in the center of the beam. This specimen did not contain a preformed crack. Stirrups were spaced at 6 in. (152 mm) throughout the length of the beam. Four titanium 5/8 in. (16 mm) round bars were used as the NSM retrofit material. The two interior NSM bars had a 12.5 ft (3.81 m) out to out length. The exterior two titanium bars were 11.5 ft (3.51 m) out-to-out.

The baseline specimens were used for comparison. Specimen SPR IT.45.Ld2(10).(5) was identical to IT.45.Ld3(10).Ti except the two cutoff bars extended 1/2 of their theoretical development length past the preformed crack. Specimen SPR IT.45.Ld2(10).(6) was similar, but had four fully anchored flexural bars and two cutoff bars for a total of six #11 (M36) flexural reinforcing bars. Lastly, specimen SPR IT.0.0(10).(5) had five fully anchored #11 (M36) flexural reinforcing bars. This specimen did not contain a preformed crack or any cutoff bars. Elevations and cross-sections for each of the retrofitted and baseline specimens are shown in Figure 3.2 to Figure 3.12.

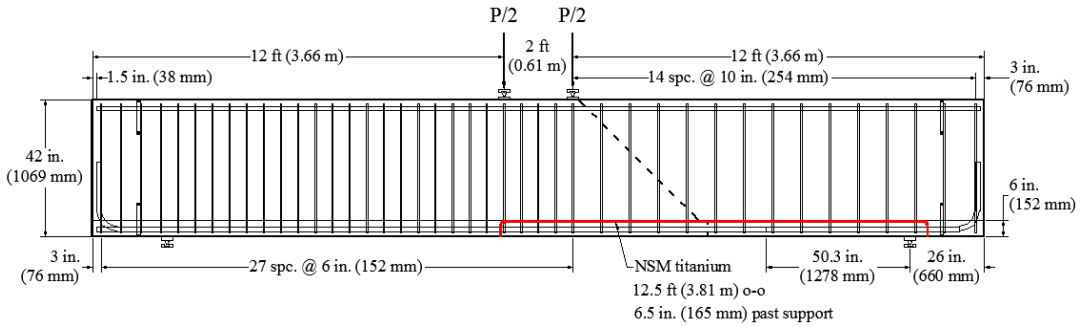


Figure 3.2 – Elevation of specimen IT.45.Ld3(10).Ti

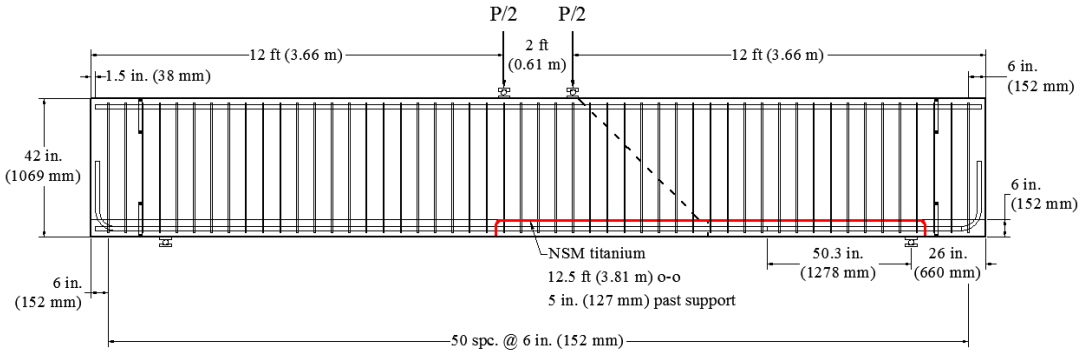


Figure 3.3 – Elevation of specimen IT.45.Ld3(6).Ti

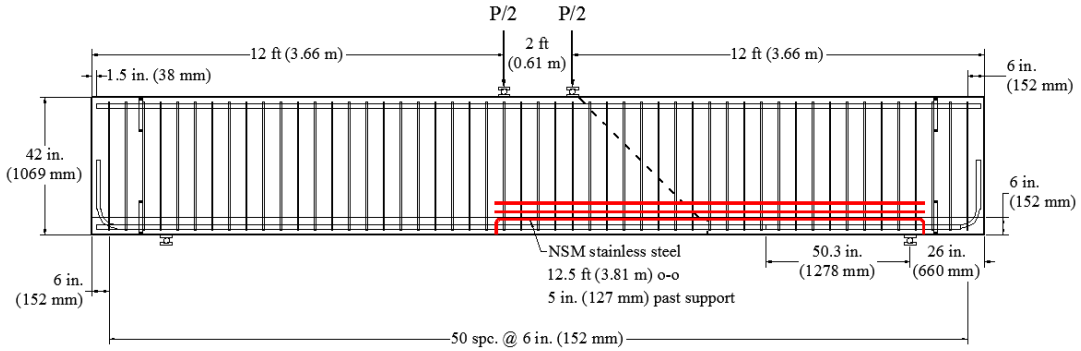


Figure 3.4 – Elevation of specimen IT.45.Ld3(6).SS

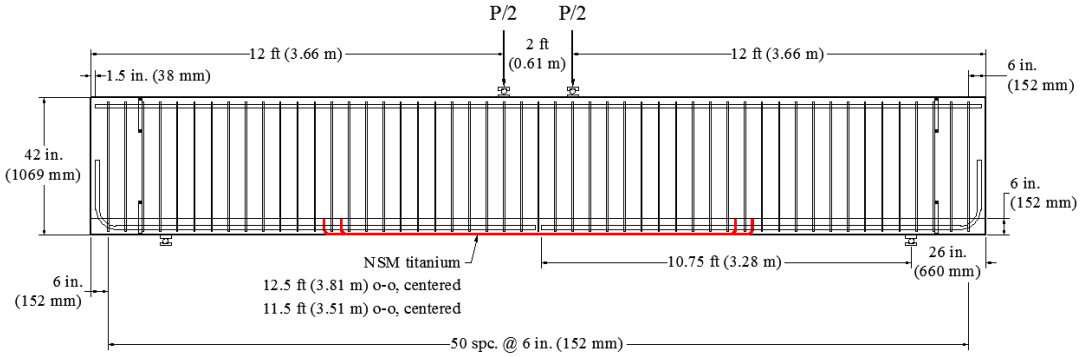


Figure 3.5 – Elevation of specimen IT.0.0(6).Ti

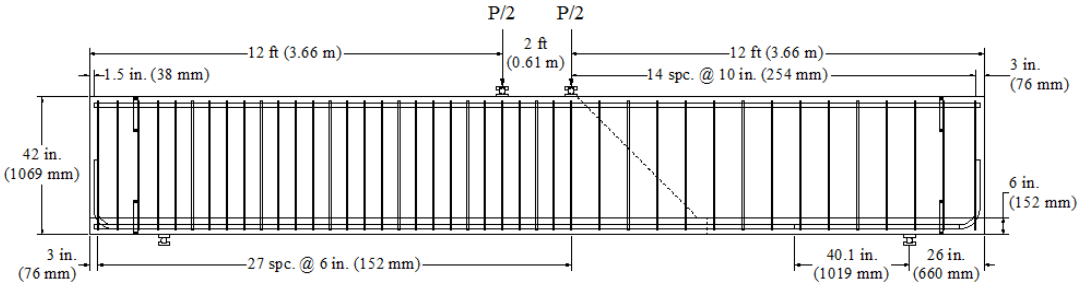


Figure 3.6 – Elevation of specimens SPR IT.45.Ld2(10).(5) and SPR IT.45.Ld2(10).(6)

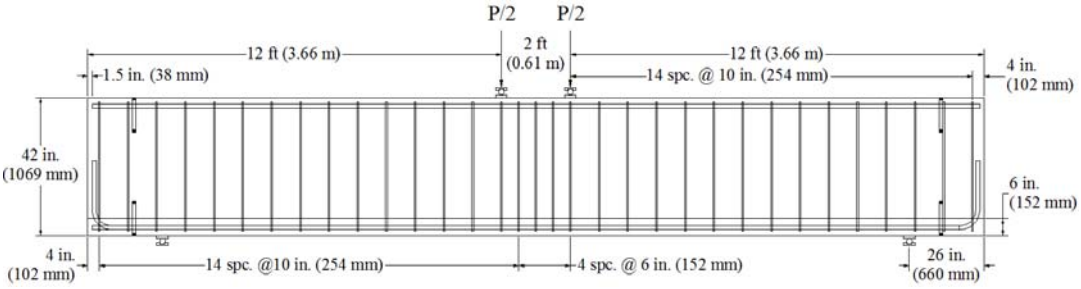


Figure 3.7 – Elevation of specimen SPR IT.0.0(10).(5)

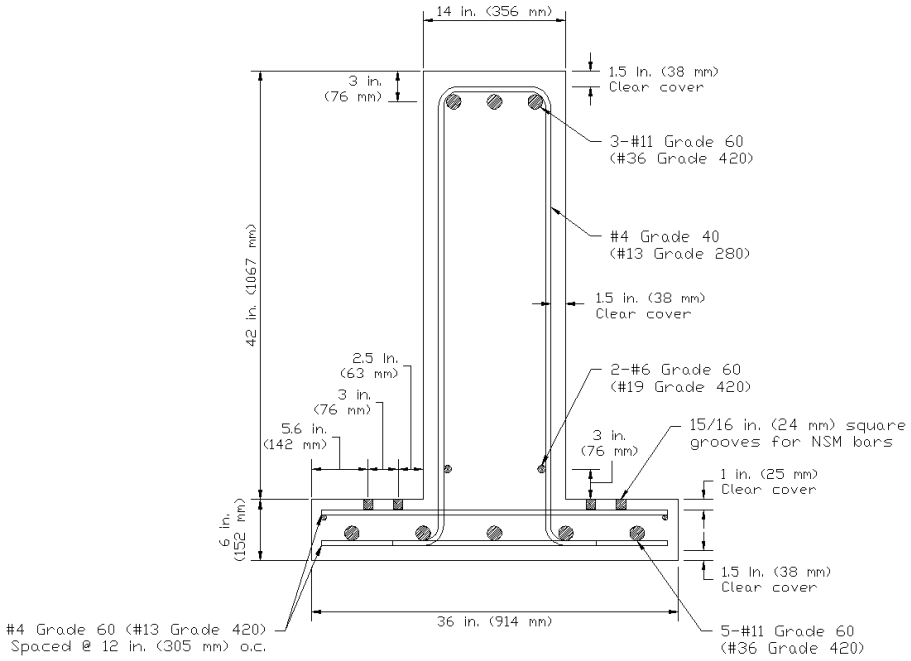


Figure 3.8 – Specimens IT.45.Ld3(10).Ti and IT.45.Ld3(6).Ti cross-sections

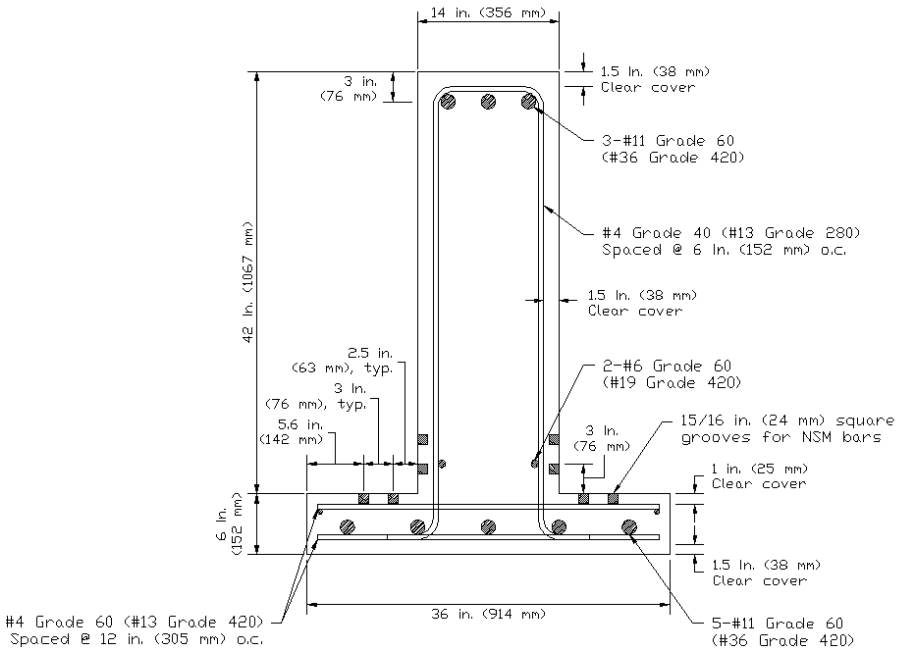


Figure 3.9 – Specimen IT.45.Ld3(6).SS cross-section

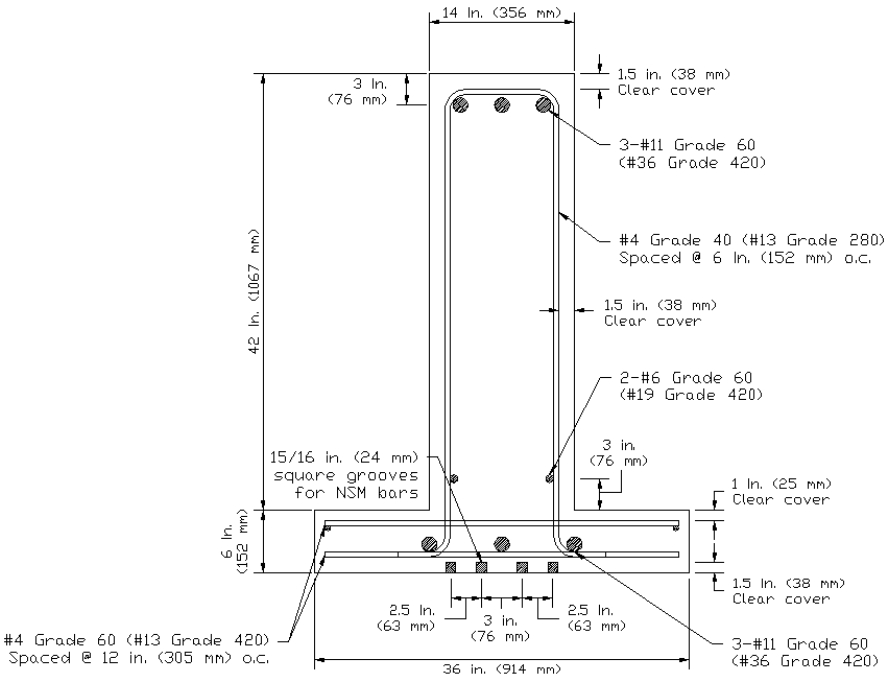


Figure 3.10 – Specimen IT.0.0(6).Ti cross-section

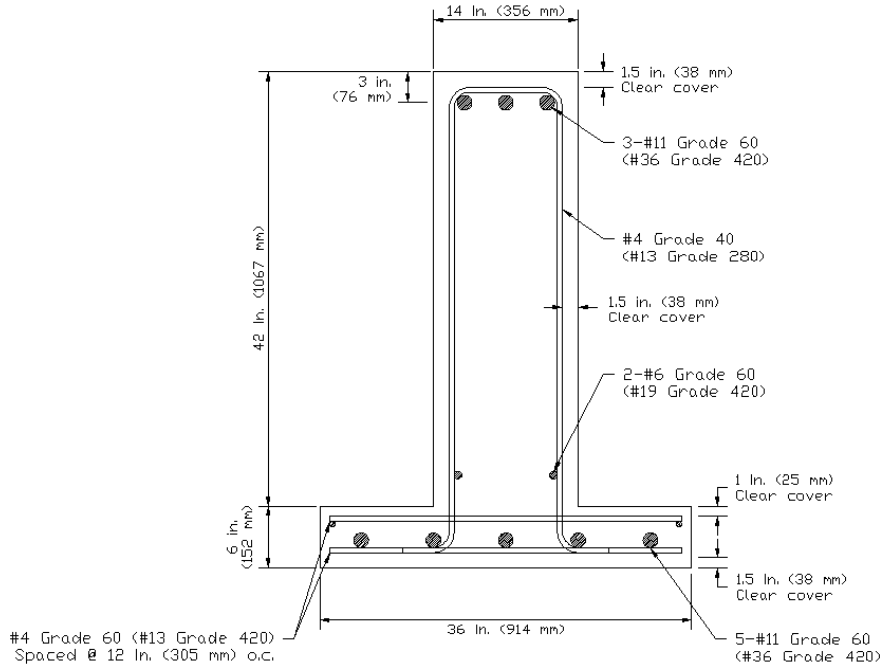


Figure 3.11 – Specimens SPR IT.45.Ld2(10).(5) and SPR IT.0.0(10).(5) cross-sections

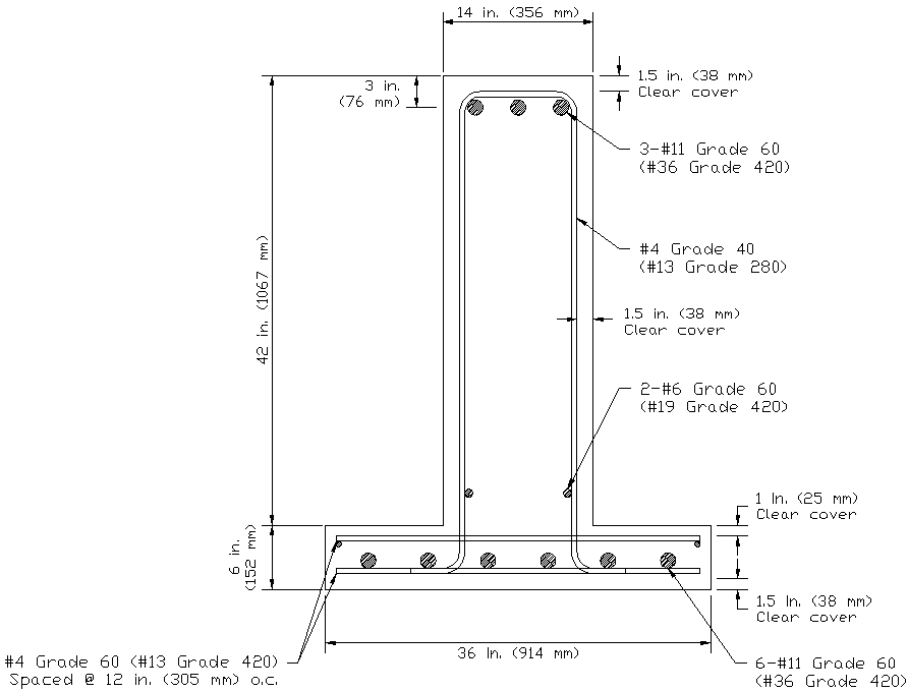


Figure 3.12 – Specimen SPR IT.45.Ld2(10).(6) cross-section

### 3.2.2. Specimen Construction

#### *3.2.2.1. Reinforcing Steel Cage*

Before building each reinforcing steel cage, select transverse and flexural reinforcing bars were strain gaged at specified locations along the bar lengths. IT specimen reinforcing cages were constructed in a T beam configuration for ease of construction. The steel reinforcing cages were fabricated using conventional rebar tying methods to maintain dimensional stability of the reinforcing cage. The two longitudinal cutoff bars were saw-cut to the required length using a band saw prior to installation in the cage to a length that would extend them 1/3 of their development length past where they crossed the preformed diagonal crack. Foam blockouts were installed at the ends of the cutoff bars in order to apply slip sensors during testing. Coil ties were installed in on both ends of the top and bottom of the specimen

for moving the beam after concrete casting and curing. The coil ties were fastened to the center longitudinal bars and to a nearby piece of deck steel or stirrup on the top and bottom, respectively. A finished reinforcing cage can be seen in Figure 3.13.

Figure 3.13 – Finished rebar cage

Double leg open stirrups were hung from the top flexural bars and tied in place, and longitudinal compression steel was tied in the web to the interior bottom of the stirrups. The top layer of transverse deck steel was tied to the top of the tension bars in the flange. The bottom layer was a "floating" layer created by placing the transverse steel on top of the longitudinal #6 (M19) bars and the transverse steel to two longitudinal #4 (M13) bars. On the fully anchored end of the beam, one stirrup that had been bent outward to a "W" shape was tied to the regular stirrups on each side of the cage to help provide cage stability for both moving the cage and during casting.

#### *3.2.2.2. Clear Cover*

Clear cover dimensions on the web and flange were achieved by using spacers as shown in Figure 3.14. The bottom layer of deck steel "floated" to the correct placement with the correct cover once placed in the formwork using chairs. Metal chairs were tied diagonally to

the bottom of the cage to provide the clear cover depth and to support the cage when it was placed in the formwork.

Figure 3.14 – Chair used to ensure cover concrete

*3.2.2.3. Preformed Diagonal Crack*

A preformed diagonal crack was used to investigate the influence of an existing diagonal crack on anchorage behavior and NSM material demands at a known and well instrumented section of the specimen. The approach is similar to that by Goodall (2010). The common assumption of shear-dominated beam behavior results in an idealized 45˚ diagonal crack. For the specimens, a 45˚ diagonal crack angle projected up to be coincident with the edge of the beam loading plate, and extended from depth of the theoretical compression zone down to the flexural tension steel. To produce a simulated diagonal crack, a 1/16 in. (1.6 mm) thick polycarbonate sheet was placed between the stirrups legs within the web and extended toward the bottom of the theoretical compression zone and around the flexural bars in the flange as seen in Figure 3.15. Small holes were drilled in the polycarbonate sheet at locations where it crossed the internal reinforcing steel to allow attachment of the plastic to the cage thereby restricting movement during concrete casting.

Figure 3.15 – Preformed crack placement

*3.2.2.4. Cage Placement and Concrete Casting*

After construction, the reinforcing cage was placed into the formwork using an overhead bridge crane as seen in Figure 3.16.

Figure 3.16 – Typical cage lifting process

Concrete casting was done with a 2 $yd^3$ (1.53 $m^3$) clamshell bucket. The concrete was placed into the forms and consolidated using a mechanical vibrator (Figure 3.17). Concrete was carefully placed around the preformed diagonal crack to balance the pressure on both faces

in the stem. After placing, the concrete was screeded and the surface was finished using hand trowels.

a)  b) 

Figure 3.17 – a) Clamshell bucket carrying concrete and b) Consolidating concrete

After curing for a minimum of seven days, the specimens were removed from the formwork and carefully rotated into the IT configuration. The process used to rotate a specimen into the position required for testing is shown in Figure 3.18. After rotation, specimens were moved onto the laboratory floor for NSM installation and testing.

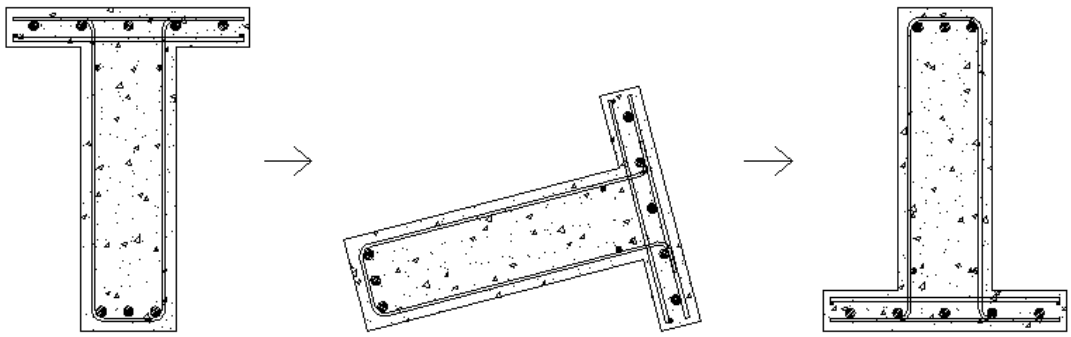

Figure 3.18 – Rotation progression for IT specimens

3.2.3. NSM Dimensions and Installation

While ACI 440.2R-08 is a design guide used for FRP systems, the methodology was used to design the metallic NSM retrofit systems. ACI 440 provides guidelines for groove width, depth, and spacing. For circular bars, groove widths and depths are prescribed to be greater than or equal to 1.5 times the diameter of the bar, $d_b$. To avoid overlapping of the tensile stresses around the NSM bars, the minimum clear spacing between grooves should be greater than twice the groove depth. A clear distance between a groove and the edge of the concrete should be provided at a minimum distance of four times the groove depth in order to minimize effects on the edges that could accelerate failure due to debonding. These guidelines are summarized in Figure 3.19.

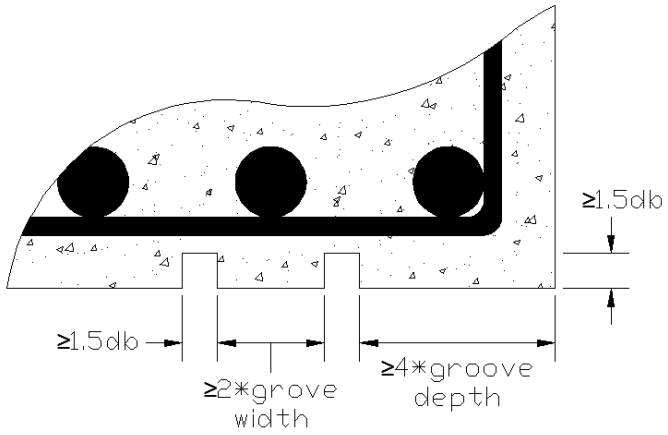


Figure 3.19 – ACI 440 groove spacing and dimension guidelines

The stainless steel and titanium bars were 0.625 in. (15.9 mm) diameter #5 (M16) bars shown below in Figure 3.20. Based on the given bar diameters, 15/16 in. (24 mm) square grooves were used. The grooves were spaced 2 in. (51 mm) apart and at least 4 in. (102 mm) from the edge of the concrete.

Figure 3.20 – Stainless steel and titanium bar examples

After each specimen was rotated into the IT configuration, the grooves were cut into the beam. The designed groove placement was sketched onto the beam and a local concrete cutting company cut the grooves. Grooves were cut by making three passes with the concrete saw and chipping out the remaining concrete using a rotohammer. Each of the NSM bars contained a 5.5 in. (138 mm) 90° hook at each end to prevent drilling through the relatively thin concrete deck. To accommodate the hooks, a 3/4 in. (19 mm) hole was drilled into each groove end. The diameter of the hole was based on the typical diameter for a post-installed anchor. The holes were intended to be drilled at approximately a 5.75 in. (146 mm) depth. In specimens IT.45.Ld3(10).Ti, IT.45.Ld3(6).Ti and IT.45.Ld3(6).SS due to the thin amount of deck left at this depth, the drill created a spall on the bottom of the flange. To account for the NSM bar bend radius, the intersection between the hole and the groove was manually chipped away using a chisel or rotohammer.

The stainless steel hooks were cold bent around a 2 in. (51 mm) bending pin in a rebar bending machine. The titanium hooks were fabricated using heat in order to prevent material fracture. Heating was performed using an acetylene torch or a two burner forge

(IT.45.Ld3(6).Ti) and color indication was used to tell the temperature of the bar (Figure 3.21). The titanium NSM bars for IT.45.Ld3(10).Ti and IT.45.Ld3(6).Ti were bent at approximately 900 ˚F (482 ˚C) while the bars for IT.0.0(6).Ti were bent around 1250 ˚F (677 ˚C). After heating to the specified temperature, the bars were inserted into the rebar bending machine and bent around a 2 in. (51 mm) diameter bending pin. Both the stainless steel and the titanium experienced springback while bending; therefore, the bars were over-bent in order to produce a 90° end result.

a)  b) 

Figure 3.21 – Color indication at a) 900 ˚F (482 ˚C) and b) 1250 ˚F (677 ˚C)

After the grooves were given sufficient time to dry after the concrete cutting, the NSM materials were installed. Installation consisted of placing a pass of epoxy in the holes and groove, pushing the NSM bar into the groove with the hooks extending into the holes, and placing a second layer of epoxy over the bar. The NSM bars were centered in the grooves during the epoxy placement. The epoxy was finished flush with the surface of the concrete Two passes of epoxy helped to ensure less air bubbles during the installation process. In order to prevent the epoxy from sagging, the least amount of finishing necessary was done. Installation photos are shown in Figure 3.22.

a)  b) 

Figure 3.22 – a) First epoxy layer and b) Finished NSM installation

Specimens that had spalled concrete on the bottom of the flange were duct taped underneath and had wood clamped next to the tape to prevent the epoxy from draining out of the hole. For these specimens, the area where the spall occurred was filled with epoxy. The epoxy was allowed to cure for a minimum of seven days between the manufacturer's recommended curing temperatures of 60˚ to 80˚. A heat tent was formed around the specimen using tarps and heaters and, taking readings every hour, the curing temperature over a 7 day period was recorded. Note that the NSM installation for specimen IT.0.0(6).Ti occurred while it was still in the formwork in the T configuration.

## 3.3. Material Properties

### 3.3.1. Concrete

Concrete was provided by a local ready-mix supplier. Each specimen required approximately 6 $yd^3$ (4.59 $m^3$) of concrete. The concrete design was based the AASHO "Class A" 3,000 psi (21 MPa) mixture used for vintage concrete bridges. Actual strengths around 4,000 psi (28 MPa) are more likely the present day strengths in these bridges due to in-situ strength gain.

This design is congruent with previous research on similar sized specimens at Oregon State University. Standard slump tests were conducted and water added if necessary to achieve a 5 in. (127 mm) slump. The actual concrete compressive and tensile strengths were performed in accordance with ASTM C39/C39M-09 and ASTM C496/C496M-11, respectively. Average test day concrete cylinder compressive and tensile strengths are reported in Table 4. Specimens had a test day minimum compressive strength target of 3300 psi (22.8 MPa) not to exceed 4100 psi (28.3 MPa).

Table 4 – Average test day specimen concrete compressive and tensile strengths

| **Specimen** | **Concrete Age (days)** | **$f_c'$ psi (MPa)** | **$\sigma, f_c'$ psi (MPa)** | **$f_{ct}$ psi (MPa)** | **$\sigma, f_{ct}$ psi (MPa)** |
|---|---|---|---|---|---|
| IT.45.Ld3(10).Ti | 44 | 4056 (28.0) | 371 (2.56) | 476 (3.3) | 36.7 (0.25) |
| IT.45.Ld3(6).Ti | 35 | 3734 (25.7) | 38.0 (0.26) | 385 (2.7) | 59.6 (0.41) |
| IT.45.Ld3(6).SS | 42 | 3525 (24.3) | 76.3 (0.53) | 394 (2.7) | 35.7 (0.25) |
| IT.0.0(6).Ti | 59 | 3397 (23.4) | 263 (1.81) | 429 (3.0) | 42.6 (0.29) |
| SPR IT.45.Ld2(10).(5) | n/a | 3603 (24.8) | n/a | n/a | n/a |
| SPR IT.45.Ld2(10).(6) | n/a | 3918 (27.0) | n/a | n/a | n/a |
| SPR IT.0.0(10).(5) | 63 | 3290 (22.6) | n/a | 367 (2.5) | n/a |

3.3.2. Internal Reinforcing Steel

All reinforcing steel was provided by local rebar fabricators. The transverse reinforcing bars were ASTM A615 (2009) Gr. 40, #4 (Grade 280, M13) and were made from a steel heat with the lowest available yield stress. The longitudinal reinforcement was ASTM A706 (2009) Gr. 60, #11 (Grade 420, M36). The material properties for all the steel reinforcement were determined in accordance with ASTM E8/E8M-13a. The average measured material properties from three replicate samples are reported in Table 5 and Table 6 below. The transverse reinforcing steel used in the specimens was a reasonable approximation of ASTM A305 (1950) Gr. 40 (Grade 276) steel available in the 1950's. Regrettably, Gr. 40 (Grade 276) #11 (M36) bars are not commercially available and Gr. 60 (Grade 420) bars were used as a substitute. These provide larger bond demands and lower dowel action compared to the lower grade bars and will provide conservative results.

Table 5 – Average reinforcing steel properties (three replicates)

| **Reinforcement Type** | **Bar Size** | **Grade ksi (MPa)** | **$f_y$ ksi (MPa)** | **σ, $f_y$ ksi (MPa)** | **$f_u$ ksi (MPa)** | **σ, $f_u$ ksi (MPa)** |
|---|---|---|---|---|---|---|
| Transverse | #4 (M13) | 40 (280) | 50.2 (346) | 0.12 (0.83) | 79.6 (549) | 0.17 (1.17) |
| Longitudinal | #11 (M36) | 60 (420) | 71.6 (494) | 1.26 (8.69) | 107 (738) | 0.93 (6.41) |

Table 6 – Average SPR reinforcing steel properties (three replicates)

| Specimen | Transverse Reinforcement | | Flexural Reinforcement | |
|---|---|---|---|---|
| | $f_y$ ksi (MPa) | $f_u$ ksi (MPa) | $f_y$ ksi (MPa) | $f_u$ ksi (MPa) |
| SPR IT.45.Ld2(10).(5) | 53.5 (369) | 84.6 (583) | 71.7 (494) | 104.7 (722) |
| SPR IT.45.Ld2(10).(6) | | | | |
| SPR IT.0.0(10).(5) | 50.7 (350) | 78.9 (544) | 75.8 (523) | 111.7 (770) |

3.3.3. NSM Materials

Two NSM materials were used in the test program: titanium and stainless steel. The stainless steel was #5, Gr. 75 (M16, Grade 520) and conformed to ASTM A955/955M (2012). The material properties of the stainless steel were determined in accordance with ASTM E8/E8M-13a. The modulus of elasticity was taken as 29,000 ksi (200,000 MPa), the same as steel. The yield stress was found using the 0.2% offset method because stainless steel does not have a well-defined yield stress. The stainless steel material properties are listed in Table 7.

The titanium material used in this study was an alloy with 6% aluminum and 4% vanadium (Ti-6Al-4V). The alloy meets ASTM B348 (2013) and is aircraft quality titanium. The titanium is high strength, impervious to chlorides, and has a low coefficient of thermal expansion around 8.6 μm/m ºC. The bars were 0.625 in (16 mm) round bars with an average area of 0.2975 $in^2$ (192 $mm^2$). The average cross-sectional area of the titanium was determined by weighing the full-length bars (~14 ft (14.3 m)) of known length and dividing by the unit weight of 276 $lb/ft^3$ (4,419 $kg/m^3$). The titanium was fabricated with a unique

surface treatment in lieu of the standard rebar deformation pattern in order to enhance bond at the titanium and epoxy interface.

Material tests were conducted in accordance with ASTM E8/E8M-13a. Stress-strain curves show that the titanium exhibited almost perfectly elasto-plastic behavior. Because the material does not exhibit a well-defined yield plateau, the yield stress was found using a 0.2% strain offset. The nominal modulus of elasticity for titanium is 15,500 ksi (106,800 MPa), while the average measured modulus was computed as 15,120 ksi (104,200 MPa). The stiffness of titanium is approximately half that of steel. Table 7 describes the material properties.

Table 7 – Average NSM reinforcing properties (three replicates)

| **Reinforcement Type** | **Bar Size** | **Bar Area $in^2$ ($mm^2$)** | **Grade ksi (MPa)** | **$f_y$ ksi (MPa)** | **σ, $f_y$ ksi (MPa)** | **$f_u$ ksi (MPa)** | **σ, $f_u$ ksi (MPa)** |
|---|---|---|---|---|---|---|---|
| Stainless Steel | #5 (M16) | 0.31 (7.9) | 75 (520) | 83.0 (572) | 0.68 (4.69) | 127.3 (878) | 0.35 (2.41) |
| Titanium | #5 (M16) | 0.2975 (7.6) | n/a | 145.4 (1002) | 1.56 (10.75) | 158.1 (1090) | 1.39 (9.58) |

The stainless steel and titanium bars were bonded to the concrete grooves using a commercially available general purpose gel epoxy adhesive (CONCRESIVE 1420). This is a non-sag epoxy that is widely used for bonding to concrete. The manufacturer reported material properties for the epoxy were tensile strength of 4 ksi (27.6 MPa), elongation at

break of 1.0%, compressive yield strength of 12.5 ksi (86.2 MPa), and 2-day cure bond strength greater than 2 ksi (13.8 MPa).

## 3.4. Instrumentation

Global and local specimen responses were measured using an array of instruments. Data from sensors were acquired and stored for later analysis using commercially available data acquisition hardware and software. Data were sampled at a rate of 5 Hz. Sensors consisted of strain gages bonded to stirrups, flexural reinforcing steel bars, and the NSM bars, numerous displacement sensors, rotation sensors, and a load cell. Digital photographs and both tape and digital videos were used to document the specimen response during each load step, at failure, and after failure.

### 3.4.1. Reinforcing Steel Strain Gages

Strain gages were applied to only one half of the specimen assuming that the specimens behaved symmetrically about the longitudinal axis. Strain gages were placed on the longitudinal flexural bars to measure the tensile force and the bond stress distribution. The strain gages were waterproofed and their wires fastened to the reinforcement in order to mitigate gage failure from water and vibration during the casting process (Figure 3.23). Once the reinforcing cage was tied, the long lead wires on the strain gages were zip-tied along the steel up to the top of the cage where they were designed to stick out of the flange edge. The ends of the leads were placed in plastic bags to prevent water and concrete from damaging the wires during casting.


Figure 3.23 – Strain gage waterproofing and protection

For the three specimens with a 45˚ preformed diagonal crack, the continuous flexural reinforcing steel bars had 10 strain gages and the cutoff reinforcing steel bars had six gages. Gages on the cutoff reinforcing steel bars were placed along the development length, at the preformed diagonal crack location, and at three corresponding locations at each end of the NSM bars. Specimen IT.0.0(6).Ti had three gages on each of the cut bars in the center and on one side of the beam, for a total of 12 strain gages. This specimen also had strain gages placed on a #6 (M19) bar at midpoint and lining up with the furthest gaged location in each direction on the cutoff bars (totaling 3) and at midpoint of the center and edge compression bars. Gages on the main tension steel for this specimen (#11 (M36)) bars were placed along the reinforcing steel bar development length. Strain gage locations are shown for the different specimens in Figure 3.24 to Figure 3.27

Strain gages were also applied to stirrup legs at mid-height and at locations where the stirrups crossed the preformed crack. Specimen IT.45.Ld3(10).Ti had 9 stirrup strain gages, IT.45.Ld3(6).Ti and IT.45.Ld3(6).SS had 12 stirrup strain gages due to the decreased stirrup spacing, and IT.0.0(6).Ti had 6 stirrup strain gages.

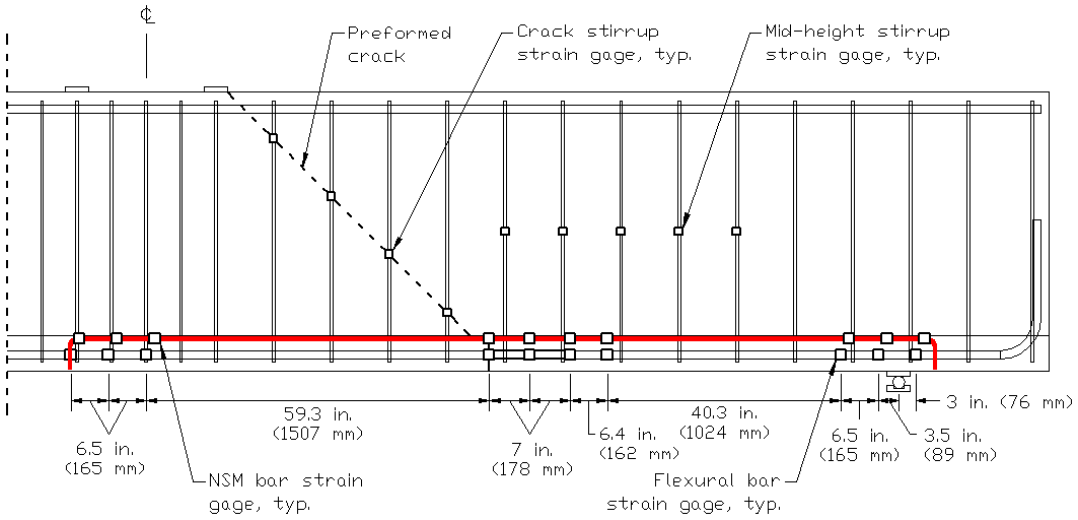


Figure 3.24 – Specimen IT.45.Ld3(10).Ti strain gage locations

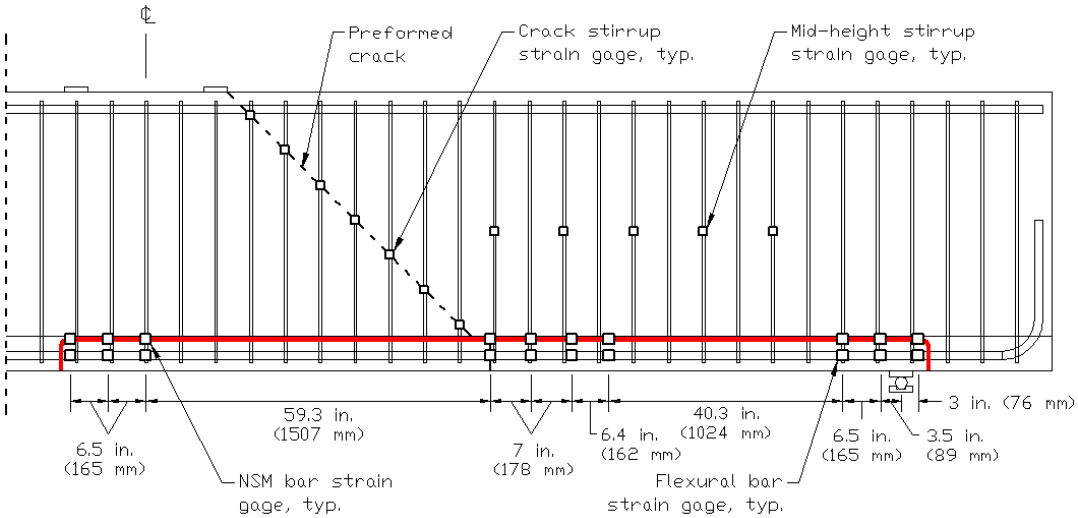


Figure 3.25 – Specimen IT.45.Ld3(6).Ti strain gage locations

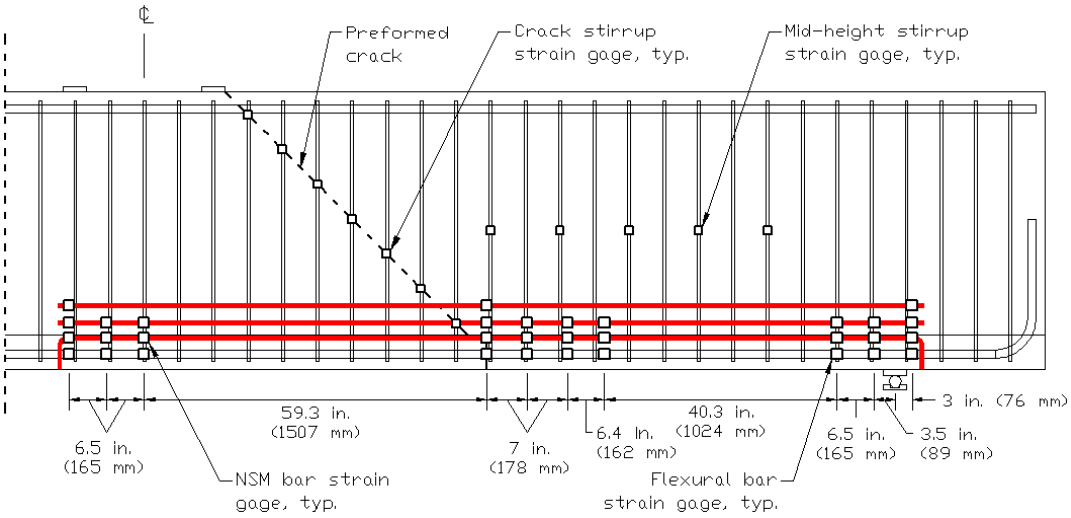


Figure 3.26 – Specimen IT.45.Ld3(6).SS strain gage locations.

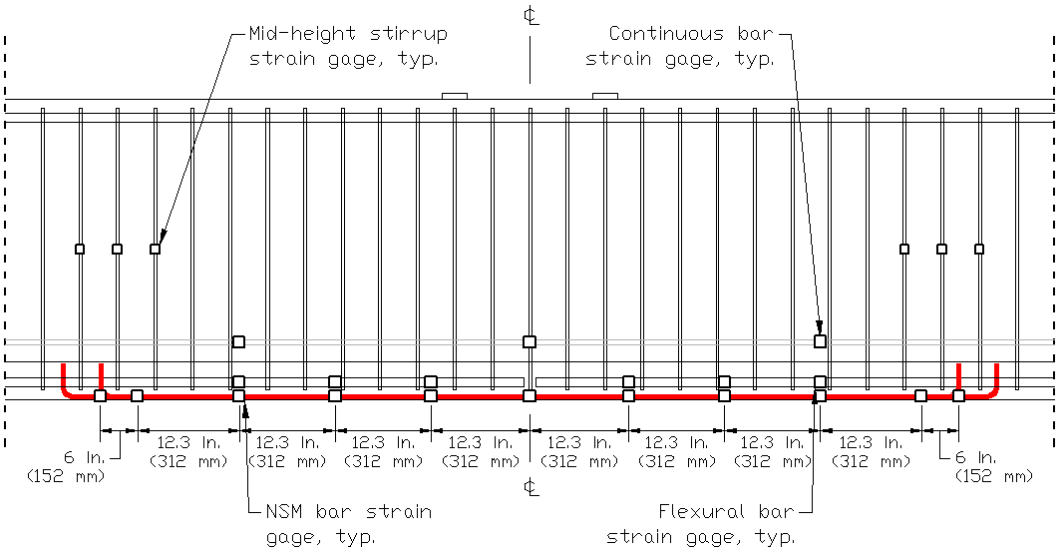


Figure 3.27 – Specimen IT.0.0(6).Ti strain gage locations.

### 3.4.2. NSM Strain Gages

Strain gages were installed on the NSM reinforcing materials prior to installation in the saw-cut grooves. Like the internal reinforcing steel strain gages, only one half of the NSM bars were instrumented, assuming symmetrical behavior along the longitudinal axis of the specimens. The deformations on the NSM bars were removed by grinding at the strain gage locations. The locations of the gages on the NSM bars were intended to line up (in elevation) with the strain gages on the internal longitudinal reinforcing steel.

Strain gages on the NSM bars in specimens IT.45.Ld3(10).Ti and IT.45.Ld3(6).Ti were placed coincident with those along the development length of the internal cutoff reinforcing steel bars; at the preformed diagonal crack location, and at three locations on each end of the titanium alloy bars. The specimens each had two titanium bars on each side of the beam. Both NSM bars located on one side of the specimen were strain gaged, bringing the total NSM strain gage count to 20 for each specimen. On the IT.45.Ld3(10).Ti specimen, the holes were drilled in the flange of the specimen for the titanium hooks prior to the NSM gaging. During drilling, it was found that the designated placement of the NSM hooks coincided with reinforcing steel located in the deck. To clear the deck steel, the NSM bars were shifted 1.5 in (38 mm) towards the support. Upon gaging the bars, the three gages at each end were shifted with the bar, while the four middle gages remained in line with the internal steel. This is shown in Figure 3.24.

The IT.45.Ld3(6).SS specimen had four stainless steel bars placed on each side of the beam: two were installed in the flange and two were in the web. The two more interior NSM bars

were instrumented similarly to those described above, with each bar containing 10 strain gages. The two exterior bars had three strain gages each. These were placed at the location where the preformed diagonal crack crossed the internal cutoff reinforcing steel bar and the very ends of each NSM bar as shown in Figure 3.26.

### 3.4.3. Diagonal String Potentiometers

Pairs of diagonal displacement sensors with a range of 2 in. (50.8 mm) were used to measure the concrete deformations during testing. As cracks opened and propagated during loading, the lower sensors measured elongation while the upper sensors measured contraction. For the IT.45.Ld3(10).Ti specimen, the deformations were only measured on the north side (six sensors). The IT.45.Ld3(6).Ti and IT.45.Ld3(6).SS specimens had a total of 12 sensors measuring both the north and south sides. The sensors on the south side of the specimens mirrored those of the north side shown in Figure 3.28.

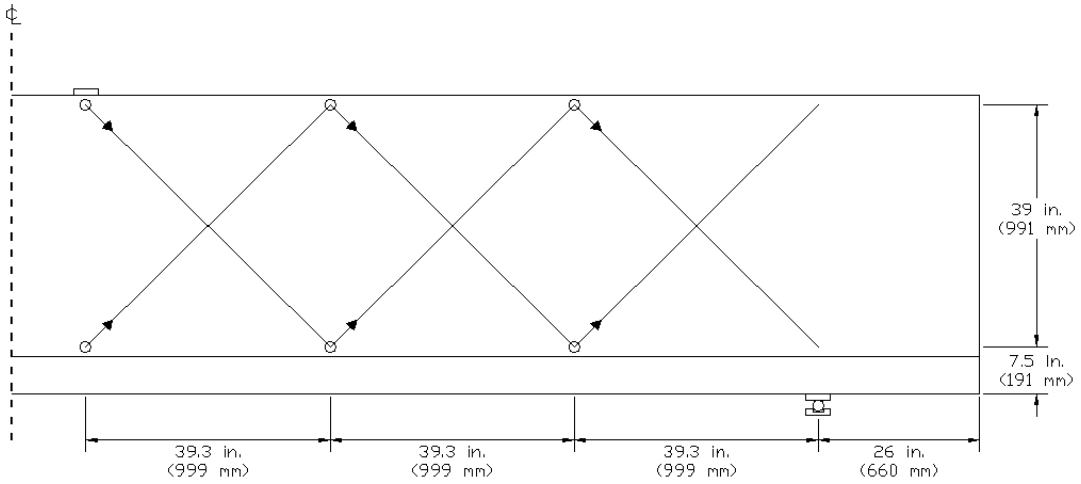


Figure 3.28 – IT.45.Ld3 specimen diagonal displacement sensor layout

Specimen IT.0.0(6).Ti contained discontinuous internal reinforcing steel at midspan and the diagonal sensor array was modified to capture the distortions at midspan, as seen in Figure 3.29.

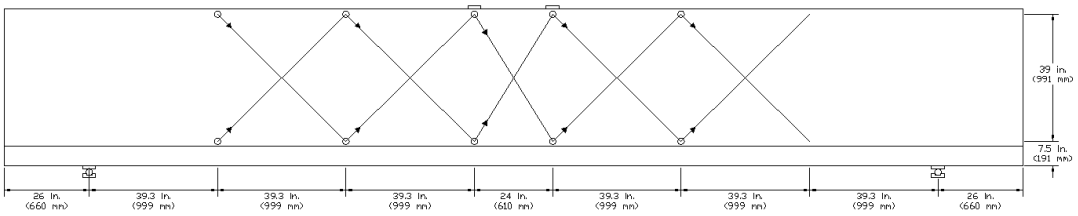


Figure 3.29 – Specimen IT.0.0(6).Ti diagonal displacement sensor layout

### 3.4.4. Global Specimen Deflection

String potentiometers with a 10 in. (254 mm) stroke were used to measure specimen displacement at midspan relative to the laboratory floor. One sensor was placed on the east face and one on the west face. The gross midspan displacement was taken as the average of the two sensors. The sensors were attached to mid-height of the flange as seen in in Figure 3.30 a).

To account for rigid-body deformations, support settlements were measured relative to the laboratory floor using 1.5 in. (38.1 mm) vertically oriented displacement sensors. The sensors were attached to the web and placed above the support centerlines on all each corners of the specimen as shown in Figure 3.30 b). The measured support displacements were averaged and then subtracted from the gross midspan displacement values to determine the net midspan deflection.

a)  b) 

Figure 3.30 – a) Midspan string potentiometer and b) Support displacement sensor

### 3.4.5. End Rotation Sensors

Rotation sensors were affixed to each end of the beam over centerline of support. Beam end rotations were measured in degrees.

### 3.4.6. Anchorage Slip

The cutoff reinforcing steel bar slip was measured in specimens IT.45.Ld3(10).Ti, IT.45.Ld3(6).Ti, and IT.45.Ld3(6).SS using 1 in. (25.4 mm) stroke displacement sensors. The sensors measured the deformation of the reinforcing steel bar relative to the surrounding concrete (slip) as illustrated in Figure 3.31.

Figure 3.31 – Cutoff bar slip sensor

### 3.5. Test Protocols

Specimens were tested in the Structural Engineering Research Laboratory at Oregon State University. A reaction frame anchored to the strong floor allowed a four-point loading system to be used. Load was applied using a closed-loop 500 kip (2224 kN) capacity servo-hydraulic actuator under load control. A steel spreader beam produced a 24 in. (610 mm) long constant moment region in the specimens. The actuator force was distributed through the spreader beam to the specimens via two 2 in. (51 mm) diameter rollers placed on two 4 in. (102 mm) wide plates. To ensure uniform load application across the plates, the plates were leveled and grouted into place using a quick-setting, high-strength gypsum cement.

The span length of the specimens was 21.7 ft (6.60 m) between centerlines of support. The end support reactions were also distributed through 4 in. (102 mm) wide plates resting on captive rollers as seen in Figure 3.32. Specimens were simply supported. The loading setup is shown schematically in Figure 3.33.

Figure 3.32 – End support reaction setup

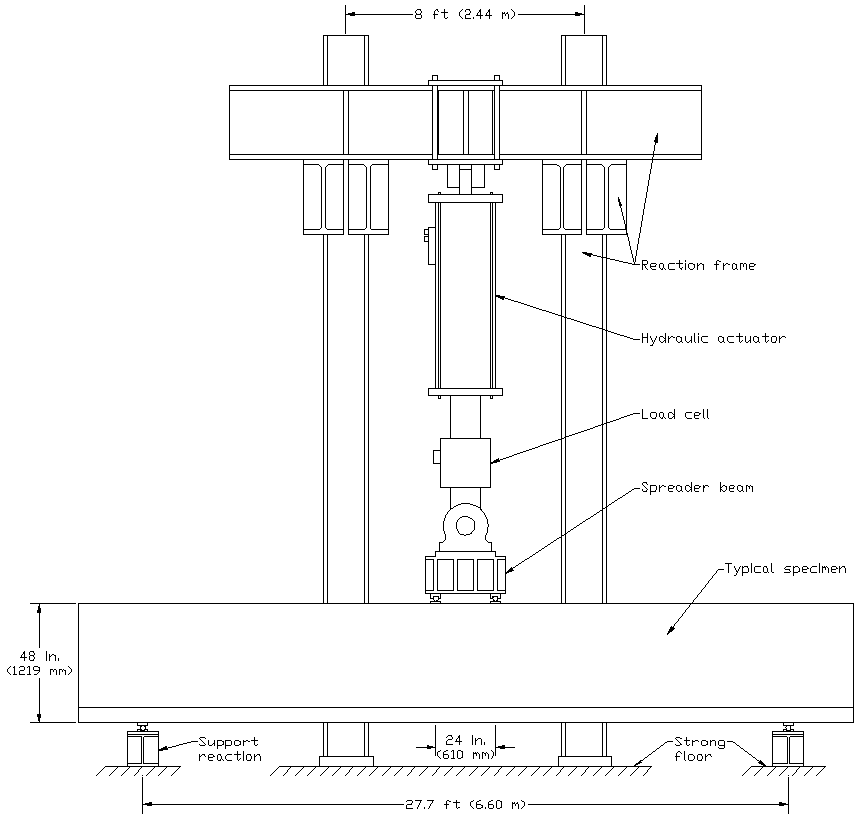


Figure 3.33 – Four-point load configuration used for specimen testing

Before testing, the actuator was plumbed and the specimens were leveled in the transverse direction. The specimen was centered in the load frame in both the transverse and longitudinal directions. All instruments were initialized to zero. Tests were conducted using pseudo-static cyclic loading without load reversals. Each load step was increased by 50 kips (222 kN) from the previous load cycle as seen in Table 8. Load was applied at a rate of 1 kip/sec (4.45 kN/sec) in a series of cycles until failure. Upon reaching each new load step, the load was reduced by 25 kips (111 kN) so cracks could be identified, marked, and recorded with minimized creep effects.

Table 8 – Typical specimen load cycle pattern

| **Load Step** | |
|---|---|
| **(kip)** | **(kN)** |
| 0-50 | 0-222 |
| 5-100 | 22.2-445 |
| 5-150 | 22.2-667 |
| 5-200 | 22.2-890 |
| 5-250 | 22.2-1112 |
| 5-300 | 22.2-1334 |
| 5-350 | 22.2-1557 |
| 5-400 | 22.2-1779 |
| 5-450 | 22.2-2002 |
| 5-500 | 22.2-2224 |

## 3.6. Supplemental Investigations of Titanium Bond and Hook Toughness

In addition to tensile tests, supplemental tests were performed on the titanium alloy bars to determine pullout strength and hook toughness.

### 3.6.1. Pullout Specimens

Pullout tests were performed to evaluate the strength of the titanium-epoxy interface. Titanium bars are typically fabricated to be smooth and without defects. Therefore, the manufacturer developed five alternative surface finishes including: surface blasted, rough finish, light turn, light turn blasted, and heavy turn. Examples are shown in Figure 3.34. Tensile tests were performed on each bar type. One bar of each surface roughness was used for pullout testing. After testing, the heavy turn finish was selected for retrofitting the IT specimens. Three additional pullout tests were performed on the heavy turn finished titanium alloy bars.

Figure 3.34 – Initail surface roughness samples

Four additional tests were performed on titanium alloy bars with a “bulb” end. Two of these tests used the light turn bars while the other two used the surface blasted bars. Three of the

bars were taken to a blacksmith and forged using conventional forging techniques. Of these, one light turn bar was fabricated with a bulb on the end and the blasted bars were fabricated with an end bulb on one and the other with a bulb in the middle of the length to be embedded for the pullout test. The other light turn bar was fabricated by heating with an oxy-acetylene torch and the end was hammered by hand into a bulb shape. The method of hammering by hand was not extremely effective. Examples of the fabricated "bulbs" can be seen in Figure 3.35.

Figure 3.35 – Bulb end samples for pullout testing

For the pullout tests, 0.75 in. (19 mm) diameter holes were drilled to a depth of 5 in. (127 mm) into concrete blocks. The holes were filled approximately halfway with a general purpose gel epoxy adhesive that is widely used for bonding to concrete (Concresive 1420). A bar specimen was inserted into the hole and pushed through the epoxy until it reached the bottom of the hole. The bar was centered in the hole and set perpendicular to the concrete face. Excess epoxy above the hole was removed and the epoxy was finished flush with the concrete. The epoxy was then allowed to cure for a minimum of seven days before testing.

The pullout test setup included multiple pieces to provide full bearing surfaces at the interfaces. First, a large plate with a 2 in. (51 mm) diameter hole was placed over the bar to react against the concrete. A hydraulic jack was positioned on top of the plate. The jack was connected to a hydraulic hand pump. Two additional plates were located on top of the jack. These plates allotted for full bearing between the hydraulic jack and a donut load cell. On top of the load cell, a prestressing chuck was leveled by spherical washers. Lastly, a 1.5 in. (38 mm) vertical displacement sensor was placed on the tip of the bar specimen to measure the vertical movement during loading. Figure 3.36 shows the setup for pullout tests.


Figure 3.36 – Pullout test setup and hydraulic hand pump

Tests were performed manually by increasing the hydraulic pressure to the jack by a hand pump. Tests concluded after failure of a cone of concrete and epoxy or the bar specimen sheared through the epoxy. Additional loading only provided the static friction required to drag the cone or bar specimen through the concrete or epoxy, respectively.

### 3.6.2. Hook Specimens

Tests were performed on heavy turn titanium alloy bars bent into180˚ hooks to assess the hook toughness at various bending temperatures and diameters. A testing apparatus was designed and fabricated to test the hooks by transversely pulling on both legs of the hooks. The hooks were heated in a forge using color indication to identify the temperature of the bar. After heating, the bars were inserted into a rebar bending machine and bent around a bending pin. A total of 12 samples were fabricated. Three sets of (3) replicates were heated to 900 ˚F (482 ˚C) and bent around 2 in. (51 mm), 3 in. (76 mm), and 4.5 in. (114 mm) diameter bending pins, respectively. An additional three samples were heated to 1250 ˚F (677 ˚C) and bent around the 2 in. (51 mm) diameter bending pin. An example of each set can be seen in Figure 3.37. Due to springback in the titanium alloy, the samples that were bent around the 4.5 in. (114 mm) bending pin ended up with final an inner diameter of 5.0 in. (127 mm). The inner diameters of all the other samples matched the pin they were bent around.

Figure 3.37 – 180˚ hook specimen examples

Testing was performed using a 110 kip (489 kN) universal testing machine (UTM). The hooks were inserted through 0.6875 in. (17.5 mm) diameter drilled holes in A572 Grade 50

(Grade 340) steel plates. After placing the hook through the steel plates, a prestressing chuck was inserted over each leg to prevent the titanium from pulling out during testing. The plates were gripped by the UTM machine and pulled at a rate of 0.01 kip/sec (0.254 kN/sec). A typical loading schematic is illustrated in Figure 3.38. Two displacement sensors were used to measure opening displacement of the hook (separation of the plates)

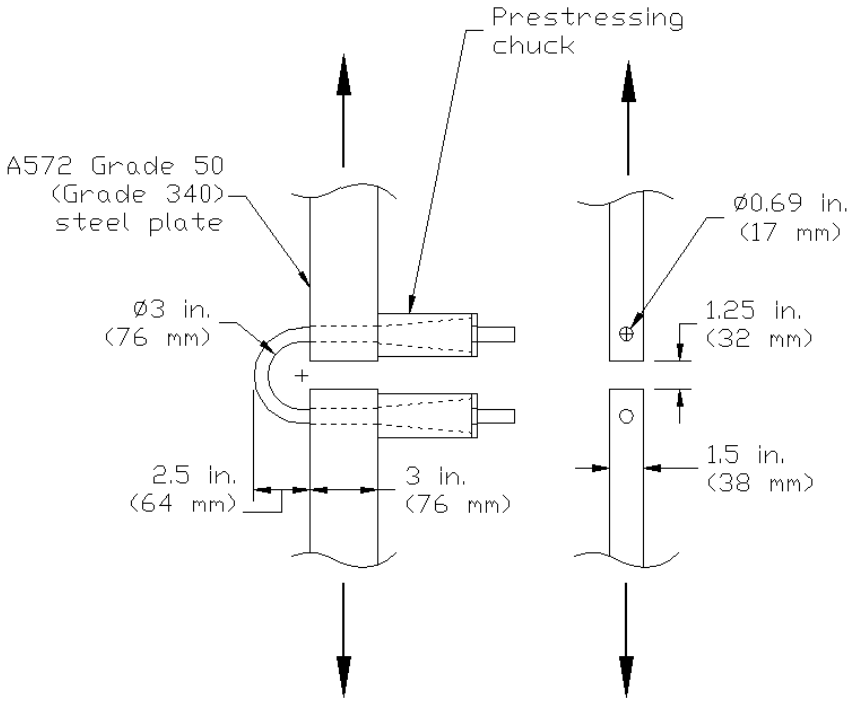


Figure 3.38 – Plan and elevation of 3 in. (76 mm) diameter hook specimen test setup

# 4. EXPERIMENTAL RESULTS

## 4.1. Overall Response of Specimens

The applied load at failure and the shear forces action on the section are reported in Table 9. The shear forces include the applied load, applied shear from the actuator, $V_{APP}$; the shear force from the portion of the self-weight of the beam acting on the failure plane, $V_{DL;}$ and the sum of these as the total shear force, $V_{EXP}$. The self-weight shear, $V_{DL}$, was calculated using a reinforced concrete unit weight of 150 lb/ft$^3$ (23.6 kN/m$^3$) to estimate the weight of concrete acting on the diagonally cracked failure plane.

Table 9 – Applied load and shear values at failure

| Specimen | Applied Load kips (MN) | $V_{APP}$ kips (kN) | $V_{DL}$ kips (kN) | $V_{EXP}$ kips (kN) |
|---|---|---|---|---|
| IT.45.Ld3(10).Ti | 420.5 (1.87) | 210.2 (935) | 3.6 (16) | 213.8 (951) |
| IT.45.Ld3(6).Ti | 448.0 (1.99) | 224.0 (996) | 0 (0) | 224.0 (996) |
| IT.45.Ld3(6).SS | 500.0 (2.22) | 250.0 (1112) | 0 (0) | 250.0 (1112) |
| IT.0.0(6).Ti | 191.3 (0.85) | 95.7 (426) | 0 (0) | 95.7 (426) |
| SPR IT.45.Ld2(10).(5) | 358.9 (1.60) | 179.5 (798) | 4.8 (26) | 184.3 (820) |
| SPR IT.45.Ld2(10).(6) | 450.8 (2.01) | 225.4 (1003) | 3.4 (19) | 228.8 (1018) |
| SPR IT.0.0(10).(5) | 401.4 (1.79) | 200.7 (893) | 4.6 (20) | 205.3 (913) |

Specimens IT.45.Ld3(6).Ti and IT.45.Ld3(6).SS both failed in flexure at the ends of the NSM bars near midspan. No anchorage failures were observed for these specimens.

Specimen IT.45.Ld3(10).Ti failed in shear which subsequently resulted in pullout of the anchorage. The specimen with discontinuous reinforcement at midspan (IT.0.0(6).Ti) failed in flexure with the titanium alloy bars eventually debonding, resulting in one of the hooks pulling out of the specimen. The failure modes, failure crack angles, and midspan displacement at peak load are provided in Table 10.

Table 10 – Failure mode, failure crack angle, midspan displacement at failure

| **Specimen** | **Failure Mode** | **Failure Crack Angle (deg)** | **Failure Midspan Displacement in. (mm)** |
|---|---|---|---|
| IT.45.Ld3(10).Ti | Diagonal-Tension | 36 | 1.12 (28) |
| IT.45.Ld3(6).Ti | Flexure | 90 | 1.06 (27) |
| IT.45.Ld3(6).SS | Flexure | 90 | 1.15 (29) |
| IT.0.0(6).Ti | Flexure | 90 | 1.48 (38) |
| SPR IT.45.Ld2(10).(5) | Shear-Anchorage | 44 | 0.98 (25) |
| SPR IT.45.Ld2(10).(6) | Shear-Compression | 32 | 0.97 (25) |
| SPR IT.0.0(10).(5) | Anchorage | 30 | 1.20 (30) |

### 4.1.1. Displacement Results

#### *4.1.1.1. Load-Deformation Responses*

The load-deformation responses at midspan for the specimens are shown in Figure 4.1 to Figure 4.4. The midspan displacements were determined by taking the average midspan displacements and subtracting the average of the support settlements as described previously. A summary of the SPR load-deformation responses is shown in Figure 4.5.

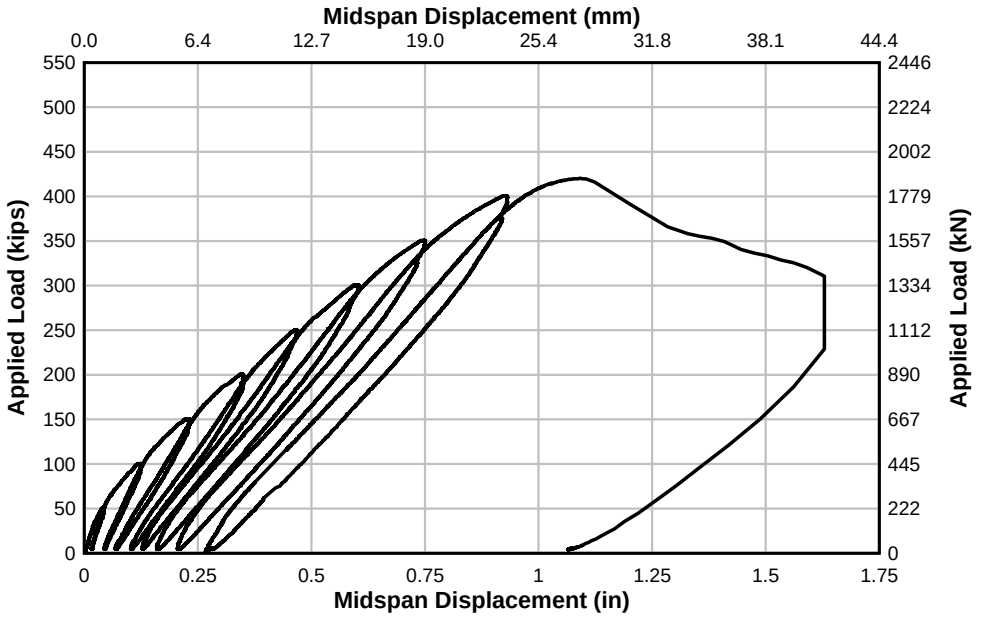


Figure 4.1 – Specimen IT.45.Ld3(10).Ti load-displacement response

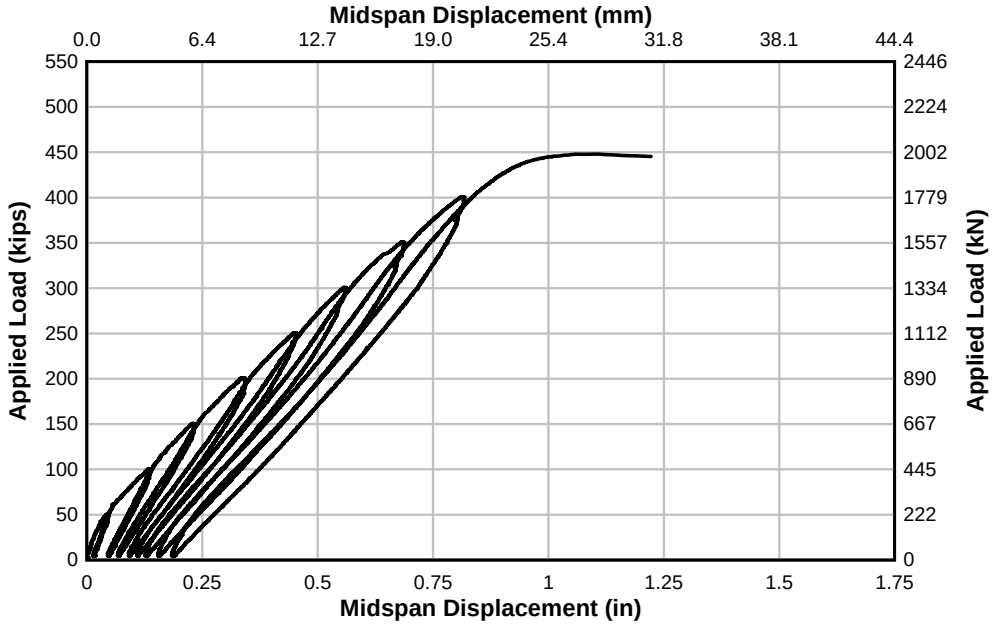


Figure 4.2 – Specimen IT.45.Ld3(6).Ti load-displacement response

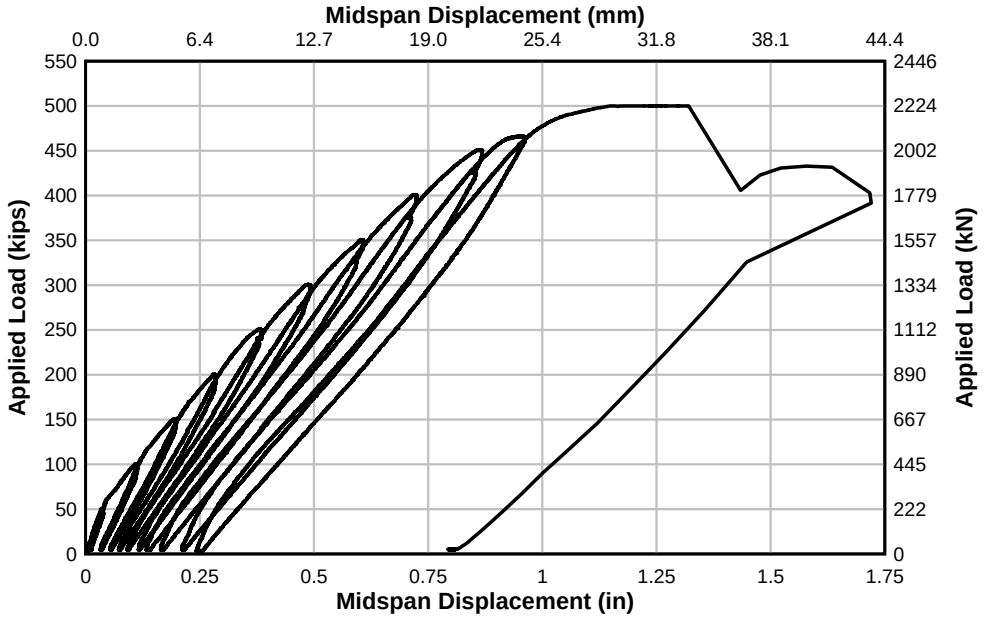


Figure 4.3 – Specimen IT.45.Ld3(6).SS load-displacement response

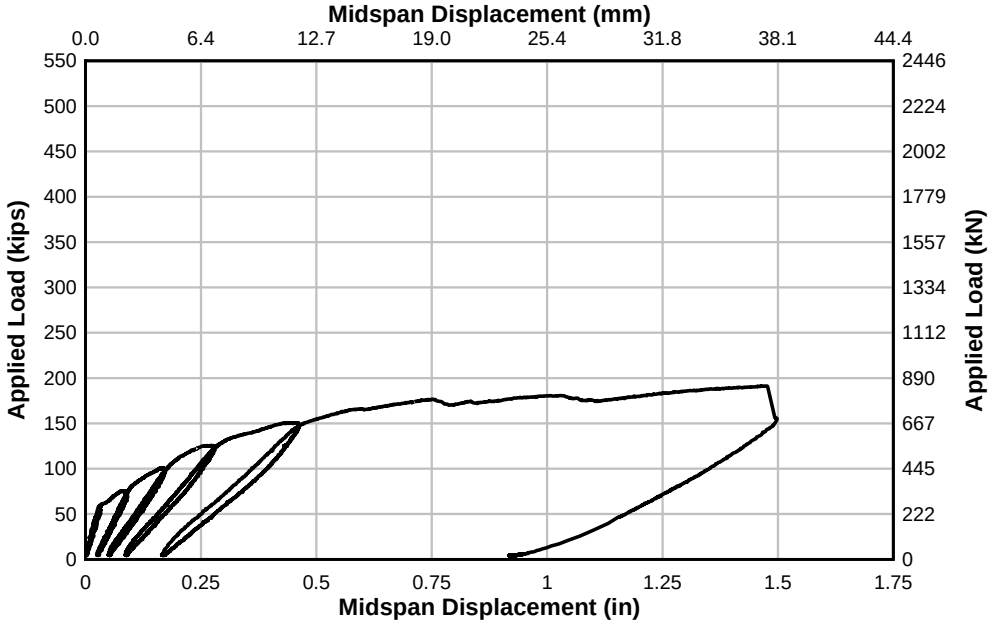


Figure 4.4 – Specimen IT.0.0(6).Ti load-displacement response

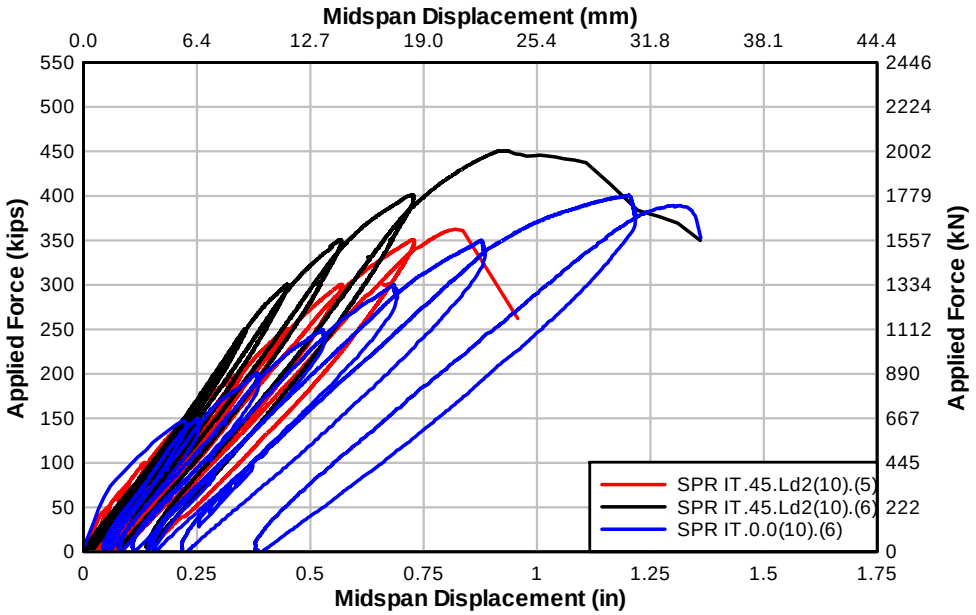


Figure 4.5 – SPR load-displacement responses

### *4.1.1.2. Crack Propagations*

Crack initiation and propagation were monitored throughout each test. After reaching each successive load level, the applied load was reduced by 25 kips (111 kN). The load was held at this lower level while new cracks were traced on the specimen in order to reduce creep deformations. Pictures were taken at each load level after crack mapping. Photographs taken after failure are shown in Figure 4.6. The anchorage damage around the preformed diagonal crack can be seen in the large chevron cracks in the flanges. The cracking initiated at the cutoff location and extended until the controlling diagonal tension or flexural crack formed. The crack patterns are shown in Figure 4.7. Note on specimens IT.45.Ld3(6).Ti and IT.45.Ld3(6).SS the NSM bars lost anchorage on the back side of the specimens.


Figure 4.6 – Failure photographs of test specimens (front and back sides)

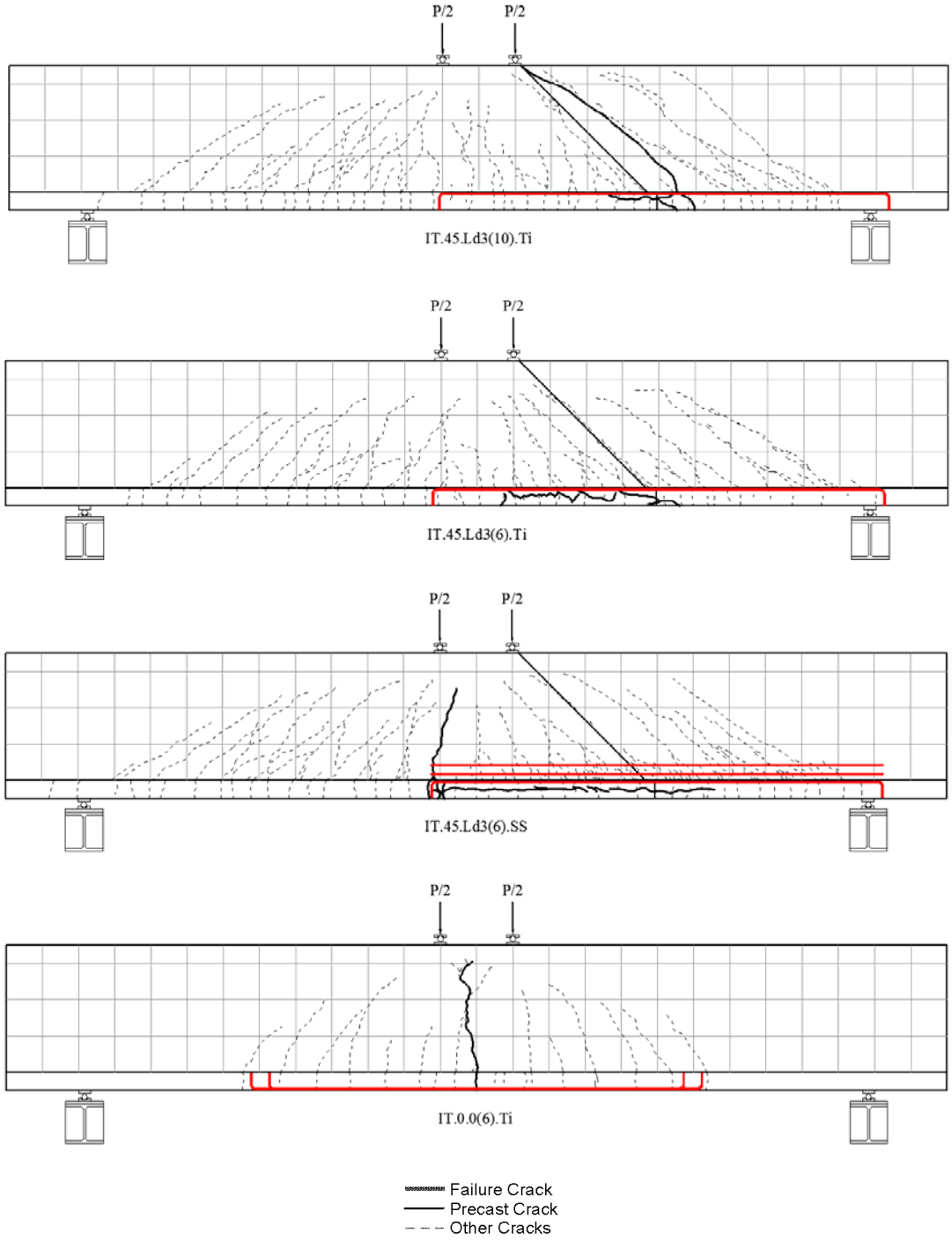


Figure 4.7 – Specimen crack mapping with failure cracks

Failure photographs and crack mapping for the SPR specimens with preformed diagonal cracks and poorly detailed flexural reinforcing steel anchorages are shown in Figure 4.8 and Figure 4.9.


Figure 4.8 – Failure photographs of SPR test specimens

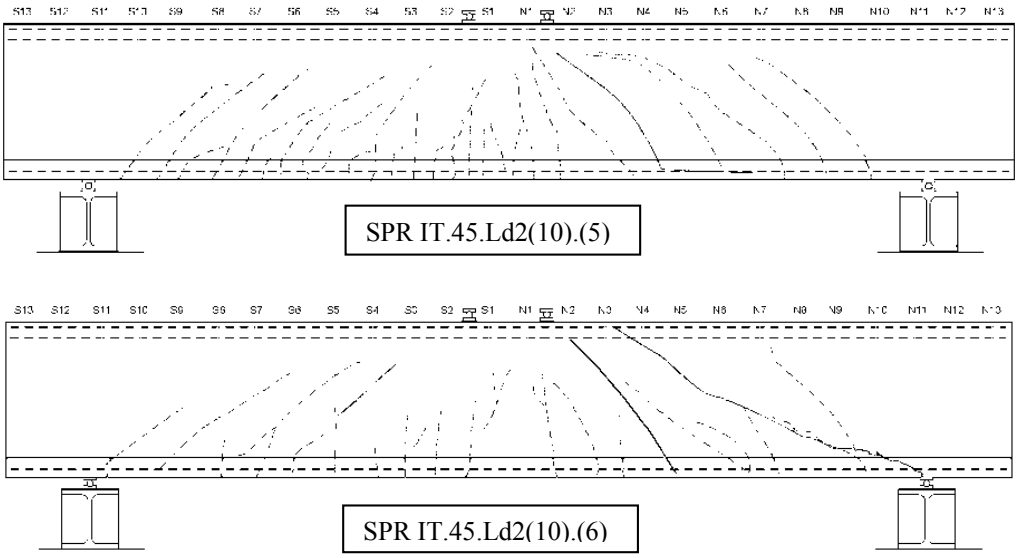


Figure 4.9 – SPR specimen crack mapping with failure cracks

*4.1.1.3. Anchorage Slip Responses*

The cutoff bar slip was measured for the three specimens with preformed diagonal cracks. The applied load-slip responses are shown in Figure 4.10 to Figure 4.12. As loading increased towards failure, residual slip was observed. Slip typically was not observed until at or near failure when chevron cracking developed as the concrete cover split around the cutoff bars. As seen in the applied load-slip responses, towards failure of each specimen, one of the cutoff bars slipped more than the other. Anchorage losses occurred on the side of the specimen that exhibited the larger slip value. In comparison to IT.45.Ld3(10).Ti, specimens IT.45.Ld3(6).Ti and IT.45.Ld3(6).SS had greater shear capacities on the critical side and their respective curves show that they were able to sustain greater slip towards failure.

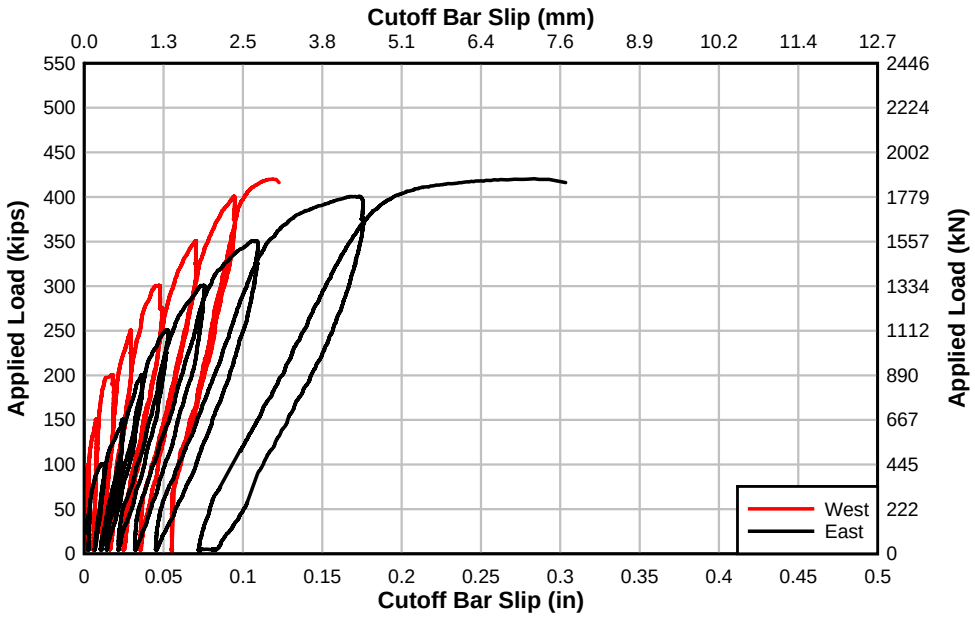


Figure 4.10 – Specimen IT.45.Ld3(10).Ti load-cutoff bar slip response

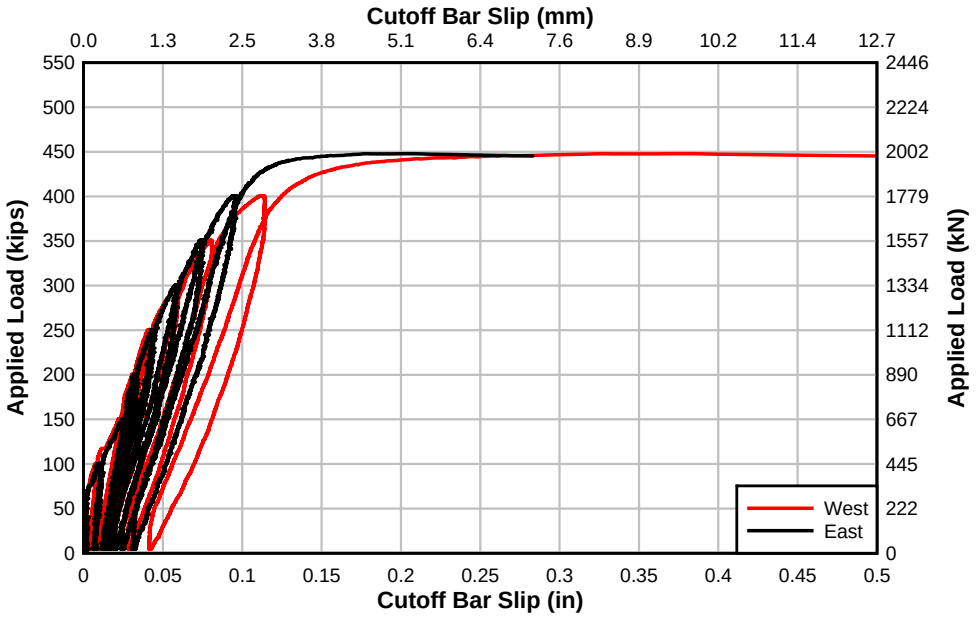


Figure 4.11 – Specimen IT.45.Ld3(6).Ti load-cutoff bar slip response

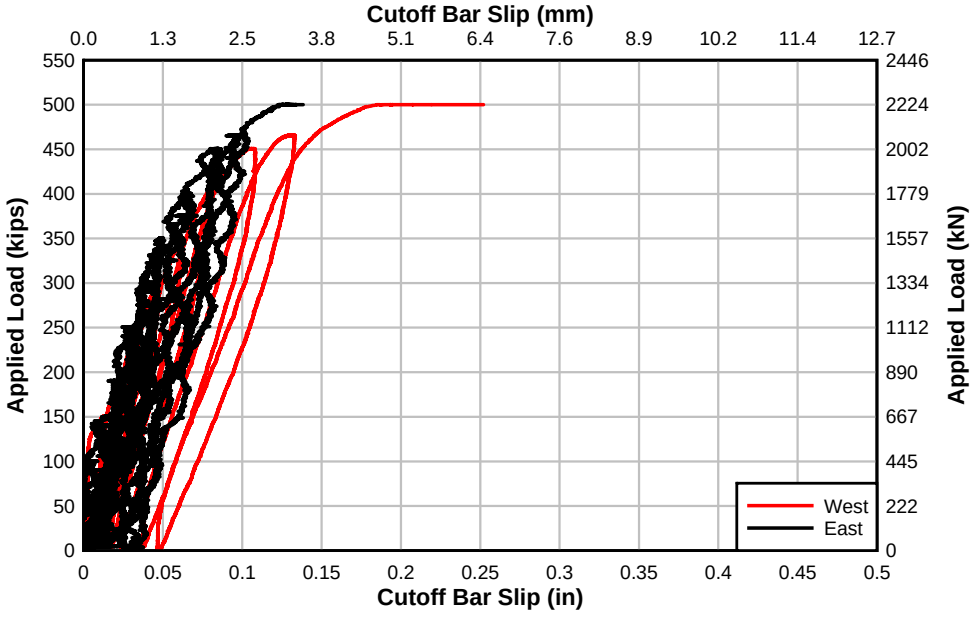


Figure 4.12 – Specimen IT.45.Ld3(6).SS load-cutoff bar slip response

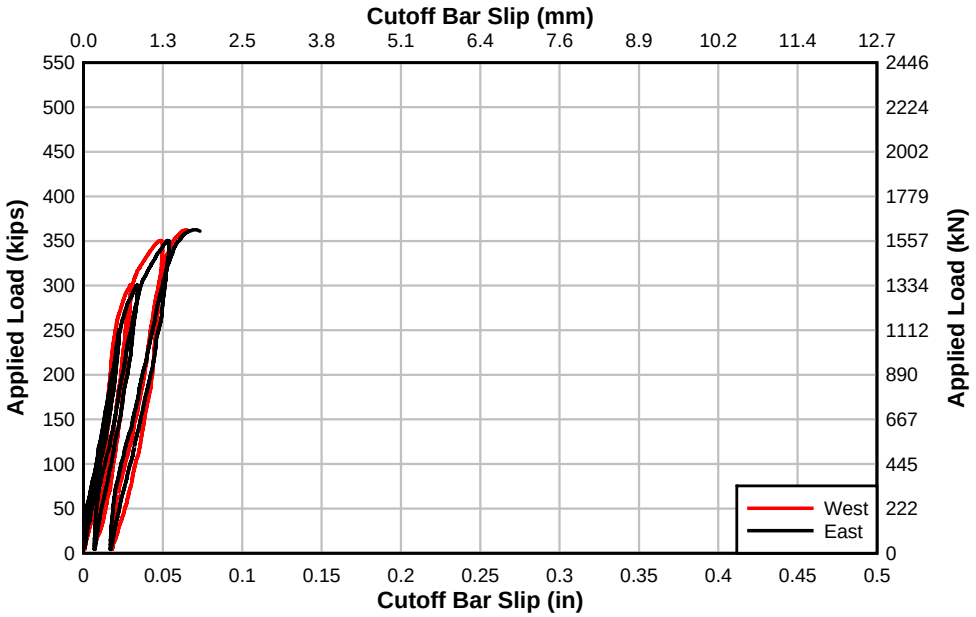


Figure 4.13 – SPR IT.45.Ld2(10).(5) load-cutoff bar slip response

Due to the sensor location, the cutoff bar slip measurement included movement due to cracks opening near the cutoff location. The horizontal crack elongation was estimated from the diagonal sensor displacements. To account for the number of effective cracks, a ratio of the number of cracks propagating before the slip sensor to the total number of cracks that cross the diagonal sensor was used. The effects of the horizontal crack elongation are compared to the cutoff bar slip in Figure 4.14 to Figure 4.16.

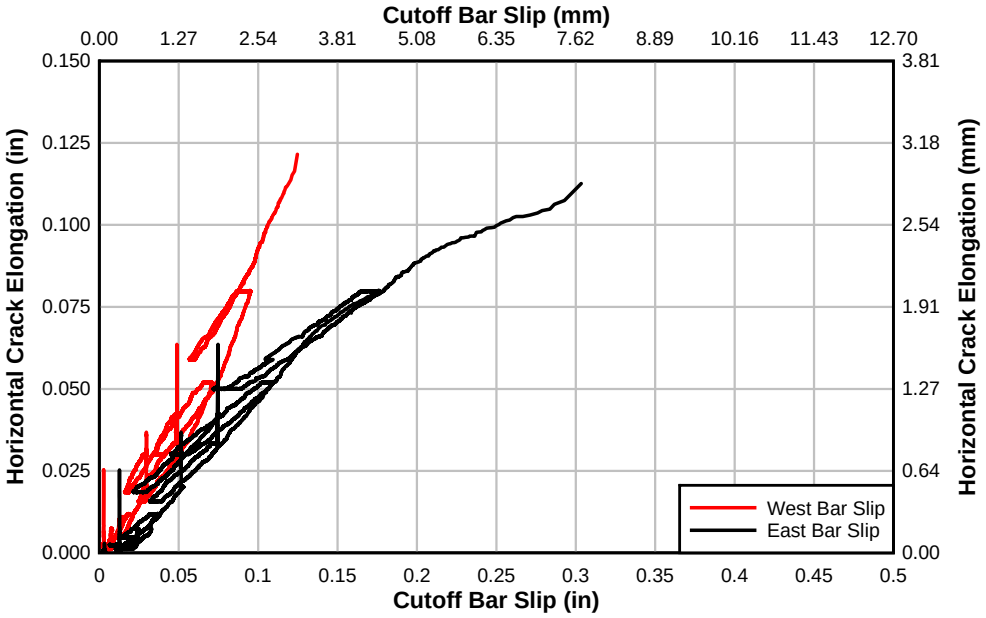


Figure 4.14 – Specimen IT.45.Ld3(10).Ti horizontal crack elongation-cutoff bar slip

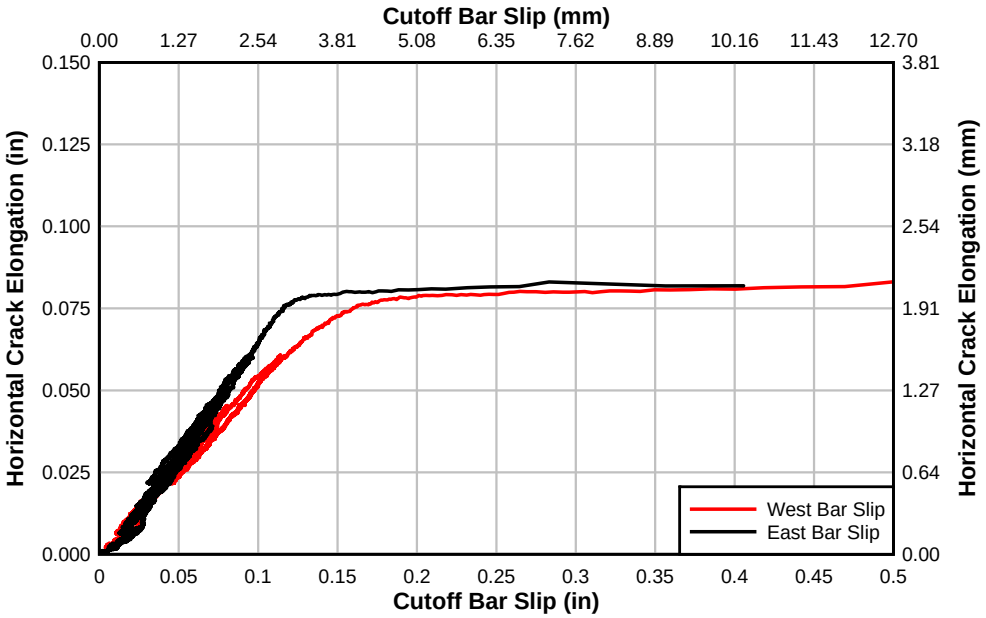


Figure 4.15 – Specimen IT.45.Ld3(6).Ti horizontal crack elongation-cutoff bar slip

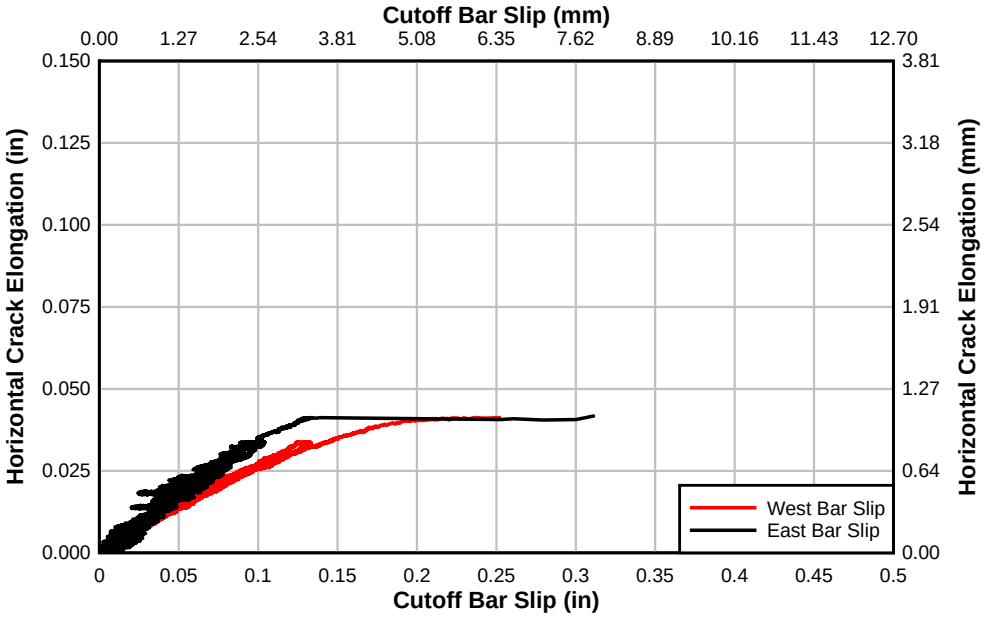


Figure 4.16 – Specimen IT.45.Ld3(6).SS horizontal crack elongation-cutoff bar slip

The most critical location in these specimens was the area from the cutoff bar to the preformed crack. Critical instrumentation on the cutoff bar was located along the 20.4 in. (516 mm), (1/3 development length) past the preformed diagonal crack. The strain gages were 20.4, 13.4, and 6.4 in. (518, 340, and 163 mm) from the end of the cutoff bar and were labeled as cutoff 4, 5, and 6, respectively. Cutoff 4 was located at the preformed crack intersection. The strain-slip response is shown in Figure 4.17 to Figure 4.19 for each of the specimens with preformed diagonal cracks. The response curves are labeled “initial slip” at points where the strain reversed due to slip in the cutoff bar. The strain reversals were caused by the lowered bond between the reinforcing bar and the surrounding concrete as the cutoff bar slipped.

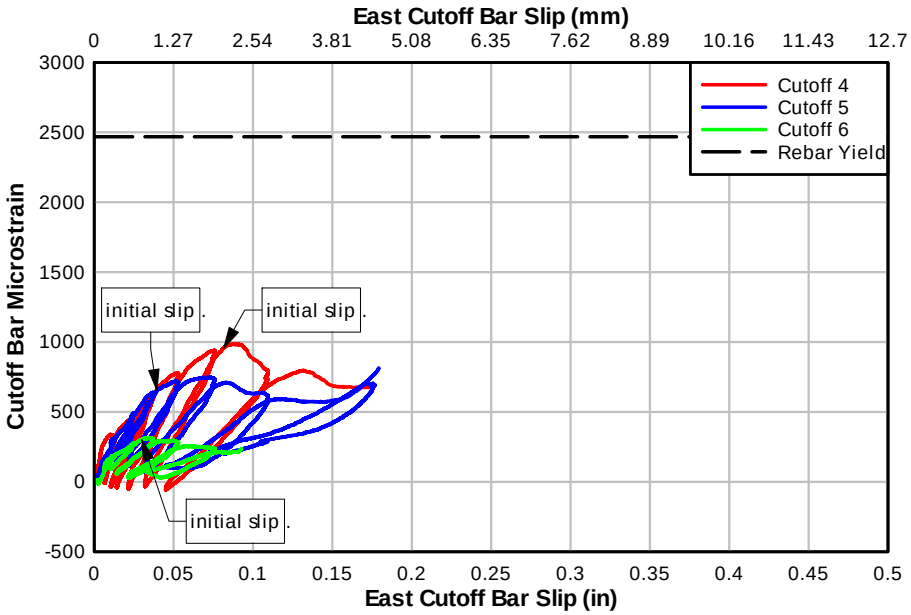


Figure 4.17 – Specimen IT.45.Ld3(10).Ti cutoff bar strain-slip

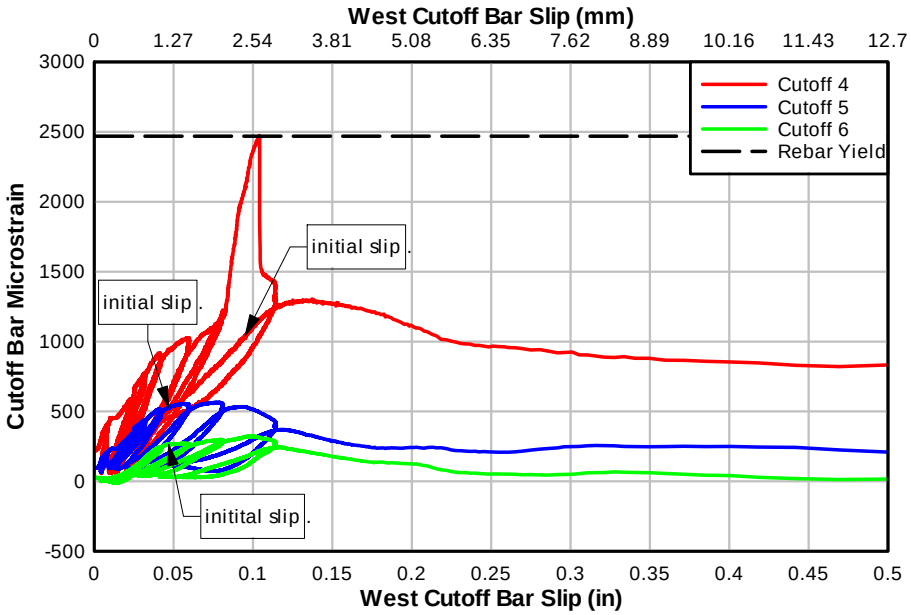


Figure 4.18 – Specimen IT.45.Ld3(6).Ti cutoff bar strain-slip

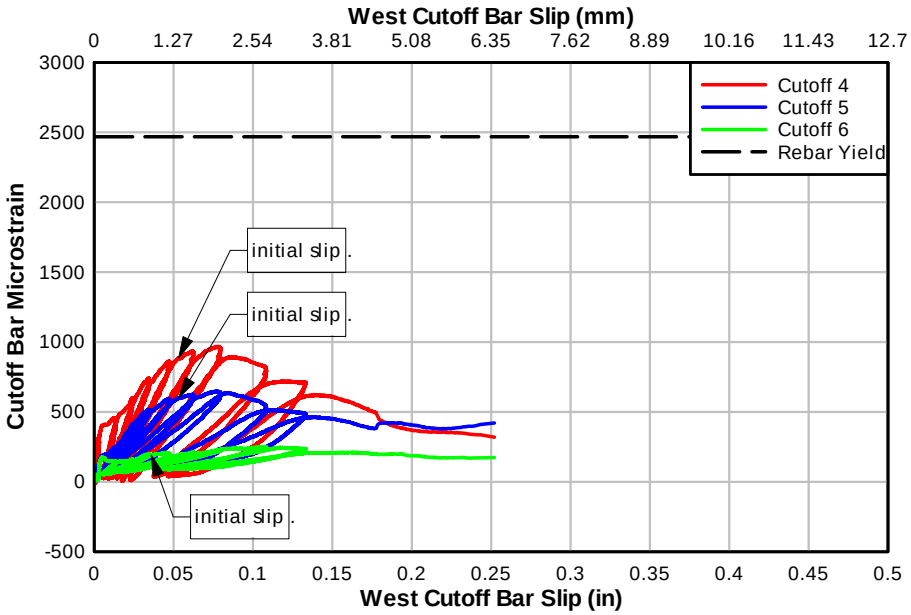


Figure 4.19 – Specimen IT.45.Ld3(6).SS cutoff bar strain-slip

### 4.1.2. Material Strains

Strain gages placed on the internal steel and NSM reinforcing measured the strains throughout each test. Comparing the reinforcing steel and NSM bar strains along the beam length at instrumented cross-sections shows the strain distributions and changes as the load amplitude increased.

#### *4.1.2.1. Comparative Material Strains*

The strains in the cutoff reinforcing steel bar, anchored reinforcing steel bar, and NSM bars were compared for each specimen. The strains for specimens IT.45.Ld3(10).Ti, IT.45.Ld3(6).Ti, and IT.45.Ld3(6).SS were similar. Examples from specimen

IT.45.Ld3(6).Ti are shown from Figure 4.20 to Figure 4.22 to illustrate the typical specimen response. The comparative strains for the other specimens are shown in Appendix A.

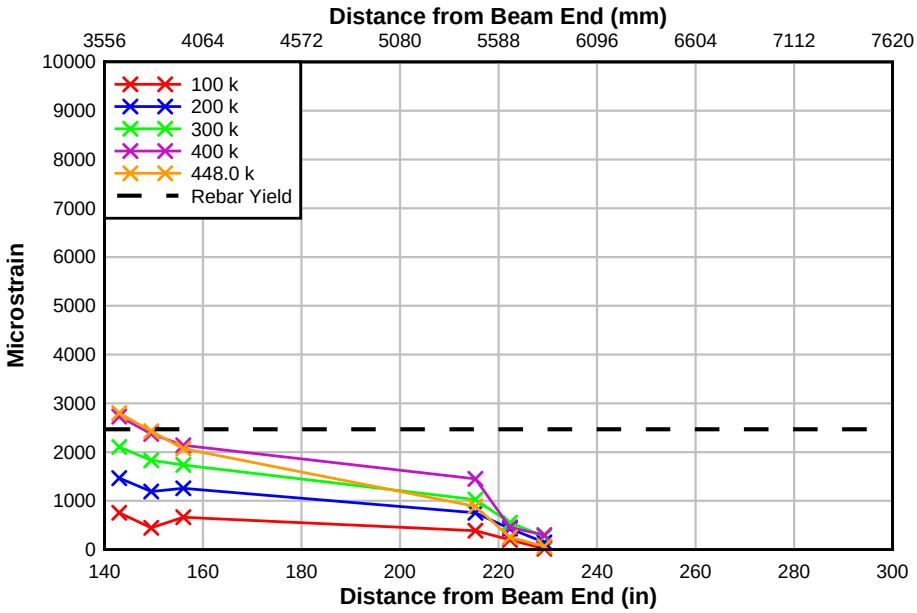


Figure 4.20 – Specimen IT.45.Ld3(6).Ti cutoff reinforcing steel bar strain along specimen length

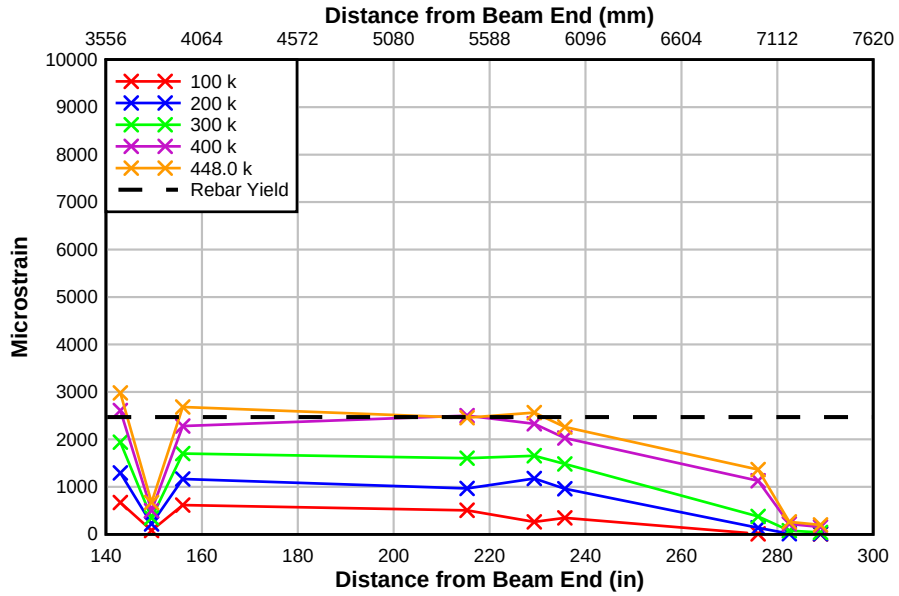


Figure 4.21 – Specimen IT.45.Ld3(6).Ti anchored reinforcing steel bar strain along specimen length

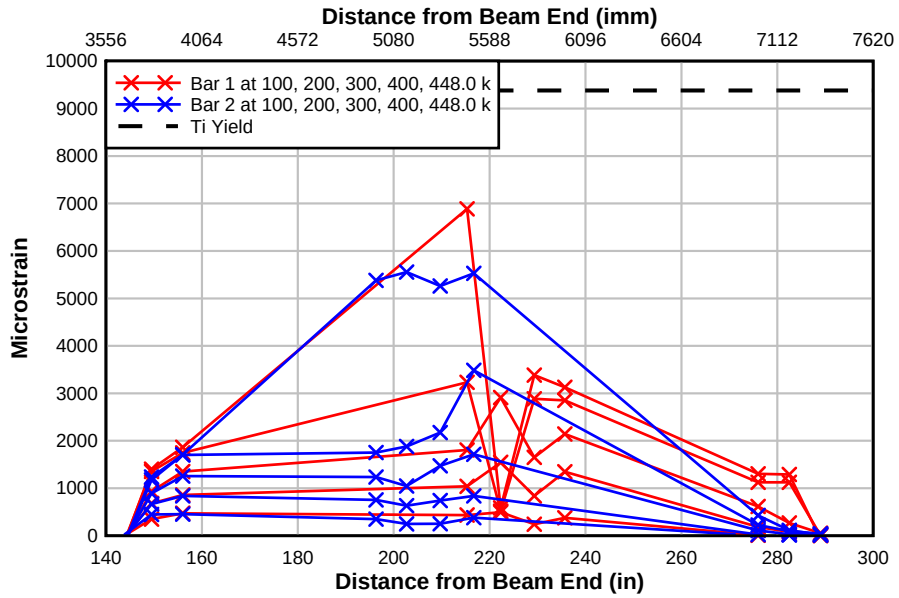


Figure 4.22 – Specimen IT.45.Ld3(6).Ti NSM titanium bar strain along specimen length

*4.1.2.2. Sectional Strains*

Specific cross-sections on each specimen were instrumented to show the strain variations throughout the specimen as load was applied to failure. The specimens with preformed cracks had instrumented sections at each end of the NSM bar hooks and along the 1/3 development length of the cutoff reinforcing steel bars. The critical locations in these specimens were the sections from the end of the cutoff bar to the preformed crack. Representative critical location strains in these sections are shown for specimen IT.45.ld3(10).Ti from Figure 4.23 to Figure 4.26. These strains were taken from the preformed crack (Section 4) to the end of the cutoff bar (Section 7). Specimen IT.0.0(6).Ti had sections by each of the hook ends, along the cut bar development length in both directions from the cutoff location, and at the center of the beam. Sectional strains for this specimen are shown from the center of the beam to the point where the cutoff bars were developed (Sections 6 to 9) from Figure 4.27 to Figure 4.30.

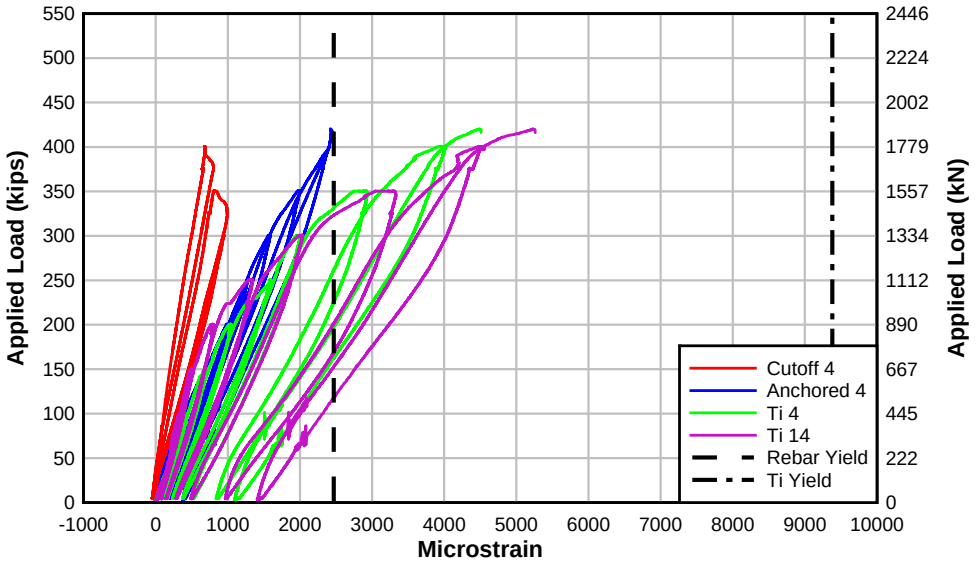


Figure 4.23 – Specimen IT.45.Ld3(10).Ti load-flexural bar strain (Section 4)

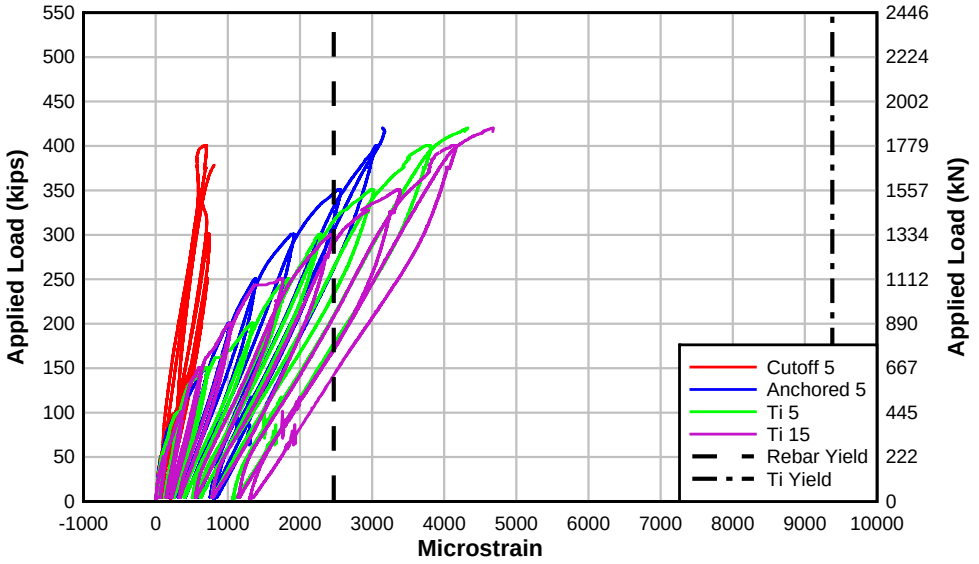


Figure 4.24 – Specimen IT.45.Ld3(10).Ti load-flexural bar strain (Section 5)

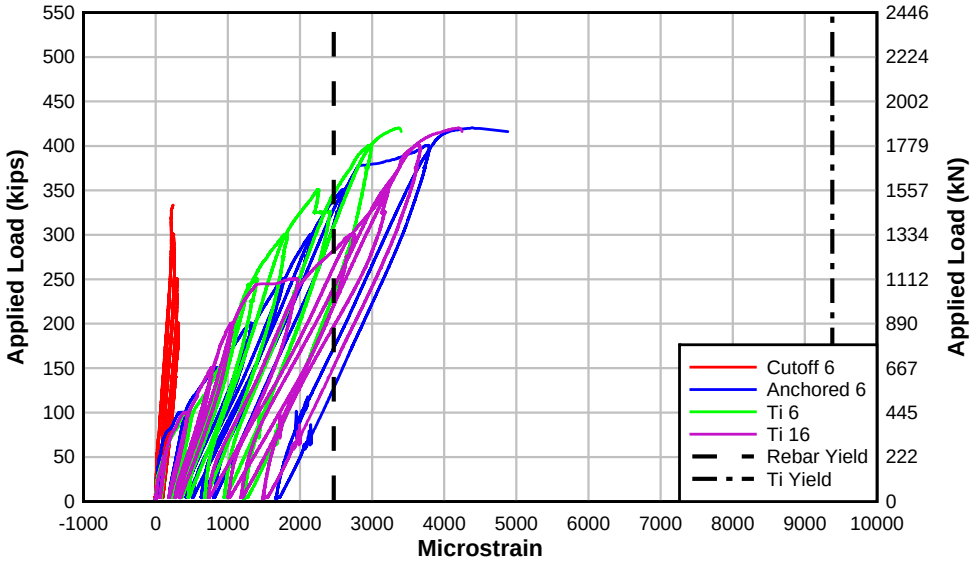


Figure 4.25 – Specimen IT.45.Ld3(10).Ti load-flexural bar strain (Section 6)

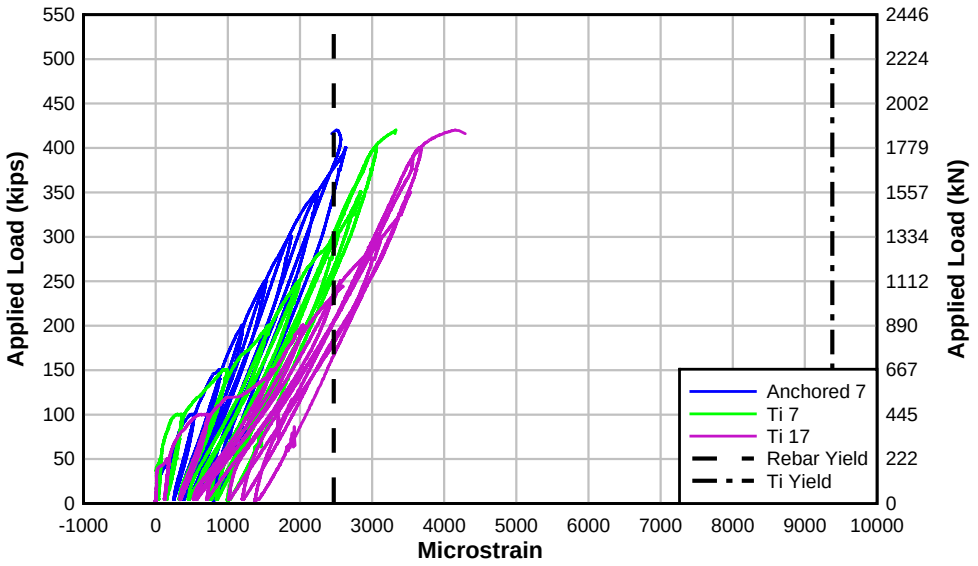


Figure 4.26 – Specimen IT.45.Ld3(10).Ti load-flexural bar strain (Section 7)

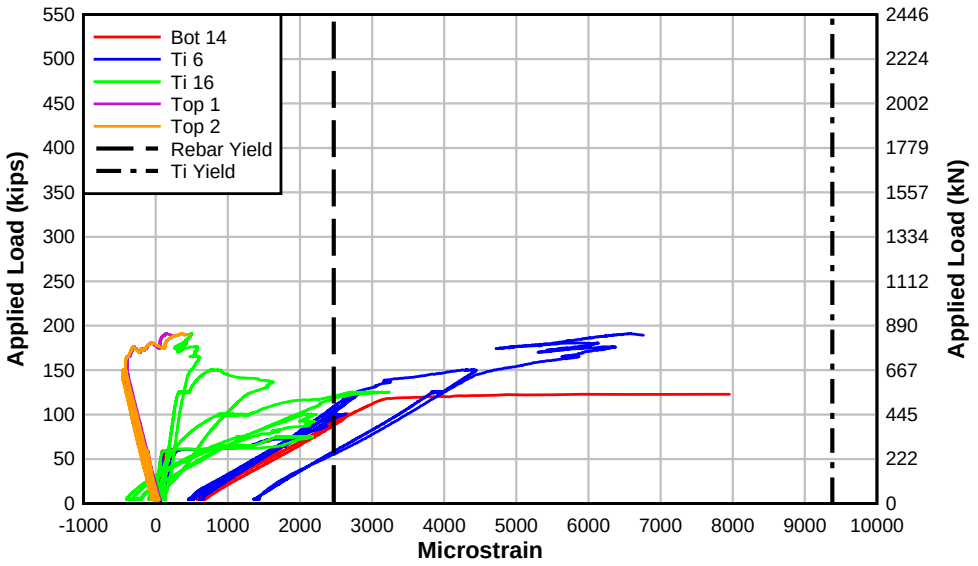


Figure 4.27 – Specimen IT.0.0(6).Ti load- flexural bar strain (Section 6)

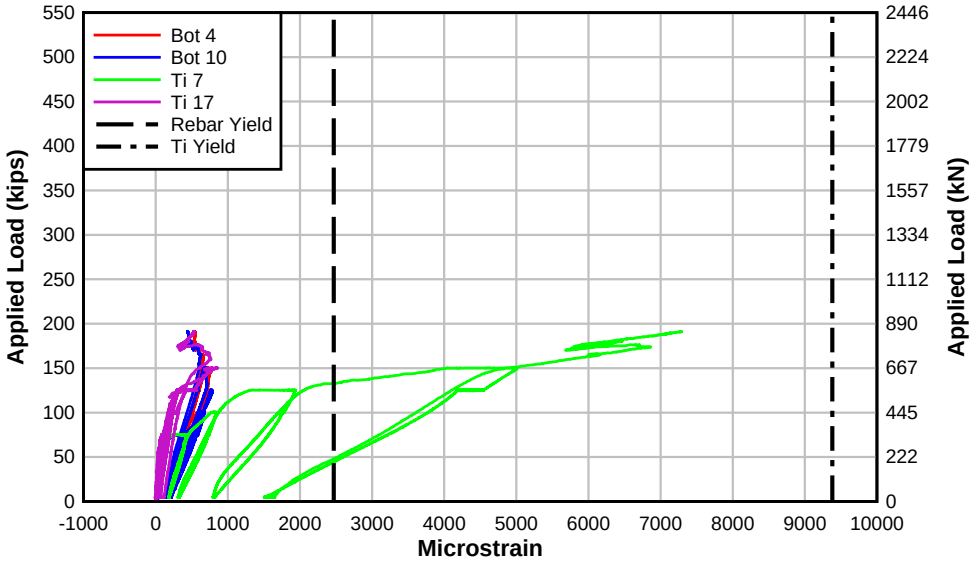


Figure 4.28 – Specimen IT.0.0(6).Ti load- flexural bar strain (Section 7)

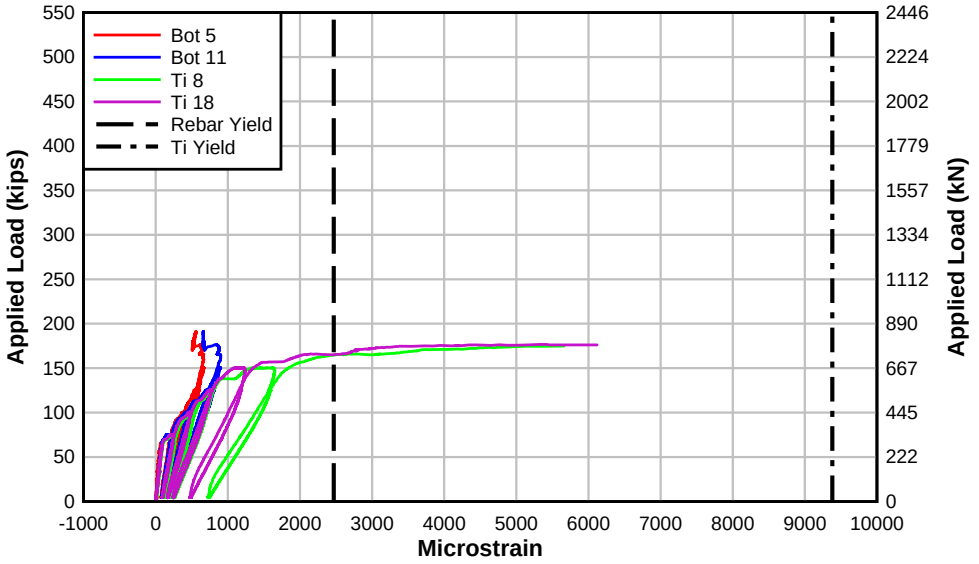


Figure 4.29 – Specimen IT.0.0(6).Ti load- flexural bar strain (Section 8)

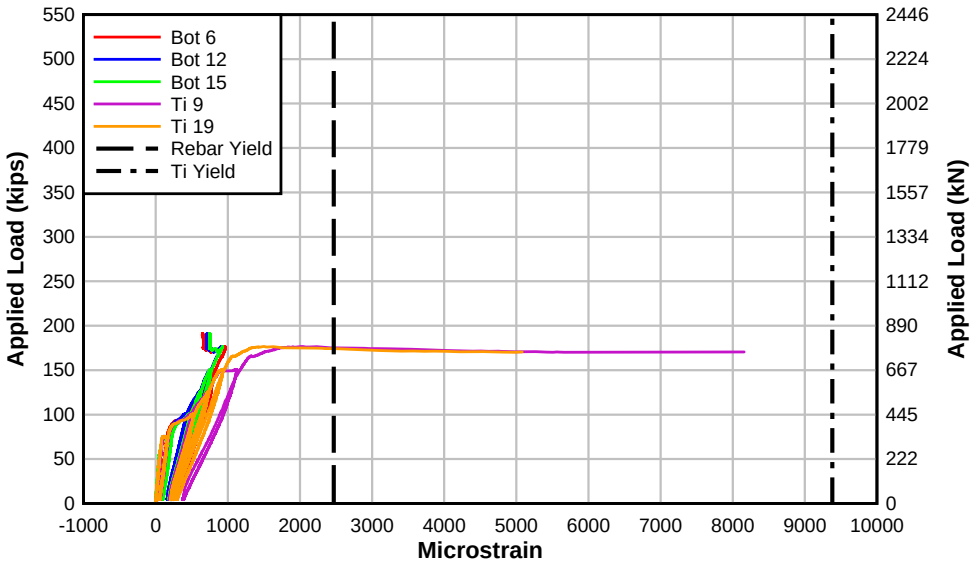


Figure 4.30 – Specimen IT.0.0(6).Ti load- flexural bar strain (Section 9)

4.1.3. Tensile Forces

Using the measured strains during each test, the tension force, $T$, in the reinforcement at a given cross-section was calculated as:

$$T = \varepsilon EA \qquad [4.1]$$

where $\varepsilon$ is the measured strain, $E$ is the modulus of elasticity of the reinforcement (ksi), and $A$ is the cross-sectional area of the reinforcing bar ($in^2$). Due to the sections containing both internal reinforcing steel and NSM bars, the total tension force for each section was determined from the sum of the individual reinforcing bar tension forces at the section. Tension forces are shown from Figure 4.31 to Figure 4.34 and were calculated at either 50 kip or 100 kip (222 kN or 445 kN) load intervals and at the failure load. The material strains were limited to their respective yield strains. The tensile force contributions from the internal steel reinforcement and the NSM bars are shown for each specimen at the failure load from Figure 4.35 to Figure 4.38. Due to a few strain gages that were compromised at higher loads, the tension forces at failure are not shown for specimens IT.45.Ld3(10).Ti and IT.0.0(6).Ti. Instead, the tension forces at the closest load increment prior to strain gage failures are shown.

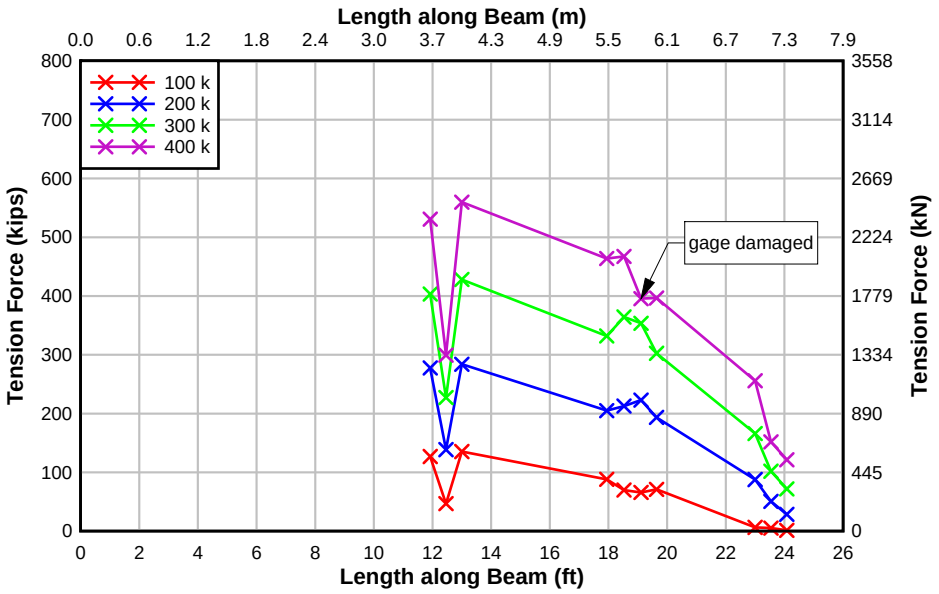


Figure 4.31 – Specimen IT.45.Ld3(10).Ti tension force in all flexural tension reinforcement along beam

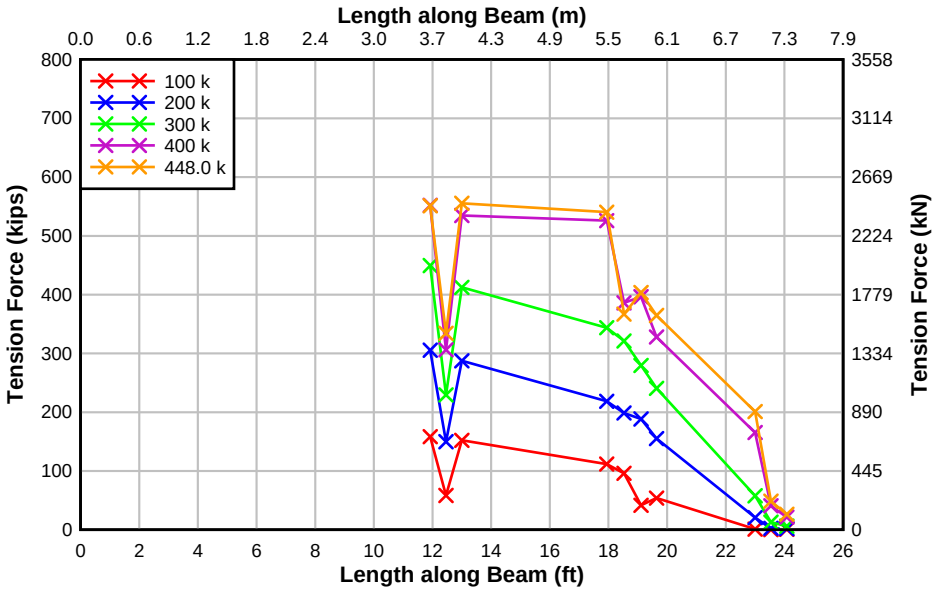


Figure 4.32 – Specimen IT.45.Ld3(6).Ti tension force in all flexural tension reinforcement along beam

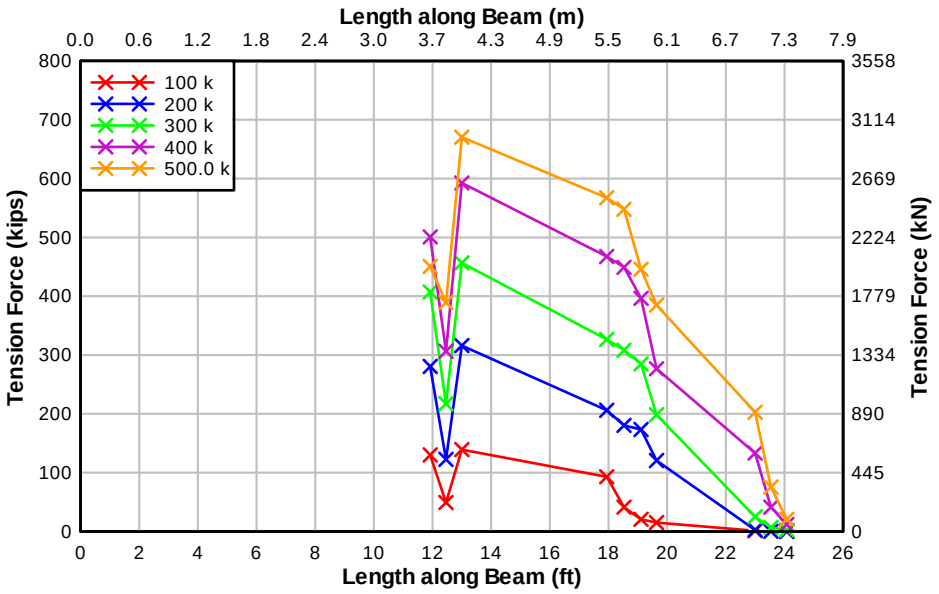


Figure 4.33 – Specimen IT.45.Ld3(6).SS tension force in all flexural tension reinforcement along beam

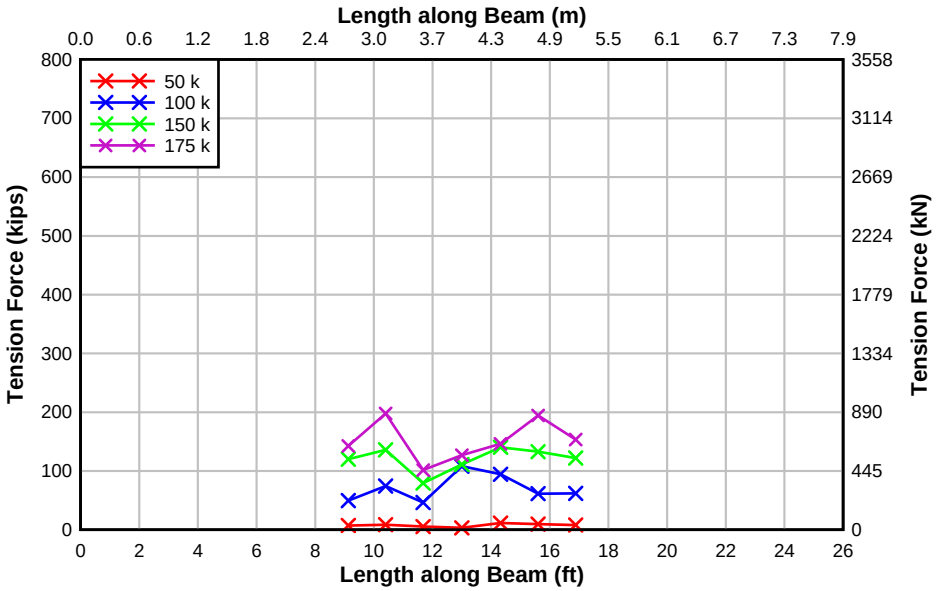


Figure 4.34 – Specimen IT.0.0(6).Ti tension force in all flexural tension reinforcement along beam

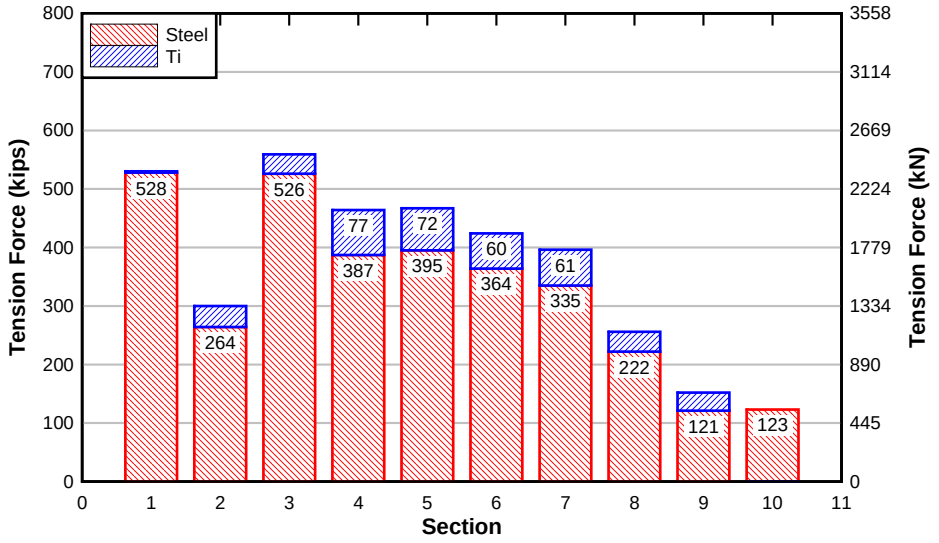


Figure 4.35 – Specimen IT.45.Ld3(10).Ti tension force contribution-section at 400 kips (1780 kN)

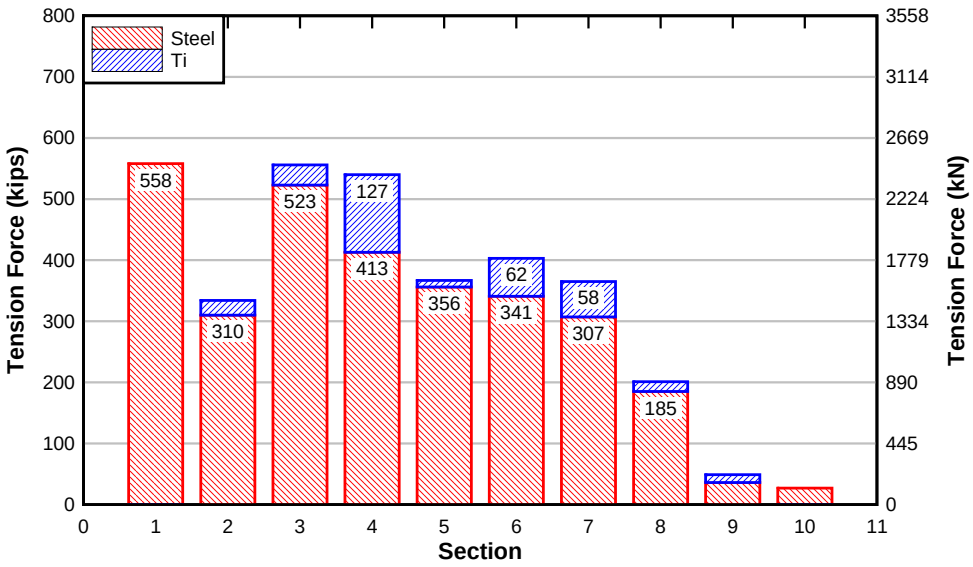


Figure 4.36 – Specimen IT.45.Ld3(6).Ti tension force contribution-section at failure

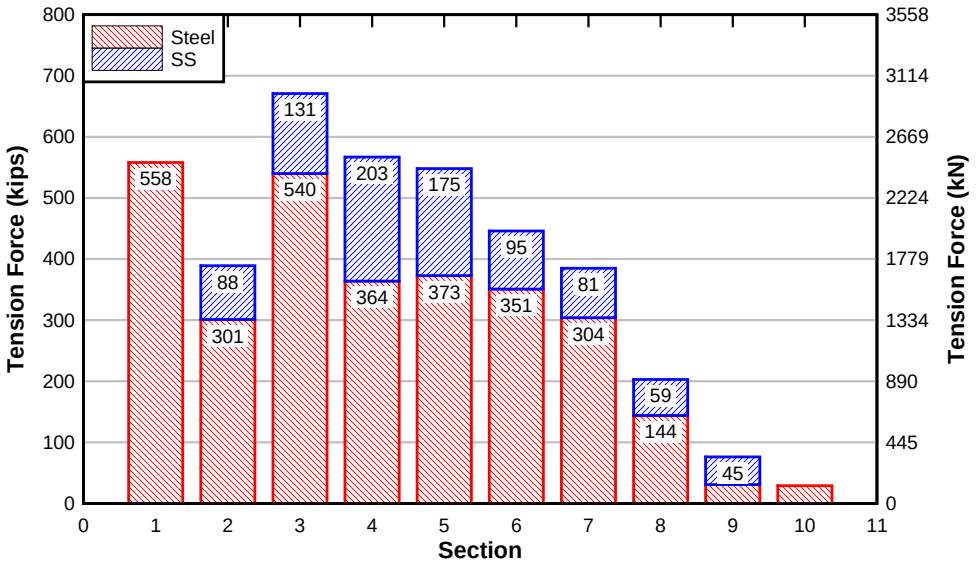


Figure 4.37 – Specimen IT.45.Ld3(6).SS tension force contribution-section at failure

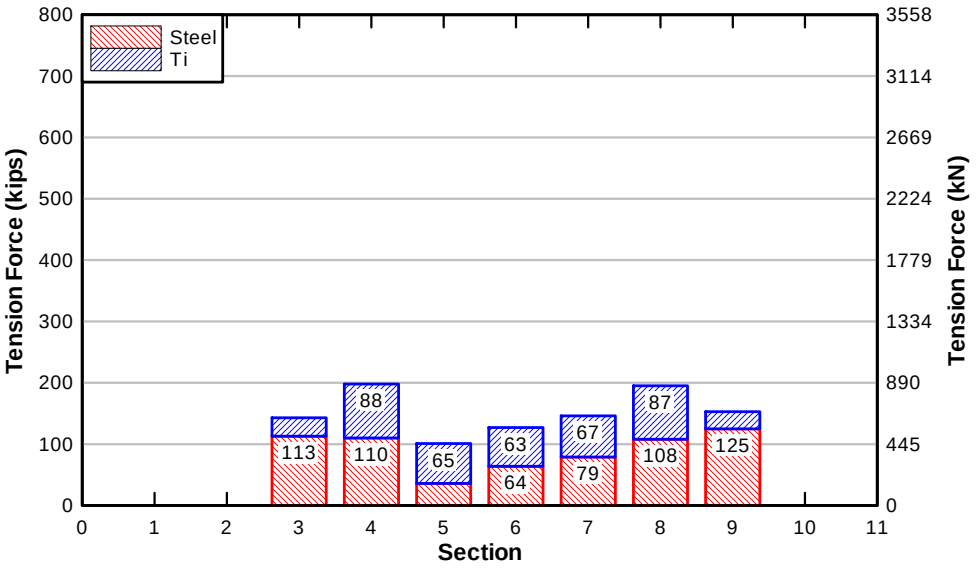


Figure 4.38 – Specimen IT.0.0(6).Ti tension force contribution-section at 175 kips (778 kN)

### 4.1.4. Bond Stresses

The average bond stress, $\mu_{avg}$, over an incremental length of reinforcement was calculated as:

$$\mu_{avg} = \frac{\Delta f_s d_b}{4\Delta l} \quad [4.2]$$

Bond stresses at failure were estimated for the applicable cutoff reinforcing steel bars, fully anchored reinforcing steel bars, and NSM bars. The average bond stress, $\overline{\mu}_{avg}$, for the cutoff reinforcing steel bars, the fully anchored reinforcing steel bars, and the NSM bars was taken as the average of the incremental bond stress measurements along the section. The peak bond stress $\mu_{max}$, of any bar was taken as the maximum incremental average bond stress along the section.

#### *4.1.4.1. Critical Location Bond Stresses*

For specimens IT.45.Ld3(10).Ti, IT.45.Ld3(6).Ti, and IT.45.Ld3(6).SS, the critical section bond stresses were located between the preformed crack and the end of the cutoff bar. For specimen IT.0.0(6).Ti, the critical section bond stresses were determined from the midspan cutoff point along the development length of the steel. The average and peak bond stresses at failure are listed in Table 11 for each of the instrumented bars. Table 12 shows the values for the SPR specimens that were instrumented around the preformed crack.

Table 11 – Summary of bond stresses at critical section

| Specimen | Cutoff Bar | | Anchored Bar | | NSM Bars | | |
|---|---|---|---|---|---|---|---|
| | $\overline{\mu}_{avg}$ psi (MPa) | $\mu_{max}$ psi (MPa) | $\overline{\mu}_{avg}$ psi (MPa) | $\mu_{max}$ psi (MPa) | Bar | $\overline{\mu}_{avg}$ psi (MPa) | $\mu_{max}$ psi (MPa) |
| IT.45.Ld3(10).Ti | 466* (3.21) | 735 (5.07) | 24 (0.17) | 73 (0.51) | 1 | 132 (0.91) | 326 (2.25) |
| | | | | | 2 | 123 (0.83) | 188 (1.30) |
| IT.45.Ld3(6).Ti | 424 (2.92) | 898 (6.19) | 164 (1.13) | 324 (2.23) | 1 | 1097 (7.56) | 2254 (15.5) |
| | | | | | 2 | n/a n/a | n/a n/a |
| IT.45.Ld3(6).SS | 263 (1.81) | 362 (2.50) | 122 (0.84) | 365 (2.52) | 1 | 304 (2.10) | 488 (3.36) |
| | | | | | 2 | 504 (3.47) | 1478 (10.2) |
| IT.0.0(6).Ti | Cutoff Bar 1 | | Cutoff Bar 2 | | 1 | 165* (1.14) | 421* (2.90) |
| | 158 (1.09) | 415 (2.86) | 156 (1.08) | 416 (2.87) | | | |
| | | | | | 2 | 326* (2.25) | 648* (4.47) |

*taken at lower load because of strain gages were lost prior to failure

Table 12 – SPR summary of bond stresses around critical location

| Specimen | Cutoff Bar | | Anchored Bar |
|---|---|---|---|
| | $\overline{\mu}_{avg}$ psi (MPa) | $\mu_{max}$ psi (MPa) | $\overline{\mu}_{avg}$ psi (MPa) |
| SPR IT.45.Ld2(10).(5) | 648 (4.47) | 2165 (14.93) | 396 (2.73) |
| SPR IT.45.Ld2(10).(6) | 405 (2.79) | 977 (6.74) | 345 (2.38) |

The bond stresses in the retrofitted IT.45.Ld3(10).Ti specimen were much lower than both of the SPR specimens. The participation of the NMS titanium bars helped reduce the bond stress in the cutoff and the anchored bars.

#### *4.1.4.2. Hook Location Bond Stresses*

Average bond stresses were calculated around the locations of the NSM material hooks. The average and peak bond stresses at failure are listed in Table 13 for each of the bars instrumented these locations.

Table 13 – Summary of bond stresses at NSM bar hook locations

| Specimen | Cutoff Bar | | Anchored Bar | | NSM Bars | | |
|---|---|---|---|---|---|---|---|
| | $\overline{\mu}_{avg}$ psi (MPa) | $\mu_{max}$ psi (MPa) | $\overline{\mu}_{avg}$ psi (MPa) | $\mu_{max}$ psi (MPa) | Bar | $\overline{\mu}_{avg}$ psi (MPa) | $\mu_{max}$ psi (MPa) |
| IT.45.Ld3(10).Ti | 81 (0.56) | 138 (0.95) | 1887 (13.0) | 3078 (21.2) | 1 | 339 (2.34) | 678 (4.67) |
| | | | | | 2 | 399 (2.75) | 861 (5.94) |
| IT.45.Ld3(6).Ti | 412 (2.84) | 649 (4.47) | 1793 (12.4) | 2661 (18.3) | 1 | 345 (2.38) | 657 (4.53) |
| | | | | | 2 | 236 (1.63) | 566 (3.90) |
| IT.45.Ld3(6).SS | 164 (1.13) | 327 (2.25) | 1780 (12.3) | 2892 (19.9) | 1 | 834 (5.75) | 2050 (14.1) |
| | | | | | 2 | 748 (5.16) | 1516 (10.5) |
| IT.0.0(6).Ti | - | - | - | - | 1 | 82* (0.57) | 160* (1.10) |

* taken at lower load because of strain gages were lost prior to failure

## 4.2. Titanium Bond and Hook Toughness Results

### 4.2.1. Pullout Tests

Tensile tests were performed on five different titanium surface treatments to assess the role of the surface treatment on the material properties. The measured applied stress-strain curves are shown in Figure 4.39 below. The titanium alloy bars did not have a well-defined yield plateau and the 0.2% offset was used to determine the yield values. The yield stress and ultimate stress values for each titanium surface treatment are summarized in Table 14. The material properties were similar for all five different surface treatments.

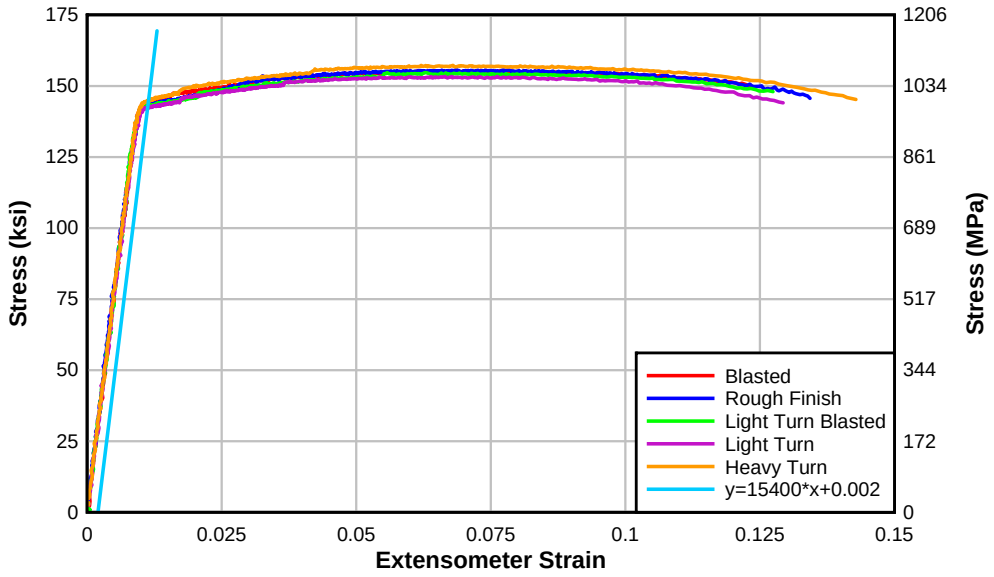


Figure 4.39 – Titanium surface treatment stress-strain curves

Table 14 – Titanium surface roughness tensile testing summary

| Surface Finish | 0.2% Offset Yield Stress ksi (MPa) | Ultimate Stress ksi (MPa) |
|---|---|---|
| Blasted | 144.5 (996) | 155.5 (1072) |
| Rough Finish | 143.8 (991) | 155.6 (1073) |
| Blasted Light Turn | 143.2 (987) | 154.7 (1067) |
| Light Turn | 142.4 (982) | 153.4 (1058) |
| Heavy Turn | 144.6 (997) | 157.2 (1084) |

Pullout tests were also performed on the five surface treatments, on four bulb end samples, and on three additional heavy turn bars. These tests were used to assess relative differences in the bond along the bars. From the applied loads, average bond stresses were calculated using Eqn. 4.2. Average bond stresses versus pullout displacement are shown from Figure 4.40 to Figure 4.42.

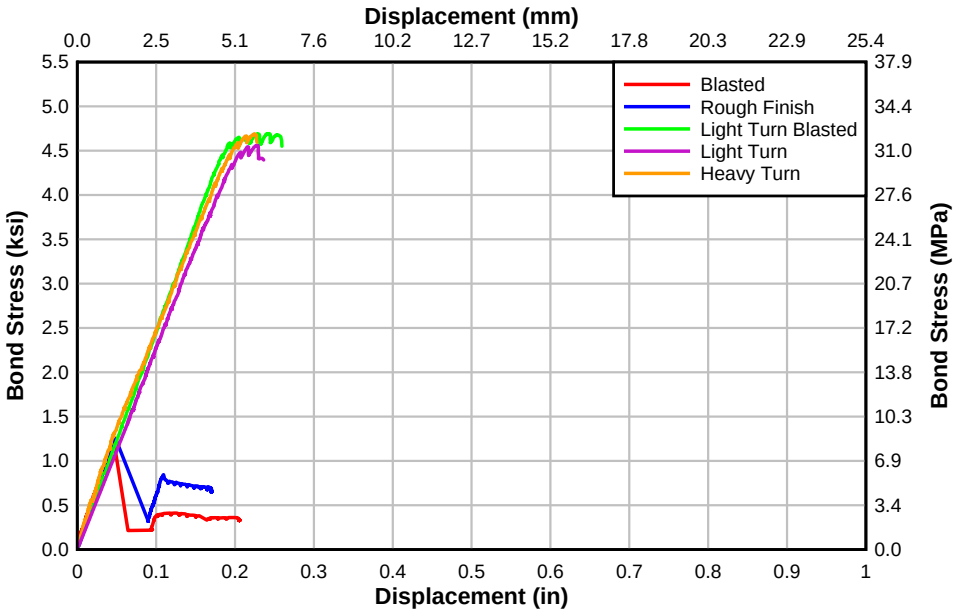


Figure 4.40 – Titanium surface treatment bond stress summary

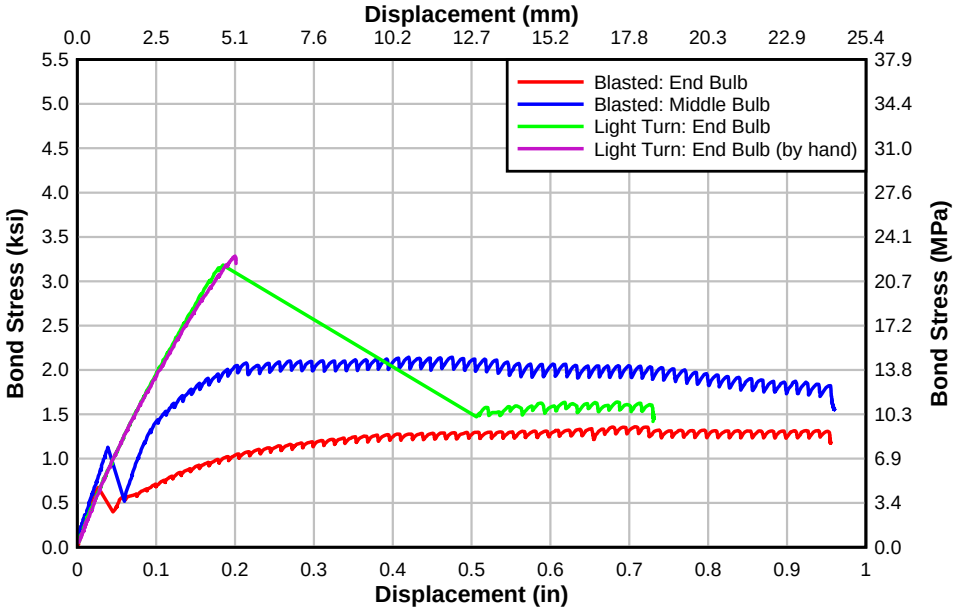


Figure 4.41 – Bulb end bond stress summary

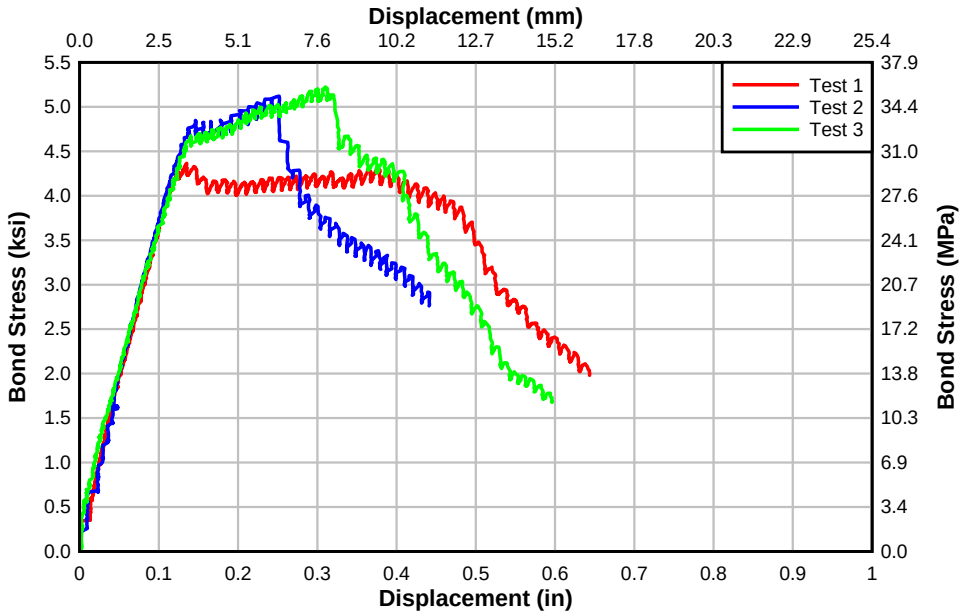


Figure 4.42 – Heavy turn bond stress results

Because of the short bond length, the bars failed along the epoxy-titanium interface. Once the bars lost chemical adhesion to the epoxy or sheared the epoxy interface, additional loading dragged the bars through the epoxy and friction controlled the behavior. In the surface roughness tests, compared to the bars with turns, the blasted and rough finish bars exhibited lower average bond stress before slipping through the epoxy. The bulb end specimens showed similar results between the light turn and the blasted finishes. None of the bulb end specimens were able to achieve bond stresses in the range of the turned bars. Based on the tensile and pullout test results, the heavy turn titanium alloy bars were selected as the NSM titanium material for retrofitting the full-scale specimens.

4.2.2. Hook Toughness Tests

The titanium alloy bars used for the hook toughness testing came from a different material heat than the titanium alloy bars used for the full-scale girder tests and the tensile and pullout tests described previously. Thus, tensile tests were performed for the titanium alloy bars used in the hook tests and the results are shown in Figure 4.43. The yield stresses were found using the 0.2% offset method. Average of three tests resulted in a yield stress of 144.7 ksi (998 MPa), an ultimate stress of 157.2 ksi (1084 MPa), and an ultimate elongation of 14%. The yield and elongation properties are nearly identical to the titanium used in the full-scale retrofits.

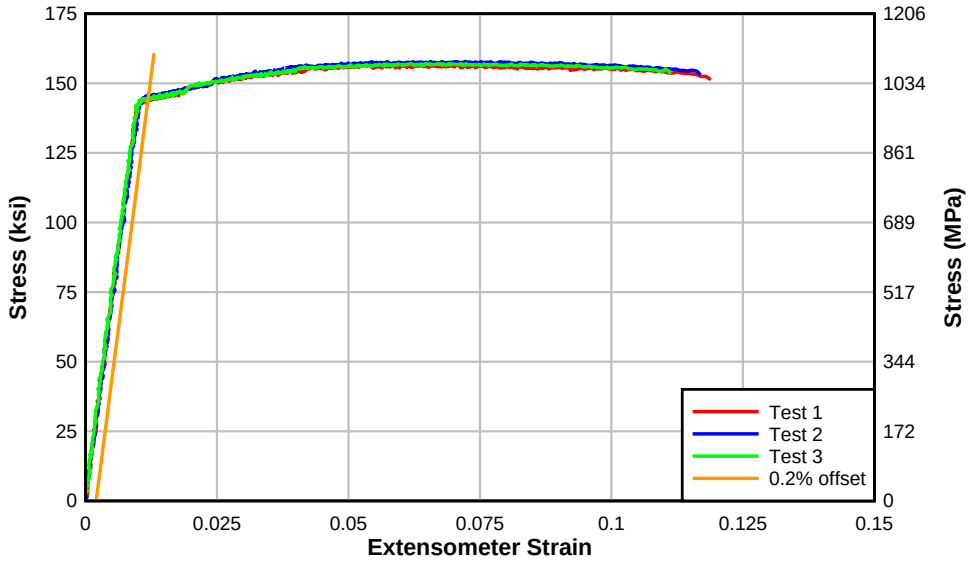


Figure 4.43 – Stress-strain curves for hook test titanium alloy bars

The tests were performed using the setup shown in Figure 3.38. To ensure repeatability of the hook tests, the distance, *e*, from the bearing plates to the outside of the hook as shown in Figure 4.44 was established as:

$$e = 2 + \left( \frac{Ø - 2}{2} \right) \quad [4.3]$$

where $Ø$ is the inside hook diameter (in.).

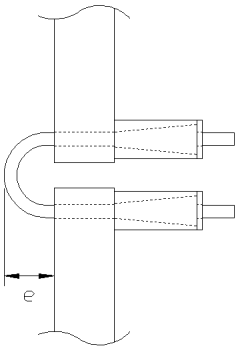


Figure 4.44 – Distance from outside of hook to bearing plate

A specimen in the setup is shown in Figure 4.45. The UTM pulled the hooks at the specified rate until fracture of the hook occurred. The first two samples of each group of three were tested without any modifications. Of these, each of the 2 in. (51 mm) hooks fractured in the center of the 180˚ bend and the 3 in. (76 mm) and 5 in. (127 mm) hooks fractured at the top or bottom bearing point location just outside the plate fixture.

Figure 4.45 – Sample 180˚ hook in test setup

For each of the hooks bent at 900 ˚F (482 ˚C), the third specimen was modified before testing. On these specimens, the deformations were removed by grinding at the previously observed fracture locations to remove the stress concentration associated with the deformations. The modified hooks were then tested and the 2 in. (51 mm) hook fractured at the bearing plate location, the 3 in. (76 mm) hook fractured at the center of the 180˚ bend, and the 5 in. (127 mm) hook fractured at the bearing point location, but the overall load and displacement were greatly increased. For the third test of the 2 in. (51 mm) and 3 in. (76 mm) hooks, the horizontal hook displacement was measured using a laser extensometer to visit the geometry change during the test.

The first test of the 2 in. (51 mm) hooks bent at 1250 ˚F (677 ˚C) had a large load of approximately 0.6 kips applied accidentally prior to the test. This accounts for the large difference in the slope for the specimen. The displacement results for each set of tests are summarized from Figure 4.46 to Figure 4.49. A summary of the test results is shown in Table 15.

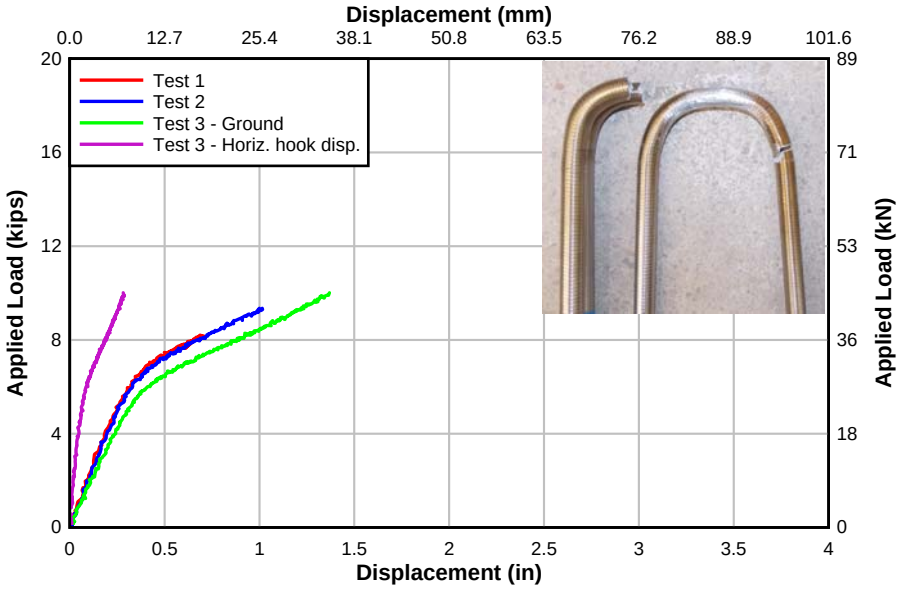


Figure 4.46 – 2 in. (51 mm) hooks bent at 900 ˚F (482 ˚C)

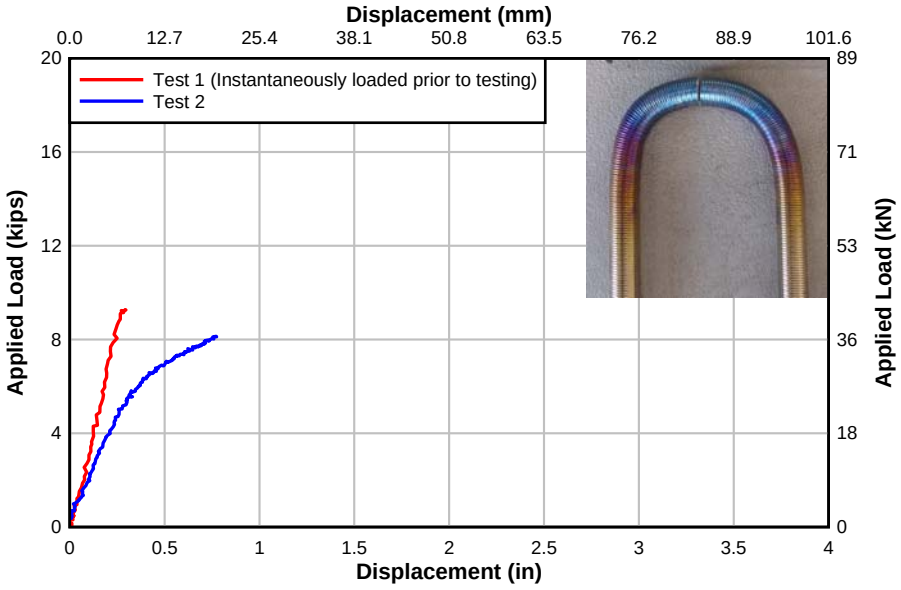


Figure 4.47 – 2 in. (51 mm) hooks bent at 1250 ˚F (677 ˚C)

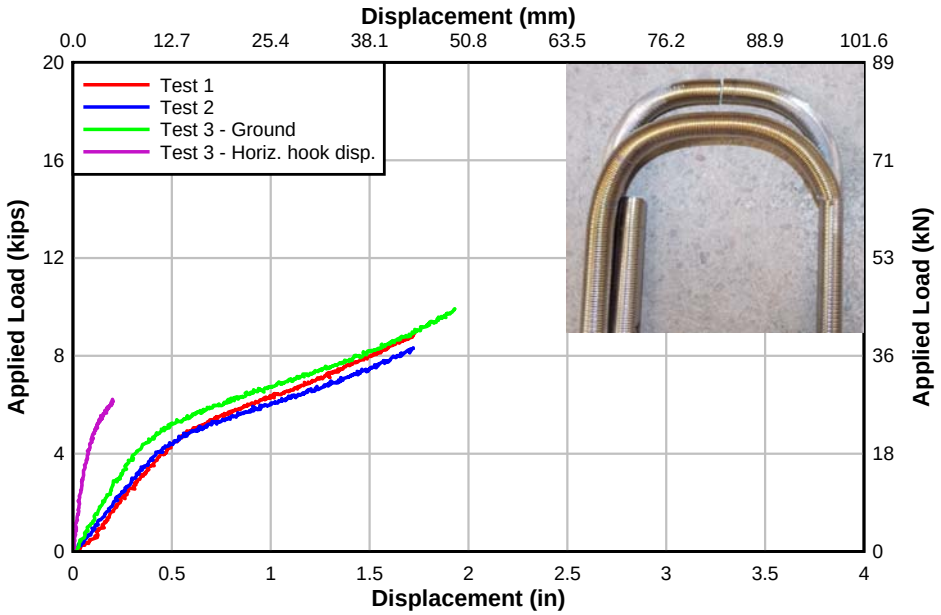


Figure 4.48 – 3 in. (76 mm) hooks bent at 900 ˚F (482 ˚C)

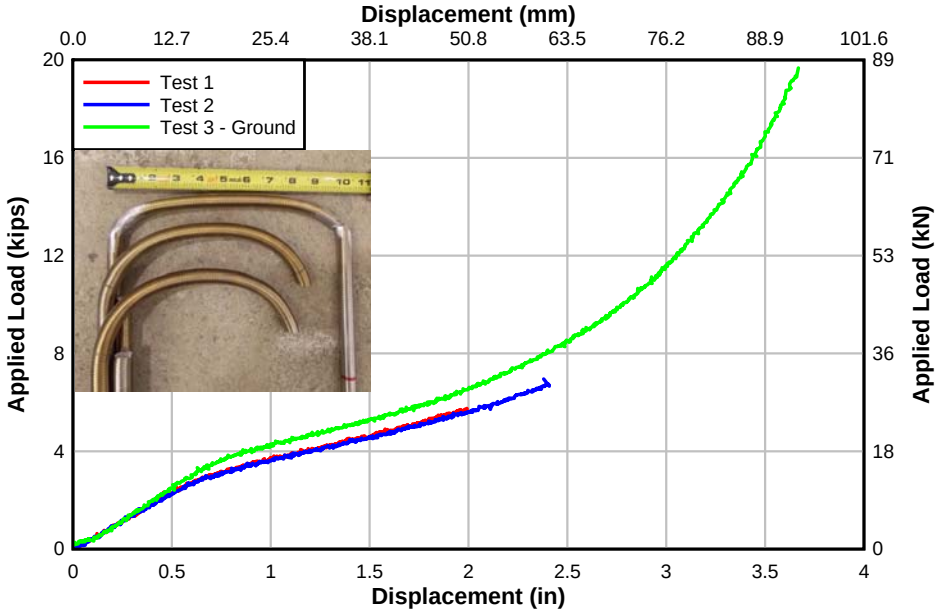


Figure 4.49 – 5 in. (127 mm) hooks bent at 900 ˚F (482 ˚C)

Table 15 – Summary of 180˚ hook tests

| Specimen | Test | $P_{max}$ kips (kN) | Max Disp. in. (mm) | Failure Location |
|---|---|---|---|---|
| 2 in. (51 mm) 900 ˚F (482 ˚C) | 1 | 8.20 (36.5) | 0.69 (17.5) | hook center |
| | 2 | 9.35 (41.6) | 1.10 (28.0) | hook center |
| | 3 | 10.0 (44.5) | 1.37 (34.8) | bearing point |
| 2 in. (51 mm) 1250 ˚F (677 ˚C) | 1 | 9.28 (41.3) | 0.292 (7.4) | hook center |
| | 2 | 8.14 (36.2) | 0.772 (18.3) | hook center |
| 3 in. (76 mm) 900 ˚F (482 ˚C) | 1 | 8.95 (39.8) | 1.73 (43.9) | bearing point |
| | 2 | 8.33 (37.1) | 1.72 (43.7) | bearing point |
| | 3 | 9.92 (44.1) | 1.93 (49.0) | hook center |
| 5 in. (127 mm) 900 ˚F (482 ˚C) | 1 | 5.75 (25.6) | 1.99 (48.8) | bearing point |
| | 2 | 6.95 (30.9) | 2.38 (60.5) | bearing point |
| | 3 | 19.7 (87.5) | 3.67 (93.2) | bearing point |

The plastic moment capacity of the titanium alloy bars, $M_p$, was calculated as:

$$M_p = zf_y \qquad [4.5]$$

where $z$ is the plastic section modulus taken as $z = 1.33r^3$, with $r$ equal to the radius of the bar, and $f_y$ is the titanium alloy yield strength. The applied load necessary to achieve the plastic moment, $P_{plastic}$, was calculated using:

$$P_{plastic} = \frac{2M_p}{e} \qquad [4.6]$$

where $e$ is the distance from the bearing plate to the outside of the hook calculated using Eqn. [4.3]. Based on the test results, the maximum surface stress in the bar, $\sigma$, at failure was calculated as:

$$\sigma = \frac{P_{\max}}{A} + \left(\frac{P_{\max} e}{2}\right)\frac{1}{S} \qquad [4.6]$$

where $P_{max}$ is the maximum load achieved at failure, $A$ is the area of the bar, and $S$ is the section modulus of bar. The summary of these calculations are shown in Table 16.

Table 16 – Summary of eccentricities, plastic loads, and bar stresses

| Specimen | Test | $P_{max}$ kips (kN) | e in. (mm) | $P_{plastic}$ kips (kN) | Stress, σ ksi (MPa) |
|---|---|---|---|---|---|
| 2 in. (51 mm) 900 ˚F (482 ˚C) | 1 | 8.20 (36.5) | 2.0 (50.8) | 5.61 (25.0) | 386 (2661) |
| | 2 | 9.35 (41.6) | | | 430 (3034) |
| | 3 | 10.0 (44.5) | | | 471 (3247) |
| 2 in. (51 mm) 1250 ˚F (677 ˚C) | 1 | 9.28 (41.3) | 2.0 (50.8) | 5.61 (25.0) | 437 (3009) |
| | 2 | 8.14 (36.2) | | | 383 (2639) |
| 3 in. (76 mm) 900 ˚F (482 ˚C) | 1 | 8.95 (39.8) | 2.5 (63.5) | 4.49 (20.0) | 519 (3577) |
| | 2 | 8.33 (37.1) | | | 483 (3329) |
| | 3 | 9.92 (44.1) | | | 575 (3963) |
| 5 in. (127 mm) 900 ˚F (482 ˚C) | 1 | 5.75 (25.6) | 3.5 (88.9) | 3.21 (14.3) | 459 (3164) |
| | 2 | 6.95 (30.9) | | | 555 (3825) |
| | 3 | 19.7 (87.5) | | | 1570 (10824) |

Based on the results, the conclusions from the 180˚ hook tests include:

- The full tensile strength of the titanium alloy bars with the surface deformations could not be developed before fracture was observed for the bend radii investigated.
- Based on the horizontal hook measurements from the laser extensometer, there is a small change in geometry due to $\Delta e$ that can be neglected.
- All fractures (before grinding) occurred at approximately the same load, but were greater than the load required to produce the plastic bending moment capacity of the titanium alloy bars, and indicates that fracture occurs in the inelastic range.

- The inside bend at the point of inflection was plastic at failure for all the hooks as seen from the comparison of $P_{max}$ to $P_{plastic}$.
- Removing the surface deformations by grinding the bars at the initially observed fracture location changed the fracture location from the center of the hook bend to the bearing point or vice versa. Local removal of the deformations reduced the stress concentrations and increased the capacity before fracture.

# 5. ANALYTICAL METHODS

## 5.1. Comparative Analysis

Comparative analyses were performed of each specimen using predictions from AASHTO-LRFD, ACI 318-11, and Response 2000.

### 5.1.1. Design Specifications, Response 2000, and Experimental Results Comparisons

#### *5.1.1.1. Development Lengths*

The analyses were performed using the minimum development lengths based on the actual material properties used in the specimens. The straight and hooked bar development lengths are reported in Table 17 and Table 18. The computed development lengths for the actual materials were smaller than those used in design of the specimens based on expected material properties.

Table 17 – Comparison of specified minimum development length for straight bars

| **Specimen** | **$f_c$ psi (MPa)** | **$f_y$ psi (MPa)** | **AASHTO in. (mm)** | **ACI 318 in. (mm)** | |
|---|---|---|---|---|---|
| | | | | **Simplified** | **Complex** |
| IT.45.Ld3(10).Ti | 4056 (28.0) | 71.6 (494) | 69.3 (1760) | 79.3 (2014) | 59.4 (1509) |
| IT.45.Ld3(6).Ti | 3734 (25.7) | | 72.3 (1836) | 82.6 (2098) | 57.6 (1463) |
| IT.45.Ld3(6).SS | 3525 (24.3) | | 74.4 (1890) | 85.0 (2159) | 59.3 (1506) |
| IT.0.0(6).Ti | 3397 (23.4) | | 75.8 (1925) | 86.6 (2200) | 60.4 (1534) |

Table 18 – Comparison of specified minimum development length for hooked bars

| Specimen | $f_c$ psi (MPa) | $f_y$ psi (MPa) | AASHTO in. (mm) | ACI-318 in. (mm) |
|---|---|---|---|---|
| IT.45.Ld3(10).Ti | 4056 (28.0) | 71.6 (494) | 26.6 (676) | 31.7 (805) |
| IT.45.Ld3(6).Ti | 3734 (25.7) | | 27.7 (704) | 33.0 (838) |
| IT.45.Ld3(6).SS | 3525 (24.3) | | 28.5 (724) | 34.0 (864) |
| IT.0.0(6).Ti | 3397 (23.4) | | 29.1 (739) | 34.6 (879) |

*5.1.1.2. Shear Capacity*

Appendix B fully details the ACI 318-11 and AASHTO-LRFD methods used to calculate the nominal shear capacities. The predicted shear capacities from ACI, AASHTO-LRFD, and Response 2000 (R2K) are shown in Table 19 versus the applied shear at failure for specimen IT.45.Ld3(10).Ti. As seen in this table, R2K very closely predicted the specimen capacity, while ACI and AASHTO were conservative. The shear strength predictions are not shown for the other specimens because they failed in the constant moment region.

Table 19 – Comparison of predicted to experimental shear capacity

| Specimen | ACI 318 kips (kN) | AASHTO kips (kN) | R2K kips (kN) | $V_{APP}$ at Failure kips (kN) | Failure Location |
|---|---|---|---|---|---|
| IT.45.Ld3(10).Ti | 163.5 (727) | 116.0 (516) | 210.4 (936) | 210.2 (935) | End of cutoff |

*5.1.1.3. Moment Capacity*

Appendix C fully describes the ACI 318-11 and AASHTO-LRFD methods for calculating the nominal moment capacities. The predicted moment capacities from ACI, AASHTO, and R2k versus the applied moment at failure are shown in Table 20 for specimens IT.45.Ld3(6).Ti, IT.45.Ld3(6).SS, and IT.0.0(6).Ti. All three methods incorporate the compression steel contribution. Because of this, the ACI and AASHTO predictions report the same moment capacity. The moment predictions are not shown for specimen IT.45.Ld3(10).Ti because it failed in shear.

Predictions for specimens IT.45.Ld3(6).Ti and IT.45.Ld3(6).SS were made at midspan without the contribution from the NSM bars. Failure cracks for these two specimens were close to the ends of the NSM bars or overlapping somewhat. For specimen IT.45.Ld3(6).Ti, the prediction with no NSM material contribution correlated well, but for specimen IT.45.Ld3(6).SS, the prediction was low. Further inspection of the cracking region near midspan for this specimen indicated that the stainless steel may have partially contributed to the moment strength, as there were three layers of bars which could intersect cracks compared to only one in the specimen with the NSM titanium allow bars. To correlate the applied moment at failure, a 54% contribution from the stainless steel provides a moment prediction from R2K of 2459.0 kip-ft (3334 kN-m). This confirmed the visual indication that approximately 4 of the 8 stainless steel bars contributed to the moment strength.

Table 20 – Comparison of predicted to experimental moment capacity

| Specimen | ACI 318 k-ft (kN-m) | AASHTO k-ft (kN-m) | R2K k-ft (kN-m) | $M_{APP}$ at Failure k-ft (kN-m) | Failure Location |
|---|---|---|---|---|---|
| IT.45.Ld3(6).Ti | 2029.2 (2751) | 2029.2 (2751) | 2209.9 (2996) | 2202.7 (2986) | Midspan |
| IT.45.Ld3(6).SS | 2029.2 (2751) | 2029.2 (2751) | 2181.5 (2959) | 2458.3 (3333) | Midspan |
| IT.0.0(6).Ti | 886.7 (1202) | 886.7 (1202) | 940.0 (1274) | 940.6 (1275) | Midspan |

*5.1.1.4. Load Capacity*

To compare all the specimens, the predicted failure loads were computed and are listed in Table 21. The predicted loads were determined from the predicted shear or moment capacities of the specimens and the given geometry of the test setup. The predicted loads for specimens IT.45.Ld3(6).Ti and IT.45.Ld3(6).SS were calculated without consideration of the NSM material, as the base section controlled the failure because effectively the cutoff location was remediated by the NSM bars. As seen in this table, R2K does an excellent job of predicting the capacity, except for specimen IT.45.Ld3(6).SS. Due to the location of the hinge region, specimen IT.45.Ld396).SS likely had a partial contribution to its capacity that was not accounted for in the prediction from the stainless steel bars present around the crack location.

Table 21 – Comparison of predicted to experimental load capacity

| Specimen | ACI 318 | | AASHTO | | R2K | | $P_{APP}$ at Failure | Failure Location |
|---|---|---|---|---|---|---|---|---|
| | kips (kN) | Bias | kips (kN) | Bias | kips (kN) | Bias | kips (kN) | |
| IT.45.Ld3(10).Ti | 327.0 (1454) | 1.29 | 232.0 (1032) | 1.81 | 420.8 (1872) | 1.00 | 420.5 (1870) | End of cutoff |
| IT.45.Ld3(6).Ti | 412.7 (1836) | 1.09 | 412.7 (1836) | 1.09 | 449.5 (1999) | 1.00 | 448.0 (1993) | Midspan |
| IT.45.Ld3(6).SS | 412.7 (1836) | 1.21 | 412.7 (1836) | 1.21 | 443.7 (1974) | 1.13 | 500.0 (2224) | Midspan |
| IT.0.0(6).Ti | 180.3 (802) | 1.06 | 180.3 (802) | 1.06 | 191.2 (850) | 1.00 | 191.3 (851) | Midspan |
| Average Bias | | 1.16 | | 1.29 | | 1.03 | | |
| Bias COV (%) | | 9.16 | | 27.3 | | 6.21 | | |

*5.1.1.5. Flexural Tension Demands and Capacity*

The tensile demands in the reinforcing steel and NSM bars were predicted and compared with the measured responses. First, the baseline specimens were determined as if they were not retrofitted, by considering only the internal reinforcing steel. Then the retrofitted specimens were computed assuming full participation of the NSM bars with the internal reinforcing steel. The tensile capacities of specimens IT.45.Ld3(10).Ti, IT.45.Ld3(6).Ti, and IT.45.Ld3(6).SS were calculated using AASHTO-LRFD and ACI 318. Response 2000 was used to calculate the tensile capacities of the retrofitted specimens, as it has been shown to provide excellent correlation with the experimental results. A comparison between different design methods is shown in Figure 5.1 to Figure 5.9 along with the experimentally measured forces (from strain gages) in the internal reinforcing steel and NSM bars. The experimental

tension force at failure was compared to the demands and capacities. For specimen IT.45.Ld3(10).Ti, the strain gages on the internal cutoff reinforcing steel bar went out before failure, therefore the experimental tension force is shown at a lower load interval.

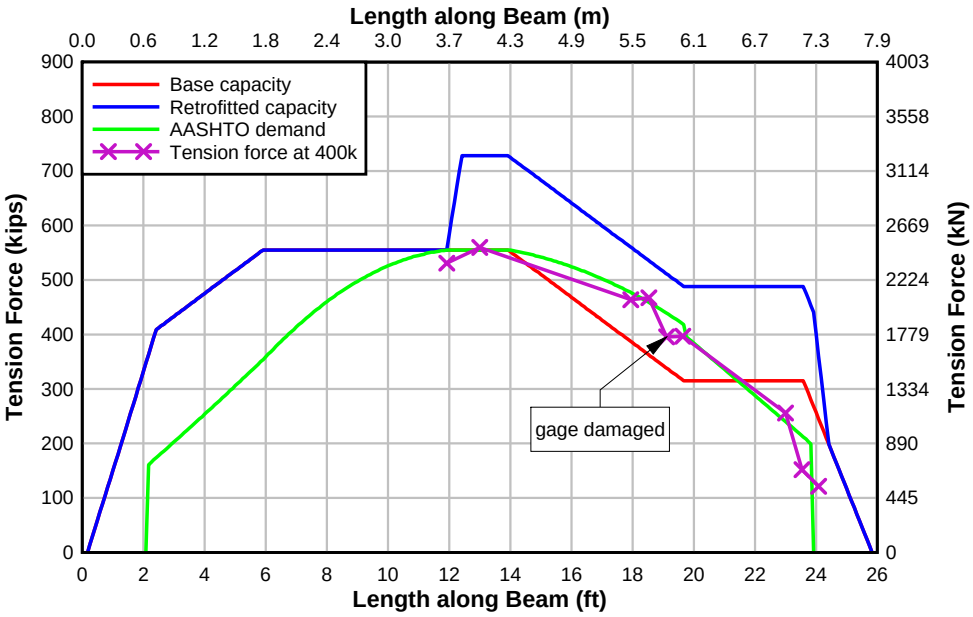


Figure 5.1 – Specimen IT.45.Ld3(10).Ti AASHTO flexural tension resultant along length of specimen

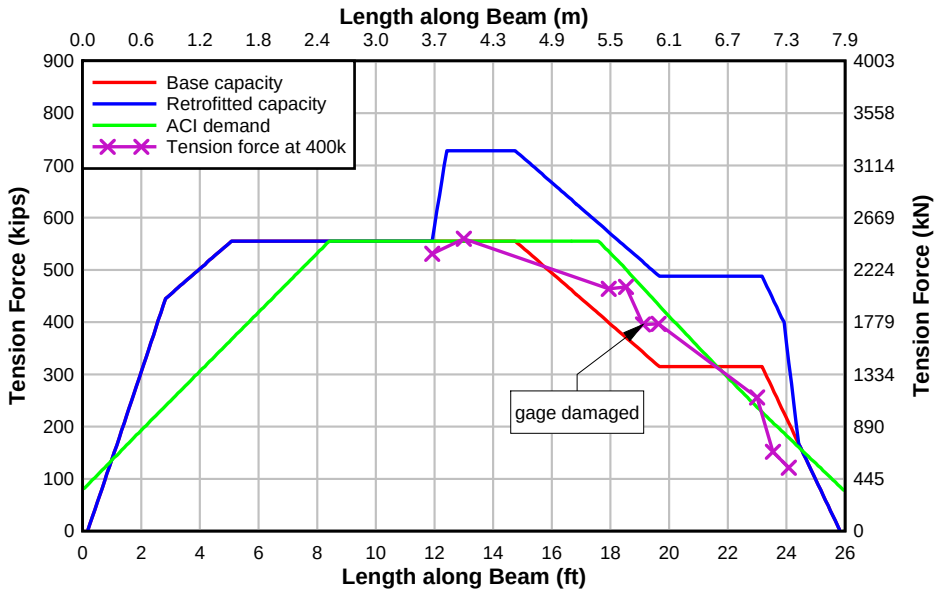


Figure 5.2 – Specimen IT.45.Ld3(10).Ti ACI flexural tension resultant along length of specimen

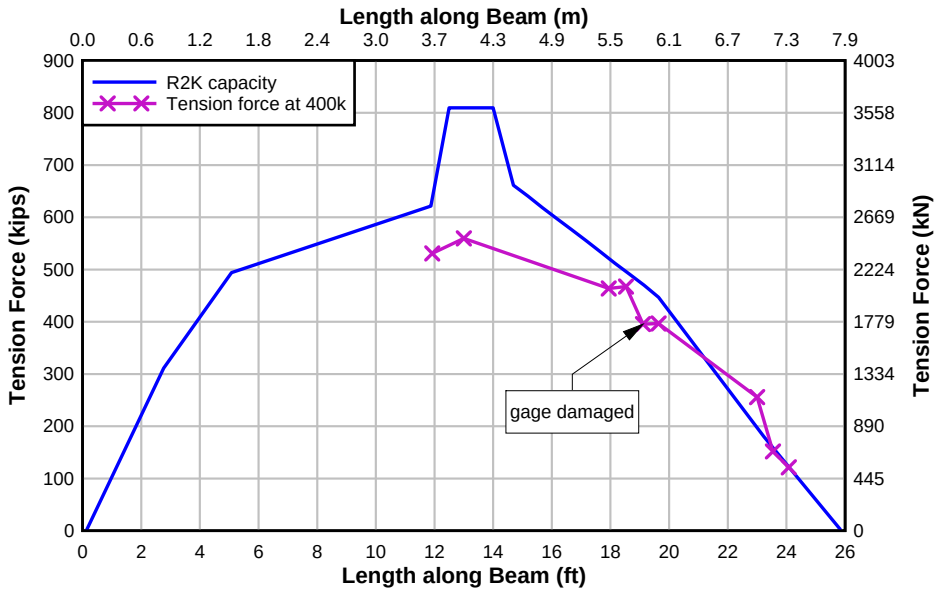


Figure 5.3 – Specimen IT.45.Ld3(10).Ti R2K flexural tension resultant along length of specimen

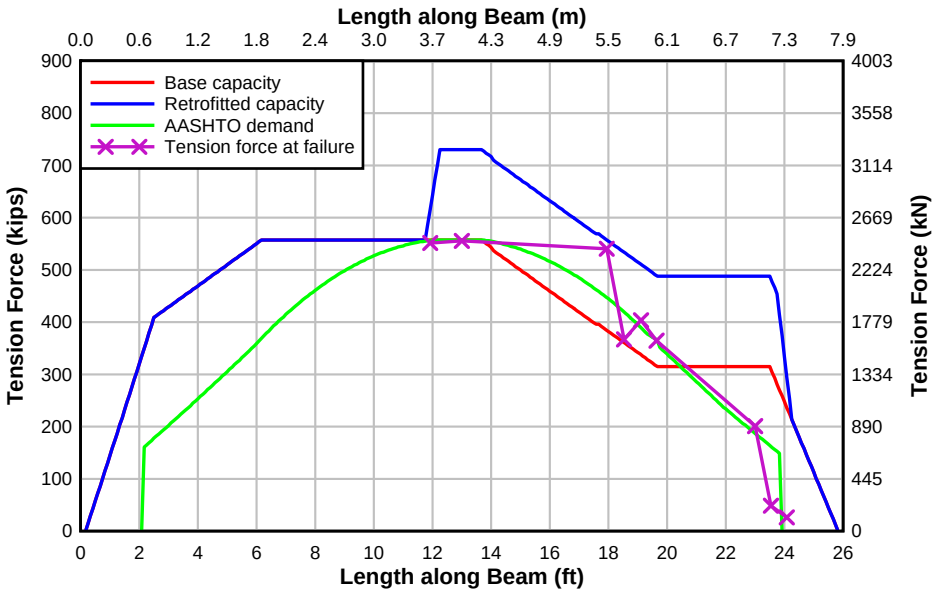


Figure 5.4 – Specimen IT.45.Ld3(6).Ti AASHTO flexural tension resultant along length of specimen

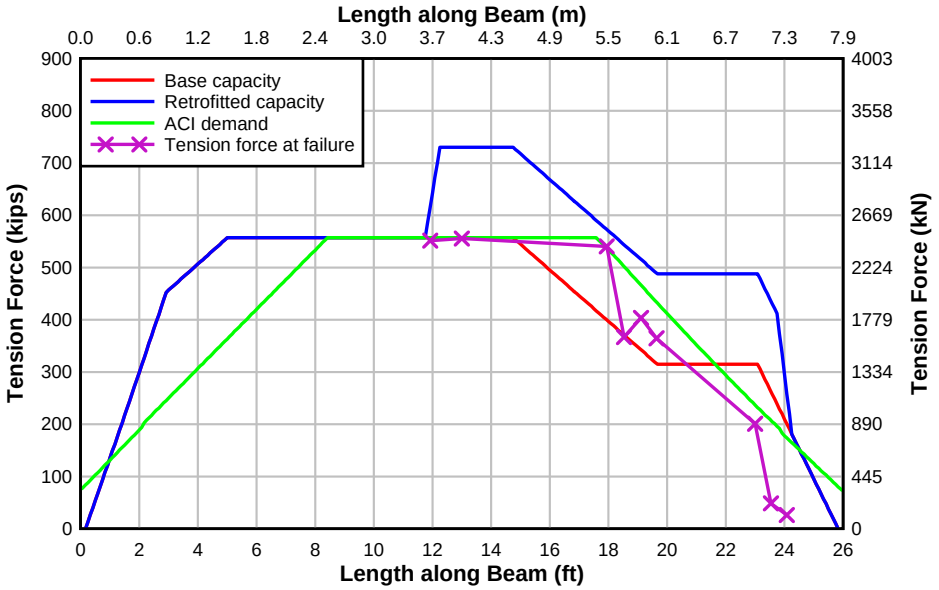


Figure 5.5 – Specimen IT.45.Ld3(6).Ti ACI flexural tension resultant along length of specimen

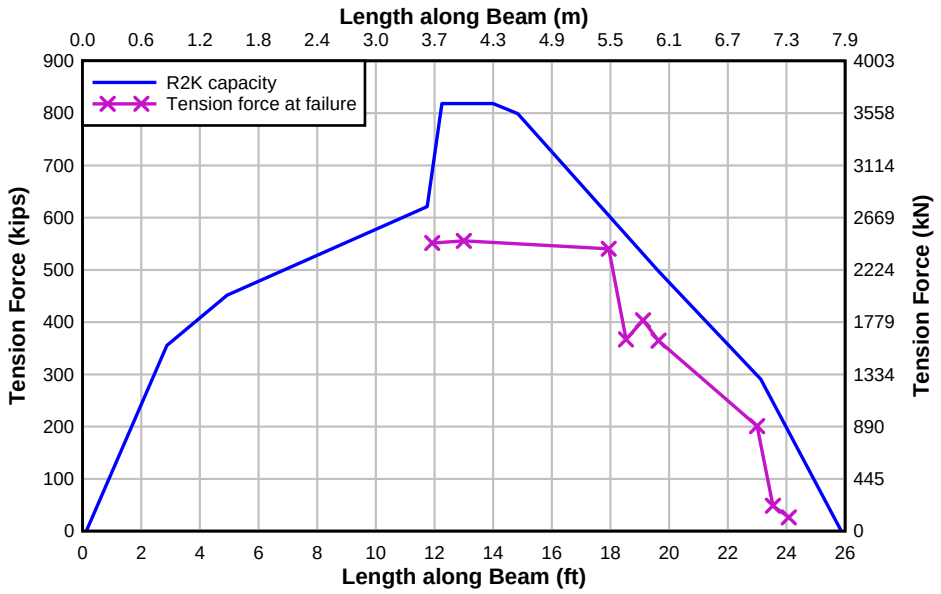


Figure 5.6 – Specimen IT.45.Ld3(6).Ti R2K flexural tension resultant along length of specimen

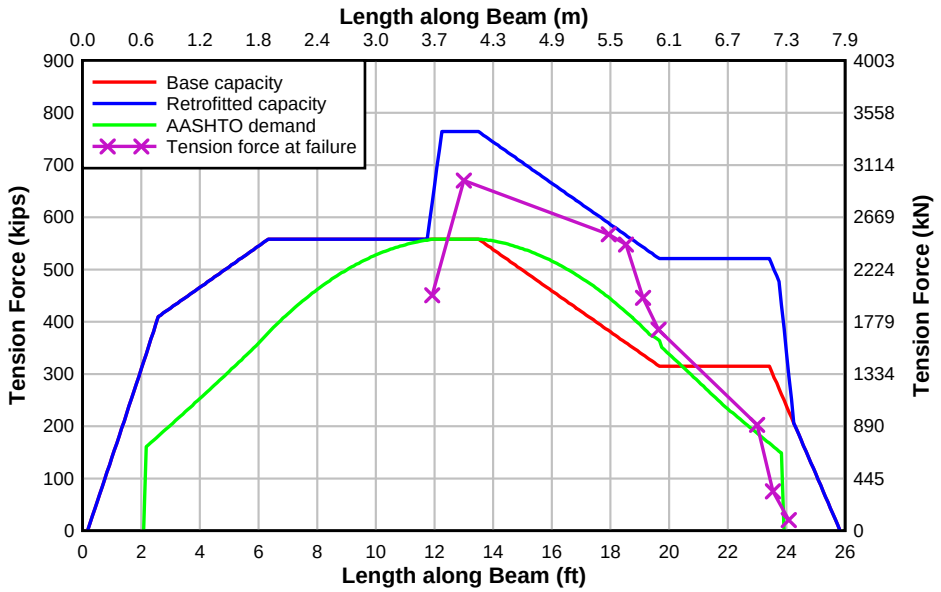


Figure 5.7 – Specimen IT.45.Ld3(6).SS AASHTO flexural tension resultant along length of specimen

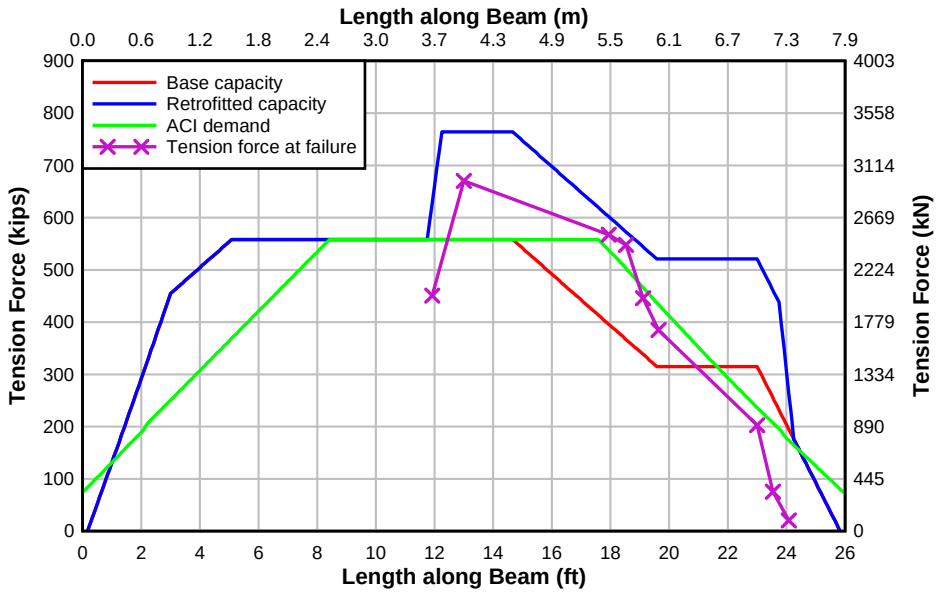


Figure 5.8 – Specimen IT.45.Ld3(6).SS ACI flexural tension resultant along length of specimen

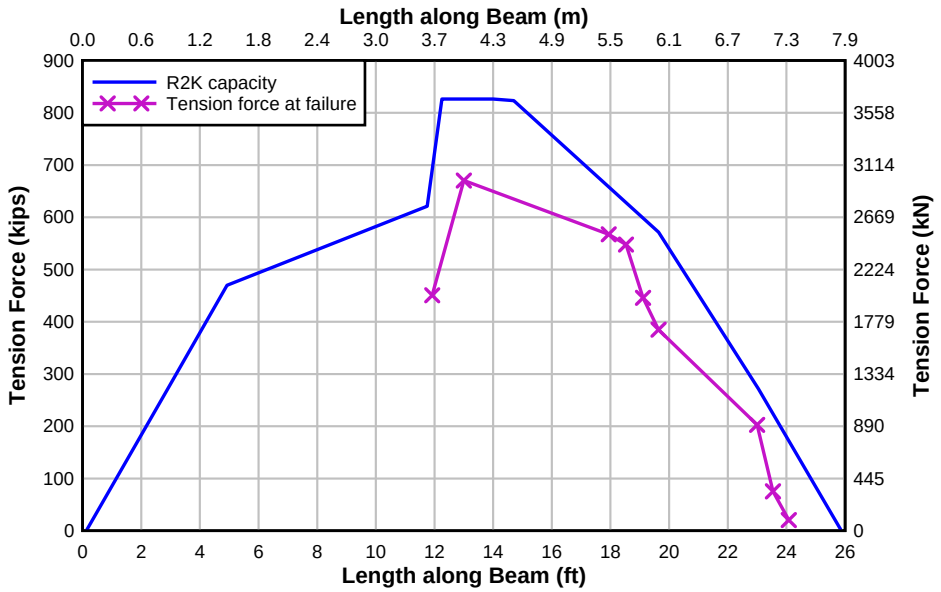


Figure 5.9 – Specimen IT.45.Ld3(6).SS R2K flexural tension resultant along length of specimen

5.1.2. Bond Stress

Bond stresses from the literature were reported in Table 1. Table 22 summarizes the bond stresses in the T and IT specimens retrofitted using the NSM method by Amneus (2014) and in this research, respectively. Stresses in the reinforcement were limited to the yield stress of each respective bar type.

Table 22 – Reported bond stress in reinforcement

| **Author** | **Bar Type** | | **Bar Diameter in. (mm)** | **$\mu_{avg}$ psi (MPa)** | **$\bar{\mu}_{max}$ psi (MPa)** |
|---|---|---|---|---|---|
| Amneus | Deformed Rebar | Cutoff | 1.41 (35.8) | 705 (4.86) | 1030 (7.10) |
| | | Anchored | | 168 (1.16) | n/a |
| | Titanium | | 0.62 (15.6) | 296 (2.04) | 960 (6.41) |
| | Stainless Steel | | 0.75 (19.1) | 370 (2.55) | 520 (3.59) |
| Barker | Deformed Rebar | Cutoff | 1.41 (35.8) | 384 (2.65) | 665 (4.58) |
| | | Anchored | | 103 (0.71) | 254 (1.75) |
| | Titanium | | 0.62 (15.6) | 369 (2.54) | 767 (5.29) |
| | Stainless Steel | | 0.75 (19.1) | 404 (2.79) | 983 (6.78) |

### 5.1.3. Effectiveness of NSM Reinforcing Bars

The intent of this research was to investigate methods of strengthening deficient flexural anchorages. The baseline specimen has inherent geometry, materials, and transverse reinforcing details that can limit the strength. The baseline specimen would fail in diagonal tension at a location $d_v$ from the loading point if it had sufficient and continuous flexural reinforcing steel over the length of the member. The variable $d_v$ is defined as the distance from the extreme compression fiber to the centroid of the tension reinforcement. If additional flexural reinforcement is added, the girder will be able to carry additional load due to shear-flexure interaction until so much flexural reinforcement is added that it will fail in diagonal tension. Knowing this behavior, the contribution of the NSM reinforcing bars in terms of equivalent flexural reinforcing steel was estimated. Using R2K, the cross-section was repeatedly analyzed at the section $d_v$ away from the loading point with larger and larger area flexural reinforcing steel. The analysis was repeated at each section for steel areas ranging from 0 $in^2$ to 30 $in^2$ (0 $cm^2$ to 194 $cm^2$). The predicted maximum applied load as a function of flexural reinforcement area as well as R2K baseline and retrofitted predictions for the specimens are shown in Figure 5.10 to Figure 5.16.

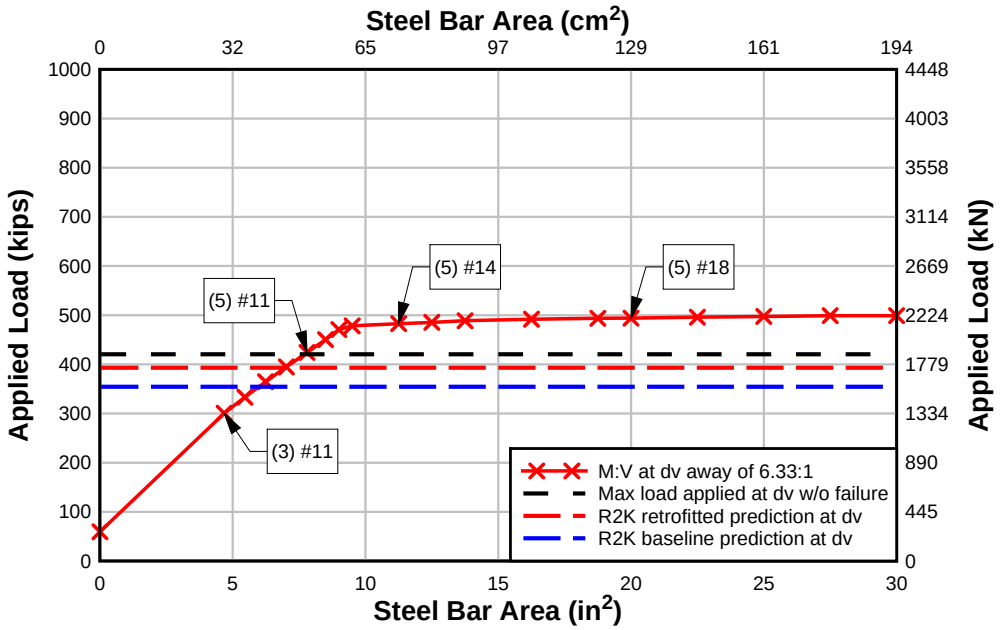


Figure 5.10 – Specimen IT.45.Ld3(10).Ti load-bar area at $d_v$ away

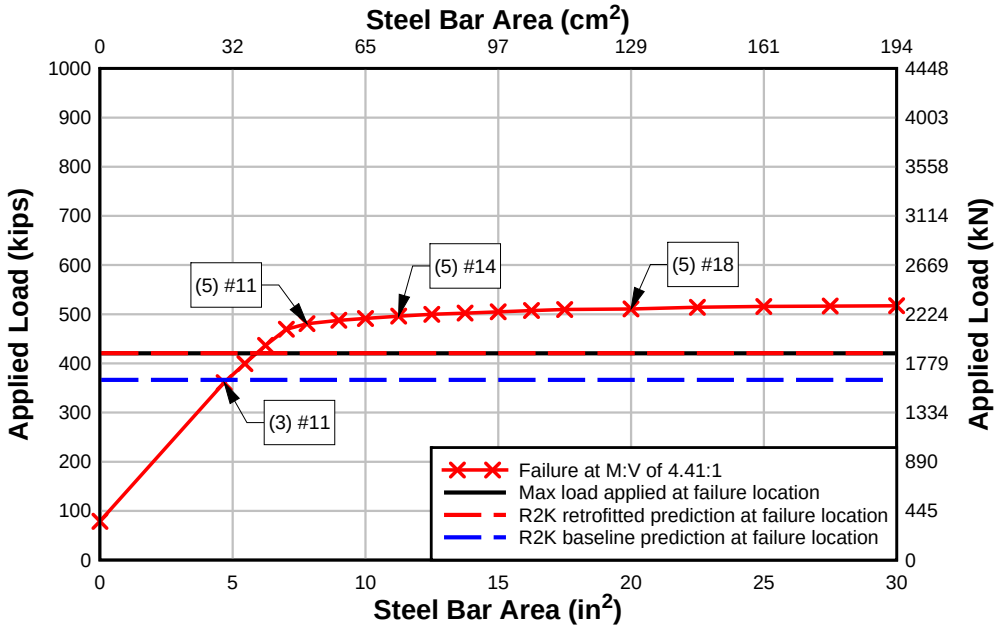


Figure 5.11 – Specimen IT.45.Ld3(10).Ti load-bar area at failure location

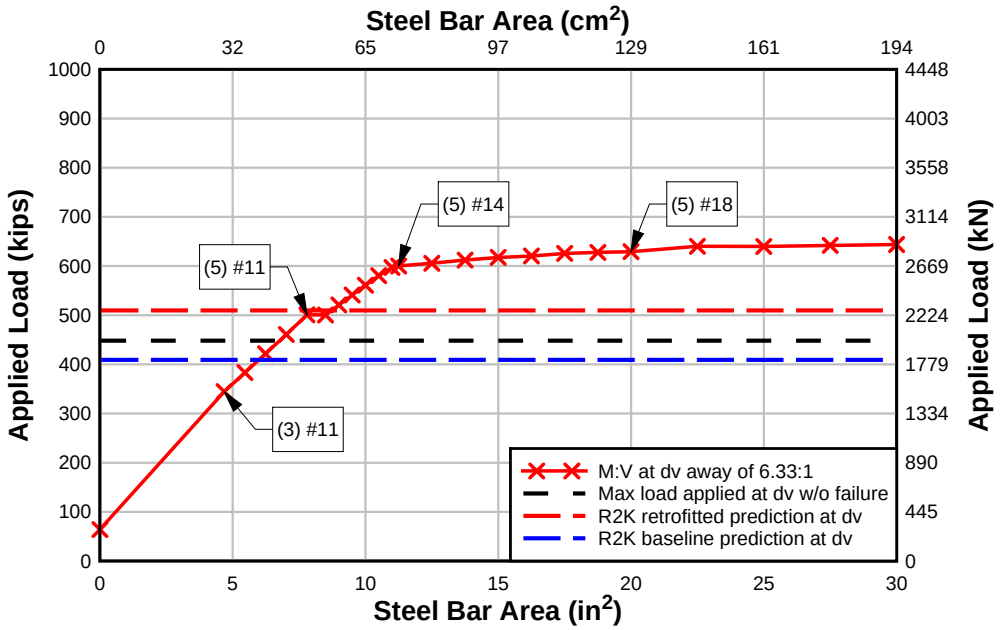


Figure 5.12 – Specimen IT.45.Ld3(6).Ti load-bar area at $d_v$ away

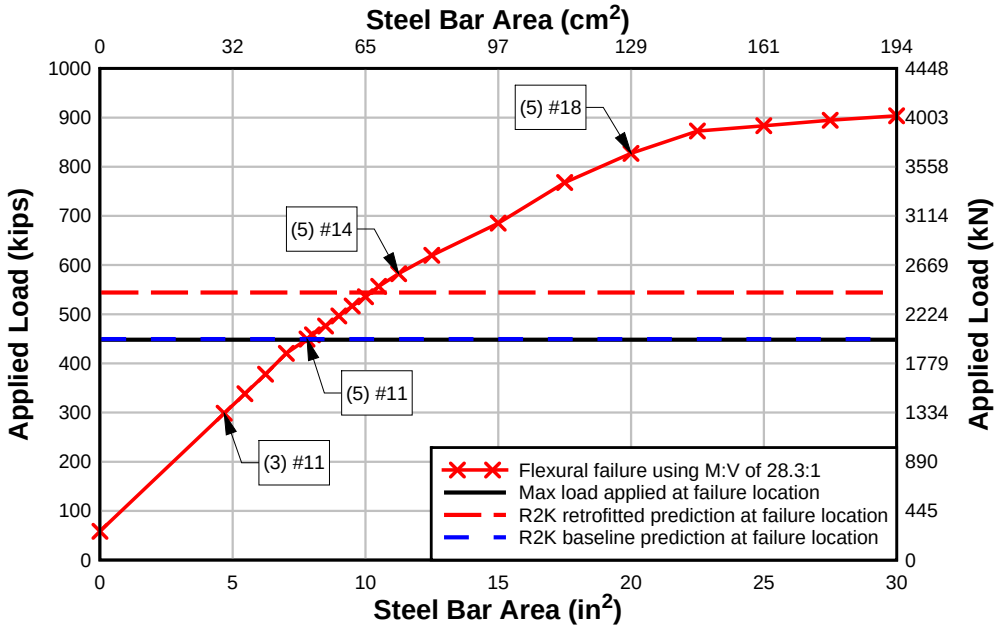


Figure 5.13 – Specimen IT.45.Ld3(6).Ti load-bar area at failure location

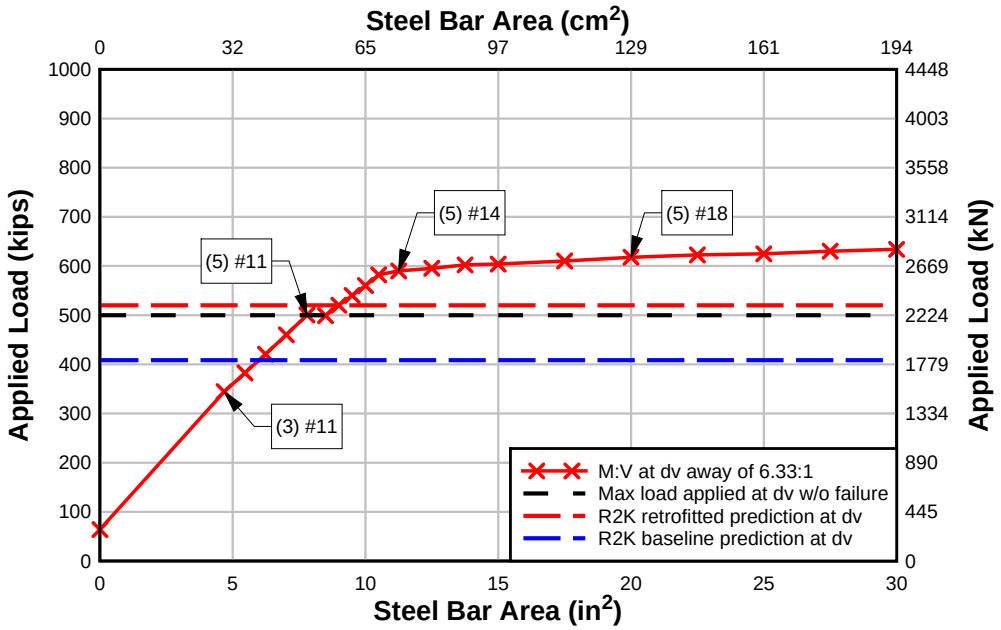


Figure 5.14 – Specimen IT.45.Ld3(6).SS load-bar area at $d_v$ away

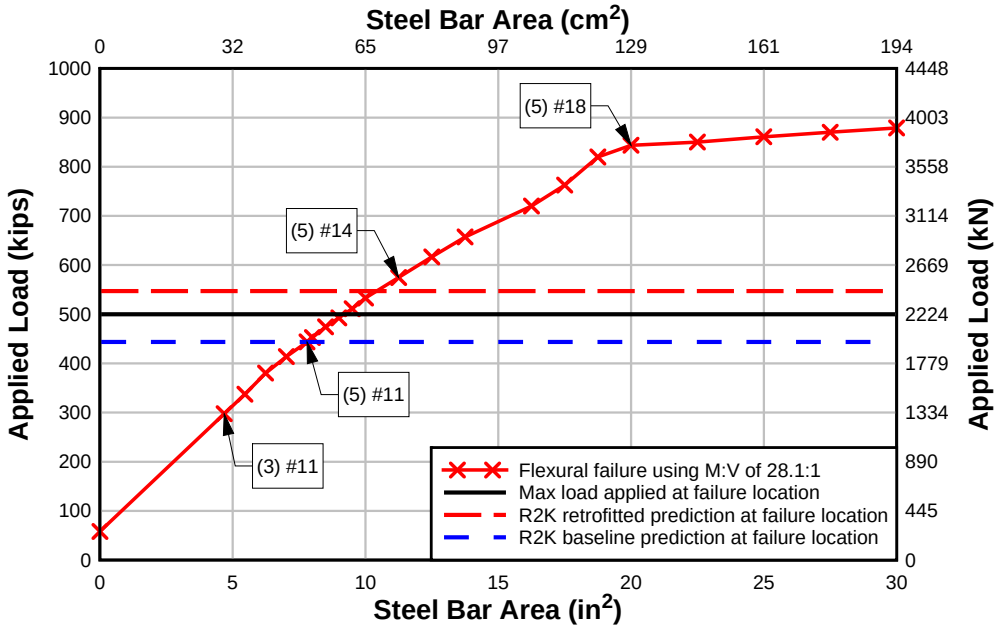


Figure 5.15 – Specimen IT.45.Ld3(6).SS load-bar area at failure location

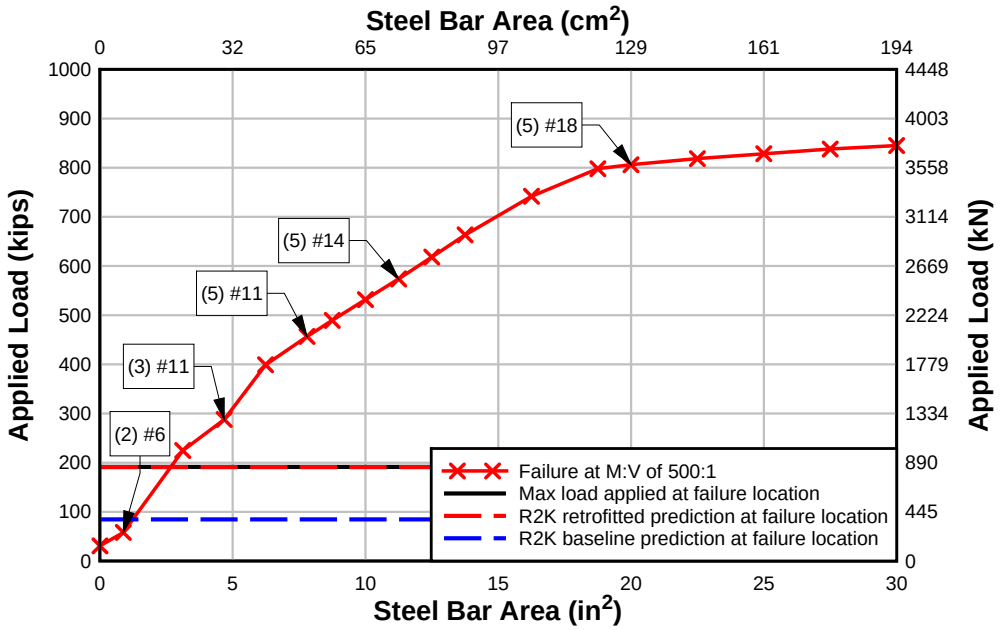


Figure 5.16 – Specimen IT.0.0(6).Ti load-bar area at failure location

From the section analyses at $d_v$ away, there is an optimum area of steel around 10 in$^2$ (65 cm$^2$) that can be utilized. Any greater area of equivalent flexural steel than that will produce only a small increase in the applied load capacity. The change in slope in these curves represents the change in the specimen from flexure to diagonal tension controlled failure.

The section analysis at the failure location for IT.45.Ld3(10).Ti shows a similar trend as in the analysis at $d_v$ away. The analyses at the failure locations for the other three specimens indicate that adding steel up to approximately 20 in$^2$ (129 cm$^2$) will continue to increase the applied load capacity with small changes in the bar area. The change of the point of inflection for these curves indicates that these beams are controlled by flexure.

The plots also provide the equivalent steel area that the NSM reinforcing provided at failure. In specimen IT.45.Ld3(10).Ti, failure occurred by the end of the cutoff bars. Without any contribution from the cutoff bars, there are only three #11 (M36) bars available to provide strength. The area of steel crossing the applied failure load reference line shows the contribution of the NSM titanium as an equivalent reinforcing steel area. Table 23 shows the equivalent steel area provided by the NSM material for each specimen.

Table 23 – Equivalent steel area from NSM material

| Specimen | NSM Material | Equivalent Steel Area $in^2$ ($mm^2$) |
|---|---|---|
| IT.45.Ld3(10).Ti | Titanium | 1.07 (690) |
| IT.45.Ld3(6).Ti | Titanium | 0 |
| IT.45.Ld3(6).SS | Stainless Steel | 1.38 (890) |
| IT.0.0(6).Ti | Titanium | 1.44 (929) |

Specimen IT.45.Ld3(6).Ti failed in flexure at the end of the NSM titanium bars. All 5 of the flexural steel bars were fully developed at this point and the applied failure load reference line crosses at this steel bar area. This intersection shows there was no contribution from the NSM bars at the failure point. The titanium alloy bars were effectively able to remediate the cutoff location and allow the section to develop its full strength. The baseline beam reference also lines up at this point. The IT.45.Ld3(6).SS specimen shows the partial contribution from the stainless steel bars as the applied load reference line crosses the curve between the retrofitted and baseline predictions. Lastly, the IT.0.0(6).Ti specimen curve at failure shows how much equivalent steel the titanium contributed. The majority of the applied load is due to the titanium alloy bars, with only a small contribution from the #6 (M19) bars.

# 6. SUMMARY & CONCLUSIONS

The objective of this research was to develop effective methods to strengthen existing diagonally cracked RCDGs with deficient flexural anchorages. To achieve this, a test plan was designed to investigate full-scale girder specimens with deficient anchorages and strengthen them using a near-surface mounted retrofitting technique. Four large-size girders were designed, constructed, and tested to failure using alternative strengthening approaches. Member design was representative of vintage construction design and practices. Three specimens were constructed with a 45˚ preformed diagonal crack that precluded aggregate interlock and placed cutoff flexural reinforcing steel bars terminating 1/3 of the minimum development length as determined by ACI 318 past the crack. The fourth specimen did not have a preformed crack and had termination of the main flexural steel at midspan. Using the empirical data from the tests, the performance of the strengthened specimens was evaluated using various analytical methods. Conclusions based on the experimental and analytical results, additional research suggestions, and strengthening recommendations are discussed in the following sections.

## 6.1. Experimental Conclusions

The three IT beam specimens tested with preformed cracks showed that the initial diagonal crack crossing the developing section of the longitudinal cutoff bars did not control the specimen failure location. Location of the final failure crack was dependent on the reinforcement detailing and load patterns, not the presence of an initial diagonal crack. Slip of the cutoff bars was observed in each of the three specimens.

These IT specimens were non-ductile due to splitting of the relatively thin concrete deck and lack of reinforcement crossing the splitting plane when the flexural reinforcing steel bar anchorage failed. Chevron cracks were observed over the embedded steel cutoff bars and were an indicator of imminent anchorage failure with little reserve capacity. Compared to the baseline specimens (Goodall, 2010), cutoff bar slip initiated at approximately the same load levels, but higher slips were achieved before failure in the NSM strengthened specimens due to their increased capacity. At the same applied load much lower bond stresses were observed in the cutoff reinforcing steel bars with the addition of the NSM bars compared to the baseline specimens.

The specimens strengthened with NSM materials achieved capacities 17% to 39% greater than the unstrengthened specimens. The strengthened specimens also achieved a higher overall deformation capacity and had a greater distribution of cracking prior to failure, than the comparison baseline specimens. These attributes provide a greater visual indication of distress than specimens without NSM bars. Due to increased shear capacity, the specimens containing transverse reinforcement spaced at 6 in. (150 mm) were able to make more use of the titanium alloy and stainless steel NSM bars. These specimens developed the core strength of the cross-section with fully anchored flexural reinforcing steel. Without the NSM bars, the specimens would have failed in diagonal tension at a reduced capacity due to the poor detailing of the cutoff reinforcing steel.

The fourth IT specimen was designed to evaluate the performance of the NSM-titanium alloy bars in pure flexure. With only #6 (M19) bars, required for construction, spanning the

unstrengthened cut section, the titanium alloy bars contributed the majority of the flexural strength for the specimen. The titanium alloy bars enabled high ductility in the specimen at failure and the specimen exhibited distributed cracking along the retrofitted length. This indicates that the addition of titanium NSM bars can be a beneficial visual stress indicator.

### 6.2. Analytical Conclusions

To predict the method of failure in the specimen, different sections along the beam length must be analyzed to determine the critical location. These sections include the end of the cutoff bar, along the development length of the cutoff bar, at the intersection of diagonal cracks, at the loading point, midspan, and near the support. At each section, the shear, moment, and anchorage capacities must be checked. Anchorage failure can be predicted if the tensile demand exceeds the anchorage capacity at a lower load than the diagonal tension or moment strengths. The AASHTO-LRFD tensile demand must be analyzed for all possible failure planes.

An analysis of a range of equivalent flexural reinforcing steel bar areas compared to predictions of the baseline and retrofitted specimens provide a way to evaluate the contribution of the NSM bars to the specimen strength. These can also be used to predict the contribution of a strengthening material in a design.

Response 2000 (R2K) provided the best correlation of the analytical methods considered. Using Modified Compression Field Theory, R2K takes into account the strain hardening of the materials and incorporates the actual stresses in the reinforcement. R2K was also useful

in predicting strains in the reinforcing materials at loads in the actual specimens when the strain gages were compromised during the experiment.

### 6.1. Recommendations

The location of existing diagonal cracks is not a definite indicator of the final failure location. Bridge inspectors must look for the presence of chevron cracking around known cutoff locations and along their development lengths. For negative moment regions, special attention should be directed to where there is visible cracking on the underside of the deck because these cracks develop near the failure. If cracking of this type is observed, the bridge should be evaluated for load posting or strengthening based on the limited reserve capacity.

Overall, the high strength, ductility, environmental durability, and ability to fabricate mechanical anchorages of the metallic strengthening materials, such as titanium and stainless steel, make them a promising alternative for NSM strengthening of flexural anchorage deficiencies in reinforced concrete deck girders. The titanium alloy has higher strength than the stainless steel and thus fewer bars are required by a ratio of approximately 2. Fewer bars allows for more efficient placement of the strengthening material. The reduced labor and epoxy material costs provide some advantage to titanium alloy bars in spite of the relatively high material cost. For IT specimens, the strengthening material should optimally be installed in the top of the deck. This placement is ideal because installation underneath the flange is not possible due to the crossbeams. The retrofit should be covered with a wearing surface such as asphalt, or in the case of a concrete deck, grout or mortar.

## 6.2. Additional Research

The primary goal of this research was to provide effective methods to strengthen flexural anchorage deficiencies in vintage RCDG specimens. To complement this work, several future experimental and analytical projects are suggested:

- Investigate high-cycle fatigue effects on the titanium alloy and stainless steel bars, as well as bond and slip from repeated overloading (low-cycle fatigue) from large vehicles.
- Further investigate bond strength of titanium alloy and stainless steel NSM materials to fully characterize the NSM material-epoxy and epoxy-concrete interfaces.
- Quantify the development length of titanium alloy bars.
- Consider development of unbonded strengthening approaches to investigate the strength of the anchorages without any bond stresses.
- Conduct non-linear finite element analyses to model specimens with NSM metallic bars. Compare the predicted and measured member capacity as well as internal reinforcing steel and NSM bar bond stress and bar stress along the length of the member.

## 7. BIBLIOGRAPHY

Abrishami, H., and Mitchell, D. 1996. "Analysis of Bond Stress Distributions in Pullout Specimens," *Journal of Structural Engineering*, V. 122, No. 3, pp. 255-261.

Al-Mahmoud, F., Castel, A., Francois, R., and Tourneur, C. 2009. "Strengthening of RC Members with Near-Surface Mounted CFRP Rods," *Composite Structures*, V. 91, No. 2, pp. 138-147.

Al-Mahmoud, F., Castel, A., Francois, R., and Tourneur, C. 2011. "Anchorage and Tension-Stiffening Effect between Near-Surface-Mounted CFRP and Concrete," *Cement & Concrete Composites*, V. 33, No. 2, pp. 346-352.

American Association of State Highway Officials. 1953 "Standard Specifications for Highway Bridges," 6th Edition, *AASHO*, Washington, D.C.

American Association of State Highway Officials. 1973 "Standard Specifications for Highway Bridges," 11th Edition, *AASHO*, Washington, D.C.

American Association of State Highway and Transportation Officials. 2012. "AASHTO LRFD Bridge Design Specifications," 6th edition with 2013 interims, *AASHTO*, Washington, D.C.

American Concrete Institute. 1956. "Building Code Requirements for Reinforced Concrete (ACI 318-56)." *ACI Manual of Concrete Practice*, Detroit, Michigan.

American Concrete Institute. 2008. "Guide for the Design and Construction for Externally Bonded FRP Systems for Strengthening Concrete Structures (ACI 440.2R-08)," *ACI Manual of Concrete Practice*, Farmington Hills, Michigan.

American Concrete Institute. 2011. "Building Code Requirements for Structural Concrete and Commentary (ACI 318-11)," *ACI Manual of Concrete Practice*, Farmington Hills, Michigan.

Amneus, D. 2014. "Methods for Strengthening Flexural Steel Details in Reinforced Concrete Bridge Girders using a Near-Surface Mounted Retrofit." Unpublished master's thesis, Oregon State University.

ASTM A305-50T. 1950. "Tentative Specifications for Minimum Requirements for the Deformations of Deformed Steel Bars for Concrete Reinforcement," *ASTM International*, pp. 218-220.

ASTM A615/A615M-09b. 2009. "Standard Specification for Deformed and Plain Carbon-Steel Bars for Concrete Reinforcement," *ASTM International*, West Conshohocken, Pennsylvania, 7 pp.

ASTM A706/A706M-09b. 2009. "Standard Specification for Low-Alloy Steel Deformed and Plain Bars for Concrete Reinforcement," *ASTM International*, West Conshohocken, Pennsylvania, 6 pp.

ASTM A955/A955M-12e1. 2012. "Standard Specification for Deformed and Plain Stainless-Steel Bars for Concrete Reinforcement," *ASTM International*, West Conshohocken, Pennsylvania, 13 pp.

ASTM B348/B348M-13. 2013. "Standard Specification for Titanium and Titanium Alloy Bars and Billets," *ASTM International*, West Conshohocken, Pennsylvania, 8 pp.

ASTM C39/C39M-09. 2009. "Standard Test Method for Compressive Strength of Cylindrical Concrete Specimens," *ASTM International*, West Conshohocken, Pennsylvania, 7 pp.

ASTM C496/C496M-11. 2011. "Standard Test Method for Splitting Tensile Strength of Cylindrical Concrete Specimens," *ASTM International*, West Conshohocken, Pennsylvania, 5 pp.

ASTM E8/E8M-13a. 2009. "Standard Test Methods for Tension Testing of Metallic Materials," *ASTM International*, West Conshohocken, Pennsylvania, 27 pp.

Bentz, E. 2000. "Response-2000 Reinforced Concrete Sectional Analysis using the Modified Compression Field Theory (Version 1.0.5)" [Computer Software]. *University of Toronto*, Toronto.

Bournas, D. A., and Triantafillou, T. C. 2009. "Flexural Strengthening of Reinforced Concrete Columns with Near-Surface-Mounted FRP or Stainless Steel," *ACI Structural Journal*, V. 106, No. 3, pp. 495-505.

Castro, H., Rodriguez, C., Belzunce, F.J., and Canteli, A.F. 2003. "Mechanical Properties and Corrosion Behavior of Stainless Steel Reinforcing Bars," *Journal of Materials Processing Technology*, V. 143-144, pp. 134-137.

Clark, A. 1949. "Bond of Concrete Reinforcing Bars," *Journal of the American Concrete Institute*, V 21, No 3, pp. 161-184.

Darwin, D., Zuo, J., Tholen, M., and Idun, E. 1996. "Development Length Criteria for Conventional and High Relative Rib Area Reinforcing Bars," *ACI Structural Journal*, V. 93, No. 3, pp. 1-13.

De Lorenzis, L., Nanni, A., and La Tegola, A. 2000. "Strengthening of Reinforced Concrete Structures with Near Surface Mounted FRP Rods," *International Meeting on Composite Materials*, Milan, Italy, pp. 1-8.

Doerr, K.. 1978. “Bond Behavior of Ribbed Reinforcement under Transversal Pressure,” *Nonlinear behavior of reinforced concrete spatial* structures, pp. 13-24.

Ferguson, P., and Thompson J. 1962. “Development Length for Large High Strength Reinforcing Bars,” *ACI Journal*, V 59, No 7, pp 71-91.

Goodall, J. 2010. “Influence of Diagonal Cracks on Negative Moment Flexural Anchorage Performance in Reinforced Concrete Bridge Girders,” *Master’s Thesis, Oregon State University*, Corvallis.

Google Maps, 2014. *Mosier Oregon 45˚41’0.96”N, 121˚23’47.04”W, elevation 50m. < https://www.google.com/maps/@45.6847759,-121.397013,1589m/data=!3m1!1e3> [Viewed 10 June 2014]*.

Harajli, M. H. 2004. “Comparison of Bond Strength of Steel Bars in Nominal- and High-Strength Concrete,” *Journal of Materials in Civil Engineering*, V. 16, No. 4, pp. 365-374.

Hassan, T., and Rizkalla, S. 2003. “Investigation of Bond in Concrete Structures Strengthened with Near Surface Mounted Carbon Fiber Reinforced Polymer Strips,” *Journal of Composites for Construction*, August, pp. 248-257.

Hassan, T., and Rizkalla, S. 2004. “Bond Mechanism of Near-Surface-Mounted Fiber-Reinforced Polymer Bars for Flexural Strengthening of Concrete Structures,” *ACI Structural Journal*, V. 101, No. 6, pp. 830-839.

Higgins, C., Miller, T., Rosowsky, D., Yim, S., *et al.* 2004. “Assessment Methodology for Diagonally Cracked Reinforced Concrete Deck Girders,” *Report No. FHWA-OR-RD-05-04*. Oregon Department of Transportation and Federal Highway Administration.

Jeppsson, J., and Thelandersson, S. 2003. “Behavior of Rinforced Concrete Beams with Loss of Bond at Longitudinal Reinforcement,” *Journal of Sructural Engineering*, V. 129, No. 10, pp. 1376-1383.

Losberg, A., and Olsson, P. 1979. “Bond Failure of Deformed Reinforcing Bars Based on the Longitudinal Splitting Effect of Bars,” *ACI Journal*, January, pp. 5-18.

Lutz, L., and Gergely, P. 1967. “Mechanics of Bond and Slip of Deformed Bars in Concrete,” *ACI Journal*, November, pp. 711-721.

Mains, R. M. 1951 “Measurement of the Distribution of Tensile and Bond Stresses Along Reinforcing Bars”, *ACI Journal*, V 23, No 3, pp. 225-252.

Malvar, L. J. 1992. “Bond of Reinforcement Under Controlled Confinement,” *ACI Materials Journal*, V. 89, No. 6, pp. 593-601.

Mylrea, T. D. 1948. "Bond and Anchorage," *Journal of the American Concrete Institute*, V. 19, No 7, pp. 521-552.

Novidis, D. G., and Pantazopoulou, S. J. 2008. "Bond Tests of Short NSM-FRP and Steel Bar Anchorages," *Journal of Composites for Construction*, V. 12, No. 3, pp. 323-333.

ODOT, 2013. Photograph.

Orangun, C. O., Jirsa, J. O., and Breen, J. E. 1977. "Re-evaluation of Test Data on Development Length and Splices," *ACI Journal*, V. 74, No. 3, pp. 114-112.

Rasheed, H., Harrison, R., Peterman, R., and Alkhrdaji, T. 2010. "Ductile Strengthening using Externally Bonded and Near Surface Mounted Composite Systems," *Composite Structures*, V. 92, No. 10, pp. 2379-2390.

Reynolds, G. G., and Beeby, A. W. 1982. "Bond Strength of Deformed Bars," *Bond in Concrete: Proceedings of and International Conference,* Applied Science Publishers, London, pp. 434-445.

Rizkalla, S., Hassan, T., and Hassan, N. 2003. "Design Recommendations for the Use of FRP for Reinforcement and Strengthening of Concrete Structures," *Progress in Structural Engineering and Materials*, V. 5, No. 1, pp. 16-28.

Soroushian, P, Choi, K., Park, G, and Aslani, F. 1991. "Bond of Deformed Bars to Concrete: Effects of Confinement and Strength of Concrete," *ACI Materials Journal*, V. 99 No. 3, pp. 227-232.

Triska, M. A., 2010 "Flexural Steel Anchorage Performance at Diagonal Crack Locations," *Master's Thesis, Oregon State University*, Corvallis.

# APPENDECIES

## APPENDIX A – EXPERIMENTAL DATA

Appendix A details the instrumentation types and labels for each of the test specimens. The purpose of each instrument is described in *Section 3.4*. Plots are provided illustrating the data gathered from testing and calculated tensile forces.

Midspan Displacement: Midspan displacement was measured on both the east and west sides of the beam. Support settlements were measured on all four corners of the specimens at the support centerlines. The average midspan displacement was found by subtracting the average of the support settlements from the average of the midspan displacements.

Cutoff Bar Slip: Sensors were located at the ends of the cutoff bars for specimens IT.45.Ld3(10).Ti, IT.45.Ld3(6).Ti, and IT.45.Ld3(6).SS. Both the west and the east cutoff bar slip were measured.

Diagonal String Potentiometers: Diagonal displacement sensors were used to measure the change in crack widths crossing the sensor. The sensors were anchored to the beam and connected to a brass wire anchored at the opposing diagonal point. The sensors were numbered, with the arrow showing the direction of measurement. The labeling diagrams are shown below in Figures A.1 through A.3.

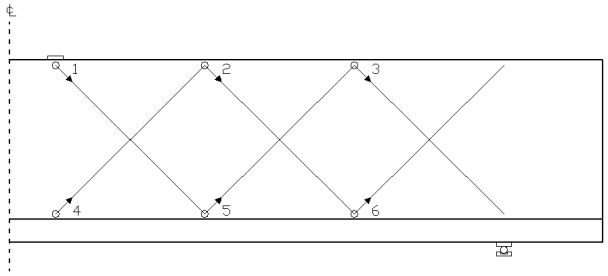


Figure A.1 – Specimens IT.45.Ld3(10).Ti, IT.45.Ld3(6).Ti, and IT.45.Ld3(6).SS north diagonal sensor numbering

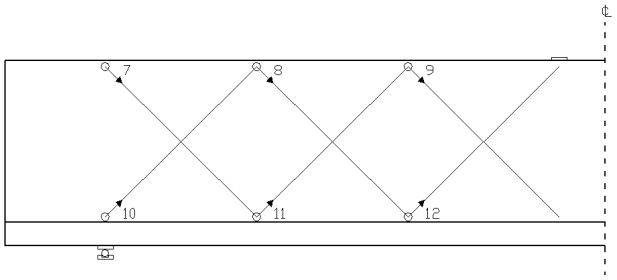


Figure A.2 – Specimens IT.45.Ld3(6).Ti and IT.45.Ld3(6).SS south diagonal sensor numbering

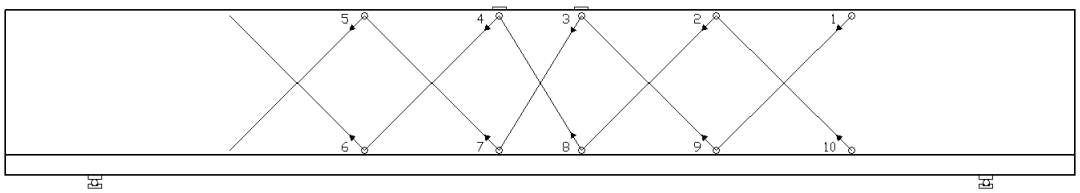


Figure A.3 – Specimen IT.0.0(6).Ti diagonal sensor numbering

Strain Gages: Strain gages were placed on specimens IT.45.Ld3(10).Ti, IT.45.Ld3(6).Ti, and IT.45.Ld3(6).SS along the cutoff bar development length to the preformed crack. Gages were also used around the NSM hook locations. Stirrups had gages at points where they crossed the preformed crack and at mid-height north of the preformed crack. For specimen

IT.0.0(6).Ti, gages were placed along the development length of the cut bars and on the titanium at the hook locations. Gages were installed mid-height on stirrups around the titanium hook locations. Figures A.4 through A.7 illustrate the strain gage and section labeling convention for the specimens. The second instrumented titanium bar in specimen IT.45.Ld3(6).Ti was installation backwards, therefore the critical section gages 14-17 are in the incorrect locations. Strains are shown along the beam as measured, but strain data from the first titanium bar were used to represent both bars in the critical section.

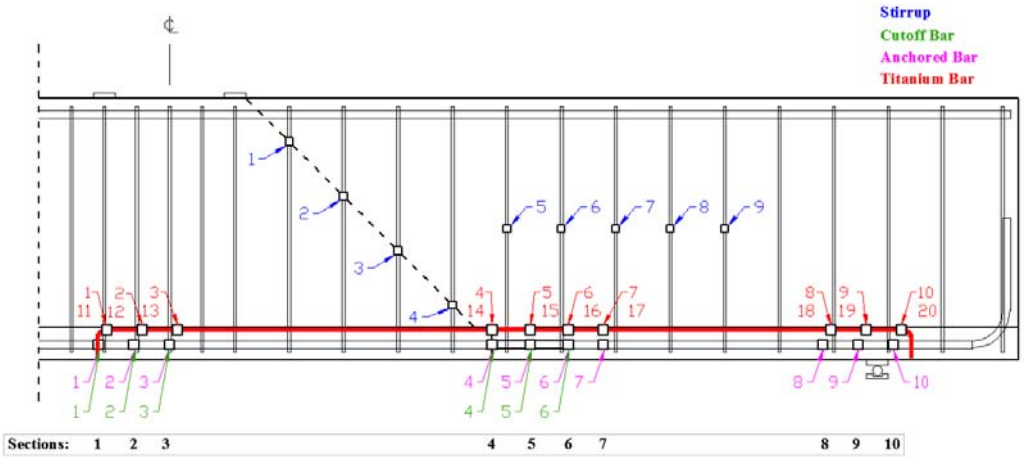


Figure A.4 – Specimen IT.45.Ld3(10).Ti strain gage labeling convention

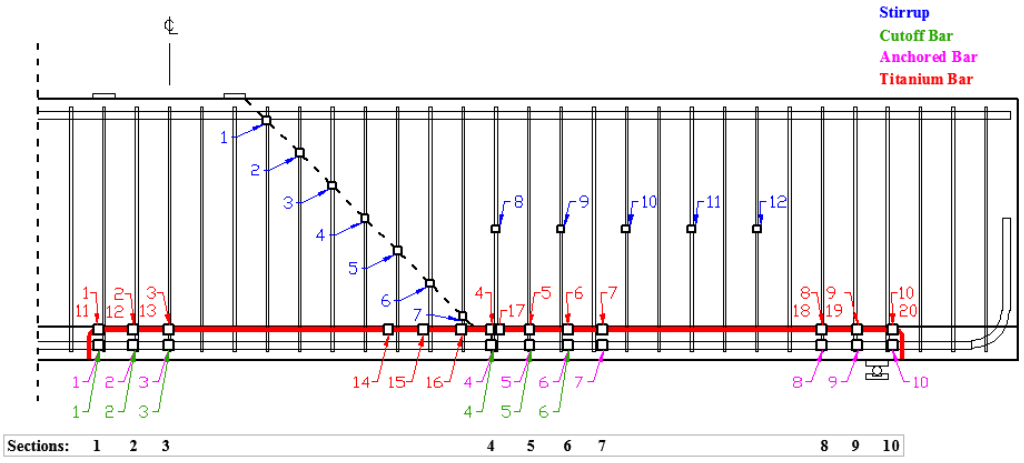


Figure A.5 – Specimen IT.45.Ld3(6).Ti strain gage labeling convention

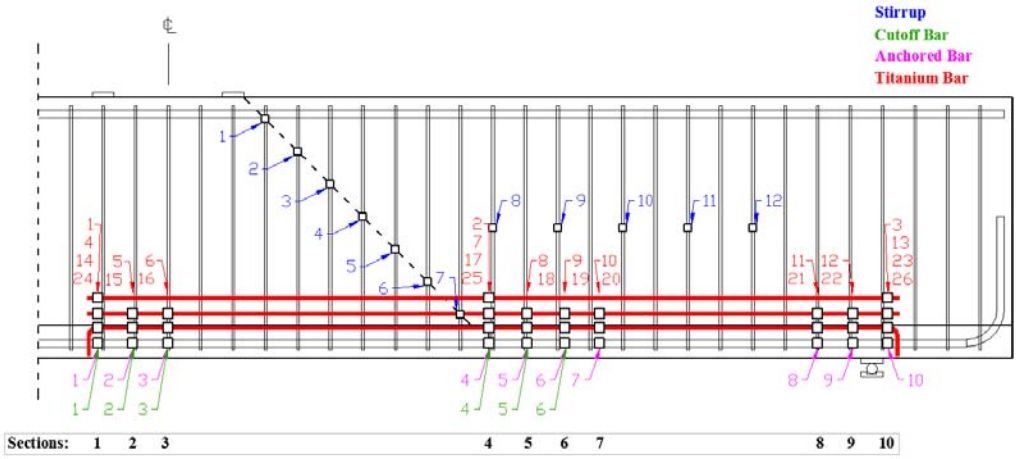


Figure A.6 – Specimen IT.45.Ld3(6).SS strain gage labeling convention

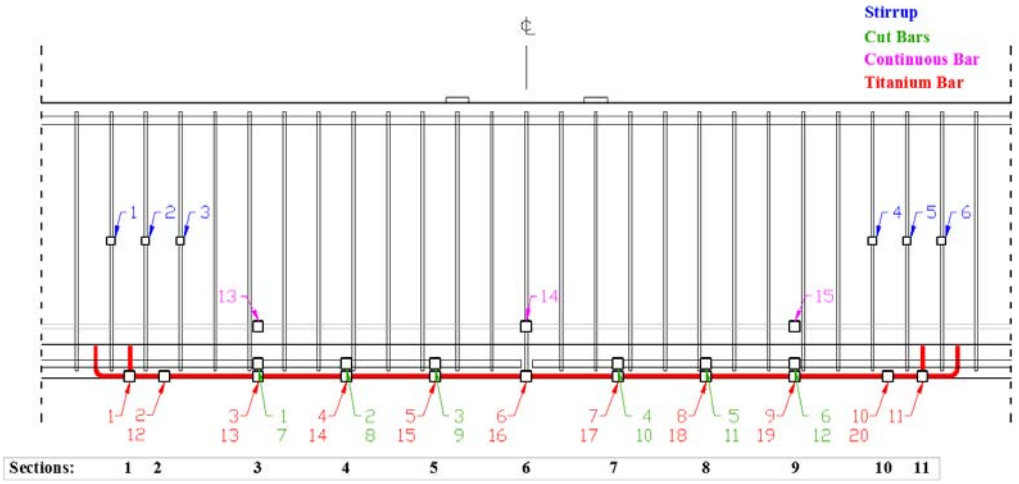


Figure A.7 – Specimen IT.0.0(6).Ti strain gage labeling convention

Figures A.8 through A.103 show the data collected by the instrumentation and the calculated tensile forces.

Figure A.8 – Specimen IT.45.Ld3(10).Ti front and back failure photographs

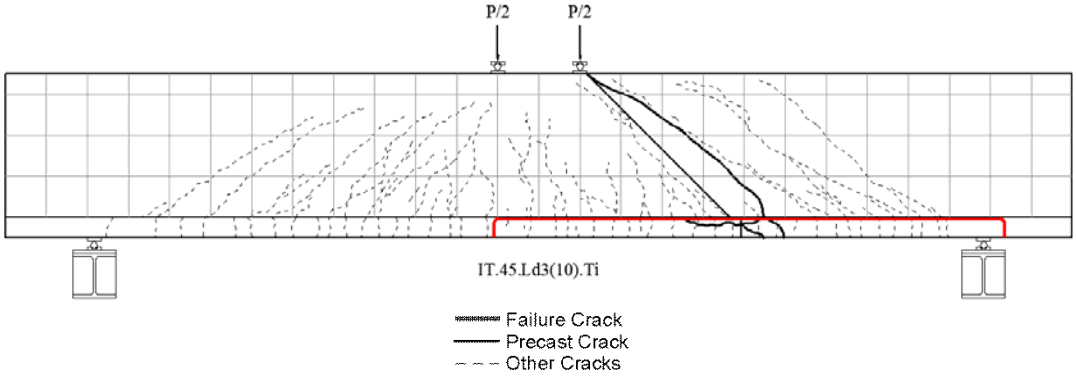


Figure A.9 – Specimen IT.45.Ld3(10).Ti crack mapping with failure cracks

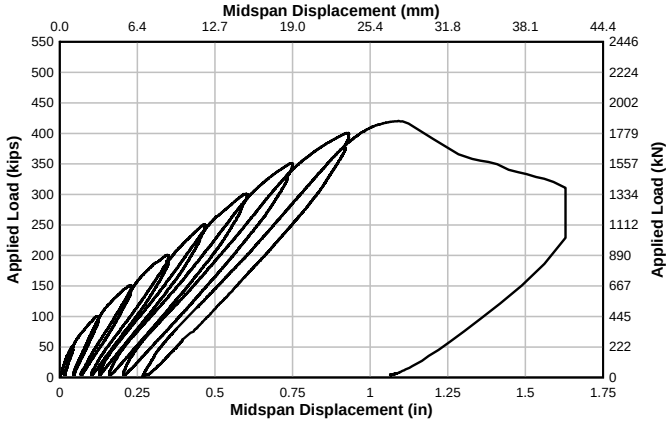


Figure A.10 – Specimen IT.45.Ld3(10).Ti load-displacement response

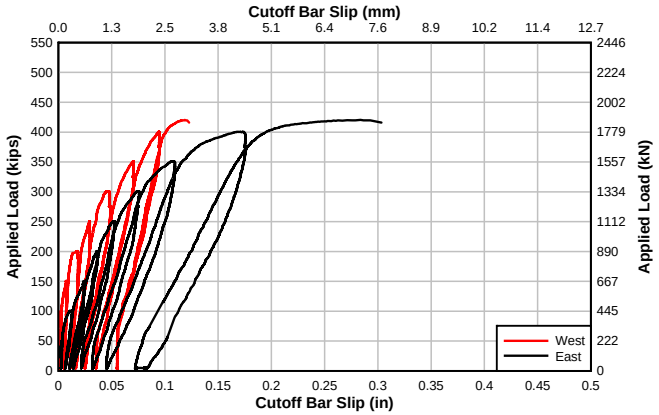


Figure A.11 – Specimen IT.45.Ld3(10).Ti load-cutoff bar slip response

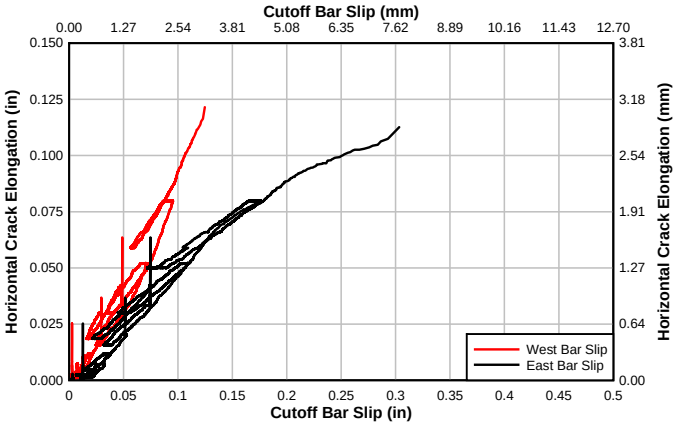


Figure A.12 – Specimen IT.45.Ld3(10).Ti horizontal crack elongation-cutoff bar slip

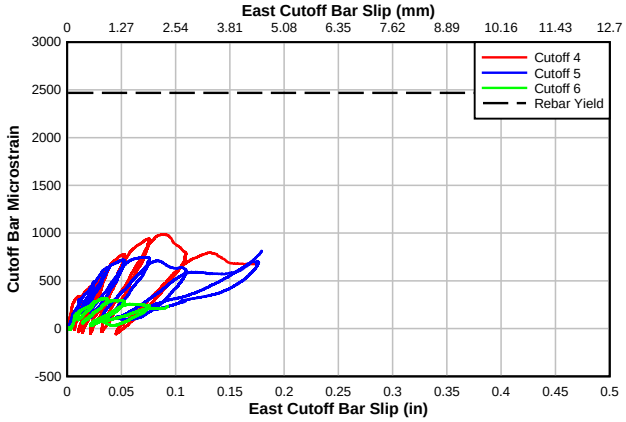


Figure A.13 – Specimen IT.45.Ld3(10).Ti cutoff bar strain-slip

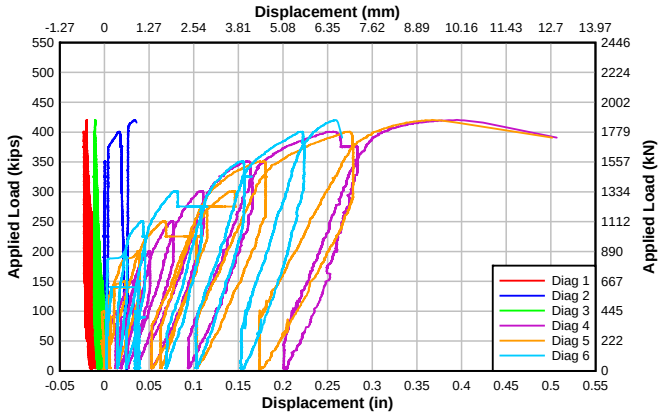


Figure A.14 – Specimen IT.45.Ld3.(10).Ti load-diagonal displacement

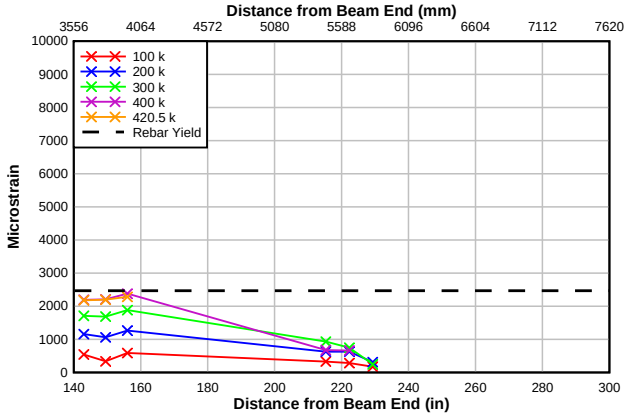


Figure A.15 – Specimen IT.45.Ld3(10).Ti cutoff reinforcing steel strain along specimen length

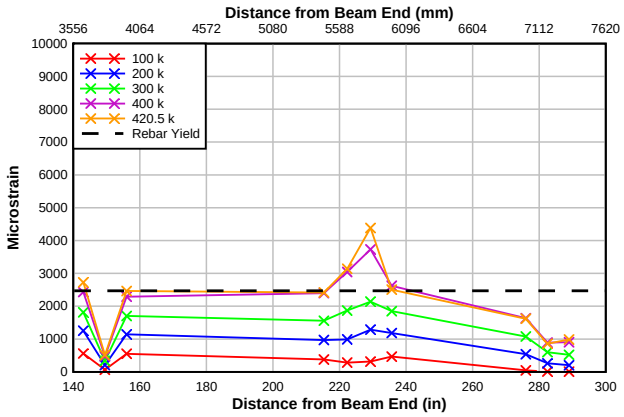


Figure A.16 – Specimen IT.45.Ld3(10).Ti anchored reinforcing steel strain along specimen length

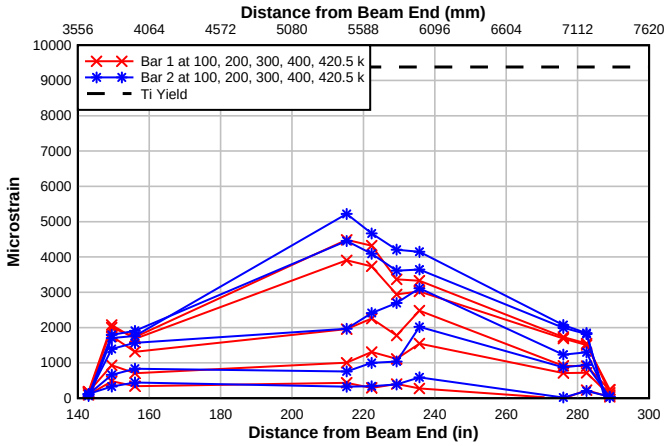


Figure A.17 – Specimen IT.45.Ld3(10).Ti titanium bar strain along specimen length

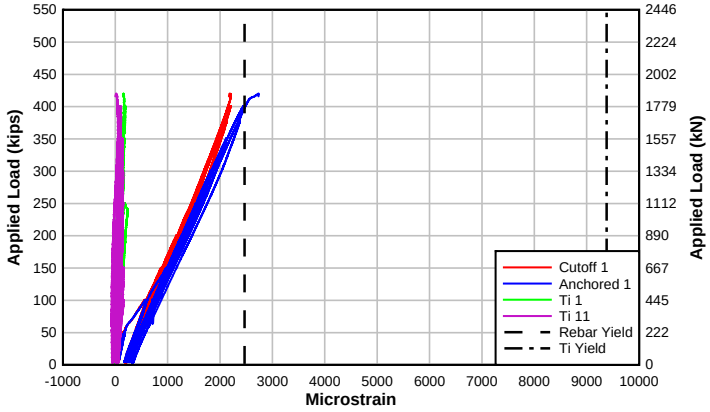


Figure A.18 – Specimen IT.45.Ld3(10).Ti load-flexural bar strain (Section 1)

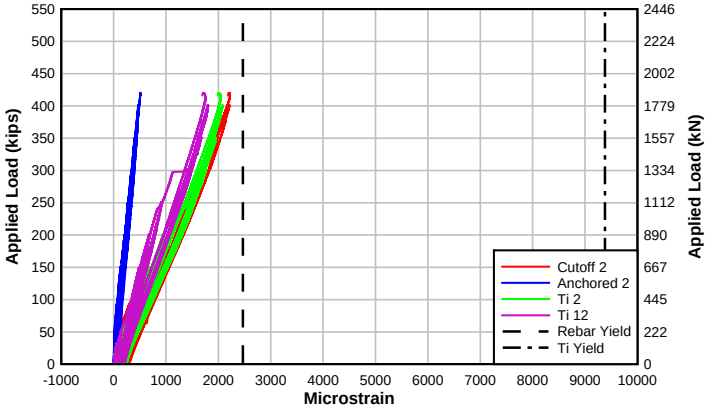


Figure A.19 – Specimen IT.45.Ld3(10).Ti load-flexural bar strain (Section 2)

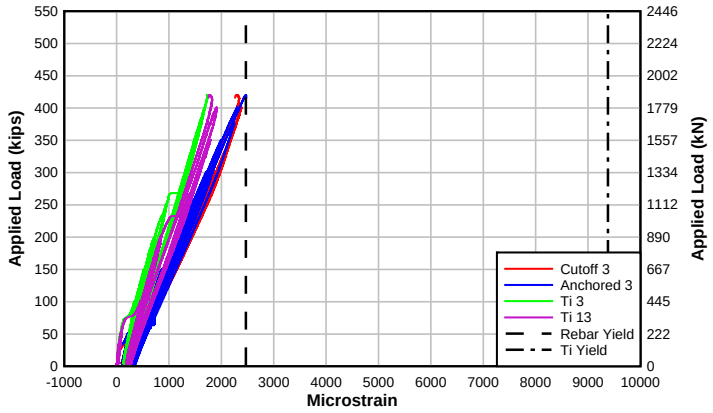


Figure A.20 – Specimen IT.45.Ld3(10).Ti load-flexural bar strain (Section 3)

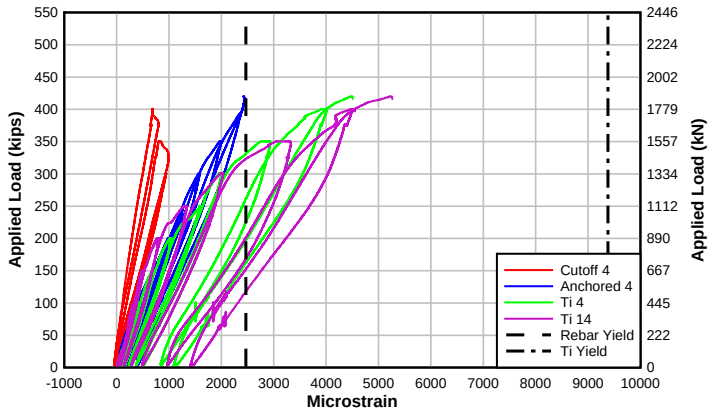


Figure A.21 – Specimen IT.45.Ld3(10).Ti load-flexural bar strain (Section 4)

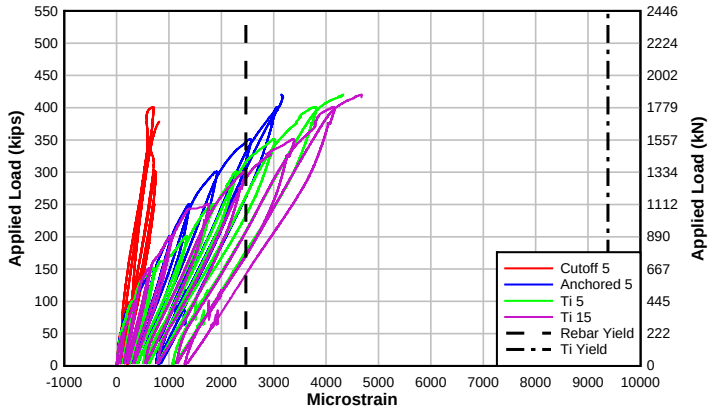


Figure A.22 – Specimen IT.45.Ld3(10).Ti load-flexural bar strain (Section 5)

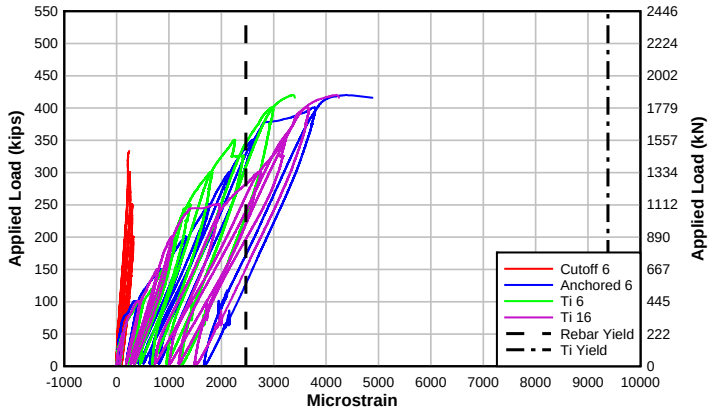


Figure A.23 – Specimen IT.45.Ld3(10).Ti load-flexural bar strain (Section 6)

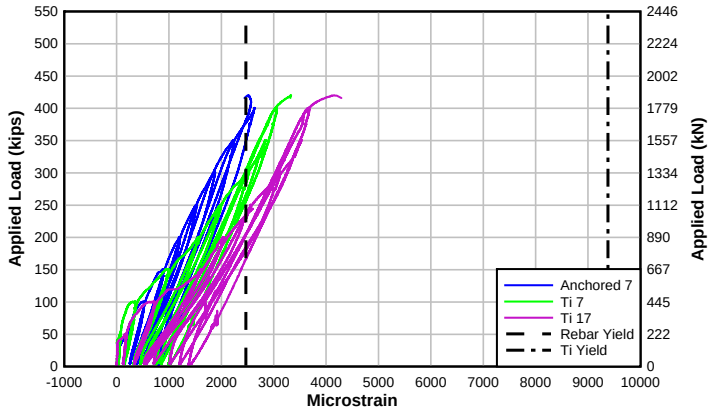


Figure A.24 – Specimen IT.45.Ld3(10).Ti load-flexural bar strain (Section 7)

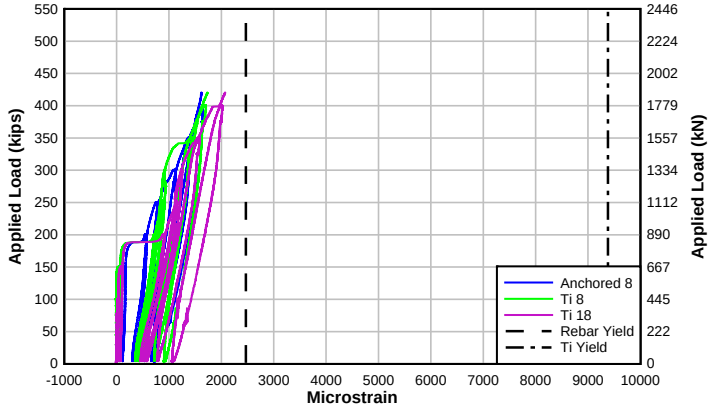


Figure A.25 – Specimen IT.45.Ld3(10).Ti load-flexural bar strain (Section 8)

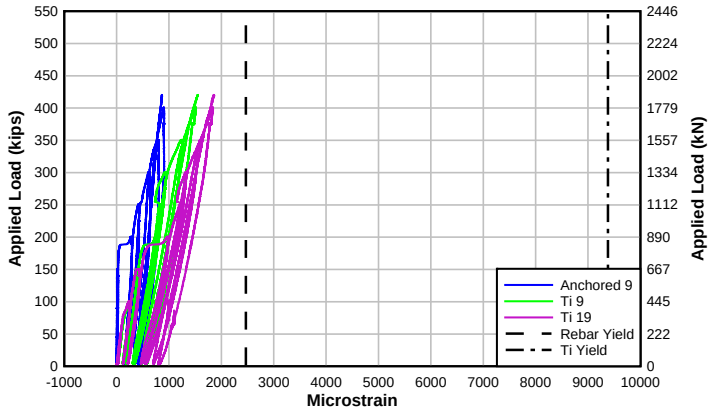


Figure A.26 – Specimen IT.45.Ld3(10).Ti load-flexural bar strain (Section 9)

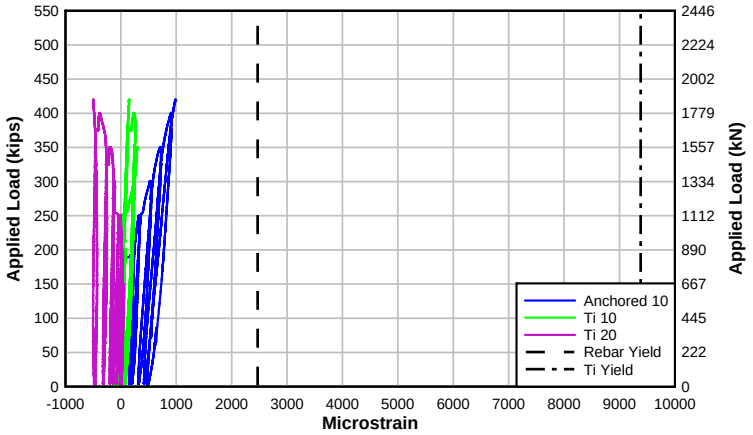


Figure A.27 – Specimen IT.45.Ld3(10).Ti load-flexural bar strain (Section 10)

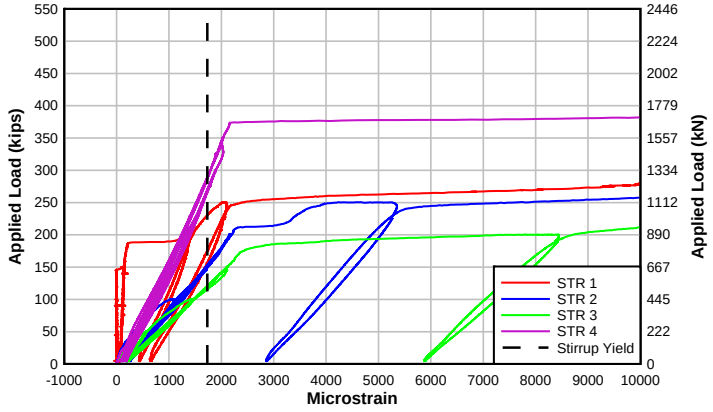


Figure A.28 – Specimen IT.45.Ld3(10).Ti load-preformed crack stirrup strain

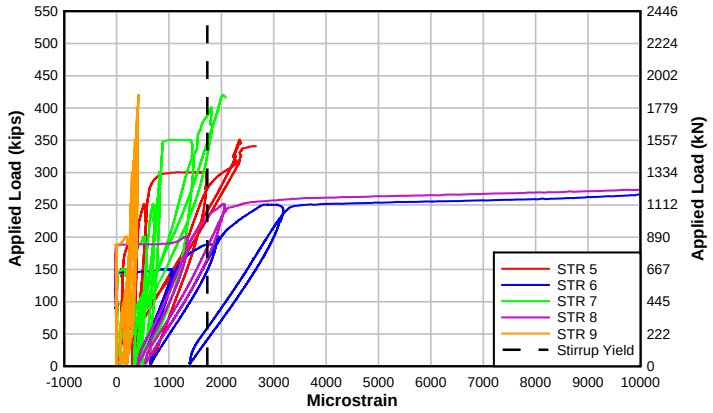


Figure A.29 – Specimen IT.45.Ld3(10).Ti load-mid-height stirrup strain

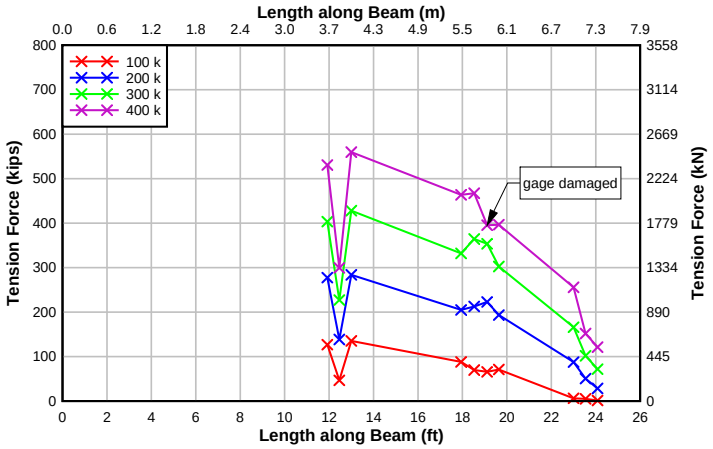


Figure A.30 – Specimen IT.45.Ld3(10) tension force in all flexural tension reinforcement along beam

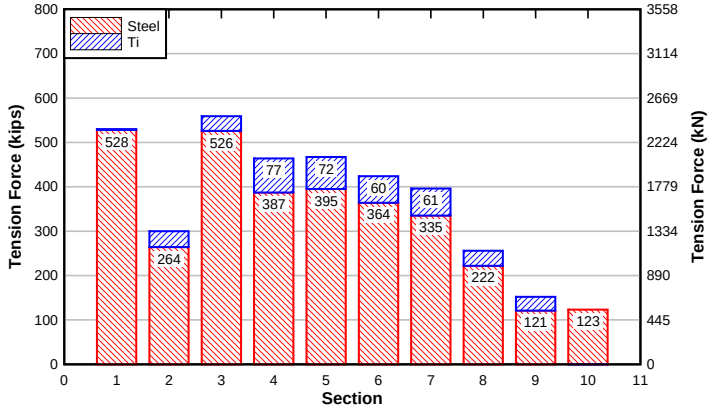


Figure A.31 – Specimen IT.45.Ld3(10).Ti tension force contribution-section at 400 kips (1780 kN)

Figure A.32 – Specimen IT.45.Ld3(6).Ti front and back failure photographs

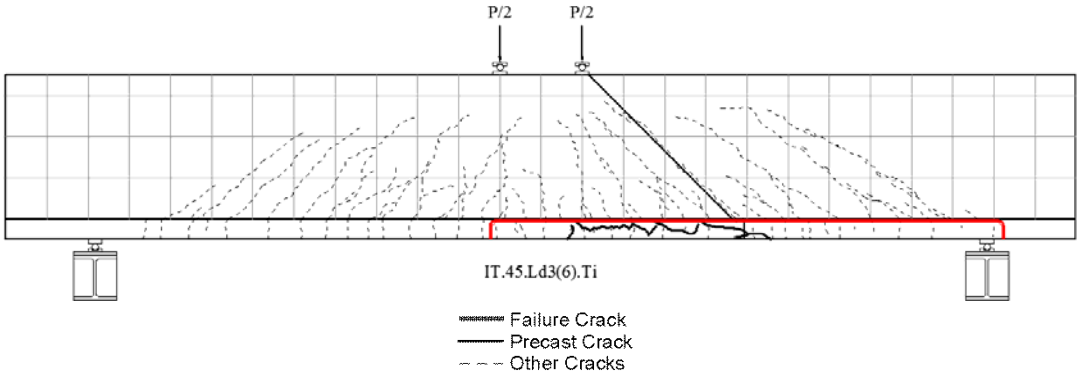


Figure A.33 – Specimen IT.45.Ld3(6).Ti crack mapping with failure cracks

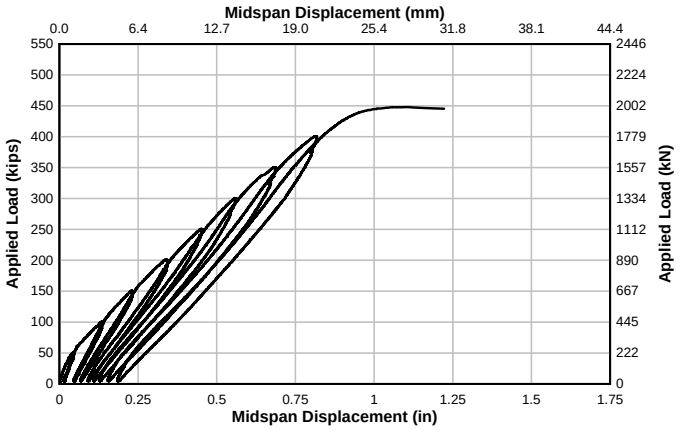


Figure A.34 – Specimen IT.45.Ld3(6).Ti load-displacement response

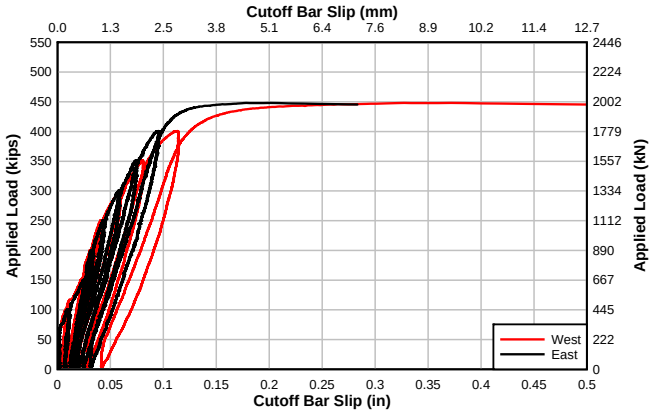


Figure A.35 – Specimen IT.45.Ld3(6).Ti load-cutoff bar slip response

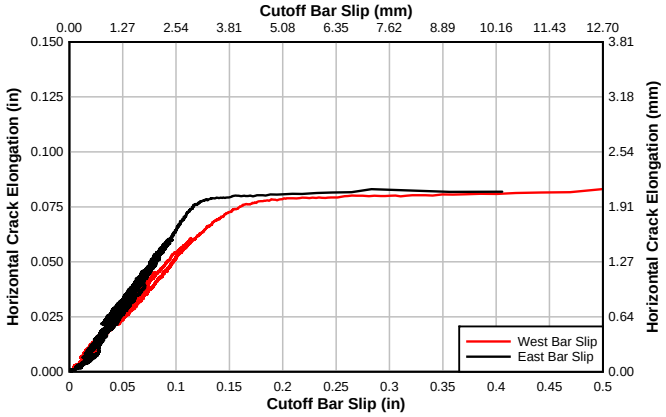


Figure A.36 – Specimen IT.45.Ld3(6).Ti horizontal crack elongation-cutoff bar slip

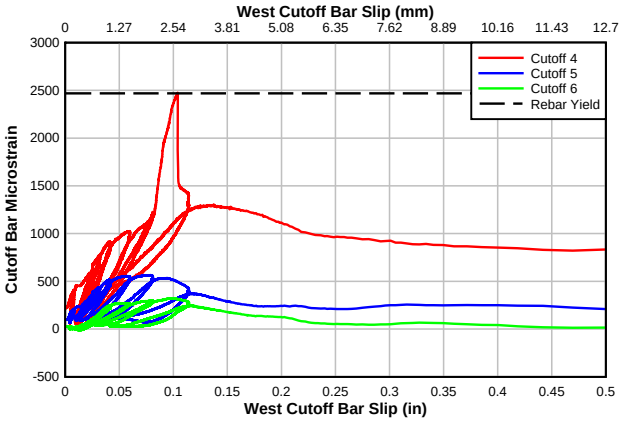


Figure A.37 – Specimen IT.45.Ld3(6).Ti cutoff bar strain-slip

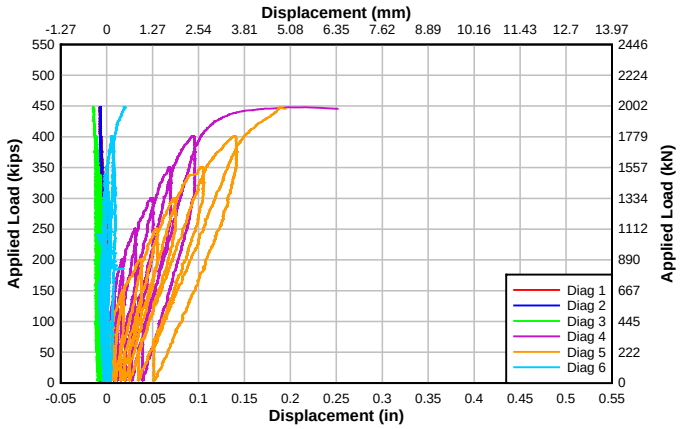


Figure A.38 – Specimen IT.45.Ld3(6).Ti load-diagonal displacement (north)

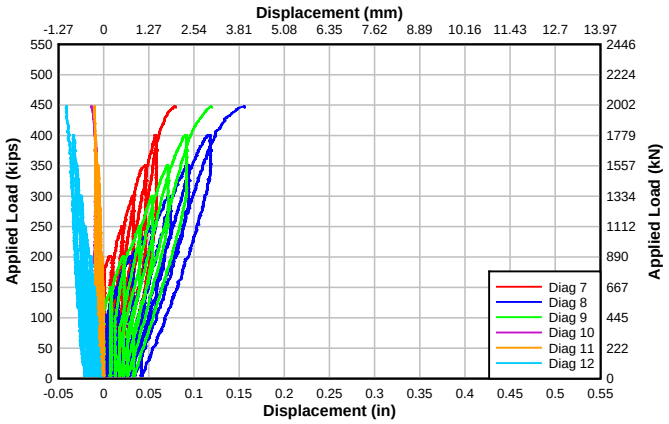


Figure A.39 – Specimen IT.45.Ld3(6).Ti load-diagonal displacement (south)

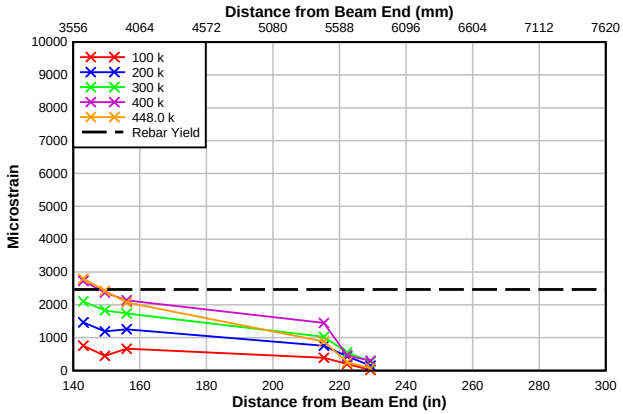


Figure A.40 – Specimen IT.45.Ld3(6).Ti cutoff reinforcing steel strain along specimen length

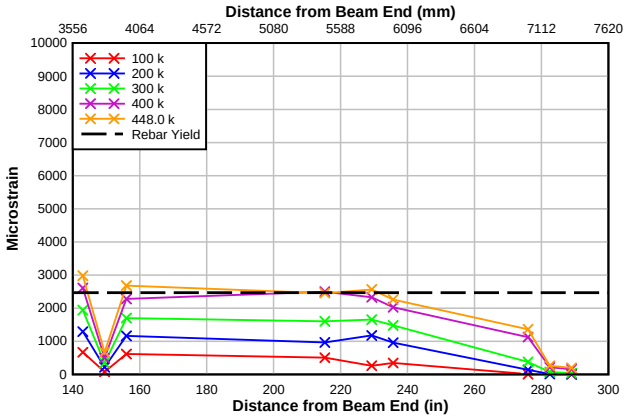


Figure A.41 – Specimen IT.45.Ld3(6).Ti anchored reinforcing steel strain along specimen length

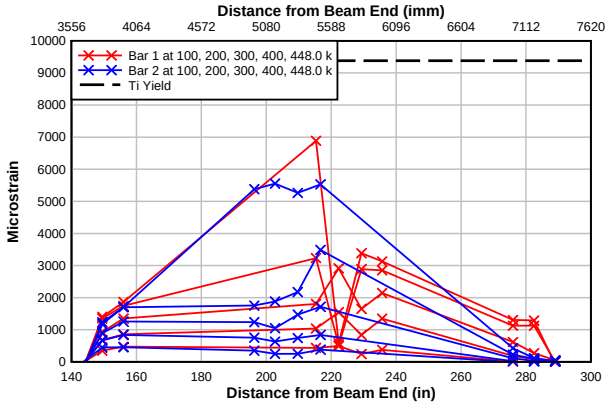


Figure A.42 – Specimen IT.45.Ld3(6).Ti titanium bar strain along specimen length

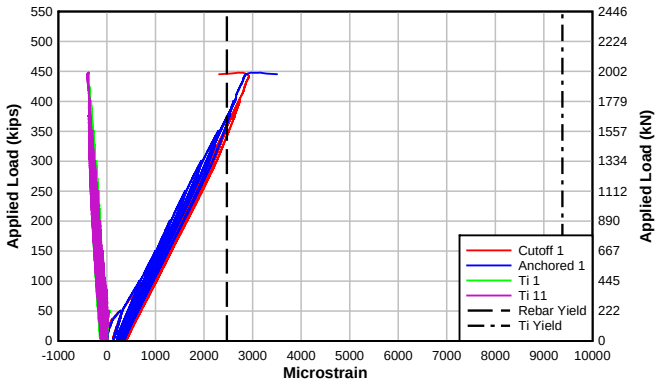


Figure A.43 – Specimen IT.45.Ld3(6).Ti load-flexural bar strain (Section 1)

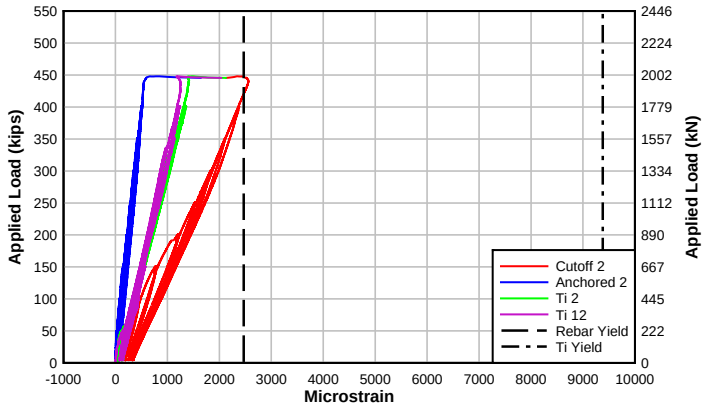


Figure A.44 – Specimen IT.45.Ld3(6).Ti load-flexural bar strain (Section 2)

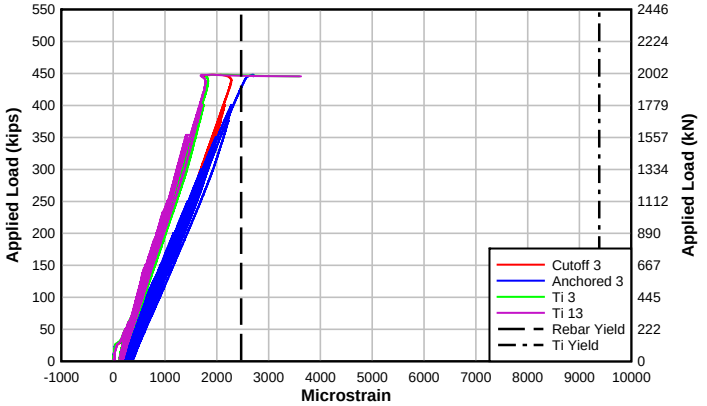


Figure A.45 – Specimen IT.45.Ld3(6).Ti load-flexural bar strain (Section 3)

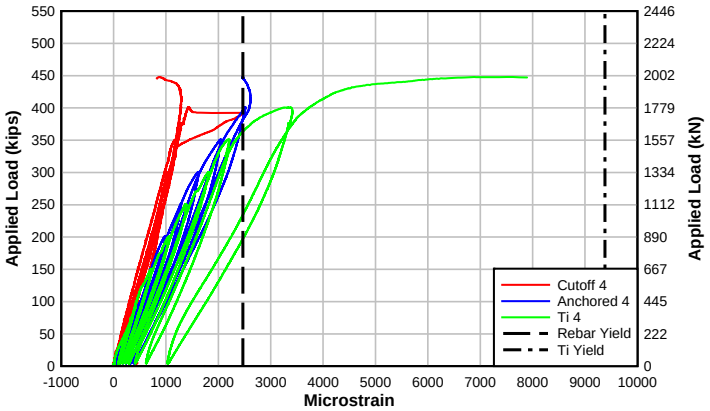


Figure A.46 – Specimen IT.45.Ld3(6).Ti load-flexural bar strain (Section 4)

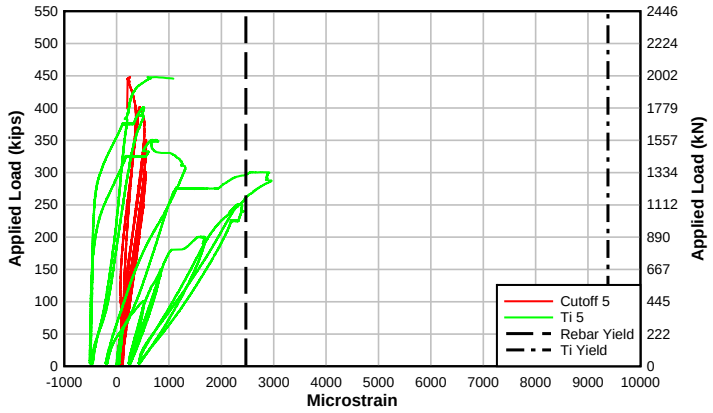


Figure A.47 – Specimen IT.45.Ld3(6).Ti load-flexural bar strain (Section 5)

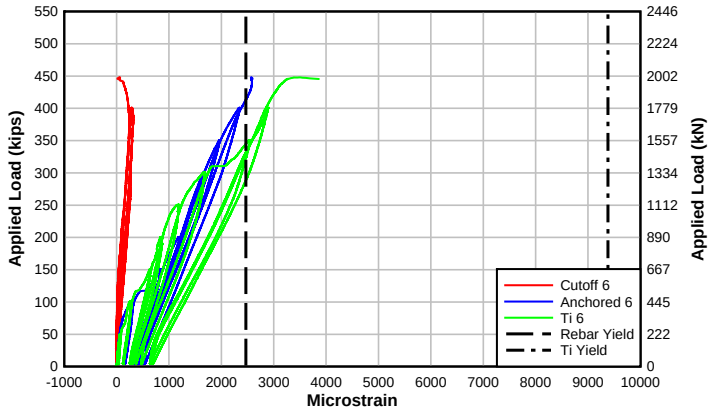


Figure A.48 – Specimen IT.45.Ld3(6).Ti load-flexural bar strain (Section 6)

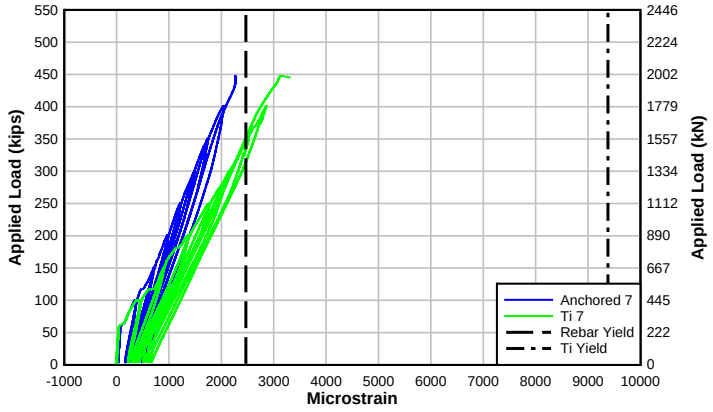


Figure A.49 – Specimen IT.45.Ld3(6).Ti load-flexural bar strain (Section 7)

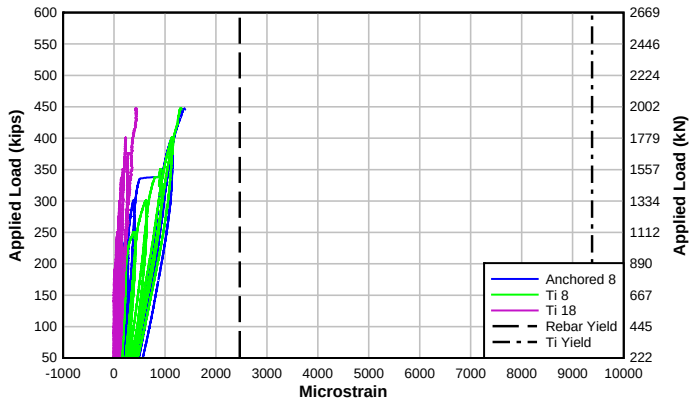


Figure A.50 – Specimen IT.45.Ld3(6).Ti load-flexural bar strain (Section 8)

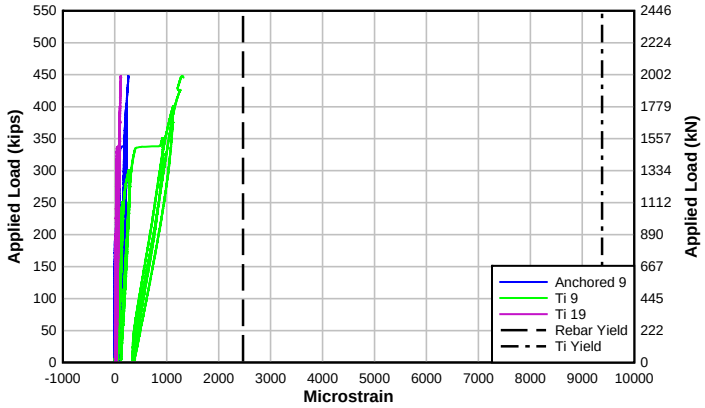


Figure A.51 – Specimen IT.45.Ld3(6).Ti load-flexural bar strain (Section 9)

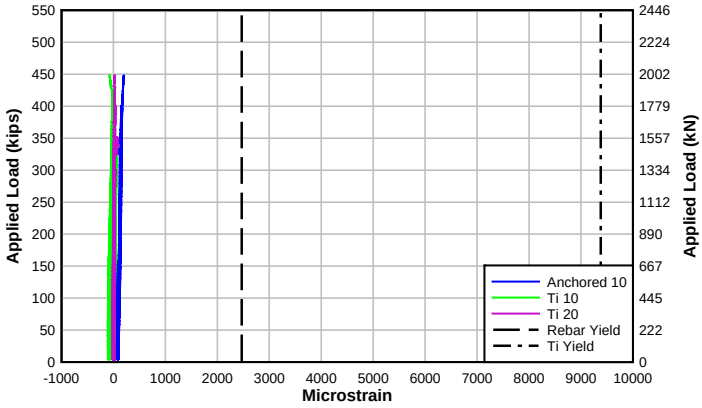


Figure A.52 – Specimen IT.45.Ld3(6).Ti load-flexural bar strain (Section 10)

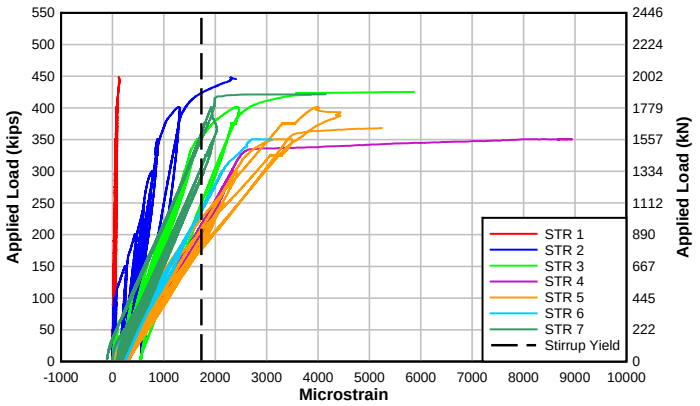


Figure A.53 – Specimen IT.45.Ld3(6).Ti load-preformed crack stirrup strain

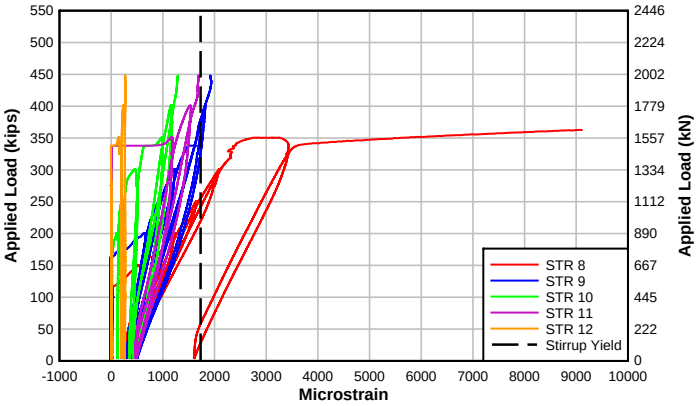


Figure A.54 – Specimen IT.45.Ld3(6).Ti load-mid-height stirrup strain

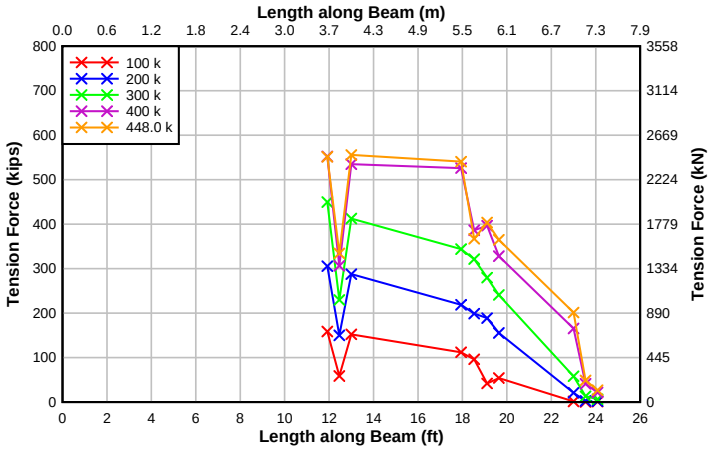


Figure A.55 – Specimen IT.45.Ld3(6).Ti tension force in all flexural tension reinforcement along beam

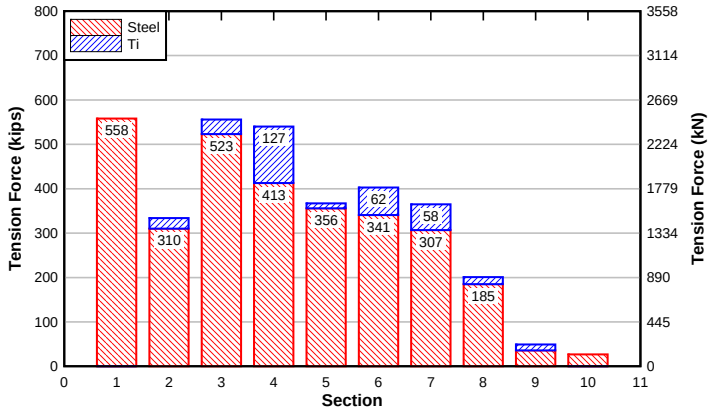


Figure A.56 – Specimen IT.45.Ld3(6).Ti tension force contribution-section at failure

Figure A.57 – Specimen IT.45.Ld3(6).SS front and back failure photographs

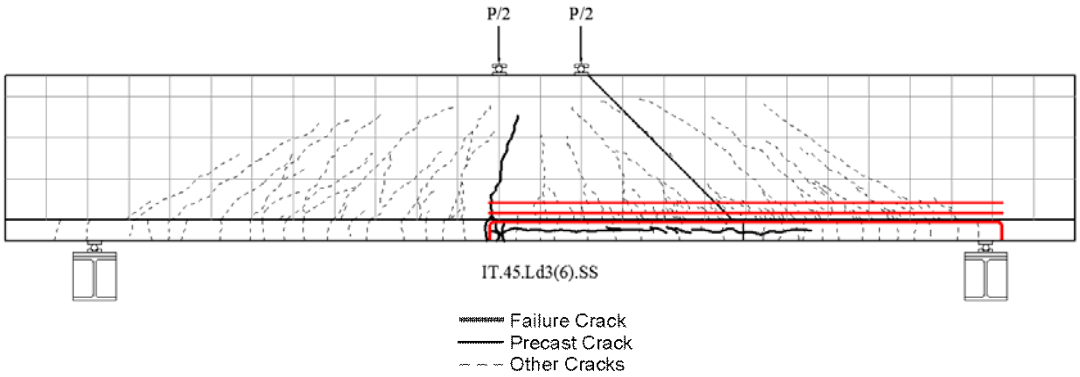


Figure A.58 – Specimen It.45.Ld3(6).SS crack mapping with failure cracks

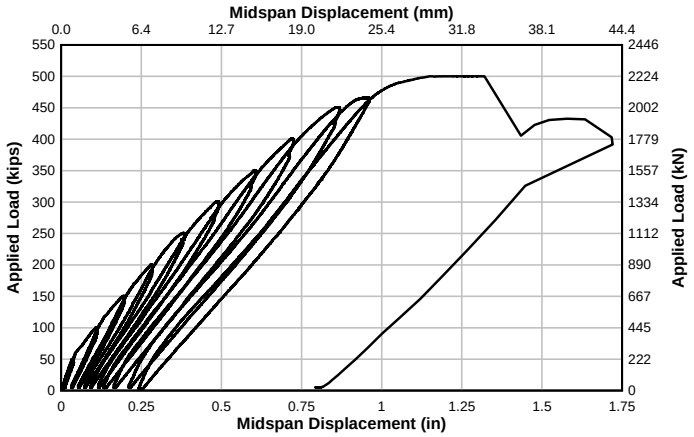


Figure A.59 – Specimen IT.45.Ld3(6).SS load-displacement response

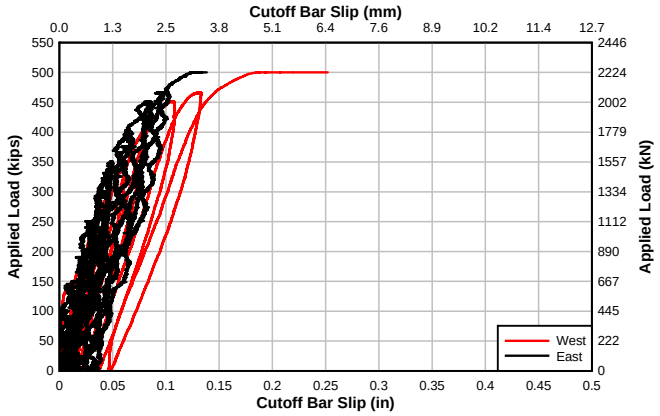


Figure A.60 – Specimen IT.45.Ld3(6).SS load-cutoff bar slip response

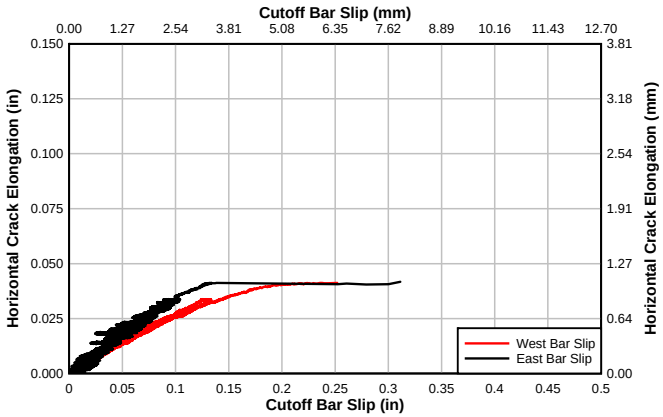


Figure A.61 – Specimen IT.45.Ld3(6).SS horizontal crack elongation-cutoff bar slip

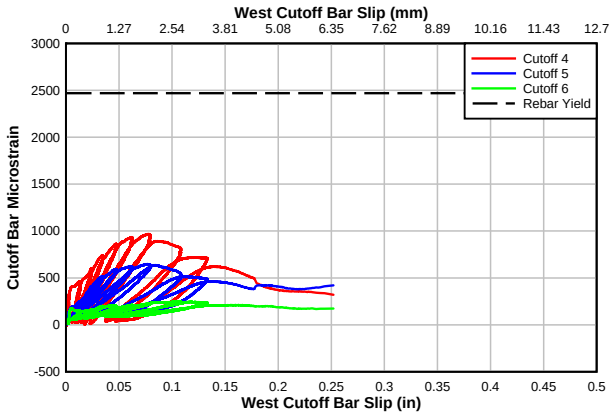


Figure A.62 – Specimen IT.45.Ld3(6).SS cutoff bar strain-slip

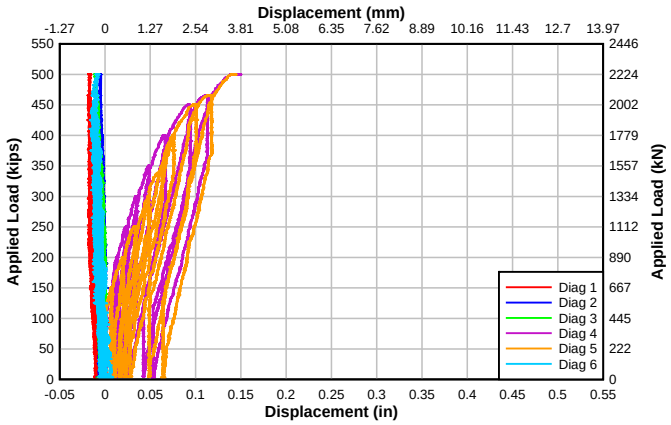


Figure A.63 – Specimen IT.45.Ld3(6).SS load-diagonal displacement (north)

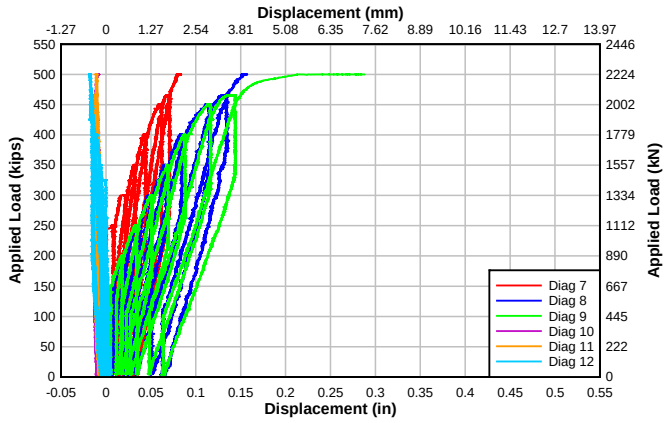


Figure A.64 – Specimen IT.45.Ld3(6).SS load-diagonal displacement (south)

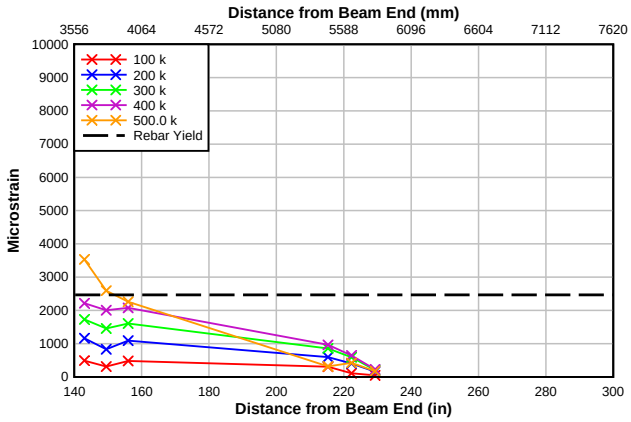


Figure A.65 – Specimen IT.45.Ld3(6).SS cutoff reinforcing steel strain along specimen length

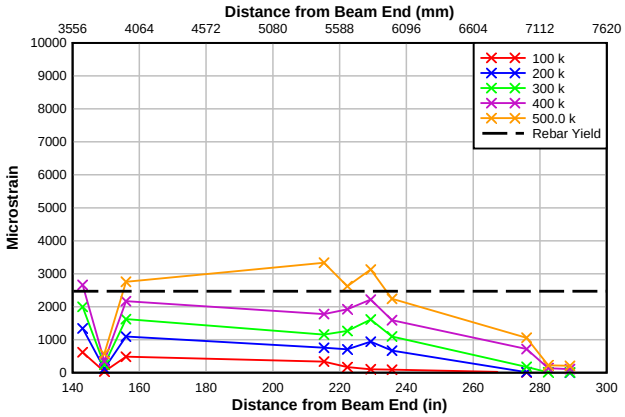


Figure A.66 – Specimen IT.45.Ld3(6).SS anchored reinforcing steel strain along specimen length

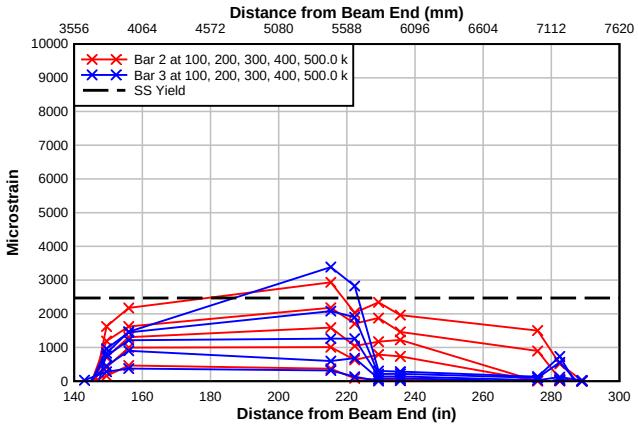


Figure A.67 – Specimen IT.45.Ld3(6).SS stainless steel strain along specimen length

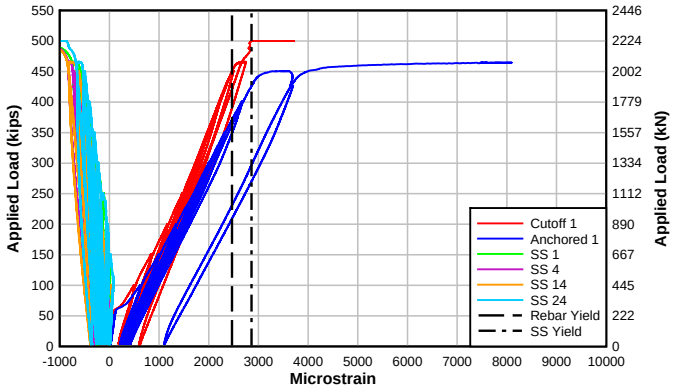


Figure A.68 – Specimen IT.45.Ld3(6).SS load-flexural bar strain (Section 1)

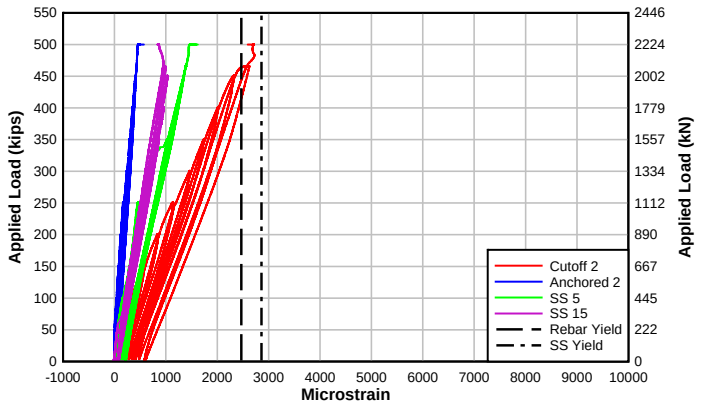


Figure A.69 – Specimen IT.45.Ld3(6).SS load-flexural bar strain (Section 2)

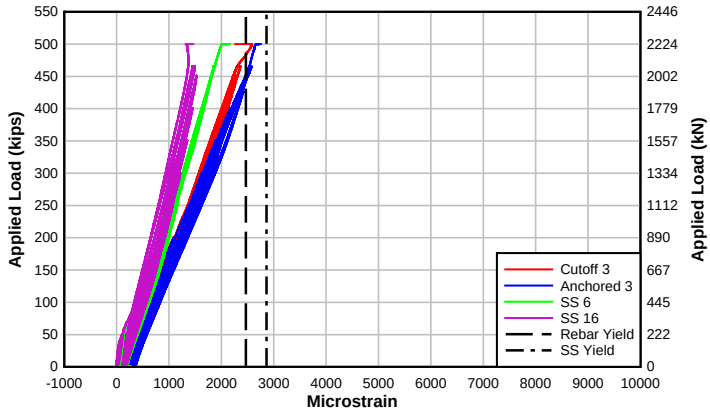


Figure A.70 – Specimen IT.45.Ld3(6).SS load-flexural bar strain (Section 3)

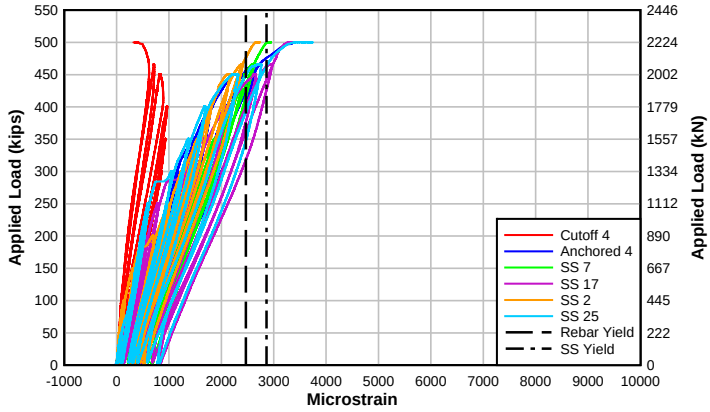


Figure A.71 – Specimen IT.45.Ld3(6).SS load-flexural bar strain (Section 4)

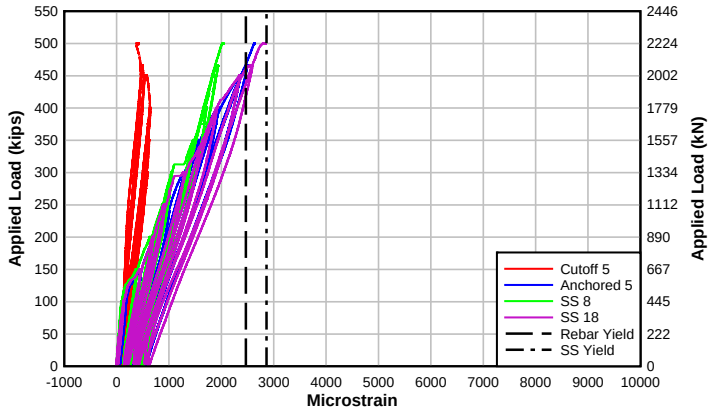


Figure A.72 – Specimen IT.45.Ld3(6).SS load-flexural bar strain (Section 5)

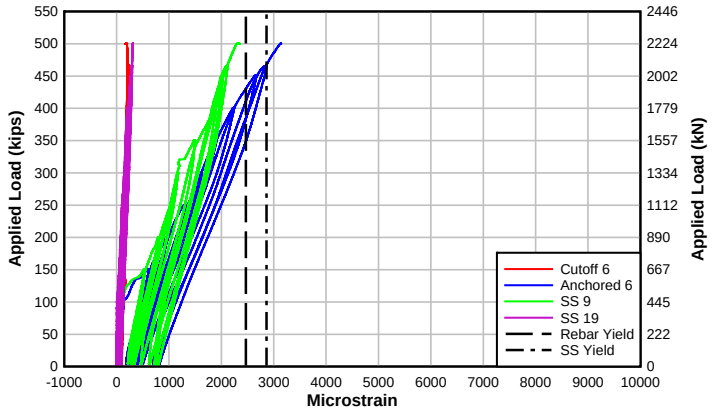


Figure A.73 – Specimen IT.45.Ld3(6).SS load-flexural bar strain (Section 6)

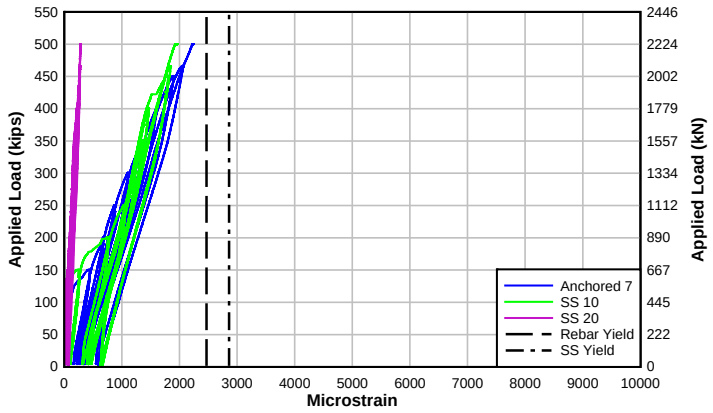


Figure A.74 – Specimen IT.45.Ld3(6).SS load-flexural bar strain (Section 7)

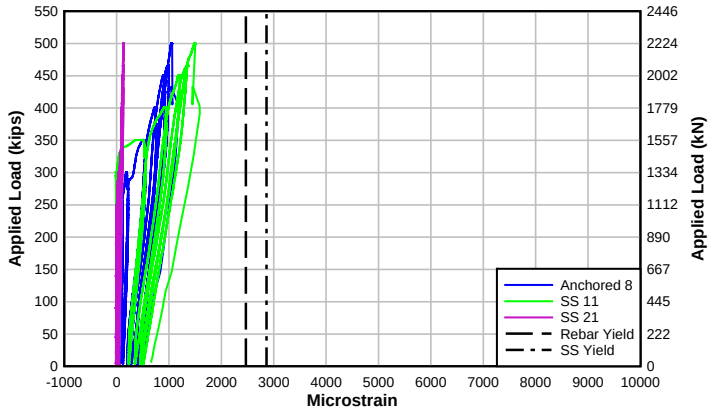


Figure A.75 – Specimen IT.45.Ld3(6).SS load-flexural bar strain (Section 8)

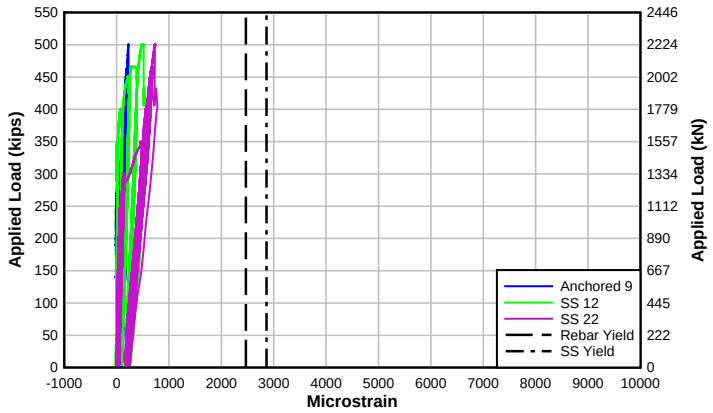


Figure A.76 – Specimen IT.45.Ld3(6).SS load-flexural bar strain (Section 9)

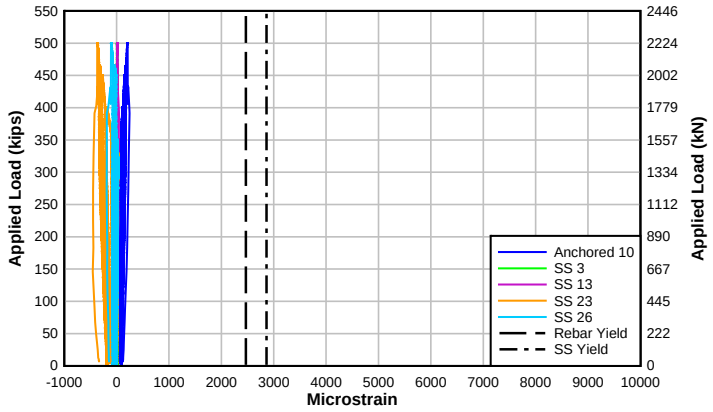


Figure A.77 – Specimen IT.45.Ld3(6).SS load-flexural bar strain (Section 10)

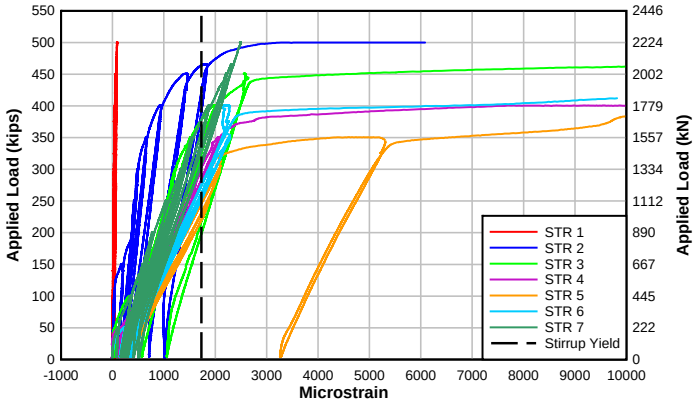


Figure A.78 – Specimen IT.45.Ld3(6).SS load-preformed crack stirrup strain

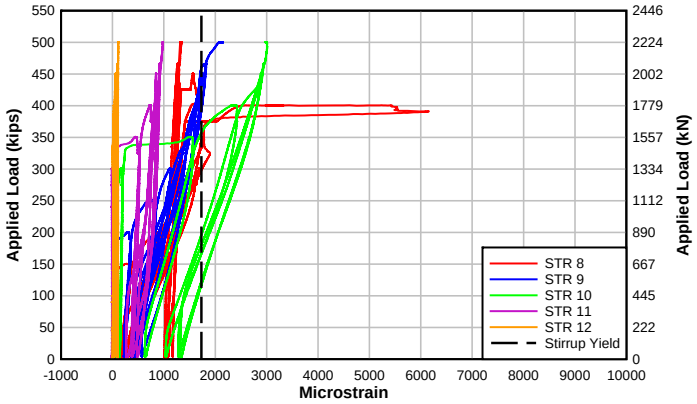


Figure A.79 – Specimen IT.45.Ld3(6).SS load-mid-height stirrup strain

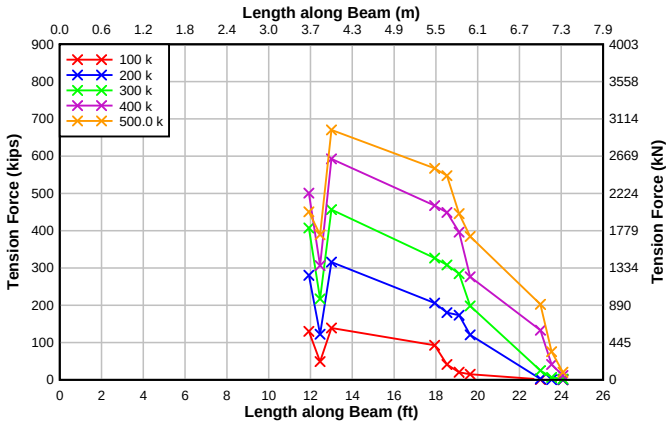


Figure A.80 – Specimen IT.45.Ld3(6).SS tension force in all flexural tension reinforcement along beam

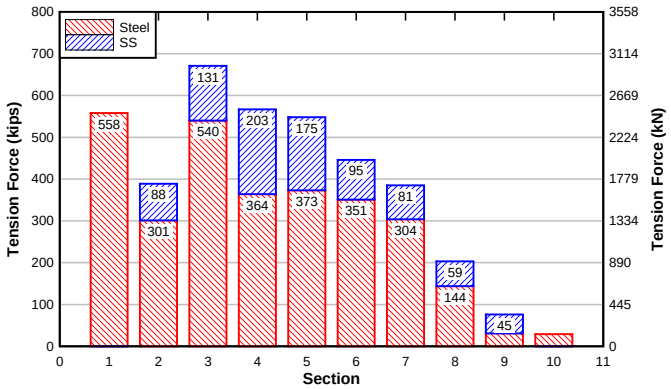


Figure A.81 – Specimen IT.45.Ld3(6).SS tension force contribution-section at failure

Figure A.82 – Specimen IT.0.0(6).Ti front and back failure photographs

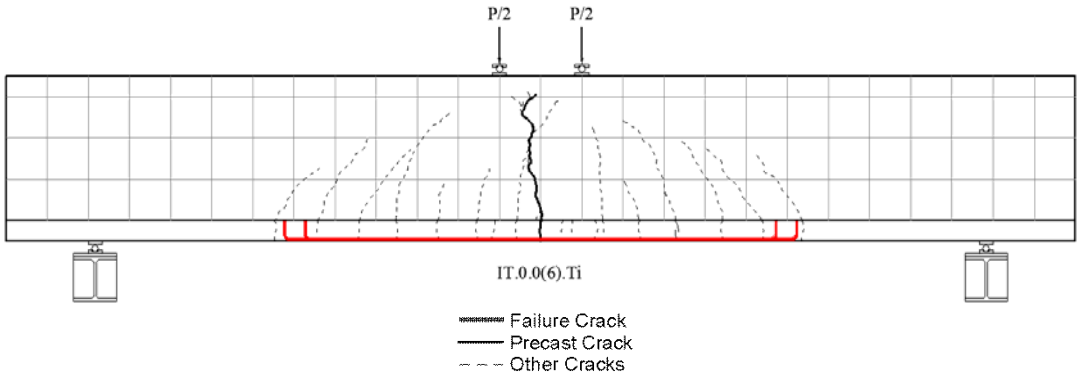


Figure A.83 – Specimen IT.0.0(6).Ti crack mapping with failure cracks

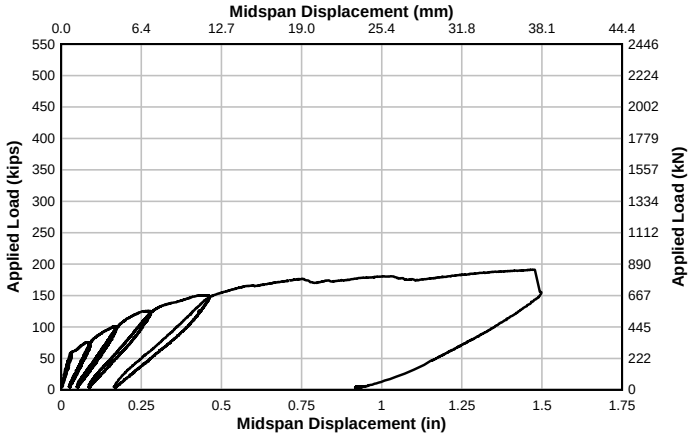


Figure A.84 – Specimen IT.0.0(6).Ti load-displacement

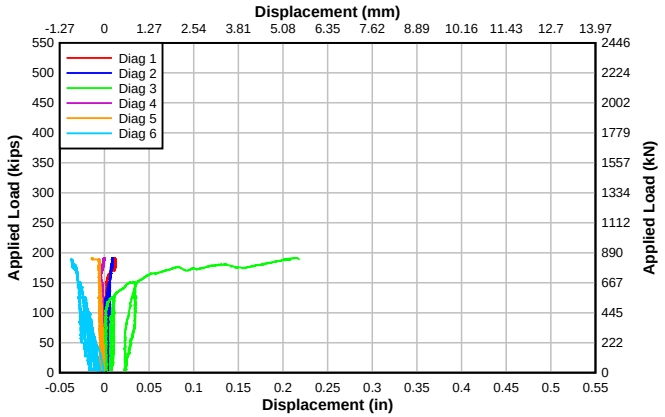


Figure A.85 – Specimen IT.0.0(6).Ti load-diagonal displacement

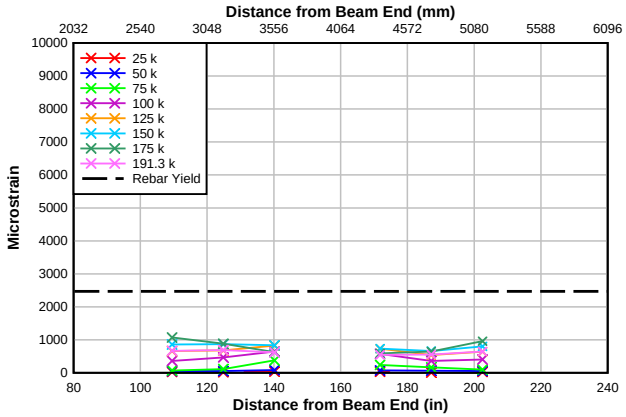


Figure A.86 – Specimen IT.0.0(6).Ti center cutoff reinforcing steel strain along specimen length

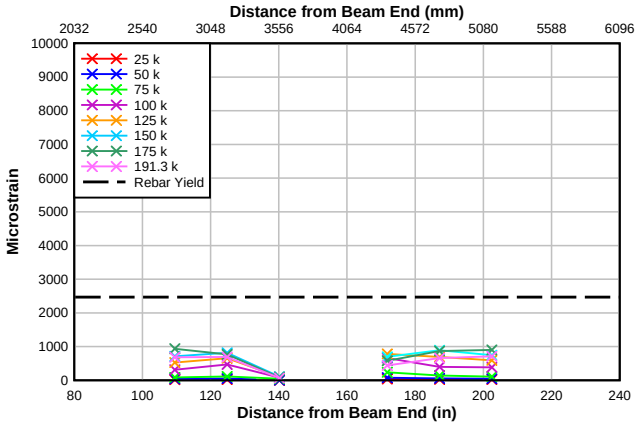


Figure A.87 – Specimen IT.0.0(6).Ti outside cutoff reinforcing steel strain along specimen length

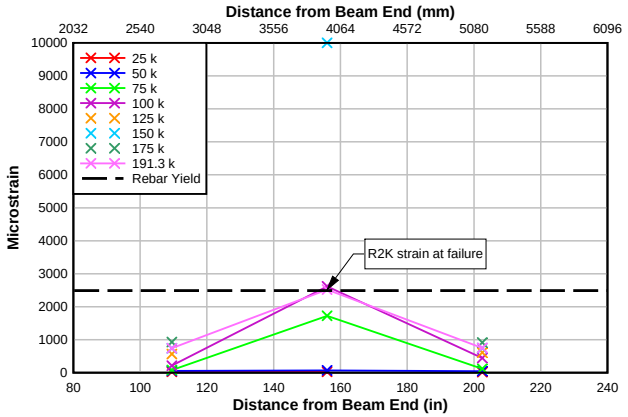


Figure A.88 – Specimen IT.0.0(6).Ti continuous #6 reinforcing steel strain along specimen length

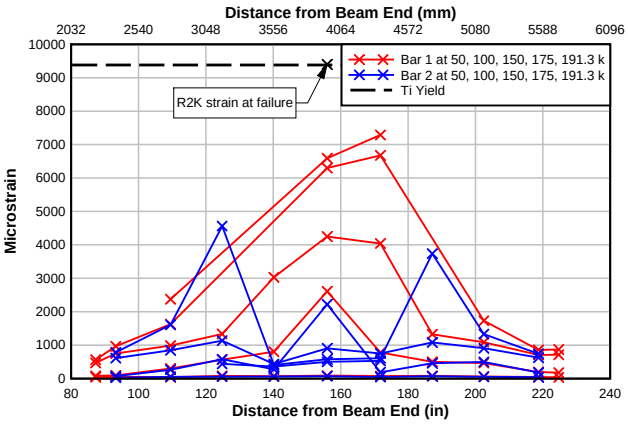


Figure A.89 – Specimen IT.0.0(6).Ti titanium bar strain along specimen length

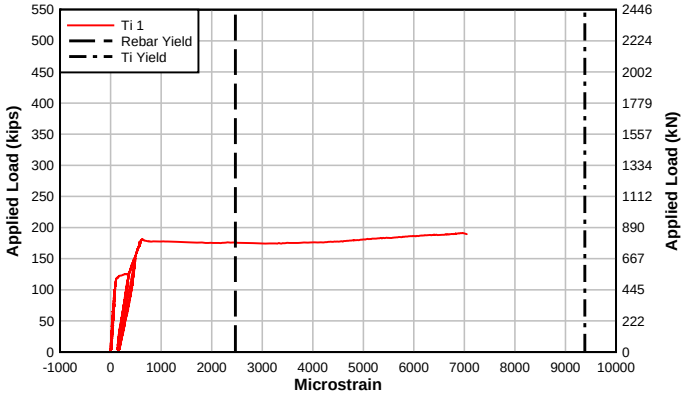


Figure A.90 – Specimen IT.0.0(6).Ti load-flexural bar strain (Section 1)

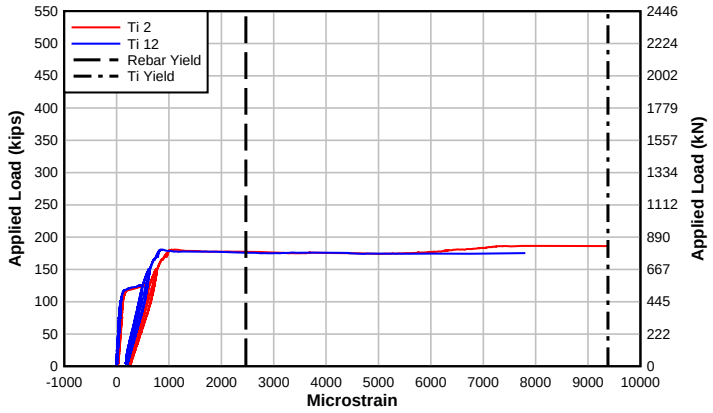


Figure A.91 – Specimen IT.0.0(6).Ti load-flexural bar strain (Section 2)

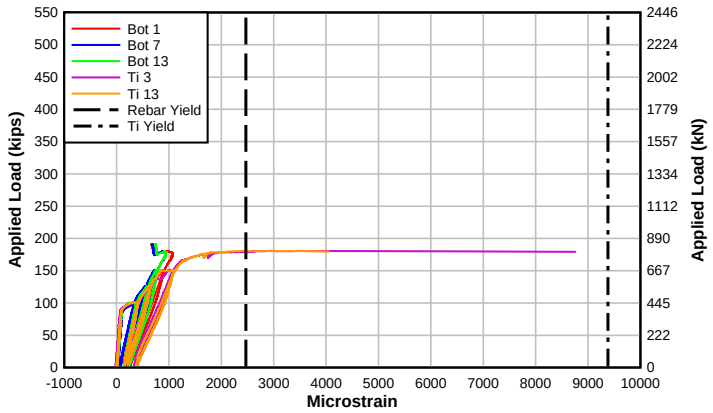


Figure A.92 – Specimen IT.0.0(6).Ti load-flexural bar strain (Section 3)

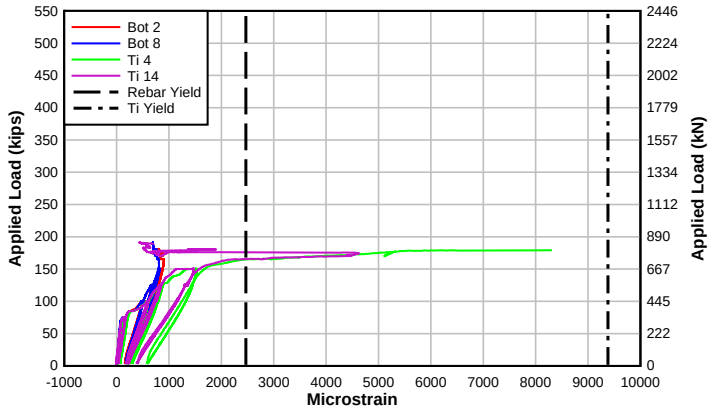


Figure A.93 – Specimen IT.0.0(6).Ti load-flexural bar strain (Section 4)

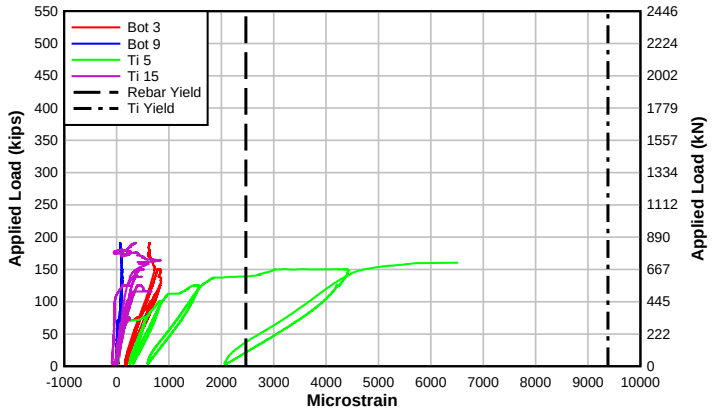


Figure A.94 – Specimen IT.0.0(6).Ti load-flexural bar strain (Section 5)

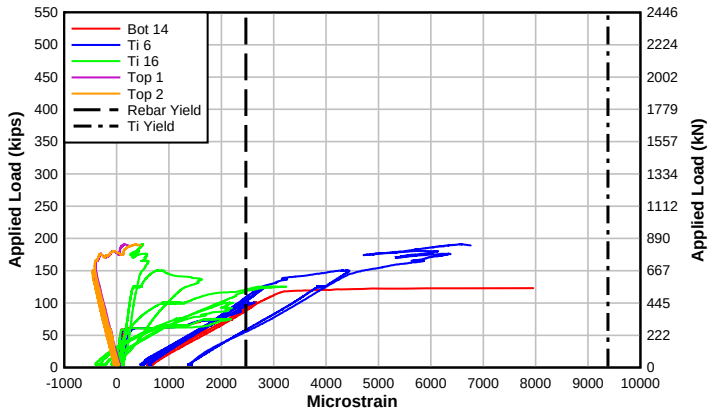


Figure A.95 – Specimen IT.0.0(6).Ti load-flexural bar strain (Section 6)

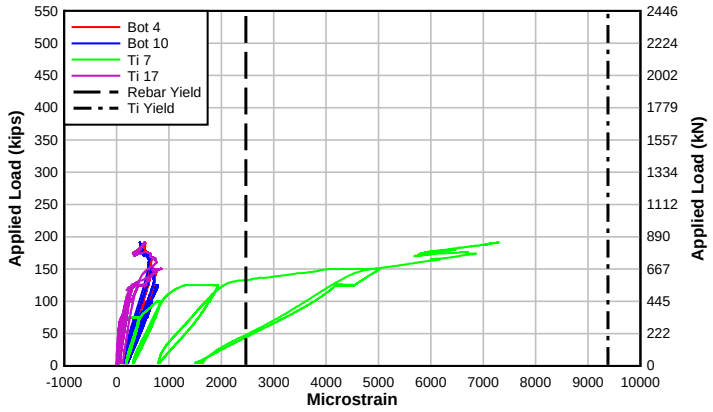


Figure A.96 – Specimen IT.0.0(6).Ti load-flexural bar strain (Section 7)

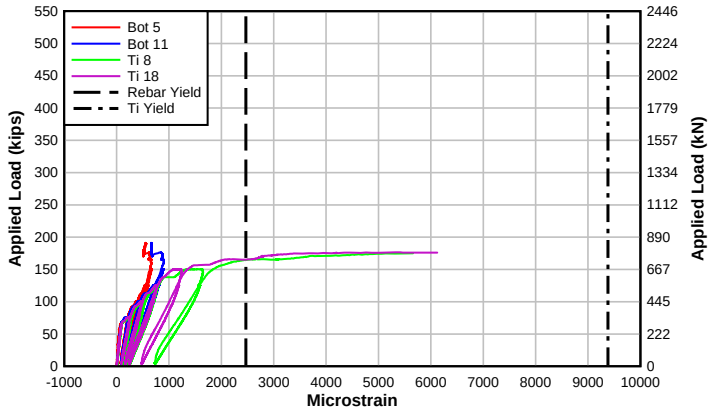


Figure A.97 – Specimen IT.0.0(6).Ti load-flexural bar strain (Section 8)

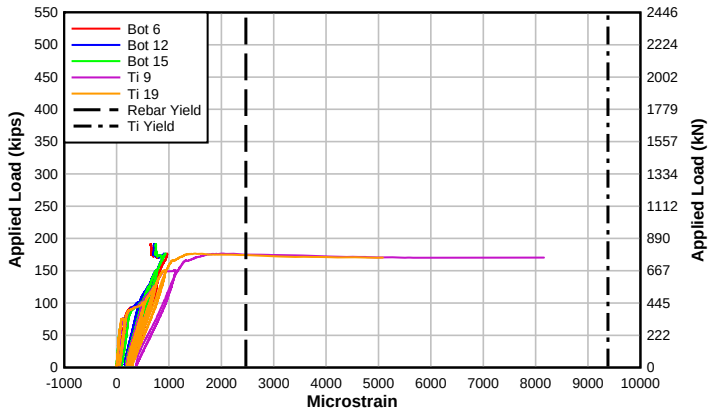


Figure A.98 – Specimen IT.0.0(6).Ti load-flexural bar strain (Section 9)

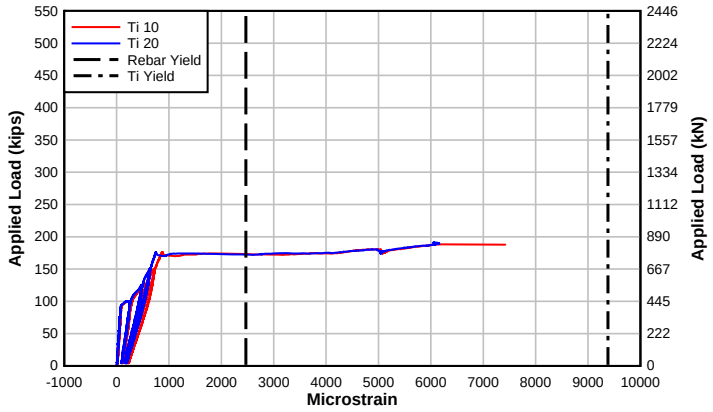


Figure A.99 – Specimen IT.0.0(6).Ti load-flexural bar strain (Section 10)

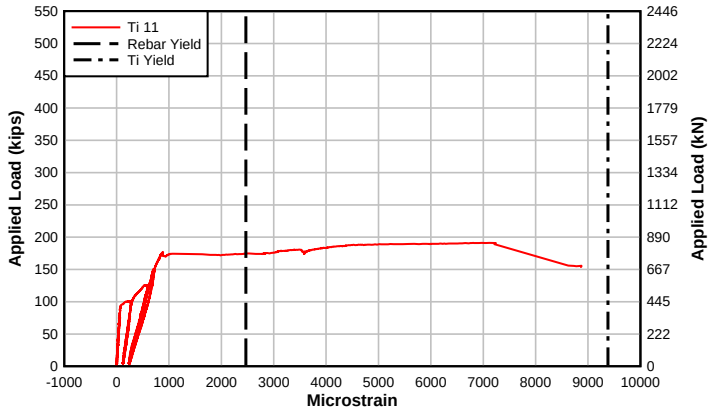


Figure A.100 – Specimen IT.0.0(6).Ti load-flexural bar strain (Section 10)

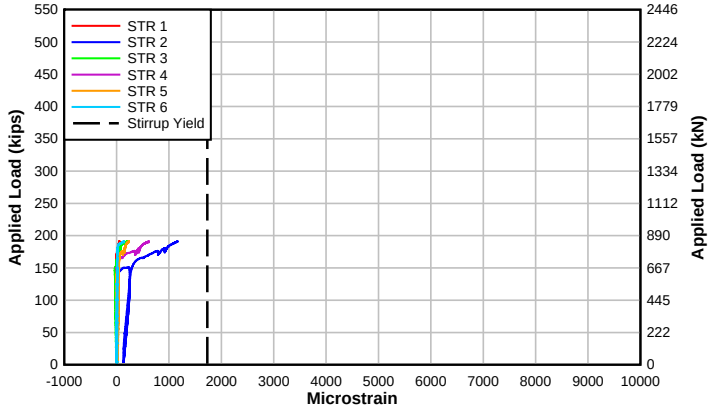


Figure A.101 – Specimen IT.0.0(6).Ti load-mid-height stirrup strain

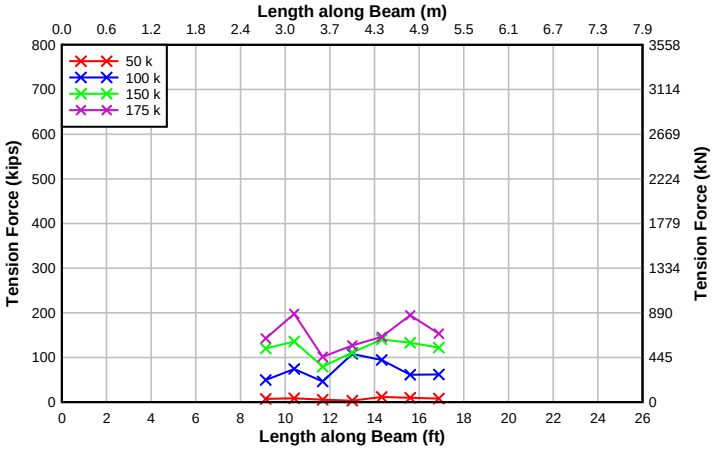


Figure A.102 – Specimen IT.0.0(6).Ti tension force in all flexural tension reinforcement along beam

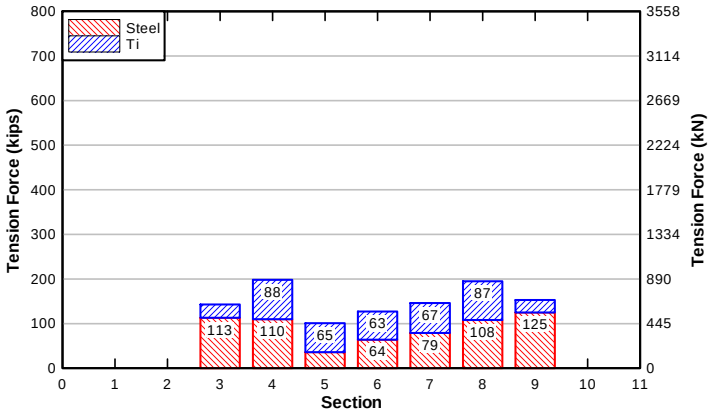


Figure A.103 – Specimen IT.0.0(6).Ti tension force contribution-section at 175 kips (780 kN)

# APPENDIX B – DESIGN SHEAR CAPACITY CALCULATIONS

## B.1 ACI 318-11 American Building Code Requirements for Structural Concrete

Chapter 11 of the ACI 318-11 design code presents the nominal shear capacity, $V_n$, as the sum of the shear in the concrete, $V_c$, and stirrups, $V_s$:

$$V_n = V_c + V_s \qquad \text{ACI 318-11 (11-2)} \quad [B.1]$$

The concrete shear capacity is a function of the modification factor, $\lambda$, based on the type of concrete, the concrete strength, $f_c'$, is in psi, the web width, $b_w$, is in inches, and the distance from the extreme compression fiber to the centroid of the longitudinal tension reinforcement, $d$, is in inches. $V_c$, is defined as:

$$V_c = 2\lambda\sqrt{f_c'}\,b_w d \qquad \text{ACI 318-11 (11-3)} \quad [B.2]$$

Where shear reinforcement is perpendicular to the axis of the member used, the area of the shear reinforcing, $A_v$, is in in$^2$, the stirrup yield strength, $f_{yt}$, is in psi, and the stirrup spacing, $s$, is in inches. Therefore, the nominal shear strength, $V_s$, is:

$$V_s = \frac{A_v f_{yt} d}{s} \qquad \text{ACI 318-11 (11-15)} \quad [B.3]$$

The minimum area of steel shear reinforcement shall be no less than:

$$A_{v,\min} = 0.75\sqrt{f_c'}\,\frac{b_w s}{f_{yt}} \geq \frac{50 b_w s}{f_{yt}} \qquad \text{ACI 318-11 (11-13)} \quad [B.4]$$

The maximum stirrup spacing is limited in Section 11.4.5 of ACI 318-11 to the lesser of $d/2$ or 24 in. (610 mm). Additionally, where $V_s$, exceeds $4\sqrt{f_c'}\,b_w d$, the maximum stirrup spacing is reduced to the lesser of $d/4$ or 12 in. (305 mm).

**B.2 AASHTO-LRFD Bridge Design Specifications**

As determined in Section 5.8.3.3 of AASHTO-LRFD code, the nominal shear capacity, $V_n$, is taken as the lesser of:

$$V_n = V_c + V_s + V_p \qquad \text{AASHTO-LRFD (5.8.3.3-1)} \qquad [B.5]$$

$$V_n = 0.25 f_c^{'} b_v d_v + V_p \qquad \text{AASHTO-LRFD (5.8.3.3-2)} \qquad [B.6]$$

where $f_c$' is the concrete strength (psi), $b_v$ is the effective web width (in.), and $d_v$ is the effective shear depth (in.) taken as the distance between the resultants of the tensile and compressive forces due to flexure, but not less than the greater of $0.9d_e$ or $0.72h$, where $h$ is the height of the beam (in.), and $d_e$ is the distance from the top of the concrete to the resultant of the flexural tensile force (in.). Note that the AASHTO-LRFD accounts for shear in the prestressing strands, $V_p$, in addition to the shear carried by the concrete, $V_c$, and the stirrup, $V_s$. The ACI method has a separate set of equations for dealing with the shear forces from prestressing.

The design procedure in AASHTO-LRFD for determining the shear capacity of a concrete section was derived from the Modified Compression Field Theory (MCFT). MCFT is a comprehensive behavioral model that analyzes the response of diagonally cracked concrete subject to normal stresses and in-plane shear. The theory recognizes the effect on the strength of concrete due to the interaction between shear and moment. AASHTO-LRFD assumes that "the concrete shear stresses are uniformly distributed over an area $b_v$ wide and $d_v$ deep, that the direction of principal compressive stresses, [defined by angle $\theta$], remains constant over $d_v$, and that the shear strength of the section can be determined by considering the biaxial

stress conditions at just one location on the web" (AASHTO 2012). The concrete shear capacity, $V_c$, can be found using:

$$V_c = 0.0316\beta\sqrt{f_c'}\,b_v d_v \qquad \text{AASHTO-LRFD (5.8.3.3-3)} \qquad [B.7]$$

Where $\beta$ is a factor relating the effect of longitudinal strain on the shear capacity of the concrete, as indicated by the ability of diagonally cracked concrete to transmit tension, $\theta$ is the angle of inclination of the diagonal compressive stresses in degrees. The steel shear capacity is:

$$V_s = \frac{A_v f_y d_v (\cot\theta)}{s} \qquad \text{AASHTO-LRFD (5.8.3.3-4)} \qquad [B.8]$$

Where $A_v$ is in $in^2$, $f_y$ is in ksi, and $s$ is in inches. The area of stirrup reinforcing steel $A_v$, shall not be taken less than:

$$A_v \geq 0.0316\sqrt{f_c'}\,\frac{b_v s}{f_y} \qquad \text{AASHTO-LRFD (5.8.2.5-1)} \qquad [B.9]$$

# APPENDIX C – DESIGN MOMENT CAPACITY CALCULATIONS

## C.1 ACI 318-11 American Building Code for Structural Concrete

The flexural design assumptions in ACI 318-11 are listed in Section 10.2. These assumptions are 1) plane sections remain plane; 2) the maximum usable strain at the extreme compression fiber is limited 0.003; 3) stress in reinforcing that has not yielded shall be computed by taking the modulus of elasticity, $E_s$, times the strain in the steel, $\varepsilon_s$, and, conversely, when the reinforcing strains are above yield the reinforcing stresses should be taken independent of strain and equal to $f_y$; 4) the tensile strength of the concrete is neglected; 5) the relationship between the compressive stress distribution and the concrete strain shall be taken as rectangular, trapezoidal, or parabolic to predict strengths that agree with the testing ; and 6) the concrete compressive stress block may be taken as rectangular.

Assuming the flexural tensile steel yields and ignoring the contribution from the compression steel, the nominal cross-section moment capacity, $M_n$, is calculated as:

$$M_n = T\left(d_t - \frac{a}{2}\right) \qquad [C.1]$$

where $T$ is the tensile capacity of the flexural reinforcing bars in kips, $d_t$ is the distance between the extreme compression fiber to the centroid of the longitudinal tension reinforcement in inches, and $a$ is the effective depth of the Whitney Stress Block in inches. $T$ is found by:

$$T = A_s f_y \qquad [C.2]$$

where $A_s$ is the cross-sectional area in in$^2$ of the tension reinforcement scaled to reflect the percentage of developed reinforcement at that section and $f_y$ is the steel yield stress in ksi. $A_s$ shall not be less than the minimum area of flexural reinforcement $A_{s,min}$:

$$A_{s,\min} = \frac{3\sqrt{f_c'}}{f_y} b_w d \geq \frac{200 b_w d}{f_y} \qquad \text{ACI 318-11 (10-3)} \quad [C.3]$$

The effective depth, $a$, is calculated as:

$$a = \beta_1 c \qquad \text{ACI 318-11 Sec. 10.2.7.1} \quad [C.4]$$

where $\beta_1$ is a factor relating $a$ to $c$ and $c$ is the distance from the extreme compression fiber to the neutral axis in inches. For $f_c'$ above 4,000 psi, $\beta_1$ is calculated as:

$$\beta_1 = 1.05 - 0.05 \frac{f_c'}{1000} \qquad \text{ACI 318-11 Sec. 10.2.7.3} \quad [C.5]$$

but shall not be taken greater than 0.85 or less than 0.65.

The distance to the neutral axis, $c$, is:

$$c = \frac{A_s f_s}{\beta_1 0.85 f_c' b} \qquad [C.6]$$

The previous assumption that the flexural tensile steel yields must be validated. The section is tension controlled if the extreme tensile strain, $\varepsilon_t$ is greater than 0.005:

$$\varepsilon_t = 0.003 \left( \frac{d_t - c}{c} \right) \qquad [C.7]$$

**C.2 AASHTO-LRFD Bridge Design Specifications**

In flanged sections without prestressing strands and when $h_f$ is less than $a$, the nominal moment capacity, $M_n$, may be taken as:

$$M_n = A_s f_s \left( d_s - \frac{a}{2} \right) - A_s^{'} f_s^{'} \left( d_s^{'} - \frac{a}{2} \right) + 0.85 f_c^{'} (b - b_w) h_f \left( \frac{a}{2} - \frac{h_f}{2} \right)$$ AASHTO-LRFD (5.7.3.2.2-1) [C.8]

where $A_s$ and $A_s'$ are respectively the areas of the tensile and compressive steel in in$^2$, $f_s$ and $f_s'$ are the tensile and compressive stresses in ksi, respectively, and $d_s$ and $d_s'$ are respectively the distances in inches from the extreme compression fiber to the centroid of the tension and compression reinforcement. The cross-sectional area, $A_s$, of the tension reinforcement is scaled to reflect the percentage of developed reinforcement at that section. The depth of the Whitney Stress Block is defined as $a$, in inches. The concrete compressive strength is taken in ksi as $f_c'$. The width of the flange and web are $b$ and $b_w$, respectively, in inches. The height of the flange is defined as $h_f$ and taken in inches. The effective depth, $a$, is defined as:

$$a = c\beta_1$$ AASHTO-LRFD Sec. 5.7.3.2.2 [C.9]

where the distance from the extreme compression fiber to the neutral axis, $c$, is defined in inches as:

$$c = \frac{A_s f_s - A_s^{'} f_s^{'}}{0.85 f_c^{'} \beta_1 b_w}$$ AASHTO-LRFD (5.7.3.1.2-4) [C.10]

For $f_c'$ above 4.0 ksi, $\beta_1$ is calculated as:

$$\beta_1 = 1.05 - 0.05 f_c^{'}$$ AASHTO-LRFD Sec. 5.7.2.2 [C.11]

but shall not be taken greater than 0.85 or less than 0.65. In an IT section, the compressive section is rectangular, therefore $b_w$ shall be taken as $b$. Eqn. [C.8] then reduces to:

$$M_n = A_s f_s \left( d_s - \frac{a}{2} \right) - A_s^{'} f_s^{'} \left( d_s^{'} - \frac{a}{2} \right)$$ [C.12]

## APPENDIX D – ANALYSIS OF R2K CAPACITIES

Response 2000 (R2K) is a straightforward sectional analysis program developed at the University of Toronto by Evan Bentz and Michael Collins. The software program is free and available on the internet (See http://www.ecf.utoronto.ca/~bentz/r2k.htm). The program can run two-dimensional, non-linear sectional analysis on both beams and columns. R2K calculates the strength and ductility of reinforced concrete sections based on applied shear, moment, and axial load. Based on the Modified Compression Field Theory (MCFT), the three loads are simultaneously applied to the section and the program provides a complete load-deformation response.

R2K was used to determine both the shear and flexural capacities of each specimen. The program requires simple user inputs in order to calculate the sectional capacity. These inputs include the cross-sectional shape and dimensions, the concrete and steel material properties, and the location, grade, and size of the reinforcement (Figure D.1).

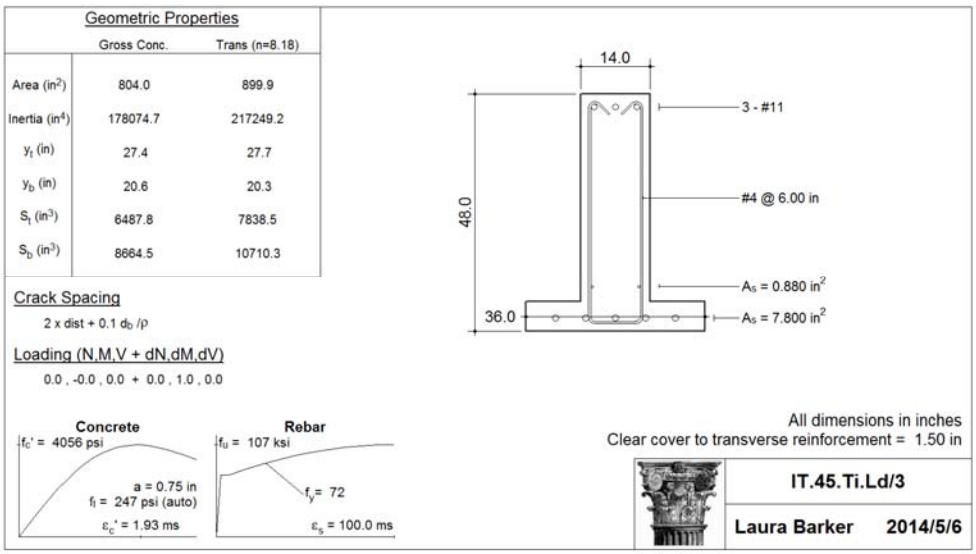


Figure D.1 – Sample R2K Input Screen

Based on the location of the cross-section being analyzed, inputs included the net area of longitudinal steel and the moment-shear ratio as the loading parameter. Each specimen was analyzed at critical locations using R2K to predict the section capacity. These critical cross-sections occurred along the development length of the cutoff bars, at an effective depth distance, $d_v$, from the loading point, and at the end of the NSM reinforcement in the constant moment region. Analysis locations for each test and the corresponding M/V ratios are listed below in Table D.1:

Table D.1 – R2K analysis locations

| **Specimen** | **M/V ratio ft (m)** | | | | |
|---|---|---|---|---|---|
| | **Midspan w/ NSM** | **Midspan w/o NSM** | **$d_v$** | **Crack** | **Cutoff** |
| IT.45.Ld3(10).Ti | 34.7 (10.6) | 29.0 (8.84) | 6.36 (1.94) | 5.89 (1.80) | 4.19 (1.28) |
| IT.45.Ld3(6).Ti | 34.4 (10.5) | 28.3 (8.63) | 6.36 (1.94) | 5.89 (1.80) | 4.19 (1.28) |
| IT.45.Ld3(6).SS | 34.5 (10.5) | 28.1 (8.56) | 6.42 (1.96) | 5.89 (1.80) | 4.19 (1.28) |
| IT.0.0(6).Ti | 500 (152) | n/a | 6.31 (1.92) | n/a | n/a |

After the necessary inputs were supplied for each specimen, a M/V interaction curve was generated based on AASHTO-LRFD code specifications. The interaction curve generated for each location was used to determine the controlling shear and moment capacities for each specimen. The results from this analysis are shown below in Table D.2.

Table D.2 – R2K predicted failure results

| Specimen | Result | | Midspan w/ NSM | Midspan w/o NSM | $d_v$ | Crack | Cutoff |
|---|---|---|---|---|---|---|---|
| IT.45.Ld3(10).Ti | V | k (kN) | 77.4 (340) | 77.5 (345) | 196 (870) | 199 (884) | 211 (939) |
| | M | k-ft (kN-m) | 2701 (3663) | 2245 (3044) | 1245 (1688) | 1172 (1589) | 884 (1199) |
| IT.45.Ld3(6).Ti | V | k (kN) | 77.4 (344) | 77.5 (345) | 256 (1137) | 258 (1149) | 264 (1172) |
| | M | k-ft (kN-m) | 2676 (3628) | 2210 (2996) | 1625 (2204) | 1522 (2064) | 1106 (1499) |
| IT.45.Ld3(6).SS | V | k (kN) | 77.5 (345) | 77.4 (344) | 260 (1156) | 264 (1173) | 272 (1211) |
| | M | k-ft (kN-m) | 2690 (3647) | 2182 (2958) | 1668 (2262) | 1554 (2107) | 908 (1231) |
| IT.0.0(6).Ti | V | k (kN) | 1.8 (8) | n/a | 214 (953) | n/a | n/a |
| | M | k-ft (kN-m) | 940 (1274) | | 1350 (1831) | | |

# APPENDIX E – MATERIAL PROPERTIES

## E.1 Concrete Mixture Design

Concrete was supplied by a local ready-mix supplier. The mixture design had a 28-day target compressive strength of 3000 psi (21 MPa) which was based on the AASHO "Class A" mixture used for vintage concrete bridges. The concrete used rounded river rock and had a water to cement ratio of 0.55 to imitate concrete mixtures typically used during the 1950's. Water reducing and air entraining admixtures were added for workability. Grace Daravair 1000 was the air entraining admixture and was dosed at a rate of 1.4 oz/yd$^3$ (54.5 mL/m$^3$). Grace WRDA-64 was used to reduce the water and was dosed at a rate of 18.8 oz/yd$^3$ (727.3 mL/m$^3$). The mixture had a target slump of 5 in. (127 mm). Table E.1 describes the concrete mixture design used for the specimens.

Table E.1 – Typical Concrete Mixture Design

| **Material** | **Specific Gravity** | **Weight lb (kg)** | **Volume ft$^3$ (m$^3$)** |
|---|---|---|---|
| Cement | 3.15 | 470 (279) | 2.39 (0.089) |
| Water (Total) | 1.00 | 259 (154) | 4.15 (0.154) |
| 3/4 - #4 Round PCC | 2.60 | 1741 (1032) | 10.73 (0.397) |
| Manufactured Sand | 2.56 | 209 (124) | 1.31 (0.048) |
| PCC Sand | 2.58 | 1183 (702) | 7.35 (0.272) |
| Admixtures | 1.00 | 1 (0.78) | 0.02 (0.001) |
| Total Weight | | 3863 (2291) | |
| Total Volume (4% Air) | | | 27.00 (1.000) |

**E.2 Tensile Testing Results**

A 110 kip (489 kN) universal testing machine (UTM) was used for the steel and NSM materials tensile testing. Testing was performed under displacement control and the coupons were loaded at a rate of 0.001 in/sec (0.254 mm/sec) until past visible yield. After yielding, the loading rate was increased to 0.003 in/sec (0.0762 mm/sec). An extensometer measured the strains over the 2 in. (50.8 mm) gage length. To prevent damage, the extensometer was removed before rupture of the bars.

Three coupons each of steel, titanium, and stainless steel were pulled until rupture to measure the yield and ultimate strength of each material. The actual values of yield and ultimate were determined from averaging each set of three tests. The longitudinal steel was Grade 60 (Grade 420), the transverse steel was Grade 40 (Grade 280) and the stainless steel was Grade 75 (Grade 520). The titanium did not have a specified grade. The coupon stress was determined by dividing the applied load by the bar area. The stress-strain diagrams for each the steel reinforcing and NSM materials are shown in below in Figures E.1 and E.2. Because stainless steel and titanium do not have well-defined yield plateaus, the yields were found using the 0.2% offset method. Table E.2 shows a summary of the coupon data including yield strength, ultimate strength, and elongation.

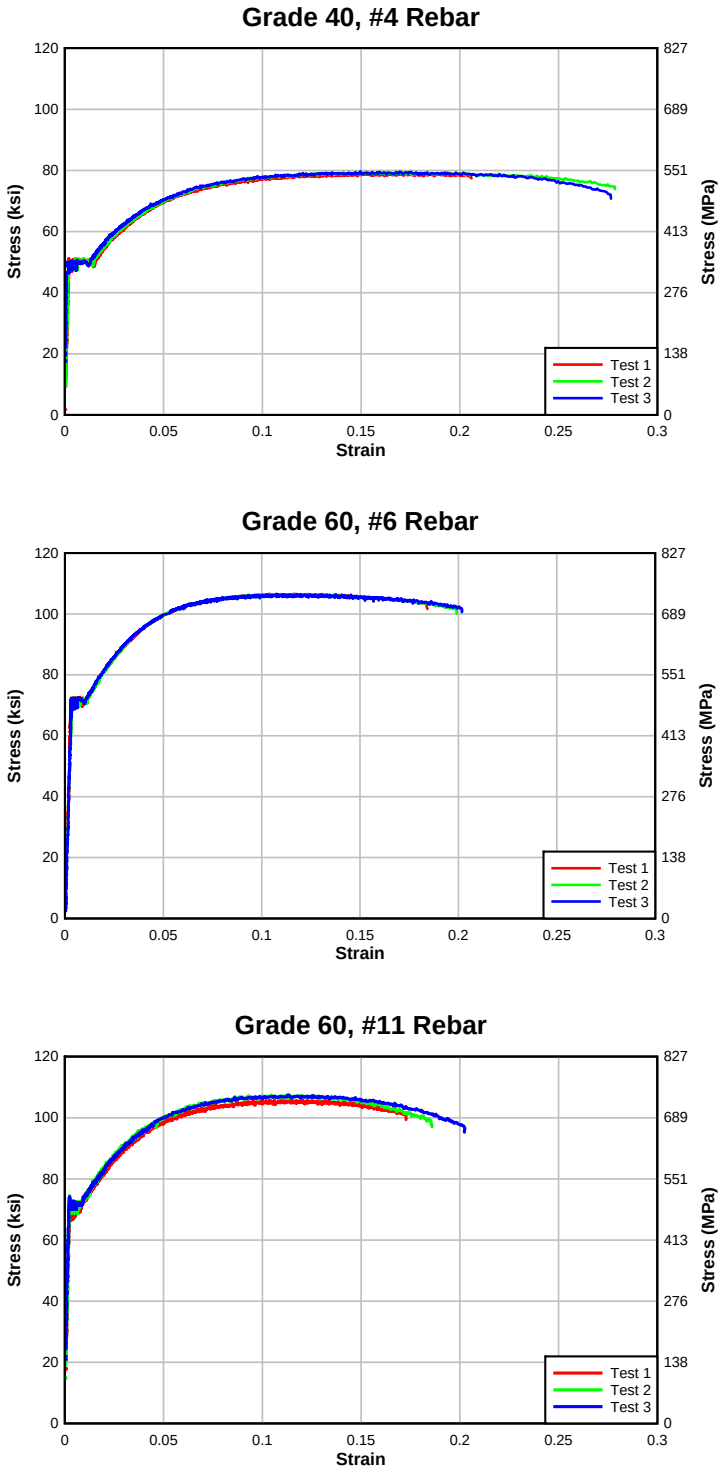


Figure E.1 – Stress-strain curves for steel reinforcement

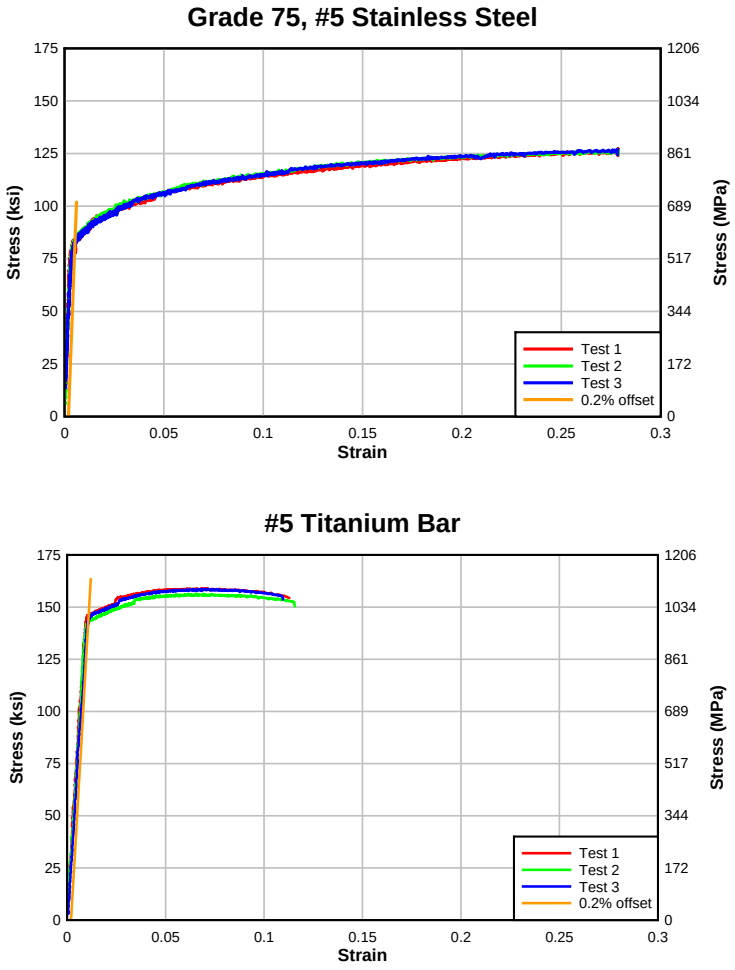


Figure E.2 – Stress-strain curves for NSM reinforcement

Table E.2 – Summary of coupon data

| Coupon | | Yield Strength, $f_y$ ksi (MPa) | Ultimate Strength, $f_u$ ksi (MPa) | Elongation, $e_u$ |
|---|---|---|---|---|
| Grade 40 #4 Rebar | 1 | 50.3 (347) | 79.4 (547) | 0.327 |
| | 2 | 50.3 (347) | 79.7 (549) | 0.282 |
| | 3 | 50.1 (345) | 79.7 (549) | 0.313 |
| | **Average** | **50.2 (346)** | **79.6 (549)** | **0.307** |
| Grade 60 #6 Rebar | 1 | 72.3 (498) | 106.7 (736) | 0.250 |
| | 2 | 72.1 (497) | 106.6 (735) | 0.244 |
| | 3 | 72.1 (497) | 106.6 (735) | 0.296 |
| | **Average** | **72.2 (498)** | **106.6 (735)** | **0.263** |
| Grade 60 #11 Rebar | 1 | 70.1 (483) | 105.9 (730) | 0.229 |
| | 2 | 72.3 (498) | 107.5 (741) | 0.233 |
| | 3 | 72.4 (499) | 107.5 (741) | 0.231 |
| | **Average** | **71.6 (494)** | **107.0 (738)** | **0.231** |
| Grade 75 #5 Stainless Steel | 1 | 82.5 (569) | 127.7 (880) | 0.513 |
| | 2 | 83.8 (578) | 127.0 (876) | 0.442 |
| | 3 | 82.8 (571) | 127.3 (878) | 0.525 |
| | **Average** | **83.0 (572)** | **127.3 (878)** | **0.494** |
| #5 Titanium | 1 | 146.2 (1008) | 159.0 (1096) | 0.106 |
| | 2 | 143.6 (1009) | 156.5 (1079) | 0.130 |
| | 3 | 146.4 (1009) | 158.8 (1095) | 0.098 |
| | **Average** | **145.4 (1009)** | **158.1 (1090)** | **0.111** |

# APPENDIX F – CASE STUDY

## F.1 Introduction and Background

In Mosier, Oregon, the only connection to Interstate 84 westbound is by use of an overcrossing known as the Mosier Connection Bridge. The Mosier Bridge is located at milepost 69.65 and is a reinforced concrete deck girder (RCDG) bridge. The bridge was built in 1950 and had three spans. In 1959, a fourth span was added to lengthen the bridge and allow for two lanes of travel in each direction of I-84. The bridge serves the city of Mosier, two quarries, and many local farmers. The bridge location is shown in Figure F.1.


Figure F.1 – Mosier Bridge location over I-84 (Google Maps, 2014)

A routine bridge inspection in May 2013 identified unusual cracking in the bridge girders. Vertical offsets at crack interfaces produced visible elevation changes at the bottom of the girders (Figure F.2). The location of the cracking is shown in Figure F.3. Over the years, the quarry trucks have hauled large quantities of rock over the bridge, likely producing some

very heavy loads on the bridge. These trucks could have possibly overloaded the structure and contributed to the severity of the girder cracking.


Figure F.2 – Vertical offset at crack interface (ODOT, 2013)

Figure F.3 – Elevation photograph of Mosier Bridge (Google Maps, 2014)

The Oregon Department of Transportation (ODOT) began looking into the issue right away by performing a load rating on the bridge in June 2013. The results from the load rating showed that the cracked areas had sufficient shear strength, but other locations along the spans and in the crossbeams were found to be deficient in shear. These deficiencies necessitated that the bridge post load restrictions. Based on the as-built construction plans, the cracking appeared to line up with critical anchorage locations. This can be seen in Figure

F.4 as a drawing of the as-built reinforcement cage is overlaid on a photograph of a cracked girder. Temporary shoring was installed in August 2013 under the crack locations in the north span and under the original crossbeams.

Figure F.4 – Rebar cage overlaying critical crack locations (ODOT, 2013)

The temporary shoring was not rated to carry the local fruit harvest loads necessitating large fruit and rock trucks to detour to access I-84. Detouring to the west or east added at least nine miles onto truck routes. Strengthening the bridge was deemed the best method to remove the need for load posting. Because orchard harvest season typically begins in June, ODOT made it a high priority to strengthen the bridge by late spring of 2014.

Anchorage retrofitting research on full-scale T and inverted-T beams using near-surface mounted (NSM) titanium and stainless steel was being performed at Oregon State University (OSU) at the time. Dr. Christopher Higgins at OSU was contacted by ODOT to look into applying the NSM-titanium retrofit methodology to the Mosier Bridge.

Three 18 ft (5.49 m) RCDG specimens were built based on Beam A and Haunch AB from the as-built construction plans shown in Figure F.5. The first specimen served as the control specimen to model the existing Mosier Bridge girders. The other two specimens were both retrofitted using the NSM retrofitting technique. The first of these was pre-failed to mimic the existing cracking and lack of achorage contribution before retrofitting and is covered in a case study by Amneus (2014). The second retrofitted specimen was constructed and retrofitted with the anchorage steel still fully intact. The control and the second retrofitted specimen are both covered in this case study.

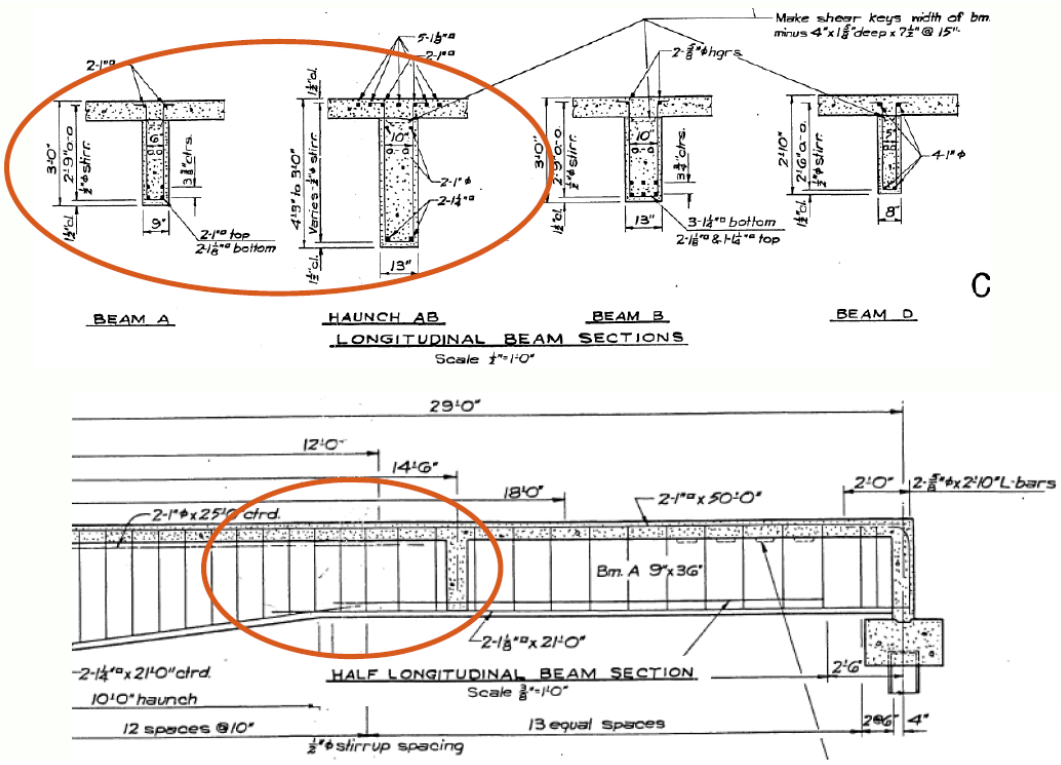


Figure F.5 – As-built Mosier Bridge construction plans (ODOT, 2013)

## F.2 Specimen Details

Two T beam specimens were designed to represent the Mosier Bridge girders. Testing the specimens using a T configuration focused on the positive moment region by placing the concrete web into flexural tension. The first specimen served as a control to illustrate the conditions in an existing Mosier Bridge girder and the second specimen was retrofitted using the methodology as listed in Section F.2.4.

### F.2.1 Geometry

Test specimens were designed to model the in-situ anchorage deficiencies in the Mosier Bridge based on the original as-built construction plans. The specimens had identical geometries and internal reinforcing. Both of the specimens were 18 ft (5.49 m) long with 36 x 6.5 in. (914 x 165 mm) decks. The stems had constant dimensions of 9 x 29.5 in. (229 x 749 mm) on the south half and were tapered and haunched beginning at midspan to 12.625 x 41.25 in. (321 x 1048 mm) on the north end.

### F.2.2 Internal Reinforcing Steel Details

All longitudinal steel was Grade 60 (Gr. 420) while the transverse steel consisted of Grade 40 (Gr. 280) stirrups. The original girders were designed with heavy negative moment steel in the flange. For the compression steel, the specimens had two straight #7 (M22) bars measuring 212 in. (5385 mm), and five straight #8 (M25) bars with varying lengths. Of the five #8 (M25) bars, two were 130 in. (3302 mm), two were 160 in. (4064 mm), and one was 212 in. (5385 mm). Deck steel was provided by #4 (M13) bars placed in two layers at 8 in. (203 mm) on center.

In the web of the constant section, the specimens had two #8 (M25) bars and two #7 (M22) bars measuring 132 in. (3353 mm) and 97.5 in. (3353 mm) in length, respectively. In the haunched section, two #9, 112 in. (M29, 2845 mm) bars served as the only flexural reinforcement. All of these bars had a standard hook at one end and straight-bar terminations towards the middle of the beam. This center region of each beam was the location of the poor anchorage details as the #8 (M25) and #9 (M29) bars only overlapped by 32 in. (813 mm). Stirrups were spaced at 12 in. (305 mm) in the critical region of the beam and between 6 and 8 in. (152 and 203 mm) towards the supports. The retrofitted specimen had decreased stirrup spacing after the termination of the NSM materials on the south side and double stirrups on the north side prior to the NSM termination until the end of the beam. This change was to ensure the retrofitted specimen did not fail in shear at the ends due to the added flexural capacity from the NSM material in the middle of the specimen. The elevations and cross-sections are detailed for the control specimen in Figures F.6 to F.11 and for the retrofitted specimen in Figures F.12 to F.18.

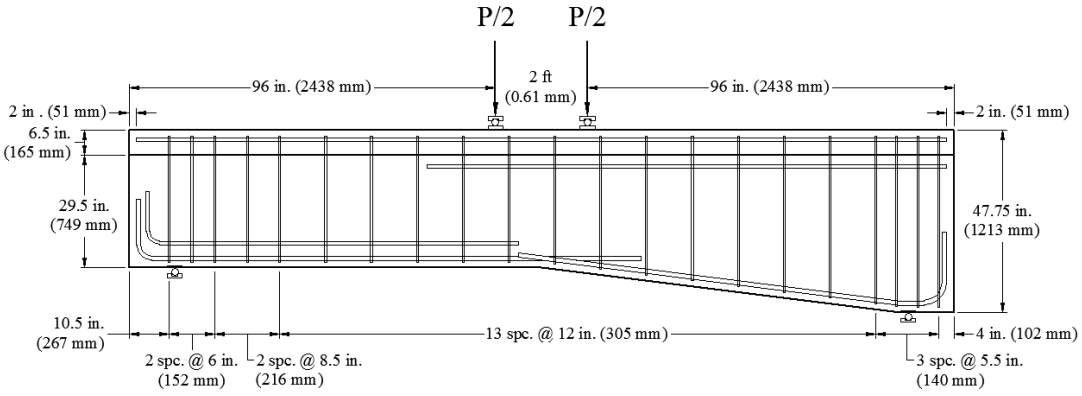


Figure F.6 – Control specimen geometry and stirrup spacing

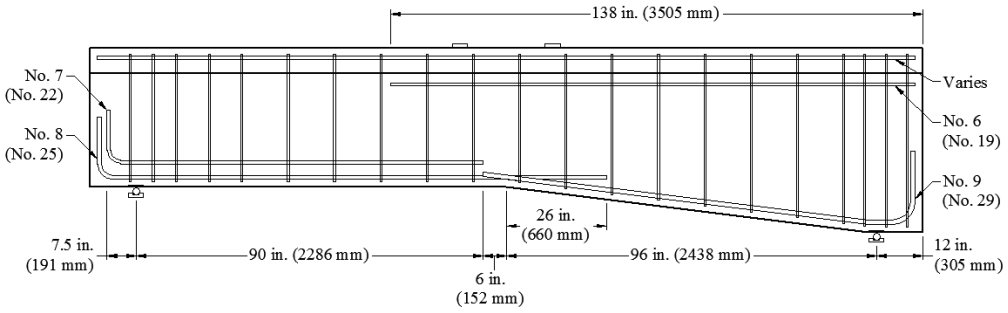


Figure F.7 – Control specimen flexural reinforcement details

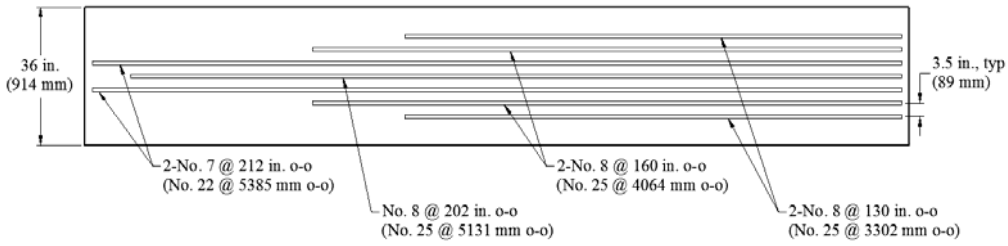


Figure F.8 – Control specimen top view: deck steel details

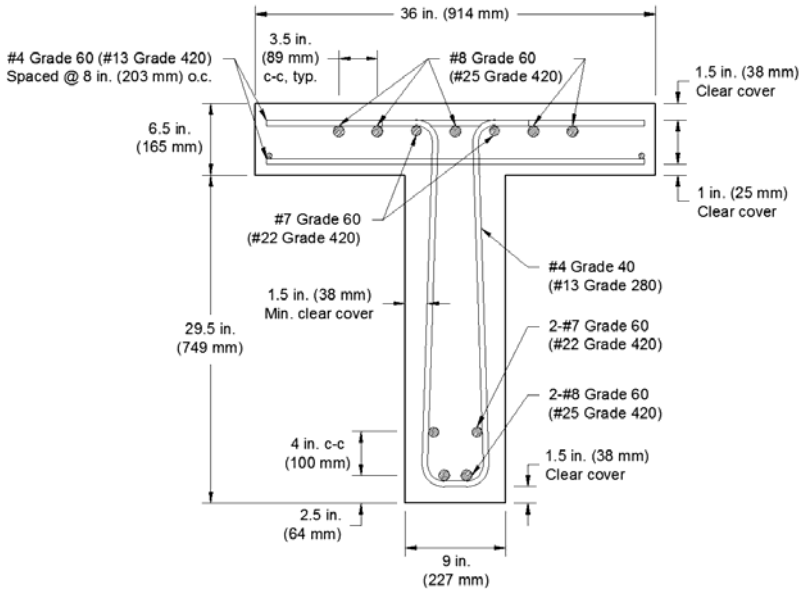


Figure F.9 – Control specimen cross-section at south support

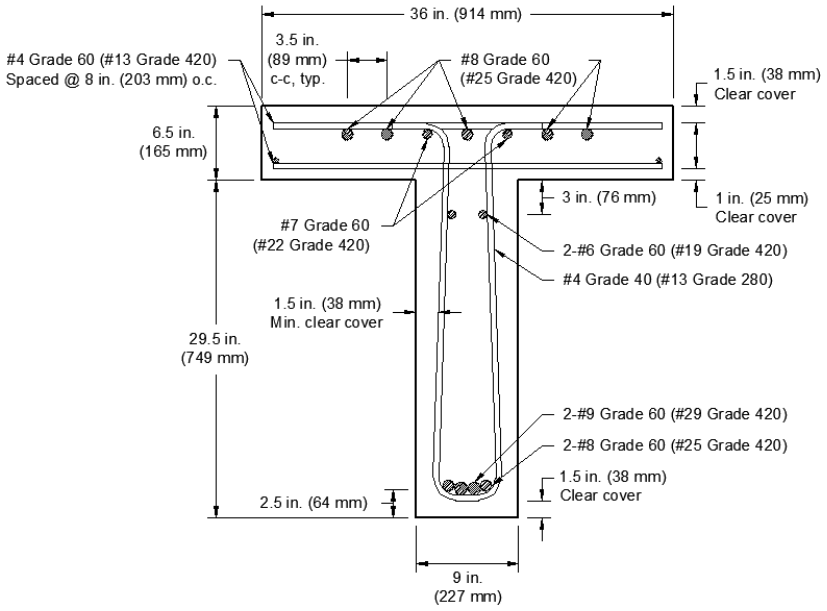


Figure F.10 – Control specimen cross-section at midspan

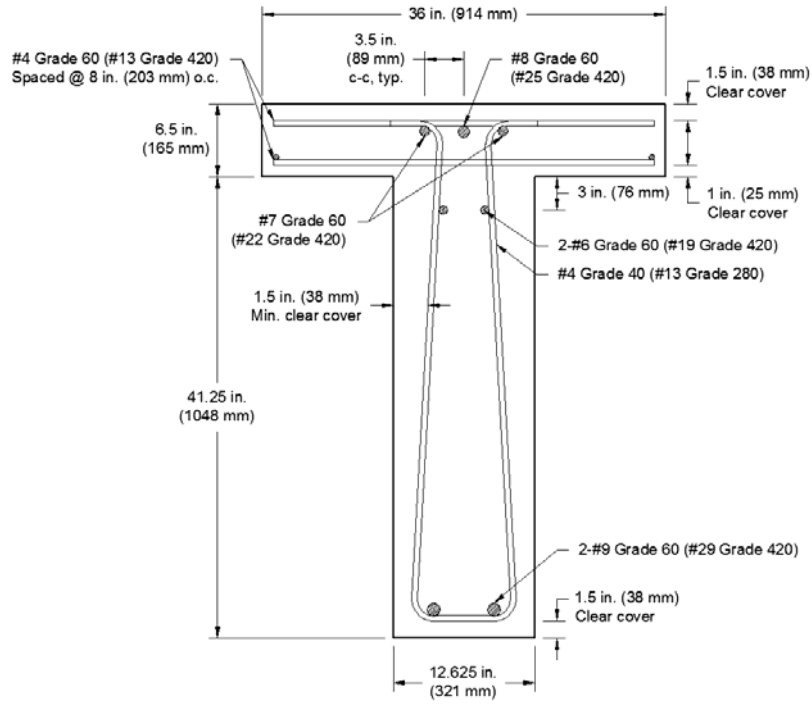


Figure F.11 – Control specimen cross-section at north support

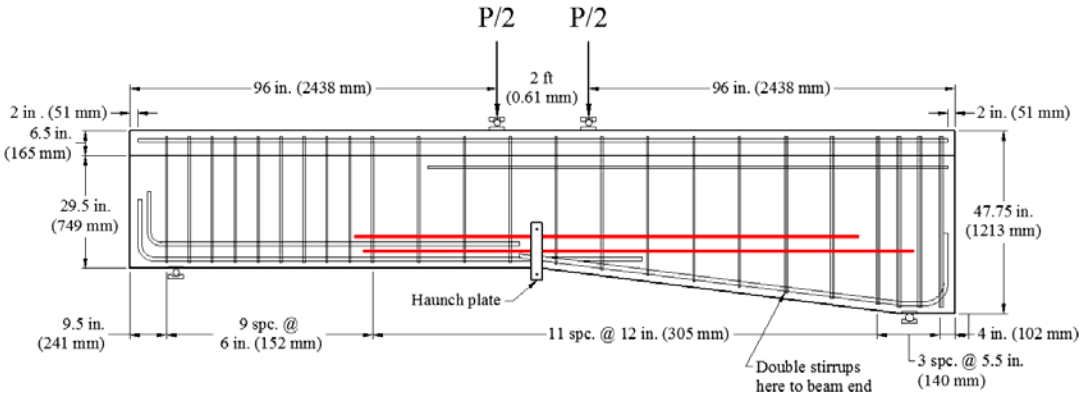


Figure F.12 – Retrofit specimen geometry and stirrup spacing

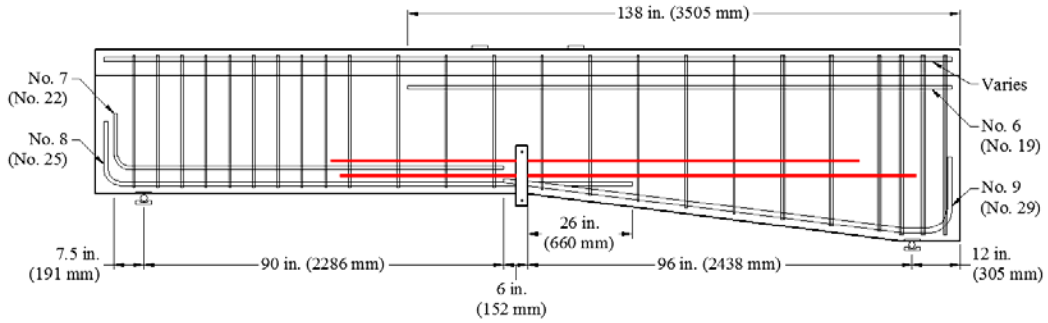


Figure F.13 – Retrofit specimen flexural reinforcement details

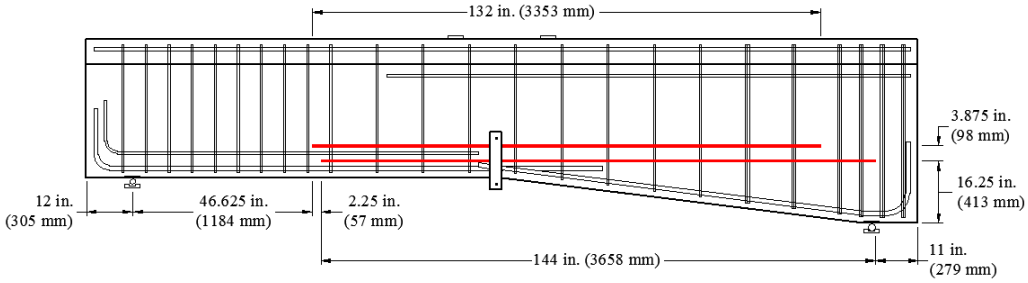


Figure F.14 – Retrofit specimen NSM reinforcement details

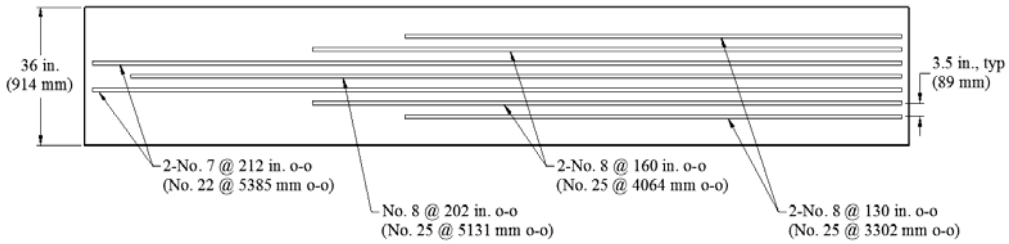


Figure F.15 – Retrofit specimen top view: deck steel details

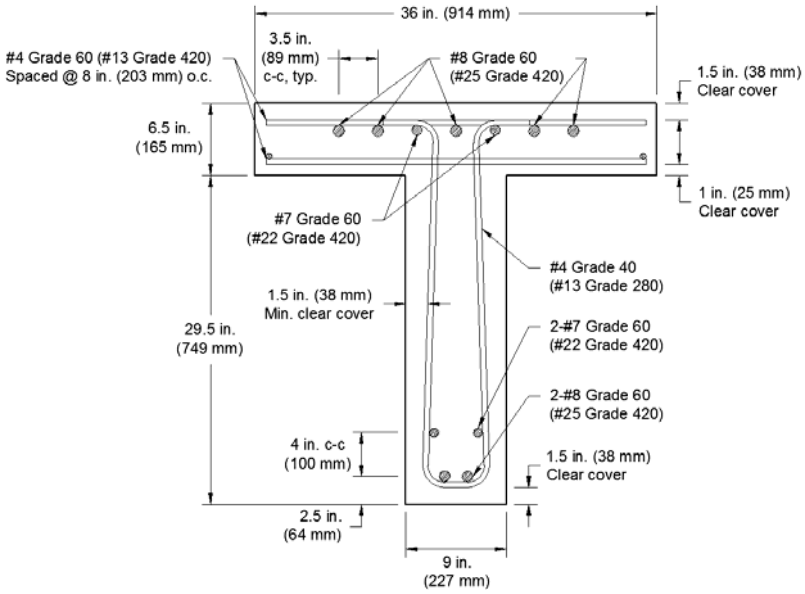


Figure F.16 – Retrofit specimen cross-section at south support

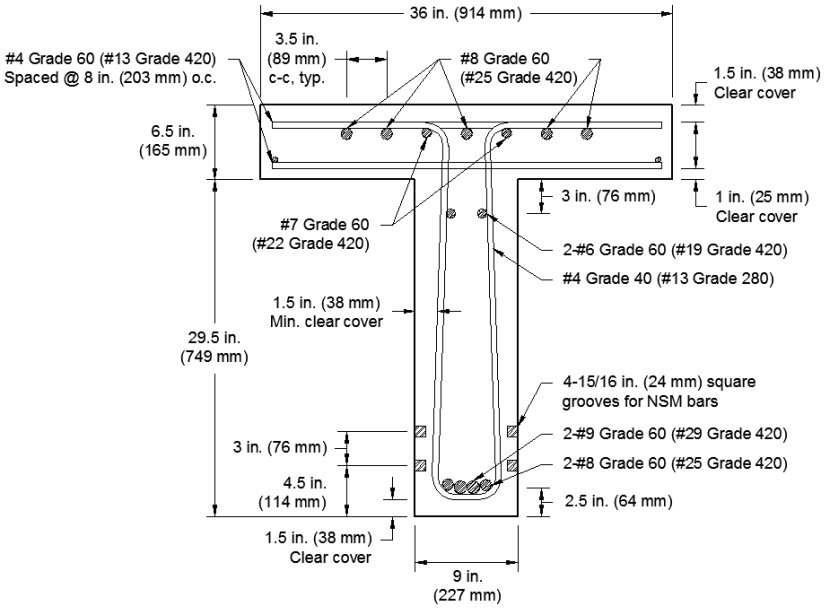


Figure F.17 – Retrofit specimen cross-section at midspan

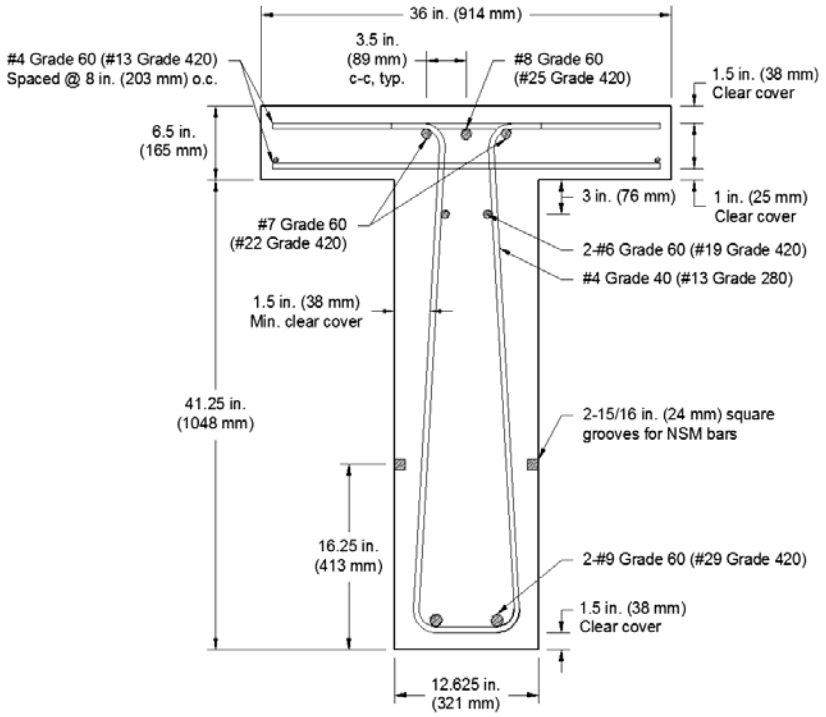


Figure F.18 – Retrofit specimen cross-section at north support

F.2.3 Specimen Construction

*F.2.3.1 Reinforcing Steel Cage*

Before building each rebar cage, select transverse and flexural bars were strain gaged at specified locations along the bar lengths. The steel reinforcing cages were fabricated using conventional rebar tying methods to maintain dimensional stability of the reinforcing cage. The hooked bars were fabricated on-site using a rebar bending machine and cut to length using a band saw. Coil ties were installed in on both ends of the top and bottom of the beam for moving the specimen after concrete casting and curing. The coil ties were fastened to the center longitudinal bars and to a nearby piece of deck steel or stirrup on the top and bottom, respectively. A finished reinforcing cage can be seen in Figure F.19.

Figure F.19 – Finished rebar cage

Double leg open stirrups were hung from the top flexural bars and tied in place, and longitudinal tension steel was tied in the flange to the interior bottom of the stirrups. The top layer of transverse deck steel was tied to the top of the tension bars in the flange. The bottom layer was a "floating" layer created by placing the transverse steel on top of the longitudinal #6 (M19) bars and the transverse steel to two longitudinal #4 (M13) bars.

*F.2.3.2 Clear Cover*

Clear cover dimensions on the web and flange were achieved by using wagon wheel spacers. The bottom layer of deck steel "floated" to the correct placement with the correct cover once placed in the formwork due to the application of wagon wheels. Metal chairs were tied diagonally to the bottom of the cage to provide the clear cover depth and to support the cage when it was placed in the formwork.

*F.2.3.3 Cage Placement, Formwork, and Concrete Casting*

After completion, the cage was lifted in to the formwork using an overhead bridge crane. For the Mosier specimens, falsework was built into the typical T-beam formwork as seen in Figure F.20. The falsework allowed the correct web widths and depths as well as the increased flange thickness to be achieved.

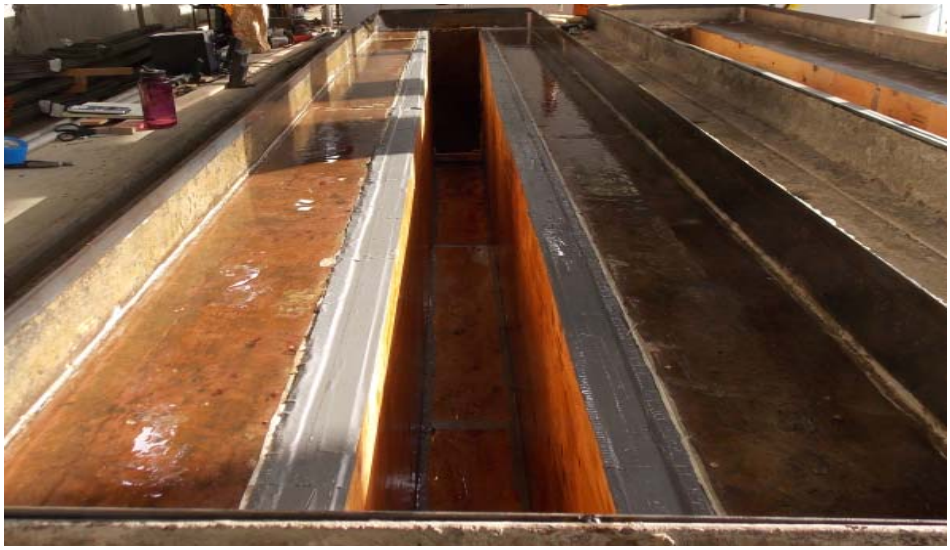

Figure F.20 – Beam falsework built in typical T-beam formwork

Concrete casting was done with a 2 $yd^3$ (1.53 $m^3$) clamshell bucket. The concrete was placed into the forms and consolidated using a mechanical vibrator. After placing, the concrete was screeded and the surface was finished using hand trowels.

F.2.4 NSM Dimensions and Installation

The Mosier Bridge showed visible distress around the anchorage details at the haunch location. Load limits were posted for the bridge immediately after the anchorage cracking was observed and the bridge was shored up. In order to mitigate the need for the shoring and load posting which rerouted all local truck traffic for the quarry, a method of externally reinforcing the girders was necessary. A retrofitting technique using near-surface mounted (NSM) bars was developed to increase the strength and ductility of deficient flexural steel cutoff details.

While ACI 440.2R-08 is a design guide for FRP systems, the methodology was used to design the NSM-titanium retrofit system. ACI 440 provided guidelines for the groove width, depth, and spacing. For the circular bars, the groove widths and depths were greater than or equal to 1.5 times the diameter of the bar, $d_b$. To avoid overlapping of the tensile stresses around the NSM bars, the minimum clear spacing between the grooves was greater than twice the groove depth. A clear distance between the groove and the edge of the concrete was provided at a minimum distance of four times the groove depth in order to minimize effects on the edges that could accelerate failure due to debonding. These guidelines are illustrated in Figure F.21.

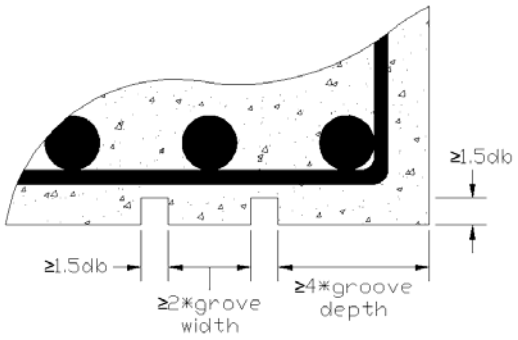


Figure F.21 – ACI 440 groove spacing and dimension guidelines

The titanium bars were 0.625 in (15.9 mm) diameter, #5 (M16) bars. A unique deformation pattern was created to enhance the bond between the bar and the epoxy; an example is shown in Figure F.22. Based on the given bar diameters, 15/16 in. (24 mm) square grooves were used. The grooves were spaced at least 2 in. (51 mm) apart and at least 4 in. (102 mm) from the edge of the concrete.

Figure F.22 –Titanium bar example

After each specimen was removed from the formwork, the grooves were cut into the beam. The designed groove placement was sketched onto the beam and a local concrete cutting company cut the grooves. Grooves were cut by making three passes with the concrete saw and chipping out the remaining concrete using a rotohammer. Each of the NSM bars contained a 6 in. (152 mm) 90° hook at each end. A 3/4 in. (19 mm) hole was drilled in to each end of the grooves to accommodate the hooks. The diameter of the hole was based on

the typical diameter for a post-installed anchor. The holes were drilled to a 6.25 in. (159 mm) depth to accommodate the 6 in. (152 mm) hook length. To account for the NSM bar bend radius, the intersection between the hole and the groove was manually chipped away using a chisel or rotohammer.

The titanium 90° hooks were fabricated using heat in order to prevent material fracture. Heating was performed using an acetylene torch and color indication was used to tell the temperature of the bar (Figure F.23). The titanium NSM bars for the control specimen were bent at approximately 900 ˚F (482 ˚C) while the bars for retrofitted specimen were bent around 1250 ˚F (677 ˚C). After heating to the specified temperature, the bars were inserted into the rebar bending machine and bent around a 2 in. (51 mm) diameter bending pin. The titanium experienced springback while bending; therefore, the bars were over-bent in order to have a 90° end result.

a)  b) 

Figure F.23 – Color indication at a) 900 ˚F (482 ˚C) and b) 1250 ˚F (677 ˚C)

After the grooves were given sufficient time to dry after the concrete cutting, the NSM materials were installed. Installation consisted of placing a pass of epoxy in the holes and

groove, pushing the NSM bar into the groove with the hooks extending into the holes, and placing a second layer of epoxy over the bar. The NSM bars were centered in the grooves during the epoxy placement. The epoxy was finished flush with the surface of the concrete. Two passes of epoxy helped to ensure fewer air bubbles in the installation process. The least amount of finishing necessary was used in order to prevent the epoxy from sagging. The epoxy was allowed to cure for a minimum of seven days between the manufacturer's recommended curing temperatures of 60˚ to 80˚. A heat tent was created around the beam using tarps and heaters and, by taking readings every hour, the 7 day curing temperature was recorded.

Two NSM-titanium bars were placed on each side of the beam over the region with inadequate flexural anchorage. On each side, the titanium bars measured 11 and 12 ft (3.35 and 3.66 m) out to out with 6 in. (152 mm) 90° hooks on each end. The top bar was offset 2.25 in. (57 mm) to the right on each side to allow the NSM to clear a nearby stirrup and allow the full 6 in. (152 mm) hook embedment. The flexibility of the titanium allowed it to conform to the small bend at midspan due to the horizontal taper of the beam. Because of this slight bend, the titanium carried a minimal outward force. To account for this force and minimize the rupture load if delamination was to occur 0.5 x 3 x 15 in. (13 x 76 x 381 mm) haunch plates were installed on both sides of the beam.

## F.3 Material Properties

### F.3.1 Concrete

Concrete was provided by a local ready-mix supplier. Each specimen required approximately 3 $yd^3$ (2.29 $m^3$) of concrete. The concrete design was based the AASHO "Class A" 3,000 psi (21MPa) mixture used for vintage concrete bridges. Actual strengths around 4,000 psi (28 MPa) are more likely the present day strengths in these bridges due to in-situ strength gain. This design is congruent with previous research on similar sized specimens at Oregon State University. Standard slump tests were conducted and water added if necessary to achieve a 5 in. (127 mm) slump. The actual concrete compressive and tensile strengths were performed in accordance with ASTM C39/C39M-09 and ASTM C496/C496M-11, respectively. Average test day concrete cylinder compressive and tensile strengths are reported in Table F.1.

Table F.1 – Average test day specimen concrete compressive and tensile strengths

| **Specimen** | **Concrete Age (days)** | $f_c'$ **psi (MPa)** | $\sigma, f_c'$ **psi (MPa)** | $f_{ct}$ **psi (MPa)** | $\sigma, f_{ct}$ **psi (MPa)** |
|---|---|---|---|---|---|
| Control | 33 | 3038 (21.0) | 76.9 (0.53) | 348 (2.40) | 25.2 (0.17) |
| Retrofit | 58 | 3344 (23.1) | 426 (2.94) | 353 (2.43) | 16.1 (0.11) |

### F.3.2 Internal Reinforcing Steel

All reinforcing steel was provided by local rebar fabricators. The transverse reinforcing bars were ASTM A615 (2009) Gr. 40, #4 (Grade 280, M13) and were made from a steel heat with the lowest available yield stress. The longitudinal reinforcement was ASTM A706

(2009) Gr. 60, #11 (Grade 420, M36). The material properties for all the steel reinforcement were determined in accordance with ASTM E8/E8M-13a. The average measured material properties from thee replicate samples are reported in Table F.2 below. The transverse reinforcing steel used in the specimens was a reasonable approximation of ASTM A305 (1950) Gr. 40 (Grade 276) steel available in the 1950's. Regrettably, Gr. 40 (Grade 276) #11 (M36) bars are not commercially available and Gr. 60 (Grade 420) bars were used as a substitute.

Table F.2 – Average reinforcing steel properties

| **Reinforcement Type** | **Bar Dia. in. (mm)** | **Grade ksi (MPa)** | **$f_y$ ksi (MPa)** | **σ, $f_y$ ksi (MPa)** | **$f_u$ ksi (MPa)** | **σ, $f_u$ ksi (MPa)** |
|---|---|---|---|---|---|---|
| Transverse #4 (M13) | 0.500 (12.7) | 40 (280) | 50.2 (346) | 0.12 (0.83) | 79.6 (549) | 0.17 (1.17) |
| Longitudinal #6 (M19) | 0.750 (19.1) | 60 (420) | 63.0 (434) | 0.48 (3.31) | 106.3 (733) | 0.15 (1.03) |
| Longitudinal #7 (M22) | 0.875 (22.2) | 60 (420) | 65.3 (450) | 0.17 (1.17) | 104.6 (721) | 0.36 (2.48) |
| Longitudinal #8 (M25) | 1.000 (25.4) | 60 (420) | 63.6 (438) | 0.68 (4.69) | 112.1 (773) | 1.00 (6.89) |
| Longitudinal #9 (M29) | 1.128 (28.7) | 60 (420) | 62.6 (432) | 0.23 (1.59) | 102.0 (703) | 0.15 (1.03) |

F.3.3 NSM Materials

Titanium is a material not commonly used in civil engineering practice. The titanium material is a nonmagnetic alloy with 6% aluminum and 4% vanadium (Ti-6Al-4V). The alloy meets ASTM B348 (2013) and is aircraft quality titanium. The titanium is high strength, impervious to chlorides, and has a low coefficient of thermal expansion around 8.6 μm/m

ºC. The bars were 0.625 in (16 mm) round bars with an average area of 0.2975 $in^2$ (192 $mm^2$). The average cross-sectional area of the titanium was determined by weighing the full-length bars (~14 ft (14.3 m)) of known length and dividing by the unit weight of 276 $lb/ft^3$ (4,419 $kg/m^3$). The titanium was fabricated with a unique surface treatment in lieu of the standard rebar deformation pattern in order to enhance the bond at the titanium and epoxy interface.

Material testing was done in accordance with ASTM E8/E8M-13a. Stress-strain curves show that the titanium exhibited almost perfectly elasto-plastic behavior. The nominal modulus of elasticity is 15,500 ksi (106,800 MPa), while the actual modulus was measured as 15,120 ksi (104,200 MPa). The stiffness of titanium is also more compatible with epoxy and concrete than standard or stainless steel. Because the material does not exhibit a well-defined yield plateau, the yield stress was found using a 0.2% strain offset. Table F.3 defines the material properties.

Table F.3 – Average NSM reinforcing properties (three replicates)

| **Reinforcement Type** | **Bar Area $in^2$ ($mm^2$)** | **Grade ksi (MPa)** | **$f_y$ ksi (MPa)** | **$f_y$ ksi (MPa)** | **$f_u$ ksi (MPa)** | **$f_u$ ksi (MPa)** | **$e_u$ (%)** |
|---|---|---|---|---|---|---|---|
| Titanium #5 (M16) | 0.2975 (7.6) | n/a (n/a) | 145.4 (1002) | 1.56 (10.75) | 158.1 (1090) | (1.39) (9.58) | 11.2 |

The titanium bars were bonded to the concrete grooves using a commercially available general purpose gel epoxy adhesive (CONCRESIVE 1420). This is a non-sag epoxy that is widely used for bonding to concrete. The manufacturer reported material properties for the

epoxy include tensile strength of 4 ksi (27.6 MPa), elongation at break of 1.0%, compressive yield strength of 12.5 ksi (86.2 MPa), and 2-day cure bond strength above 2 ksi (13.8 MPa).

### F.4 Design Capacity

The design and analytically predicted strengths for the control and retrofitted specimens are shown in Table F.4. For retrofitting the existing bridge, the designer conservatively assumed there was no contribution from the partial steel in the anchorage region. The design strength for the control specimen is less than the factored load effect for a CTP3 truck. The retrofitted specimen brings the base design capacity from 0 to 394 kip-ft (0 to 535 kN-m) based on the titanium strength alone. Even with this conservative assumption, the design strength of the titanium retrofitted girder exceeds the factored demands.

Table F.4: Design moment predictions for control and retrofitted specimens

| Specimen | Moment Prediction | k-ft (kN-m) |
|---|---|---|
| **Control** | Demand, $M_u^+$ | 219 (297) |
| | Design Strength, $\emptyset M_n$ (AASHTO): w/ partial steel | 173 (234) |
| | Predicted Strength (R2K) | 258 (350) |
| **Retrofit** | Demand, $M_u^+$ | 219 (297) |
| | Design Strength, $\emptyset M_n$ (AASHTO): Ti alone | 290 (393) |
| | Predicted Strength (R2K): Ti alone | 394 (535) |
| | Design Strength, $\emptyset M_n$ (AASHTO): Ti w/ partial steel | 421 (571) |
| | Predicted Strength (R2K): Ti w/ partial steel | 535 (725) |

## F.5 Instrumentation

Global and local specimen responses were measured using an array of instruments. Data from sensors were acquired and stored for later analysis using commercially available data acquisition hardware and software. Data were sampled at a rate of 5 Hz. Sensors consisted of strain gages bonded to stirrups, flexural reinforcing steel bars, and the NSM bars, numerous displacement sensors, rotation sensors, and a load cell. Digital photographs and both tape and digital videos were used to document the specimen response during each load step, at failure, and after failure.

### F.5.1 Reinforcing Steel Strain Gages

Strain gages were applied to only one half of the beam assuming that the specimens behaved symmetrically about the longitudinal axis. Five mid-height stirrup strain gages were used. Strain gages were placed around the poor anchorage details on the longitudinal flexural bars to determine the tensile force and the bond stress distribution. The flexural gages lined up with each other and with bar terminations. A total of six strain gages were used on the tension steel. Gages on the compression steel and the #6 (M19) bar lined up with the end of the #9 (M29) bar. These top bars had a total of five gages. Strain gage locations are shown in Figures F.24 and F.25.

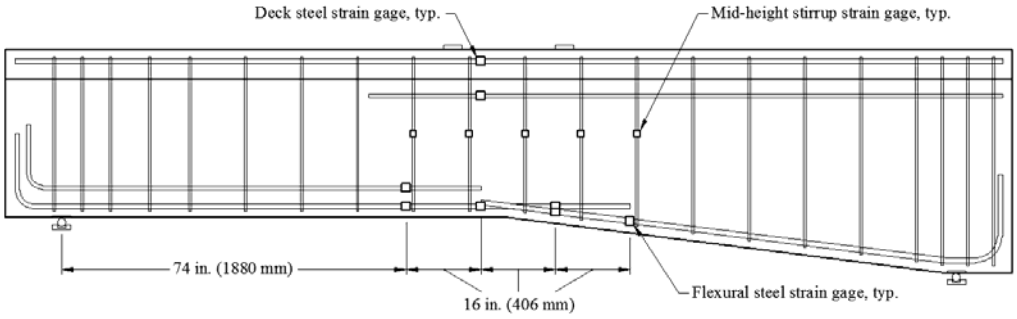


Figure F.24 – Control specimen internal sensor array

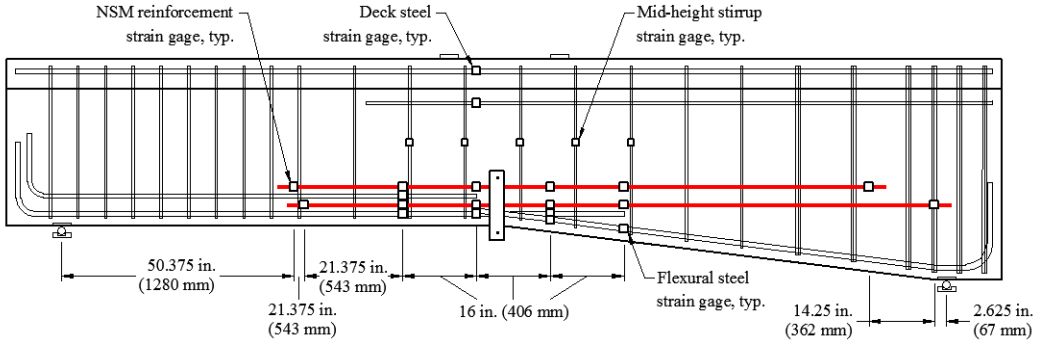


Figure F.25 – Retrofit specimen internal and NSM-titanium sensor array

## F.5.2 NSM Strain Gages

Strain gages were installed on the NSM prior to installation. Like the internal steel gages, only one half of the NSM was strain gaged. The locations of the gages on the NSM bars were intended to line up (in elevation) with the gages on the internal longitudinal steel. The data gathered from these gages were useful to understand the transfer of stress between the internal steel to the NSM. Gages were also placed at each end of the NSM bars. There were a total of 12 gages measuring strains in the NSM-titanium. Strain gage locations for the retrofitted specimen NSM-titanium can be seen in Figure F.25 above.

F.5.3 Diagonal String Potentiometers

Pairs of diagonal displacement sensors with a range of 2 in. (50.8 mm) were used to measure the concrete deformations during testing. As cracks opened during loading, the lower sensors measured elongation while the upper sensors measured contraction. The specimens had a total of eight sensors measuring both the north and south sides. The sensors were installed as shown in Figure F.26.

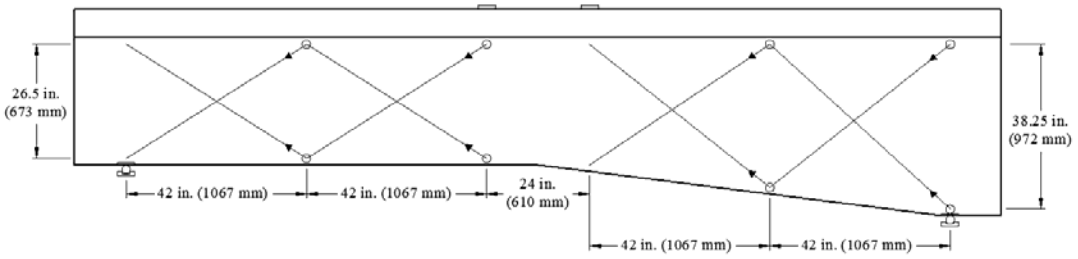


Figure F.26 – Typical specimen diagonal displacement sensor layout

F.5.4 Global Specimen Deflection

String potentiometers with a 10 in. (254 mm) stroke were used to measure specimen displacement at midspan relative to the laboratory floor. One sensor was placed on the east face and one on the west face. The gross midspan displacement was taken as the average of the two sensors. The sensors were attached to mid-height of the web.

To account for rigid-body deformations, support settlements were measured relative to the laboratory floor using 1.5 in. (38.1 mm) vertically oriented displacement sensors. The sensors were attached to the web and placed above the support centerlines on all corners of the specimen. The measured support displacements were averaged and then subtracted from the gross midspan displacement values to determine the net midspan deflection.

F.5.5 End Rotation Sensors

Rotation sensors were affixed to each end of the beam over centerline of support. Beam end rotations were measured in degrees.

## F.6 Test Protocols

Specimens were tested in the Structural Engineering Research Laboratory at Oregon State University. A reaction frame anchored to the strong floor allowed a four-point loading system to be used. Load was applied using a closed-loop 500 kip (2224 kN) servo-hydraulic actuator under load control. A steel spreader beam produced a 24 in. (610 mm) long constant moment region in the specimens. The actuator force was distributed through the spreader beam to the specimens via two 2 in. (51 mm) diameter rollers placed on two 4 in. (102 mm) wide plates. To ensure uniform load application across the plates, the plates were leveled and grouted into place using a quick-setting, high-strength gypsum cement.

The span length of the T specimens was 16 ft (4.88 m) between centerlines of support. The end support reactions were also distributed through built-in 4 in. (102 mm) wide plates resting on captive rollers. Specimens were simply supported. The captive roller-plate system at the deeper end of the beam rested directly on the floor beam. The system in the shallower beam end rested on a load cell which not only measured the load in this end of the beam, but brought the beam to the correct elevation required to be level. The overall loading schematic is illustrated in Figure F.27. The stabilizing beams have been removed for clarity.

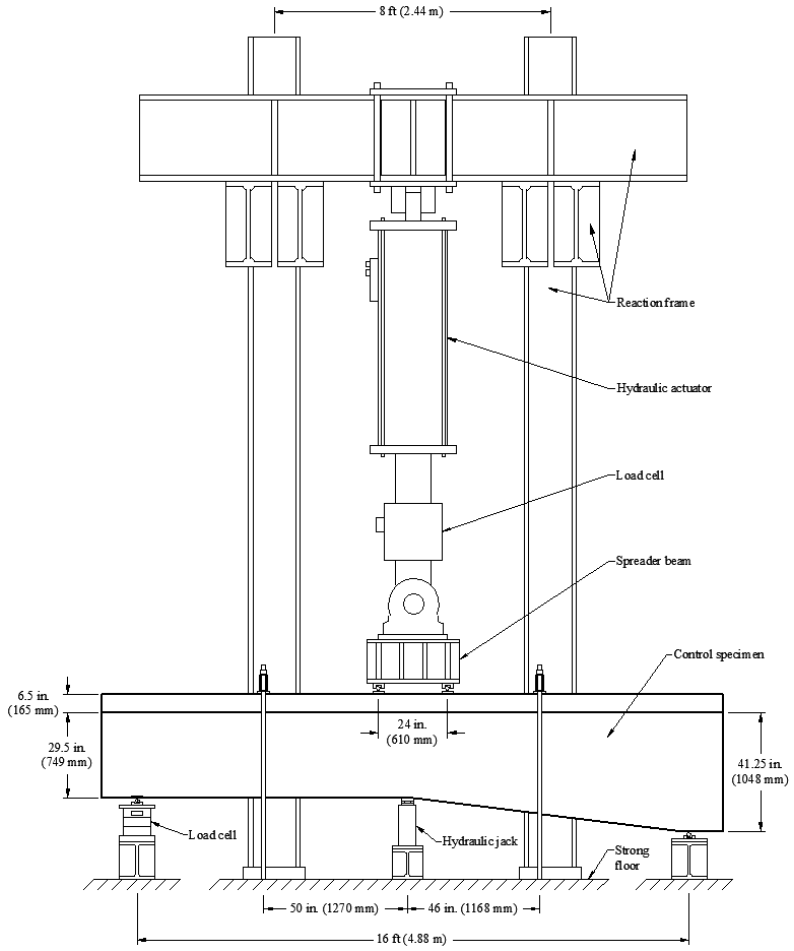


Figure F.27 – Four-point load configuration used for specimen testing

Before testing, the actuator was plumbed and the specimens were leveled in the transverse direction. The specimen was centered in the load frame in both the transverse and longitudinal directions. All instruments were initialized to zero. To induce the dead load effects that the existing bridge is under, a 34.5 kip (153 kN) load was applied to the underside of the beam using a hydraulic jack. The beam was anchored down on each side of the jack using 3 x 6 x 5/16 in. (76 x 152 x 8 mm) steel tubes tied down with rods threaded into a strong floor spaced approximately 48 in. (1219 mm) from the jack. The dead and live load

configurations for the control beam are shown in Figure F.28. For the control beam, after the beam reached the required load to induce the dead load effects, the pressure was released, the jack was removed, and live loading was performed. For the retrofitted specimen, the beam was placed into the setup after the grooves were cut, the dead load was applied and the NSM-titanium was installed and left to cure for 7 days under the dead loading. After the epoxy cured, the load was released, inducing the dead load effects into the titanium. The hydraulic jack was removed and live loading was performed.

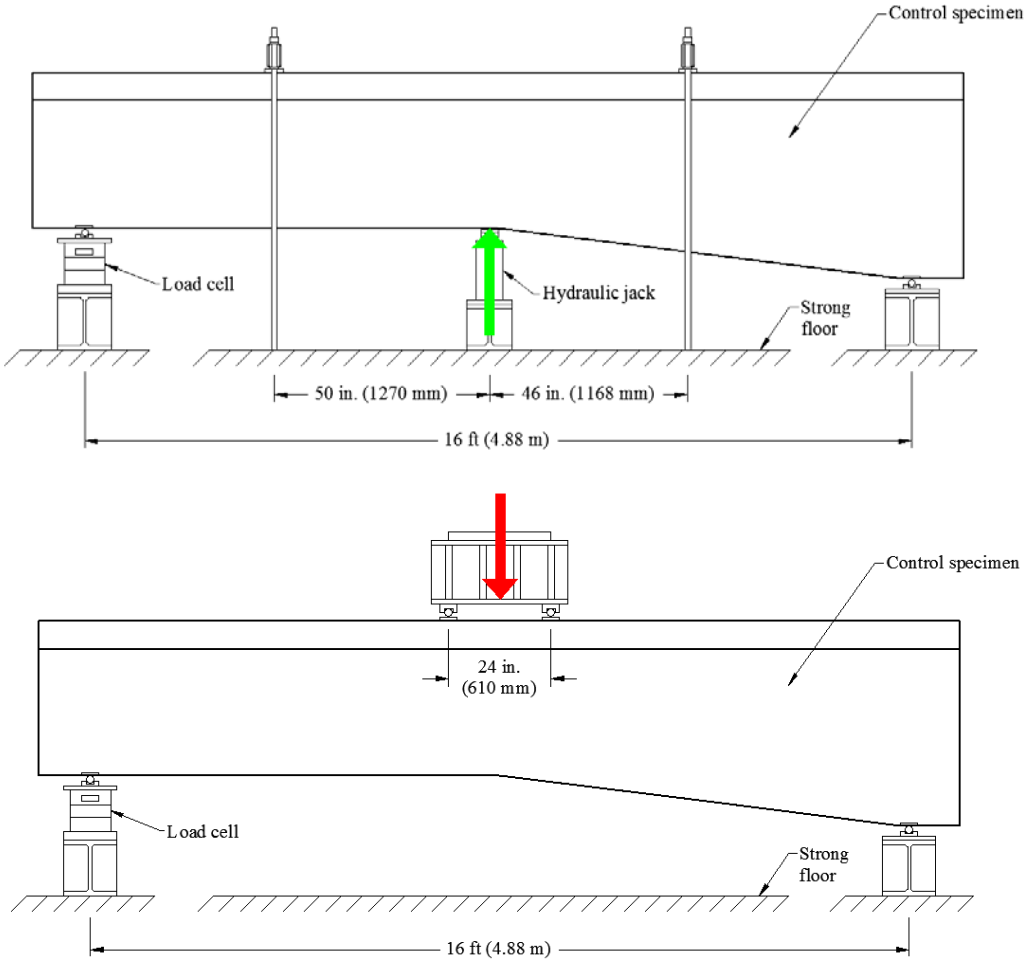


Figure F.28 – Specimen dead and live loading

Tests were conducted using pseudo-static cyclic loading without load reversals. Each load step was increased by 10 kips (44 kN) for the control specimen and 25 kips (111 kN) for the retrofit specimen from the previous load cycle as seen in Table F.5. Load was applied at a rate of 0.15 kip/sec (0.67 kN/sec). Upon reaching each new load step, the load was reduced by 5 kips (22 kN) for the control and lower load cycles for the retrofit and by 10 kips (44 kN) for higher retrofit load cycles so cracks could be identified, marked, and recorded on the beam with minimized creep effects.

Table F.5 – Specimen load cycle intervals

| **Control Load Step** | |
|---|---|
| **(kip)** | **(kN)** |
| 0-10 | 0-44.5 |
| 5-20 | 22.2-89 |
| 5-30 | 22.2-133 |
| 5-40 | 22.2-178 |
| 5-50 | 22.2-222 |
| 5-60 | 22.2-267 |
| 5-Failure | 22.2-Failure |

| **Retrofit Load Step** | |
|---|---|
| **(kip)** | **(kN)** |
| 0-10 | 0-44.5 |
| 5-25 | 22.2-111 |
| 5-50 | 22.2-222 |
| 5-75 | 22.2-334 |
| 5-100 | 22.2-445 |
| 5-Failure | 22.2-Failure |

## F.8 Experimental Results

### F.8.1 Overall Specimen Response

The applied load at failure and the shear forces action on the section are reported in Table F.6. The shear forces include the applied load, applied shear from the actuator, $V_{APP}$; the shear force from the portion of the self-weight of the beam acting on the failure plane, $V_{DL;}$

and the sum of these as the total shear force, $V_{EXP}$. The self-weight shear, $V_{DL}$, was calculated using a of reinforced concrete unit weight of 150 lb/ft$^3$ (23.6 kN/m$^3$) to estimate the weight of concrete acting on the diagonally cracked failure plane.

Table F.6 – Applied load and shear values at failure

| **Specimen** | **Applied Load kips (MN)** | **$V_{APP}$ kips (kN)** | **$V_{DL}$ kips (kN)** | **$V_{EXP}$ kips (kN)** |
|---|---|---|---|---|
| Control | 63.7 (0.283) | 31.9 (141.6) | 0.27 (1.2) | 32.1 (142.8) |
| Retrofit | 131.5 (0.585) | 65.8 (292.5) | 0 (0) | 65.8 (292.5) |

The failure modes, failure crack angles, and midspan displacement at peak load are provided in Table F.7 Secondary failure of the retrofitted specimen occurs at a maximum of 86.4 kips (384 kN) and the corresponding midspan displacement is also shown. The definition of the secondary failure is described in Section F.8.4.

Table F.7 – Failure mode, crack angle, midspan displacement

| **Specimen** | **Failure Mode** | **Failure Crack Angle (deg)** | **Failure Midspan Disp. in. (mm)** | **Secondary Failure Midspan Disp. in. (mm)** |
|---|---|---|---|---|
| Control | Anchorage | 68 | 0.26 (6.55) | n/a |
| Retrofit | Anchorage | 90 | 1.01 (25.7) | 1.60 (40.6) |

F.8.2 Displacement Results

*F.8.2.1 Load-Deformation Responses*

The load-deformation responses at midspan for the specimens are shown in Figure F.29 and F.30. The midspan displacements were determined by taking the average midspan displacements and subtracting the average of the support settlements.

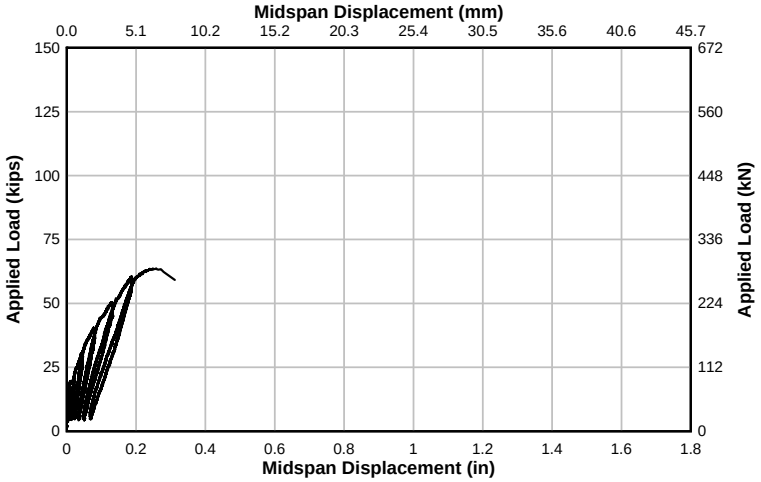


Figure F.29 – Control specimen load-midspan displacement

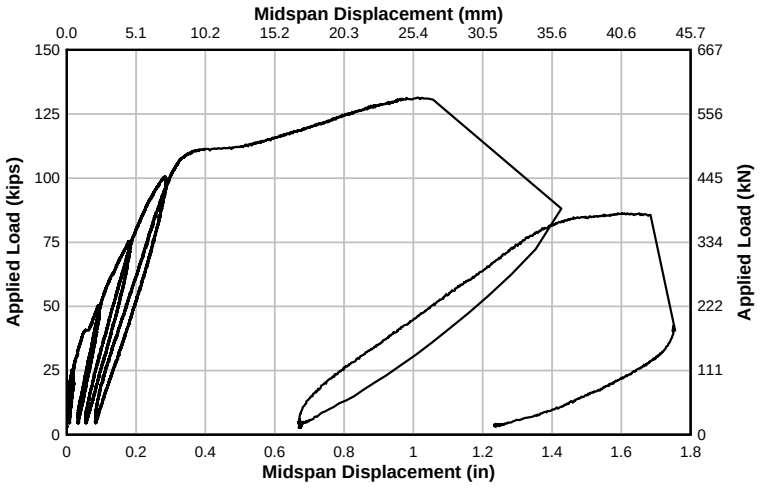


Figure F.30 – Retrofit specimen load-midspan displacement

*F.8.2.2 Load-Diagonal Displacement Responses*

Diagonal string potentiometers were used to measure the change in crack widths crossing the sensor. The sensors were numbered, as seen in Figure F.31, with the arrow showing the direction of measurement. Figures F.32 and F.33 show the load-diagonal displacement responses for each specimen.

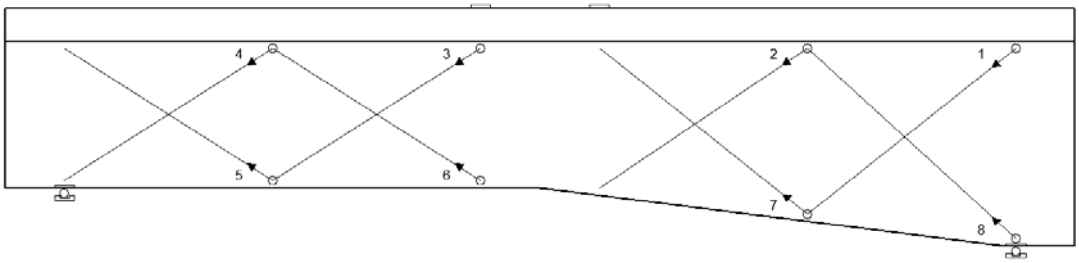


Figure F.31 – Typical specimen diagonal sensor numbering

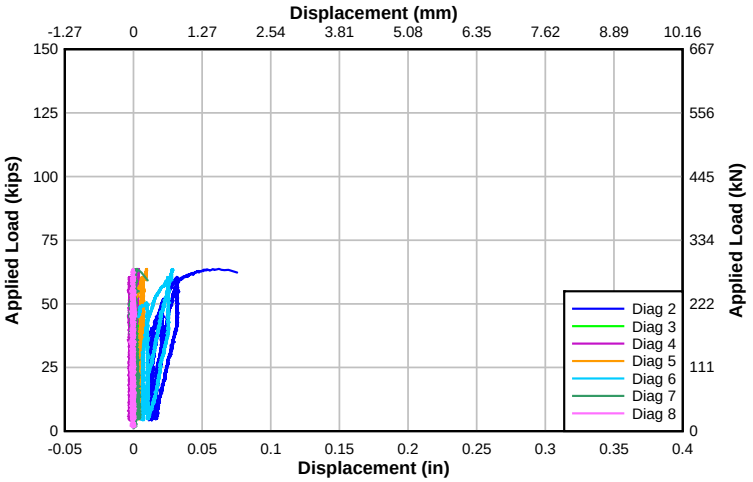


Figure F.32 – Control specimen load-diagonal displacement

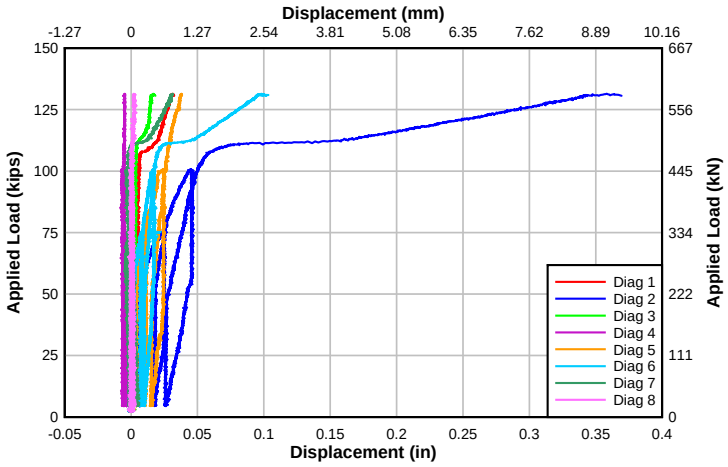


Figure F.33 – Retrofit specimen load-diagonal displacement

F.8.3 Anchorage Slip Responses

Bar slip was only measured for the control specimen. A plot of the load-slip response is shown in Figure F.34. Slip was not observed until at or near failure when chevron cracking developed as the concrete cover split around the #8 (M25 bar). The graph illustrates that throughout the specimen loading both bars slipped at almost exactly the same rate.

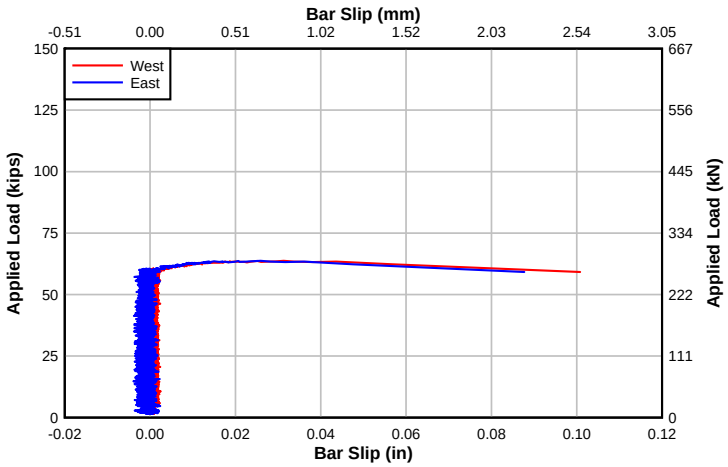


Figure F.34 – Control specimen load-bar slip

From observation of the retrofitted specimen, the chevron cracking occurred before failure and the specimen continued to carry higher loads as the titanium carried the extra stresses that the slipped bar could not.

F.8.4 Crack Propagations

Crack propagations were monitored throughout the each test. After reaching each successive load level, the applied load was reduced by 5 kips (22 kN) for the control specimen and 10 kips (44 kN) for the retrofitted specimen. The load was held at this lower level while new cracks were marked on the beam in order to reduce creep deformations in the specimen. Pictures were taken at each load level after crack mapping.

Photographs taken at failure are shown in Figure F.35. The anchorage failure in each specimen can be seen in the large longitudinal chevron cracking in the web. The cracking begins at the end of the #8 (M25) bars in both specimens and extends to the ends of the #9 (M29) bars. The control specimen also had a large shear-flexure crack open at failure due to the deformation in the beam caused by the anchorage failure. Sometime after the anchorage failed in the retrofitted specimen, the adhesion of the NSM concrete-epoxy interface was lost, effectively debonding the titanium. At this point the maximum achievable load had been reached (primary failure) and loading was stopped. The unloading curve (Figure F.30) showed that the retrofitted specimen appeared to have some reserve capacity; therefore the beam was loaded a final time. This final loading was stopped upon fracture of one titanium bar just prior to the embedded hook (secondary failure). Figure F.36 shows an illustration of the crack mapping.



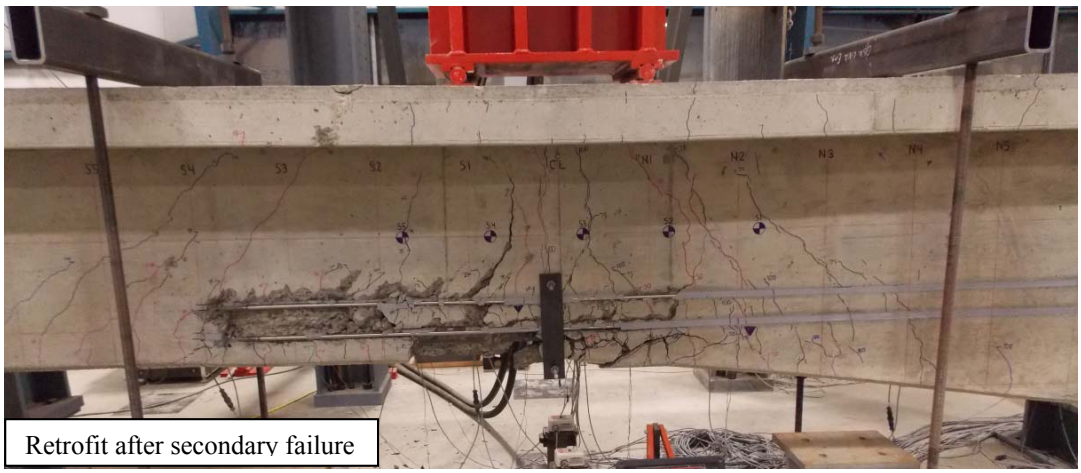


Figure F.35 – Failure photographs of test specimens

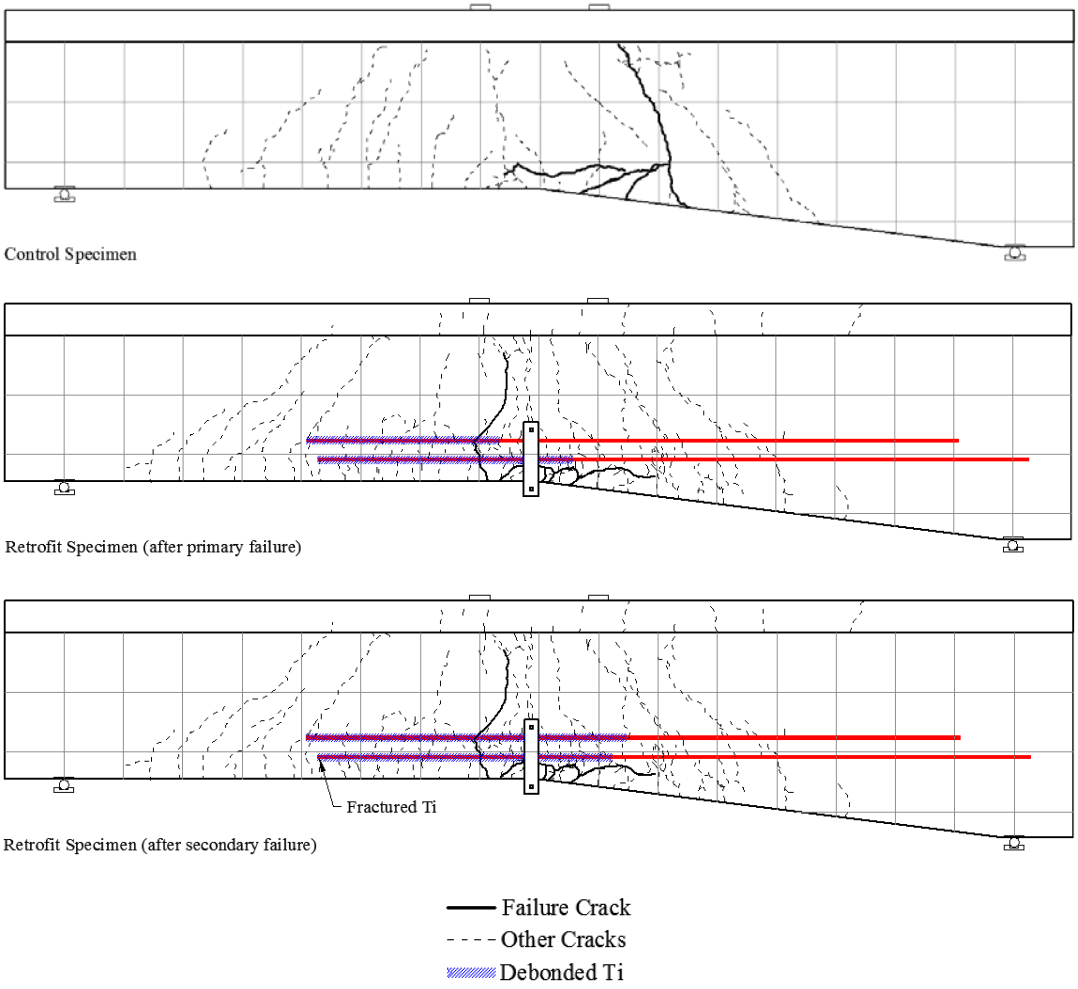


Figure F.36 – Specimen crack mapping with failure cracks

## F.8.5 Material Strains

Strain gages placed on the internal steel and NSM reinforcing (retrofit specimen) measured the strains in each beam throughout each test. Comparing the material strains along the beam length and the strains in each instrumented cross-section shows the changes in the behavior of each beam during loading.

*F.8.5.1 Comparative Material Strains*

Strains along the length of the beam in the bottom steel bars and the NSM material (retrofit specimen) were measured for each beam. The steel strains for both specimens were similar. The comparative material strains for each beam are shown from Figure F.37 to F.39.

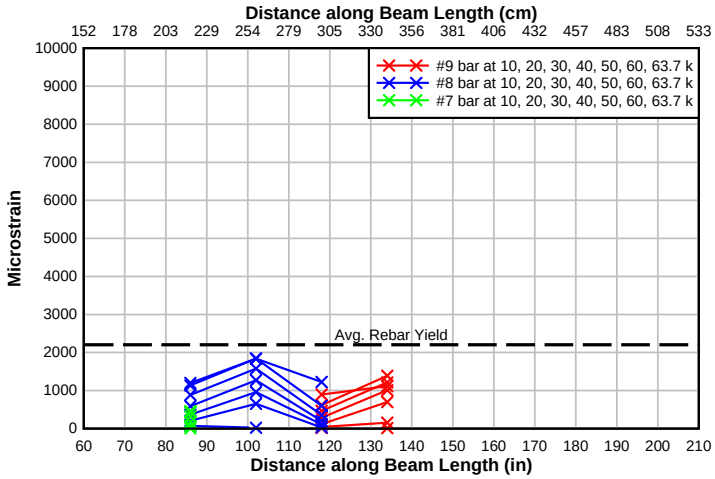


Figure F.37 – Control specimen bottom bar strain-distance along beam length

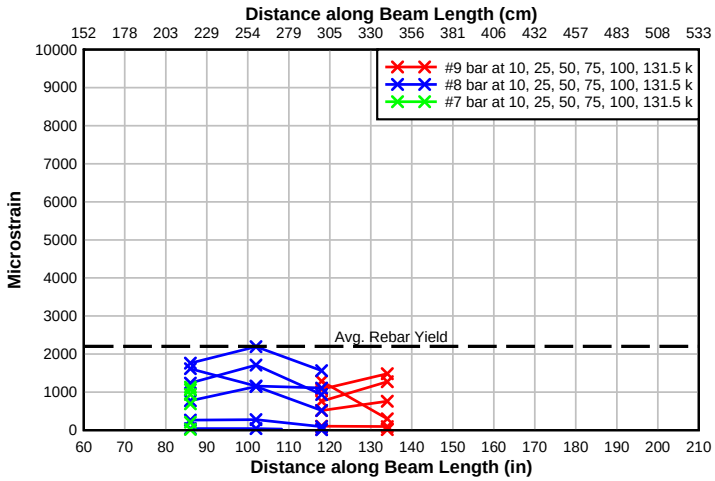


Figure F.38 – Retrofit specimen bottom bar strain-distance along beam length

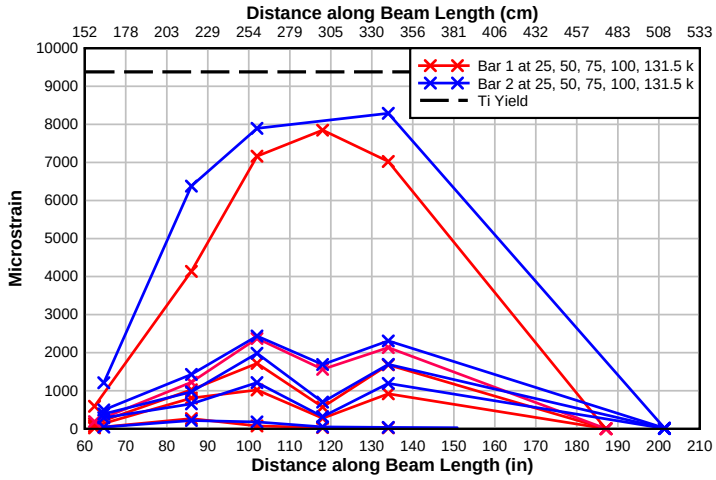


Figure F.39 – Retrofit specimen titanium bar strain-distance along beam length

*F.8.5.2 Sectional Strains*

Specific cross-sections on each beam were instrumented to show the fluctuation in strain in each material. Figures F.40 and F.41 illustrate the strain gage and section labeling convention for the specimens. Strain gages were placed on the longitudinal bars and NSM in the anchorage cutoff region and also near the hooks of the NSM bars. The critical sections in the beam spanned from Section 2 to Section 5. The section strains are shown for the control and retrofitted specimens in Figures F.42 to F.51.

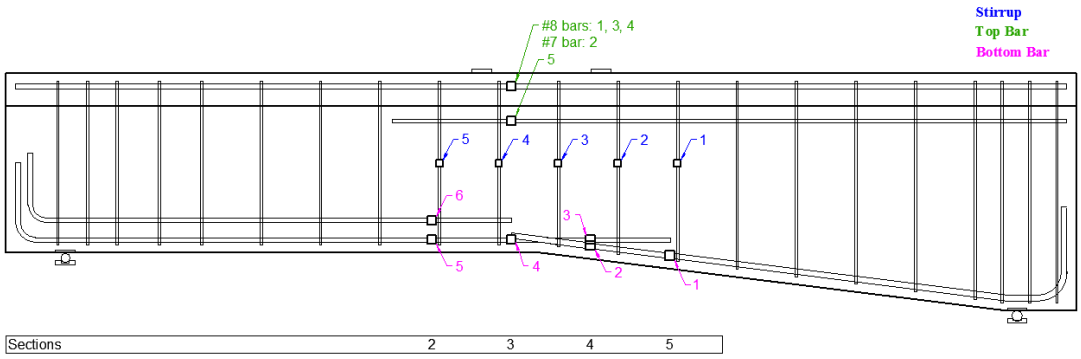


Figure F.40 – Control specimen strain gage labeling convention

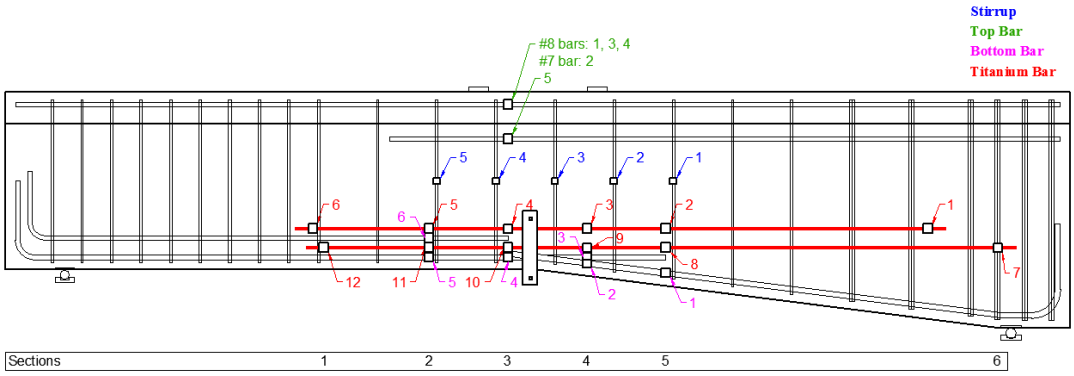


Figure F.41 – Retrofit specimen strain gage labeling convention

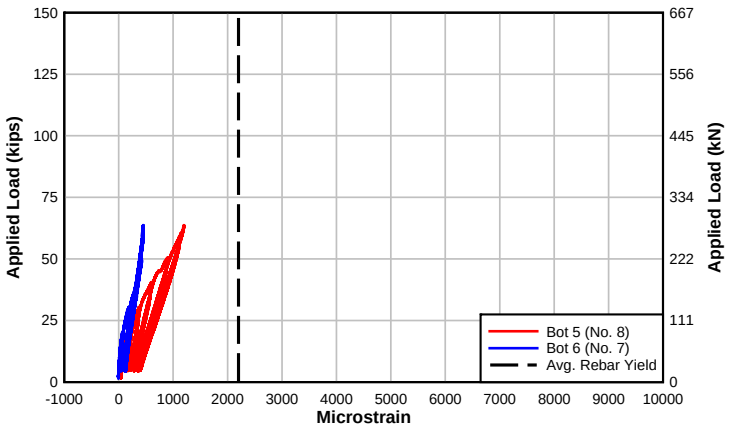


Figure F.42 – Control specimen load-flexural bar strain (Section 2)

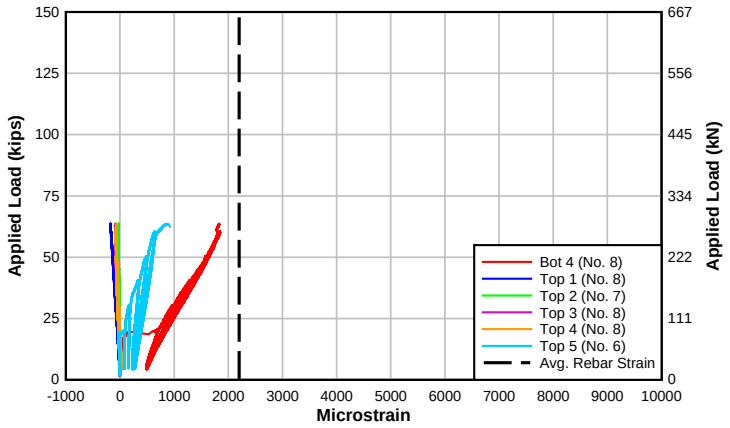


Figure F.43 – Control specimen load-flexural bar strain (Section 3)

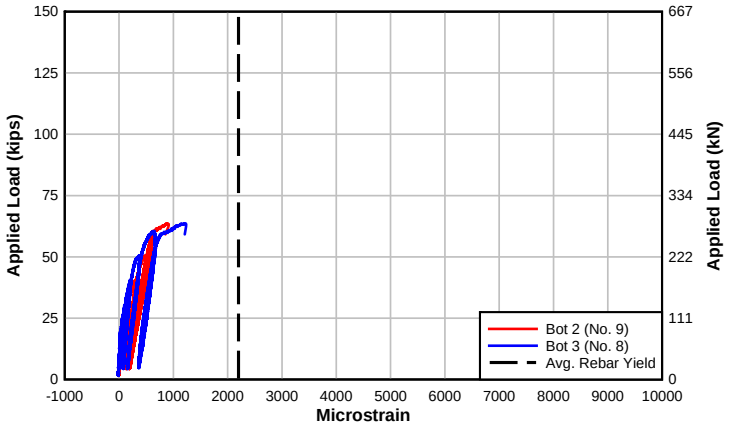


Figure F.44– Control specimen load-flexural bar strain (Section 4)

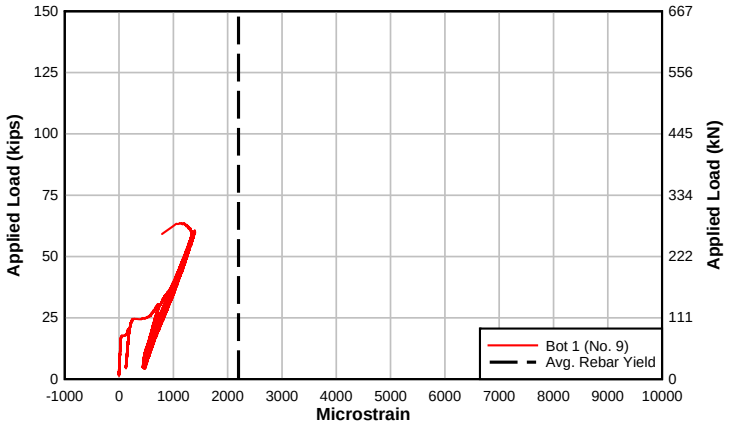


Figure F.45 – Control specimen load-flexural bar strain (Section 5)

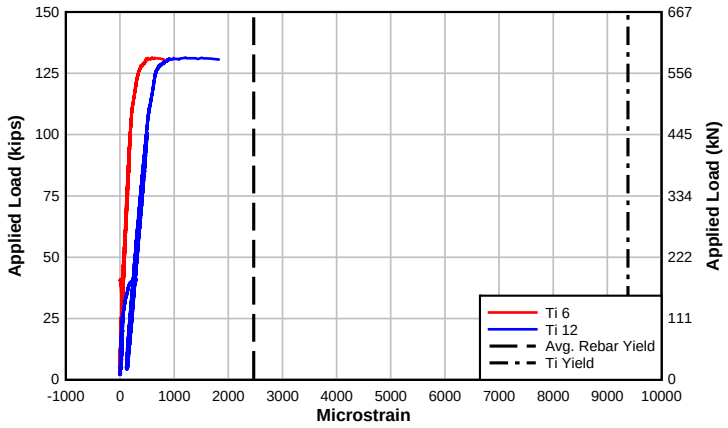


Figure F.46 – Retrofit specimen load-flexural bar strain (Section 1)

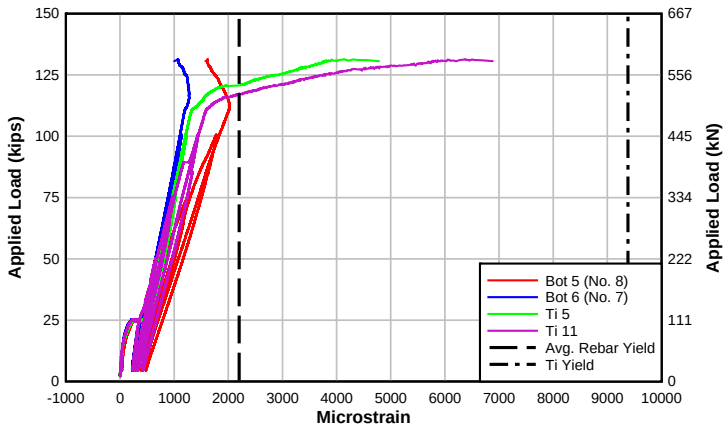


Figure F.47 – Retrofit specimen load-flexural bar strain (Section 2)

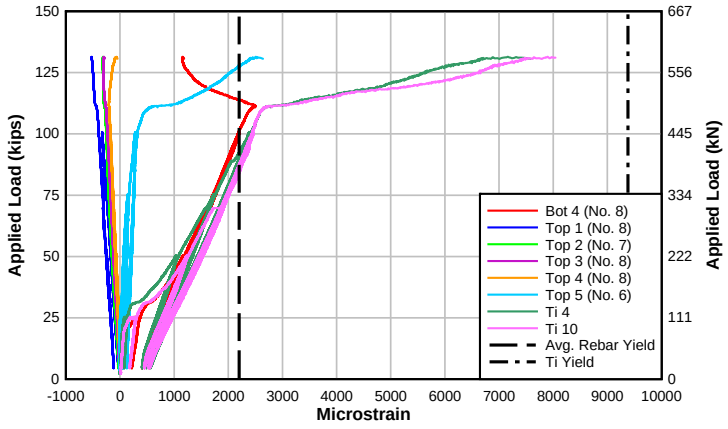


Figure F.48 – Retrofit specimen load-flexural bar strain (Section 3)

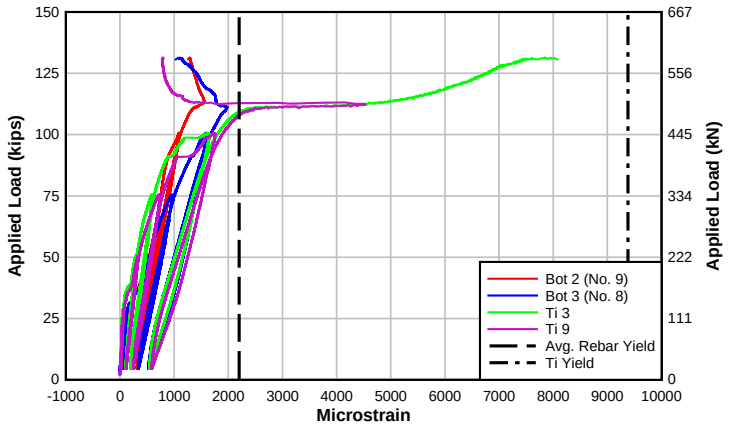


Figure F.49 – Retrofit specimen load-flexural bar strain (Section 4)

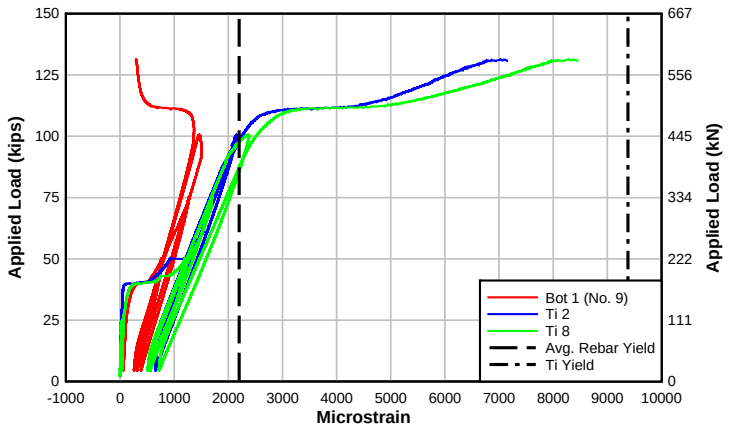


Figure F.50 – Retrofit specimen load-flexural bar strain (Section 5)

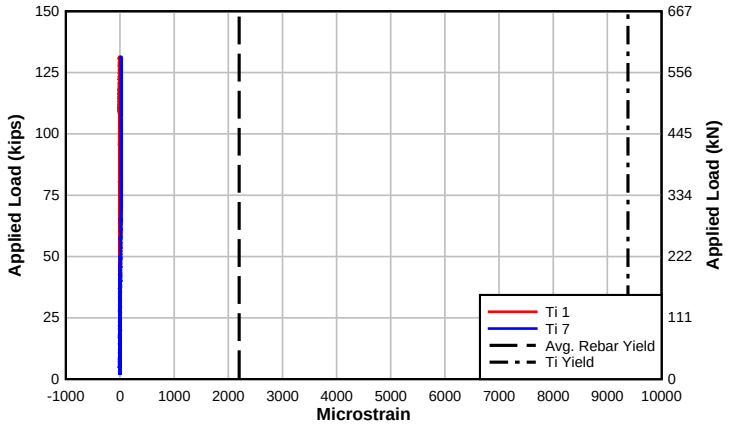


Figure F.51 – Retrofit specimen load-flexural bar strain (Section 6)

*F.8.5.3 Mid-height Stirrup Strains*

Strain gages were placed mid-height on stirrups in the anchorage cutoff region. Stirrup locations and labels are shown in Figures F.40 and F.41. The stirrup response from the control and retrofitted specimens are shown in Figures F.52 and F.53.

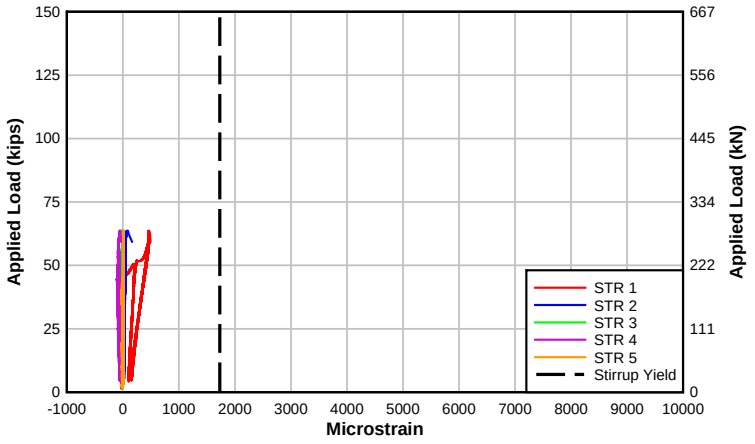


Figure F.52 – Control specimen load-mid-height stirrup strain

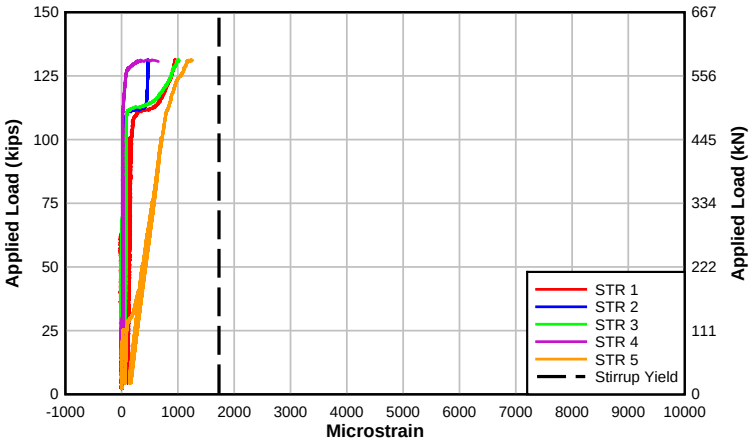


Figure F.53 – Retrofit specimen load-mid-height stirrup strain

**F.9 Design and Analytical Predictions versus Experimental Results**

The following plots in Figures F.54 and F.55 illustrate the design (AASHTO) and analytical (Response 2000) predictions for the control and retrofitted girders. The experimental moment versus midspan displacement is shown for each beam and compared to the capacity predictions. The factored demand on the girder is also shown.

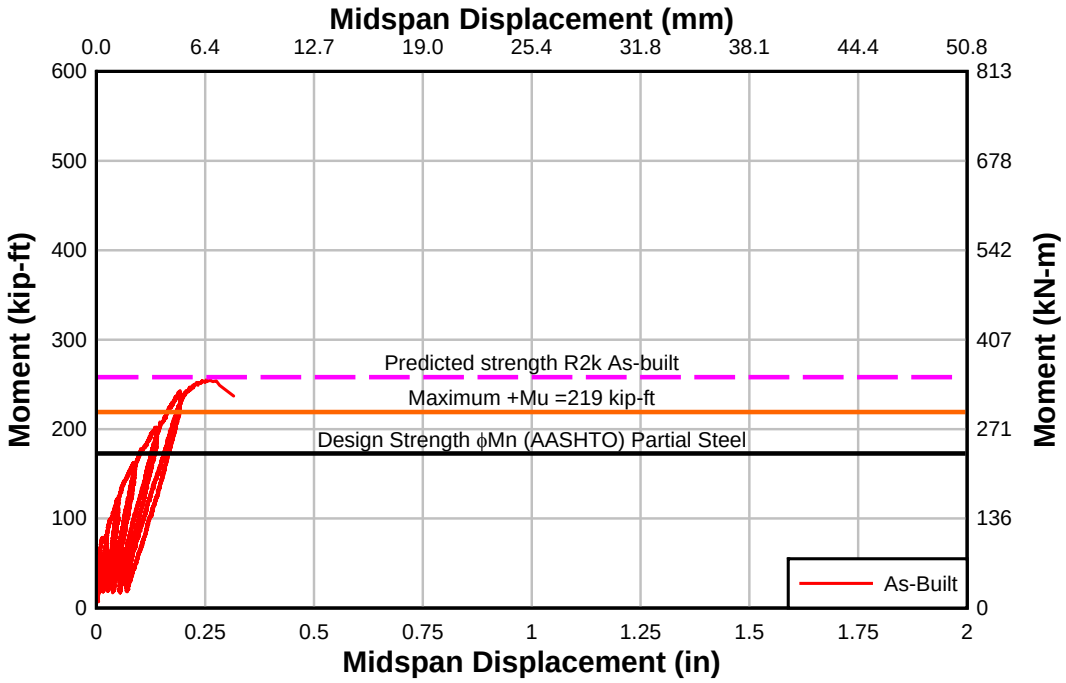


Figure F.54 – Control specimen design predictions-experimental results

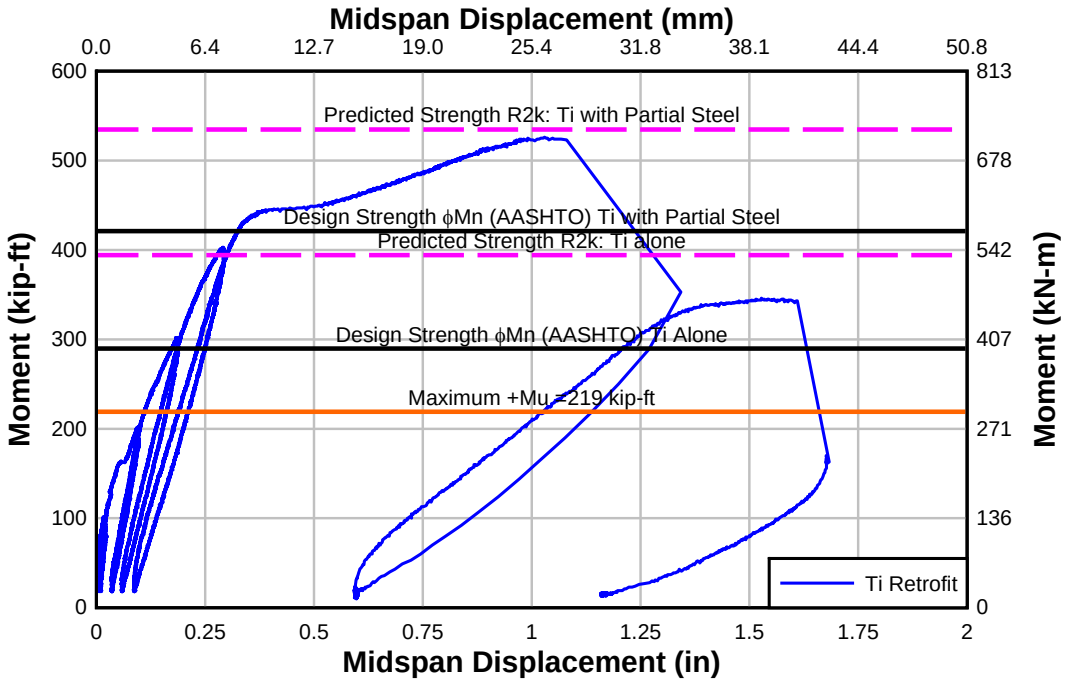


Figure F.55 – Retrofit specimen design predictions-experimental results

**F.10 Discussion of Results and Implementation**

The experimental results show an increase in beam capacity from 63.7 kips (283 kN) to 131.5 kips (585 kN). The retrofit more than doubled the capacity of the as-built specimen. The designer's assumption to exclude the contribution from the partial steel proved to be conservative as both the control specimen and retrofitted specimen showed the partial steel did in fact contribute to the overall strength of the beam. The AASHTO predictions were conservative in all cases. Response 2000 predicted the capacity of both specimens well. The retrofitted specimen showed that even with loss of anchorage and loss of bond to the titanium, there was still more than enough reserve capacity to exceed the maximum demands on the specimen.

Experimentally observed cracks in the control specimen were similar to those seen in the actual bridge. Chevron cracks were observed over the embedded steel cutoff bars prior to failure of both specimens. This type of cracking is an indicator that inspectors should look for at known cutoff locations in RCDGs. The as-built details of the control specimen exhibited poor performance in both strength and ductility. In contrast, the NSM-titanium retrofitted specimen achieved a much higher load and far greater ductility. The titanium helped to delay the cutoff bar slip, achieve a much higher overall deformation capacity, and provide a greater distribution of cracking. The high strength, ductility, environmental durability, and ability to fabricate mechanical anchorages make the Ti-6Al-4V alloy titanium reinforcement a viable material for strengthening civil infrastructure such as the Mosier Bridge.

Construction of on the actual bridge began in April 2014 and was finished by the end of May 2014. Titanium bars were installed at critical locations along the span lengths, like those in the retrofitted specimen, to increase the load capacities of the existing girders. Girders were strengthened for shear by using internal shear anchors. Negative moment capacities were also increased through installation of a single titanium bar in the deck at each of the critical locations. The deficient crossbeams were strengthened using an external post-tensioning system and cracks greater than 0.015 inches (0.381 mm) were sealed. After construction was finished, the bridge was fully reopened and the load postings were removed.